Structure Modeling and Property Calculations of Amorphous Materials

by

Ilia Ponomarev

DISSERTATION

Submitted in partial fulfillment of the requirements

For the degree of Doctor of Philosophy

At The University of Texas at Arlington

May, 2019

Arlington, Texas

Supervising committee:

Peter Kroll, Supervising Professor

Kwangho Nam

Frank W. Foss Jr

Purnendu K. Dasgupta

ABSTRACT

The demand in discovery of novel materials for a seemingly infinite list of applications is growing year by year. Even though it's not uncommon to find the application for the material after its discovery upon experimentally studying its properties, it can be essential to be able to build the material to satisfy the specific need. This kind of targeted development for a specific application requires deep understanding of the "*synthesis => structure => properties*" sequence, and this is why insights into the mechanisms of the synthesis, structure formation and structure vs. properties relations are highly desired.

Structural insights can be obtained through wide variety of spectroscopic techniques that are at our disposal nowadays. However, in solids, especially in disordered solids, these measured spectra provide a lot of room for misinterpretation, which leads to the necessity of supporting experimental findings with computations.

My research is divided into 2 parts. Part I is dedicated to the computational attempts to enhance the experimental NMR findings by providing structure vs. NMR signal relations obtained via modeling and calculations. We provide means to reinterpret the NMR spectra of hafnia-silica sol-gel glasses (Chapter I), we explore silicon nitrides (Chapter II) and help in solving crystal structure of silicophosphate (Chapter III). Part II represents a successful attempt to develop a Reactive Force Field parameterization suitable to perform accurate simulations of the formation of silicon oxycarbide ceramic materials from polymer precursors. The results of my ReaxFF simulations are in good agreement with the experimental findings on PHMS-DVB system (Chapter I) and a different polymeric system, siloxane cross-linked with 4,4'-biphenol (Chapter II).

ACKNOWLEDGEMENTS

First I would like to thank my advisor Peter Kroll. With this work I moved to the completely new field of computational research, and my work wouldn't have been possible without his valuable guidance, support and patience. I am very thankful to him for his efforts to contribute to my professional development through sending me to the conferences, meetings and collaborative work during my time as PhD student.

I want to express special gratitude my Dissertation Committee members: Dr Kwangho Nam, Dr. Frank Foss and Dr. Purnendu Dasgupta for being accommodating and dedicating their time to evaluation of my progress as PhD student.

I would like to thank the professors that worked in collaboration with us, especially Dr Adri C.T. van Duin from Pennsylvania State University for providing valuable guidance and Dr Edwin Kroke from TU Bergakademie Freiberg for giving me a chance to spend my internship doing research in his group.

I was lucky to have my colleagues from the group and the school: Beata Smith, Alena Trinidad-Denisenko, John Paul Nimmo II, Greg Monson, Susana Aguiree-Medel, Poroshat Taheri, Shariq Haseen, Aaron West, Hanof Alkhadi and Akshada Hande. My special gratitude belongs to Atreyi Dasmahapatra for providing valuable guidance in my first steps of working in the field of computations.

Thank you to the chemistry department support staff – Jill Howard, Debbie Cooke, Stephanie Henry for help in dealing with the University-related bureaucracy. I thank Dr. W. Cleaver, Dr. H. Conrad and Dr. C. Griffith for help during my teaching. Another thanks goes to Noor Alwachi for help and guidance with the laboratory hardware and software.

Finally I thank my family for support of my decision to go so far away for my PhD and patience in waiting for me to get one.

TABLE OF CONTENT

LIST OF FIGURES AND TABLES

INTRODUCTION

PART I

CHAPTER 1

CHAPTER 2

CHAPTER 3

PART II

CHAPTER 1

CHAPTER 2

LIST OF ABBREVIATIONS

DFT:	Density Functional Theory
NMR:	Nuclear Magnetic Resonance
GIPAW:	Gauge Including Projected Augmented Wave method
ReaxFF:	Reactive Force Field
MD:	Molecular Dynamics
CPU:	Central Processing Unit
VASP:	Vienna Ab initio Simulations Package
PAW:	Projected Augmented Wave method
GGA:	Generalized Gradient Approximation
PBE:	Perdew, Burke, and Ernzerhoff Generalized Gradient Approximation
LAMMPS:	Large-scale Atomic/Molecular Massively Parallel Simulator package
XRD:	X-Ray Diffraction
a-SiCO:	Amorphous silicon oxycarbide
PMHS:	Polymethylhydridosiloxane
DVB:	Divinylbenzene
δ_{iso}:	Isotropic NMR chemical shift
FWHM:	Full Width at Half Maximum
NS25, NS33:	soda-silica glasses with soda content of 25 and 33 mol-% respectively
NBO:	Non-bridging oxygen
WWW:	Wooten, Winer, Weaire network algorithm
CN:	Coordination Number
NTE:	Negative Thermal Expansion
MAS:	Magic Angle Spinning
HETCOR:	Heteronuclear Correlation NMR
REDOR:	Rotational Echo Double Resonance NMR

CP-RFDR:	Cross-Polarization – Radiofrequency Driven Dipolar Recoupling
aiMD:	ab initio Molecular Dynamics
MWCNT:	Multiwall Carbon Nanotube
TMOS:	Tetramethyl Orthosilicate
DHBP:	4,4’-dihydroxybiphenyl
PDC:	Polymer-Derived Ceramics
FTIR:	Fourier-transform infrared spectroscopy
TEM:	Transmission Electron Microscopy
STEM:	Scanning Transmission Electron Microscopy
EDS:	Energy Dispersive Spectrometry
MC:	Monte-Carlo method
MCS:	Monte-Carlo sweep
RLBM:	Radical-like breathing modes
BET:	Brunauer-Emmet-Teller analysis

INTRODUCTION

The demand in discovery of novel materials for a seemingly infinite list of applications is growing year by year. Even though it's not uncommon to find the application for the material after its discovery upon experimentally studying its properties, it can be essential to be able to build the material to satisfy the specific need. This kind of targeted development for a specific application requires deep understanding of the "*synthesis => structure => properties*" sequence, and this is why insights into the mechanisms of the synthesis, structure formation and structure vs. properties relations are highly desired.

Structural insights can be obtained through wide variety of spectroscopic techniques that are at our disposal nowadays. However, in solids, especially in disordered solids, these measured spectra provide a lot of room for misinterpretation, which leads to the necessity of supporting experimental findings with computations.

Density Functional Theory (DFT) is first-principle method based on Hohenberg-Kohn theorem and solving Kohn-Sham equations[1]; the energy of the system is a functional of its electron density. This method provides accurate predictions regarding structures and energies of the materials. It also enables first-principle calculations of spectroscopic properties, such as NMR signals within GIPAW approach[2]. However, the method is computationally intensive. To remain within reasonable wall-clock times, DFT calculations have to remain within system sizes of 1000 atoms, and last for maximum hundreds of picoseconds.

Simple empirical potentials, such as Tersoff[3], are capable of reproducing structural features like radial distribution function "on a gross scale"[4-5]. Certain properties of the materials e.g. cohesive energies[5] or thermal conductivity[6] can be calculated within Tersoff potential, and the calculations would yield the results comparable to the experiment. Such class of the potentials enables simulations of the significant system sizes and time scales: millions of atoms for nanoseconds. However, the potentials lack accuracy in describing local structural features: under- and overcoordination of atoms in the models generated via melt-quench is very common[4]. Besides that, this class of potentials is normally "unrealistic": some atom-to-atom interactions are not taken into account. This limits the range of systems that can be described and makes modeling of chemical processes with those force fields a questionable approach: it might work for very simple model systems, but it isn't universal.

Reactive Force Field (ReaxFF)[7] is an attempt to bridge the gap between "accurate but slow" quantum chemistry and "quick but flawed" empirical force field calculations. The functional form of the potential is very complicated and takes into account bonding interactions, charge balancing and Coulomb interactions, van der Waals interactions, hydrogen bonding and angle/torsion strains[7]. Additional energy terms are present for under- and overcoordination of atoms; allene and aromatic corrections are present as well:

$$\begin{aligned} E_{system} &= E_{bond} + E_{lp} + E_{over} + E_{under} + E_{val} + E_{pen} + E_{coa} + E_{C2} \\ &+ E_{tors} + E_{conj} + E_{H-bond} + E_{vdWaals} + E_{Coulomb} \end{aligned} \tag{1}$$

The equations of ReaxFF use 39 general parameters, 32 atomic parameters, 16 parameters to describe each bond (additional 7 can be used for heteroatomic bonds), 7 parameters per each angle, 6 parameters per torsion, and 4 parameters to take care of hydrogen bonding. Therefore ReaxFF requires a lot of work in parameter development in order to provide a viable description for a broad range of compositions. But once it's done, ReaxFF simulations can be at the level of accuracy comparable to DFT; for molecular reactions and even for the molecules on surfaces ReaxFF has been shown to approach DFT level of accuracy[7-9]. Some force fields[10] have shown good results for extended systems like silica[11] or silica with water[12] as well.

The calculations with this potential are obviously significantly slower than some simpler one, e.g. Tersoff; however, ReaxFF is still much faster than DFT. Table 1 provides some comparison of the computational expenses of DFT, ReaxFF and Tersoff potential.

Table 1. Approximate computational expenses on an MD simulation involving 120 atoms in CPU seconds per atom per core.

DFT	ReaxFF	Tersoff
$4\cdot10^{-1}$	$2\cdot10^{-3}$	$2\cdot10^{-6}$

Another significant point about computational expenses is scaling with the size and number of atoms N: DFT calculations within VASP (PAW, GGA, PBE)[13-16] scale ~N^3, while for ReaxFF calculations within LAMMPS[17-18] it is only ~N. Therefore almost 2 orders of magnitude difference between ab initio MD and ReaxFF MD for 100 atoms will transform into 4 orders of magnitude for 100 atoms, which is hours and days of wall-clock time instead of months and years.

One part of this work is dedicated to computational NMR investigations. The goal of the work was to find structure vs. chemical shift relations from modeling and calculations and therefore to provide means to extract structural features from the experimentally measured spectra. The list of systems I explored included:

1) Hafnia-soda silica glasses, a model system to study the effects of heavy metal oxides incorporation into glasses for applications like nuclear waste immobilization[19]. Addition of hafnia increases glass toughness and chemical durability[20]. More than that, substitution of Na onto H in these glasses converts them into models of sol-gel hafnia-silica glasses. Here I provided a set of relations between Si-O-Si/Hf angles for a variety

of Si units and, basing on my findings, suggested reinterpretation of the experimentally measured ^{29}Si NMR spectra of sol-gel hafnia-silica glasses.

2) Silicon nitrides, a set of materials with outstanding thermal and mechanical properties[21]. These are used as materials for turbocharges, temperature-resistant coatings, cutting tools, ball bearings. I explored NMR of crystalline, hypothetical crystalline and amorphous silicon nitrides and revealed structural features that affect ^{29}Si δ_{iso}: Si-N bond length and distance to 5th nearest neighbor in amorphous Si_3N_4. I also studied some other compounds with Si-N bonds, silicon diimide and silicon carbodiimide. In both cases N atom can be considered 2-connected, and I discover the effect of respectively Si-N-Si and Si-N-C angles on ^{29}Si NMR.

3) Silicophosphates, materials that comprise 6-coordinated Si at normal pressure[22]. This research was done in close collaboration with the experimental group of Prof. Kroke at TU Bergakademie Freiberg. Here I contributed to characterization of crystalline phase that was obtained via both sol-gel synthesis and dissolution of Si nanoparticles in phosphoric acid. The “Rietveld-refinable” X-Ray spectrum wasn’t obtained, but I was able to derive a model of crystalline $Si(HPO_4)_2$ from related zirconium phosphate structure. ^{29}Si and ^{31}P NMR chemical shifts of the structure matched the experimental observations; peak positions of calculated XRD spectrum matched the experimentally measured ones. Additional NMR calculations revealed potential causes of additional peaks in the measured NMR spectra.

Another part of my research was dedicated to development of ReaxFF parameterization suitable to describe amorphous silicon oxycarbide. Attractive properties of a-SiCO include high-temperature stability[23-24], chemical durability[25] and mechanical properties[26]. Applications of silicon oxycarbide include dielectric materials[27], anodes for Li-ion batteries[28], membranes for gas separation[29], thermal barrier coatings[30]. These materials are most commonly synthesized via molecular approach, such as pyrolysis of polymer precursor[31]. The composition and properties of the resulting ceramic depends heavily on the initial precursor and processing techniques, which is why better insight in the processes is highly desirable. Therefore the goal of this project was to be able to model formation of silicon oxycarbide from polymer precursors. I took Newsome parameter[32] set as the starting point of the parameter development, included C parameters by Srinivasan[33] and developed a new parameterization via extensive learning process. The final parameter set is capable of describing interactions between Si, C, O, H atoms with DFT level of accuracy; I successfully simulated polymer-to-ceramic conversion for PHMS polymer cross-linked with DVB.

References

1. Hohenberg, P.; Kohn, W., Inhomogeneous Electron Gas. *Phys Rev B* **1964**, *136*, B864-+.
2. Pickard, C. J.; Mauri, F., All-Electron Magnetic Response with Pseudopotentials: Nmr Chemical Shifts. *Phys Rev B* **2001**, *63*.
3. Tersoff, J., Empirical Interatomic Potential for Silicon with Improved Elastic Properties. *Phys Rev B* **1988**, *38*, 9902-9905.
4. Liao, N. B.; Xue, W.; Zhou, H. M.; Zhang, M., Molecular Dynamics Investigation of Structure and High-Temperature Mechanical Properties of Sibco Ceramics. *J Alloy Compd* **2014**, *610*, 45-49.
5. Munetoh, S.; Motooka, T.; Moriguchi, K.; Shintani, A., Interatomic Potential for Si-O Systems Using Tersoff Parameterization. *Comp Mater Sci* **2007**, *39*, 334-339.
6. Al-Ghalith, J.; Dasmahapatra, A.; Kroll, P.; Meletis, E.; Dumitrica, T., Compositional and Structural Atomisticstudy of Amorphous Si-B-N Networks of Interest for High-Performance Coatings. *J Phys Chem C* **2016**, *120*, 24346-24353.
7. van Duin, A. C. T.; Dasgupta, S.; Lorant, F.; Goddard, W. A., Reaxff: A Reactive Force Field for Hydrocarbons. *J Phys Chem A* **2001**, *105*, 9396-9409.
8. Soria, F. A.; Zhang, W. W.; van Duin, A. C. T.; Patrito, E. M., Thermal Stability of Organic Monolayers Grafted to Si(111): Insights from Reaxff Reactive Molecular Dynamics Simulations. *Acs Appl Mater Inter* **2017**, *9*, 30969-30981.
9. Soria, F. A.; Zhang, W. W.; Paredes-Olivera, P. A.; van Duin, A. C. T.; Patrito, E. M., Si/C/H Reaxff Reactive Potential for Silicon Surfaces Grafted with Organic Molecules. *J Phys Chem C* **2018**, *122*, 23515-23527.
10. Pitman, M. C.; van Duin, A. C. T., Dynamics of Confined Reactive Water in Smectite Clay-Zeolite Composites. *J Am Chem Soc* **2012**, *134*, 3042-3053.
11. Yu, Y. T.; Wang, B.; Wang, M. Y.; Sant, G.; Bauchy, M., Revisiting Silica with Reaxff: Towards Improved Predictions of Glass Structure and Properties Via Reactive Molecular Dynamics. *J Non-Cryst Solids* **2016**, *443*, 148-154.

12. Du, T.; Li, H.; Sant, G.; Bauchy, M., New Insights into the Sol-Gel Condensation of Silica by Reactive Molecular Dynamics Simulations. *J Chem Phys* **2018**, *148*.

13. Kresse, G.; Hafner, J., Ab-Initio Molecular-Dynamics Simulation of the Liquid-Metal Amorphous-Semiconductor Transition in Germanium. *Phys Rev B* **1994**, *49*, 14251-14269.

14. Kresse, G.; Furthmuller, J., Efficiency of Ab-Initio Total Energy Calculations for Metals and Semiconductors Using a Plane-Wave Basis Set. *Comp Mater Sci* **1996**, *6*, 15-50.

15. Blochl, P. E., Projector Augmented-Wave Method. *Phys Rev B* **1994**, *50*, 17953-17979.

16. Kresse, G.; Joubert, D., From Ultrasoft Pseudopotentials to the Projector Augmented-Wave Method. *Phys Rev B* **1999**, *59*, 1758-1775.

17. Aktulga, H. M.; Fogarty, J. C.; Pandit, S. A.; Grama, A. Y., Parallel Reactive Molecular Dynamics: Numerical Methods and Algorithmic Techniques. *Parallel Comput* **2012**, *38*, 245-259.

18. Plimpton, S., Fast Parallel Algorithms for Short-Range Molecular-Dynamics. *J Comput Phys* **1995**, *117*, 1-19.

19. Davis, L. L.; Darab, J. G.; Qian, M.; Zhao, D.; Palenik, C. S.; Li, H.; Strachan, D. M.; Li, L., Hafnium in Peralkaline and Peraluminous Boro-Aluminosilicate Glass and Glass Sub-Components: A Solubility Study. *J Non-Cryst Solids* **2003**, *328*, 102-122.

20. Bergeron, B.; Galoisy, L.; Jollivet, P.; Angeli, F.; Charpentier, T.; Calas, G.; Gin, S., First Investigations of the Influence of Ivb Elements (Ti, Zr, and Hf) on the Chemical Durability of Soda-Lime Borosilicate Glasses. *J Non-Cryst Solids* **2010**, *356*, 2315-2322.

21. Zerr, A.; Miehe, G.; Serghiou, G.; Schwarz, M.; Kroke, E.; Riedel, R.; Fuess, H.; Kroll, P.; Boehler, R., Synthesis of Cubic Silicon Nitride. *Nature* **1999**, *400*, 340-342.

22. Dupree, R.; Holland, D.; Mortuza, M. G.; Collins, J. A.; Lockyer, M. W. G., An Mas Nmr-Study of Network - Cation Coordination in Phosphosilicate Glasses. *J Non-Cryst Solids* **1988**, *106*, 403-407.

23. Rouxel, T.; Massouras, G.; Soraru, G. D., High Temperature Behavior of a Gel-Derived Sioc Glass: Elasticity and Viscosity. *J Sol-Gel Sci Techn* **1999**, *14*, 87-94.

24. Rouxel, T.; Soraru, G. D.; Vicens, J., Creep Viscosity and Stress Relaxation of Gel-Derived Silicon Oxycarbide Glasses. *J Am Ceram Soc* **2001**, *84*, 1052-1058.

25. Soraru, G. D.; Modena, S.; Guadagnino, E.; Colombo, P.; Egan, J.; Pantano, C., Chemical Durability of Silicon Oxycarbide Glasses. *J Am Ceram Soc* **2002**, *85*, 1529-1536.

26. Walter, S.; Soraru, G. D.; Brequel, H.; Enzo, S., Microstructural and Mechanical Characterization of Sol Gel-Derived Si-O-C Glasses. *J Eur Ceram Soc* **2002**, *22*, 2389-2400.

27. Chen, J. W.; Calvin, J.; Asplund, M.; King, S. W.; Woodfield, B. F.; Navrotsky, A., Heat Capacities, Entropies, and Gibbs Free Energies of Formation of Low-K Amorphous Si(O)Ch Dielectric Films and Implications for Stability During Processing. *J Chem Thermodyn* **2019**, *128*, 320-335.

28. David, L.; Bhandavat, R.; Barrera, U.; Singh, G., Silicon Oxycarbide Glass-Graphene Composite Paper Electrode for Long-Cycle Lithium-Ion Batteries. *Nat Commun* **2016**, *7*.

29. Juttke, Y.; Richter, H.; Voigt, I.; Prasad, R. M.; Bazarjani, M. S.; Gurlo, A.; Riedel, R., Polymer Derived Ceramic Membranes for Gas Separation. *Chem Engineer Trans* **2013**, *32*, 1891-1896.
30. Chiang, C. C.; Ko, I. H.; Chen, M. C.; Wu, Z. C.; Lu, Y. C.; Jang, S. M.; Liang, M. S., Physical and Barrier Properties of Pecvd Amorphous Silicon-Oxycarbide from Trimethylsilane and Co2. *J Electrochem Soc* **2004**, *151*, G704-G708.
31. Colombo, P.; Mera, G.; Riedel, R.; Soraru, G. D., Polymer-Derived Ceramics: 40 Years of Research and Innovation in Advanced Ceramics. *J Am Ceram Soc* **2010**, *93*, 1805-1837.
32. Newsome, D. A.; Sengupta, D.; Foroutan, H.; Russo, M. F.; van Duin, A. C. T., Oxidation of Silicon Carbide by O-2 and H2o: A Reaxff Reactive Molecular Dynamics Study, Part I. *J Phys Chem C* **2012**, *116*, 16111-16121.
33. Srinivasan, S. G.; van Duin, A. C. T.; Ganesh, P., Development of a Reaxff Potential for Carbon Condensed Phases and Its Application to the Thermal Fragmentation of a Large Fullerene. *J Phys Chem A* **2015**, *119*, 571-580.

PART I: COMPUTATIONAL NMR INVESTIGATIONS

CHAPTER 1: IMPACT OF TRANSITION METAL CATIONS ON THE ^{29}SI NMR SIGNAL IN METAL OXIDE GLASSES: A DFT CASE STUDY OF HAFNIA SILICA GLASS

Motivation and scope

Hafnia is a component that provides hardness[1] and chemical durability[2] to silica-based glasses; hafnia-containing glasses are known for their optical and dielectric properties[3]. HfO_2 is also a good model oxide to investigate PuO_2 incorporation into glasses due to their chemical resemblance.[4]

Silica-hafnia glasses can be synthesized via normal melt-quench procedure, but the range of compositions available through melt-quench is quite narrow (up to 4 mol-% HfO_2) due to low hafnia solubility in silica[5]. To access higher hafnia content other techniques can be utilized, such as sol-gel synthesis[6] or ion beam sputtering to produce a thin film[3].

NMR is a powerful method to define local structure of the materials. However, it is necessary to collect enough reliable data to relate measured chemical shifts to structure. For some systems necessary information can be extracted from crystalline compounds[7]; in other cases NMR calculations from first principles[8] can be the way to find structure vs. δ_{iso} relations.

In this research I explore hafnia-soda-silica glass models, with 25 and 33 mol-% of soda and up to 10 mol-% of hafnia added on top. My contribution here: computational NMR calibration, NMR calculations and data processing. I explore structural features of the glasses and relate it to calculated NMR data. I convert the hafnia-soda-silica glass models into the models of sol-gel hafnia-silica glasses and compute those to make sure this doesn’t make difference. I further suggest another way to interpret the experimental NMR spectra[6], basing on the relations I derived from computations.

References

1. R.W. Adams Jr, D. R. C., S. H. Knickerbocker, L.L. Rapp, B. Schwartz Zirconia Toughening of Glass-Ceramic Materials. 1992.
2. Bergeron, B.; Galoisy, L.; Jollivet, P.; Angeli, F.; Charpentier, T.; Calas, G.; Gin, S., First Investigations of the Influence of Ivb Elements (Ti, Zr, and Hf) on the Chemical Durability of Soda-Lime Borosilicate Glasses. *J Non-Cryst Solids* **2010**, *356*, 2315-2322.
3. Kim, N.; Bassiri, R.; Fejer, M. M.; Stebbins, J. F., Structure of Amorphous Silica-Hafnia and Silica-Zirconia Thin-Film Materials: The Role of a Metastable Equilibrium State in Non-Glass-Forming Oxide Systems. *J Non-Cryst Solids* **2015**, *429*, 5-12.
4. Davis, L. L.; Darab, J. G.; Qian, M.; Zhao, D.; Palenik, C. S.; Li, H.; Strachan, D. M.; Li, L., Hafnium in Peralkaline and Peraluminous Boro-Aluminosilicate Glass and Glass Sub-Components: A Solubility Study. *J Non-Cryst Solids* **2003**, *328*, 102-122.
5. T.P. Ledneva, K. A. B., Solubility of the Refractory Oxides Zirconium Dioxide and Hafnium Dioxide in Silica. *Steklo* **1973**, *2*, 84-87.
6. O'Dell, L. A.; Gunawidjaja, P. N.; Holland, M. A.; Mountjoy, G.; Pickup, D. M.; Newport, R. J.; Smith, M. E., Characterisation of Sol-Gel Prepared (Hfo2)(X)(Sio2)(1-X) (X=0.1, 0.2 and 0.4) by H-1, C-13, O-17 and Si-29 Mas Nmr, Ftir and Tga. *Solid State Nucl Mag* **2008**, *33*, 16-24.
7. Smith, J. V.; Blackwell, C. S., Nuclear Magnetic-Resonance of Silica Polymorphs. *Nature* **1983**, *303*, 223-225.
8. Pickard, C. J.; Mauri, F., All-Electron Magnetic Response with Pseudopotentials: Nmr Chemical Shifts. *Phys Rev B* **2001**, *63*.

Impact of Transition Metal Cations on the ^{29}Si NMR Signal in Metal Oxide Glasses: a DFT Case Study of Hafnia Silica Glass

Ilia Ponomarev[1] and Peter Kroll[*1],

[1]Department of Chemistry and Biochemistry, The University of Texas at Arlington,
700 Planetarium Place, Arlington, Texas 76019, United States.

Abstract

We investigate ^{29}Si nuclear magnetic Resonance (NMR) chemical shifts δ_{iso} of soda-silica and hafnia-soda-silica glass models by structural modeling and the Gauge-Invariant Projector Augmented Wave (GIPAW) method within Density Functional Theory (DFT). Models of soda-silica glasses with molar ratio Na_2O:SiO_2 of 1:2 and 1:3 and hafnia content of 0 to 10 mol-% are generated via a melt-quench procedure and ab initio molecular dynamic simulations. By correlating computed chemical shifts with structural data we establish angular correlation functions for Q^2, Q^3, and Q^4 units in soda-silica glasses. Addition of hafnia to soda-silica glasses results in 6-coordinated Hf surrounded by bridging O under avoidance of direct linkages between Hf-centered octahedra. Hf impacts the structural information that can be gathered from ^{29}Si NMR analysis profoundly: each Hf in 2nd coordination to Si shifts the angular correlation function for Si-O-X (X = Si, Hf) angles by 3-5 ppm. Hence, NMR signals of Q^2 and Q^3 units may overlap depending on the number of Hf surrounding Si. By substituting H for Na we convert the glass models into models of sol-gel derived HfO_2-SiO_2. The profound impact of Hf on the chemical shift of ^{29}Si calls for a reinterpretation of ^{29}Si NMR peaks observed for hafnia-silica glasses.

1. Introduction

Hafnia (HfO_2) increases the chemical durability of silica-based glasses. [1-2] Hafnia, like some other metal oxides, also increases hardness of glasses and glass-ceramic materials.[3-4] Sol-gel derived hafnia-silica glasses and thin HfO_2-SiO_2 films find broad applications in optical and dielectric materials.[5-8] Since hafnia is both a surrogate for PuO_2 and a good neutron absorber, it is also a benign component for the investigation of nuclear waste glasses. [1-2,9]

Solid-state NMR provides insight into the local environments of atoms and is a powerful method to study materials.[10] In particular, structural analysis of amorphous solids and glasses benefit from NMR studies, once the influence of the local environment on NMR parameters of a nucleus is established. With the advent of DFT calculations combined with the GIPAW method[11], modeling and simulation have substantially augmented the information content of experimental NMR spectra of disordered systems. Solid-state NMR studies enhanced with DFT calculations have become an indispensable analytical tool to characterize short- and medium range order in glasses.[12-15]

In this study we explore the impact of Hf in hafnia-soda-silica glasses on ^{29}Si NMR chemical shift by combined DFT-GIPAW calculations.[11] First we investigate ^{29}Si NMR chemical shifts of crystalline silica polymorphs and sodium silicates. Then we investigate amorphous soda-silica and establish a correlation between Si-O-Si angles and the chemical shift δ_{iso} of adjacent Si atoms. Subsequently, we add hafnia to the glass network and elucidate the impact of Hf as 2nd–nearest neighbor to ^{29}Si on its chemical shift. Finally, replacing Na by H gives us access to models of hafnia-silica sol-gel materials, for which we provide new interpretations of their ^{29}Si NMR data.

2. Methods

All our simulations are within Density Functional Theory[16] using the Vienna Ab Initio Simulation (VASP) package [17-18]. We use the Projector Augmented Wave (PAW) method[19-20] and approximate electron exchange and correlation by the Perdew-Burke-Ernzerhoff (PBE) generalized gradient approximation (GGA). We sample the Brillouin zone at the Γ-point only for amorphous models, while we choose appropriate k-point meshes for crystalline models. For final optimizations of amorphous as well as crystalline models we rely on standard pseudopotentials provided with the VASP package and use an energy cutoff of 500 eV for the expansion of the wave function into the plane-wave basis set.

We generate models of soda-silica and hafnia-soda-silica glasses using a “melt-quench” approach together with Born-Oppenheimer ab initio molecular dynamics (aiMD) simulation. Efficient model generation uses a “softer” version of the oxygen pseudopotential provided by VASP, a time-step $\Delta t=2.0$ fs, and a cutoff of 283 eV at this stage. The temperature of the system is adjusted by velocity scaling. The temperature-time profile for our melt-quench scheme is shown in Fig. 1. Once the last configuration of the trajectory (at 300 K) is obtained, we switch back to the “standard” parameters and optimize the model allowing atomic positions and cell parameters to adjust to a local energy minimum state. For amorphous models, forces are converged to $5\cdot10^{-2}$ eV/Å and stresses to lower than 2 kbar. In total we consider 40 models of soda-silica glasses consisting of 108 atoms and 246 models of hafnia-soda-silica glasses comprised of 108 to 120 atoms.

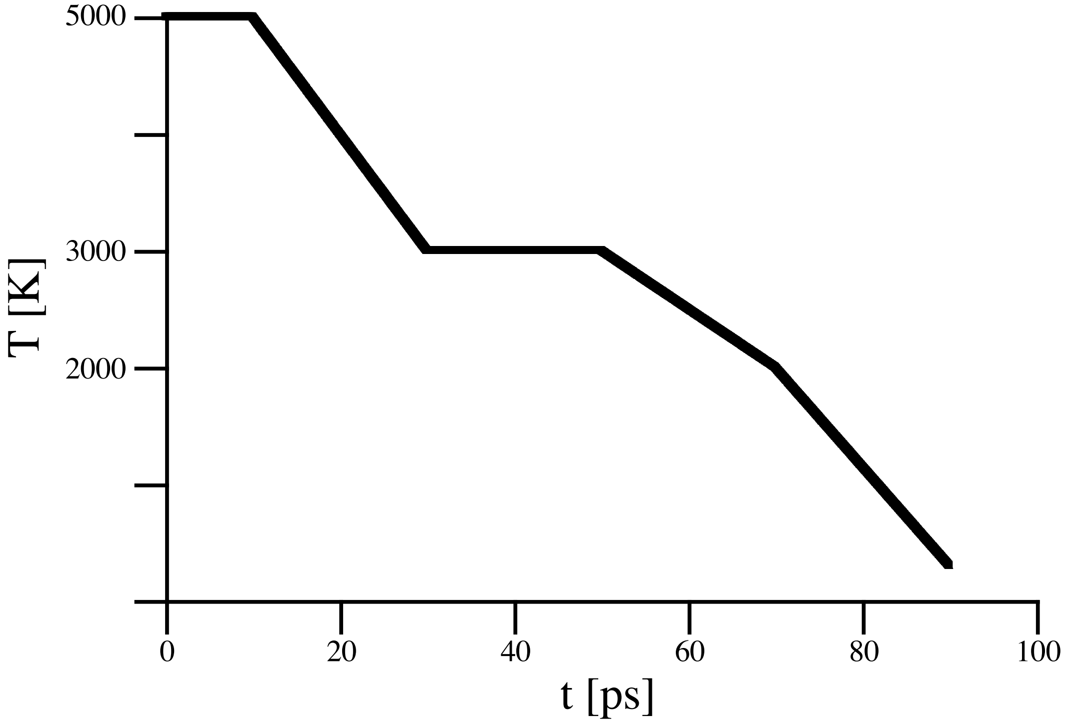

Figure 1. Temperature-time (T-t) profile for the melt-quench procedure to produce amorphous models. With a time-step Δt=2.0 fs, the total time of 90 ps corresponds to 45,000 time steps.

The NMR calculations are carried out using the GIPAW algorithm[11] as implemented in the VASP code. We choose an energy cutoff of 600 eV and find ^{29}Si NMR chemical shifts converged to better than 0.2 ppm.

For reference calculations, we select the following crystal structures from the Inorganic Crystal Structure Database: SiO_2 α-quartz[21], SiO_2 α-cristobalite[22], SiO_2 coesite[23], Na_2SiO_3[24], α-$Na_2Si_2O_5$[25], β-$Na_2Si_2O_5$[26], C-$Na_2Si_2O_5$[27]. For these structures we optimize atomic positions under the constraint of experimental lattice parameter. Forces are optimized to lower than to 5 meV/Å. Computed values of absolute chemical shifts are given in Tab. 1 and shown Fig. 2.

Table 1. Experimental ^{29}Si NMR chemical shifts δ_{iso}, computed absolute shifts σ_{iso}, and predicted δ_{iso} for silica and sodium silicate polymorphs. The prediction is based on a fit to the data, see Figure 2 and Eqn. 1.

Structure	δ_{iso} exp [ppm]	σ_{iso} comp [ppm]	δ_{iso} pred [ppm]
α-quartz	-107.1[28]	-437.2	-106.4
α-cristobalite	-108.5[28]	-437.8	-107.0
coesite Si[1]	-113.9[28]	-446.8	-116.0
coesite Si[2]	-108.1[28]	-439.3	-108.5
Na_2SiO_3	-76.8[28]	-406.9	-76.1
α-$Na_2Si_2O_5$	-94.2[28]	-426.7	-95.9
β-$Na_2Si_2O_5$ Si[1]	-86.3[28]	-417.2	-86.4
β-$Na_2Si_2O_5$ Si [2]	-88.2[28]	-418.3	-87.5
C-$Na_2Si_2O_5$ Si[1]	-87.4[27]	-418.0	-87.2
C-$Na_2Si_2O_5$ Si[2]	-86.3[27]	-417.2	-86.4
C-$Na_2Si_2O_5$ Si[3]	-86.0[27]	-417.1	-86.3
C-$Na_2Si_2O_5$ Si[4]	-88.2[27]	-418.7	-87.9

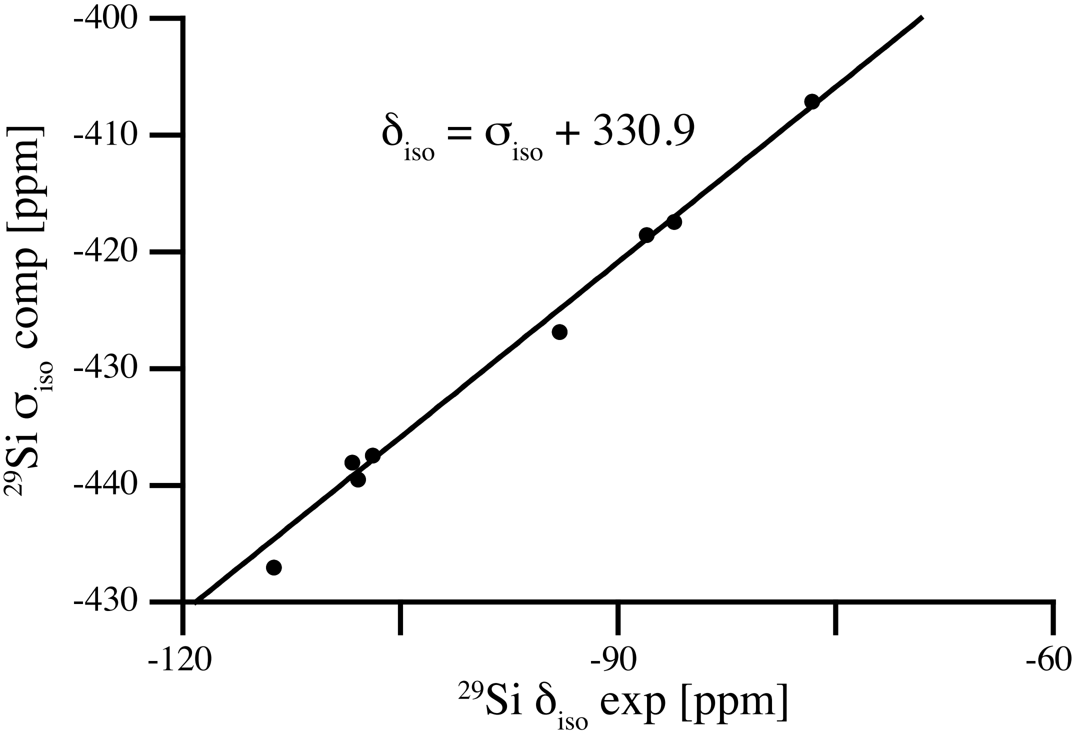

Figure 2. Correlation between experimental ^{29}Si NMR chemical shifts δ_{iso} and computed absolute shifts σ_{iso} for silica and sodium silicate polymorphs.

Several approaches have been proposed to calibrate the computed absolute shifts σ_{iso} to correlate to experimental data.[28-29] Here we choose a simple gauge by fitting a line with slope of 1 to the data of Tab. 1, see Fig. 1. We obtain

$$\delta_{iso} = \sigma_{iso} + 330.9 \quad (1),$$

and almost all values of δ_{iso} obtained this way are within 1 ppm of experimental data. Stronger deviations are observed only for α-cristobalite, coesite, and α-$Na_2Si_2O_5$.

3. Results and discussion

^{29}Si NMR of Soda-silica glasses

We modeled soda-silica glasses of two different compositions, with ratios Na_2O-SiO_2 of 1:2 and 1:3. These compositions are conventionally abbreviated as NS33 and NS25, respectively, according to the mol-content Na_2O in the glass. We generated 13 models of NS25, $(Na_2O)_9(SiO_2)_{27}$, and 27 models of NS33, $(Na_2O)_{12}(SiO_2)_{24}$, each model comprising 108 atoms.

While the crystal structure of $Na_2Si_2O_5$ exhibits only Q^3 units, the NS33 glass models contain approximately 20% each of Q^4 and Q^2 units. This is somewhat higher than a fraction of 6% to 12.5% estimated from experimental observations[30-31]. In our models we even observe a few Q^1 units. NS25 glass structures contain approximately 3% of Q^2 units and no Q^1 units. The average coordination number of Si is 4.1 for both NS25 and NS33 glasses, without any three-fold coordinated Si, however. The average Si-O bond length in glass models is 1.65 Å, which is slightly longer than found in amorphous silica models (1.62-1.63 Å)[29] and close to distances between Si and bridging O in silicates (e.g. 1.64 Å in α-$Na_2Si_2O_5$ [25] and β-$Na_2Si_2O_5$[26]). The average Si-O-Si angle found in NS25 and NS33 models is 135°, which is approximately 10° smaller than inferred from experimental NMR data of soda-silica glasses[32].

Multiple studies, both experimental and computational, have shown that in silica structures the ^{29}Si NMR chemical shift δ_{iso} of tetrahedrally coordinated Si depend on the Si-O-Si bond angle Θ found at each neighboring oxygen atom.[12, 28-29, 32-35] Different functional dependencies on Θ have been formulated, such as $\sec(\Theta)$[33], cosine expansions[12], or a simple linear dependency[34]. Common to each approach is the assumption that contributions of each Si-O-Si bond angle surrounding the central Si are independent from each other. *Charpentier et al.* analyzed this in detail for amorphous silica[35]. Hence, the expression for the relation between δ_{iso} and Si-O-Si bond angle Θ is given by

$$\delta_{iso} = \frac{1}{n_{BO}} \sum_{i=1}^{n_{BO}} F(\Theta^i_{Si-O-Si}) \quad (2)$$

with F(Θ) being the explicit analytical form of the angular dependency. For Q^4 units, which are found in many silicate structures including amorphous silica, the number of non-bridging oxygens n_{BO} equals 4. The expression (2) above can be generalized for Q^3 [$n_{BO} = 3$] and Q^2 [$n_{BO} = 2$] units as well. We find that a simple linear function is sufficient to describe the angular dependency between δ_{iso} and Θ. This simplifies equation (2) to:

$$\delta_{iso} = a_n + b_n \cdot \bar{\Theta}_{Si-O-Si} \quad (3)$$

Herein, $\bar{\Theta}_{\text{Si-O-Si}}$ is the average Si-O-Si angle found on adjacent O atoms, and a_n and b_n are coefficients to be determined for each Q^n unit. The same expression was previously used by *Ispas et al*. to describe chemical shifts of Q^4, Q^3, and Q^2 units in soda-silica and lithia-silica glasses. [32] We have previously taken a similar approach to quantify ^{29}Si NMR chemical shifts in amorphous silica (SiO_2) and mixed SiO_nC_{4-n}–tetrahedra in amorphous silicon oxycarbide (SiCO). [29]

In Figure 3 we show the computed chemical shifts δ_{iso} for Q^n units (n=2,3,4) from our collection of melt-quench modeled soda-silica glass models (a total of more than 900 sites have been collected).

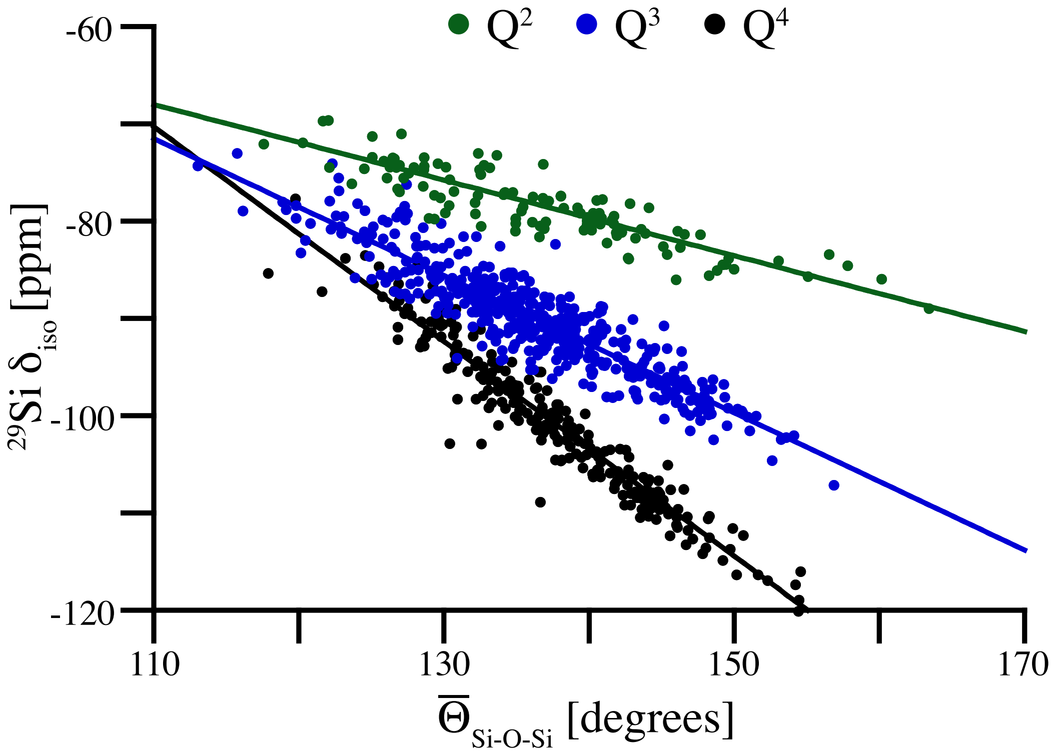

Figure 3. Computed ^{29}Si NMR chemical shift plotted versus average Si-O-Si angle on neighboring oxygens for Q^n vertices (n=2,3,4) in soda-silica glasses (compositions Na2O:SiO2 of 1:2 and 1:3 are collected together). In total the graph contains data for more than 900 Si sites. The straight line is a linear fit to the data for each Q^n vertex.

Linear fits to the data shown in Fig. 1 provide the following angular correlation functions:

$$\delta_{iso}^{Q^4} = (51.2 \pm 2.8) - (1.10 \pm 0.02) \cdot \bar{\Theta}_{Si-O-Si}$$
$$\delta_{iso}^{Q^3} = (6.1 \pm 2.0) - (0.71 \pm 0.01) \cdot \bar{\Theta}_{Si-O-Si}$$

$$\delta_{iso}^{Q^2} = (-25.2 \pm 2.5) - (0.39 \pm 0.02) \cdot \bar{\Theta}_{Si-O-Si} \quad (4)$$

For each correlation we included the error from a least-square fit into the expression. Ispas et al[32] determined fit coefficients a_4=48.5 and b_4=1.07 (Q^4 units), and a_3=6.5 and b_3=0.70 (Q^3 units). Hence, within the margin of error our results agree nicely with their data. For Q^2 units they obtained a_2=-44.6 and a_2=0.25, but their fit was based on only 7 such Q^2 units. Our results, on the other side, analyze more than 100 Q^2, 600 Q^3, and 200

Q^4 units. Inspecting the residuals of our fits, we find a Gaussian-like distribution with a FWHM of 5 ppm. The angular correlations collected in Eqn (4) also predict chemical shifts of crystalline sodium silicates (see table 1) with a maximum deviation of 2 ppm between prediction on one side and experimental or directly computed values on the other side.

Impact of hafnium on ^{29}Si NMR in hafnia-soda-silica glasses

Modeling of ternary hafnia-soda-silica glasses is achieved using the same melt-quench process as for the binary glasses. For both soda-silica glass compositions (NS33 and NS25), we added up to four units of HfO_2 to the model before starting the simulations. Hence, we generate models with compositions $(HfO_2)_k(Na_2O)_{12}(SiO_2)_{24}$ and $(HfO_2)_k(Na_2O)_9(SiO_2)_{27}$, with k=1,2,3,4. The highest hafnia content corresponds to 10 mol-% HfO_2 in the glass. This value relates to the solubility of 11 mol-% hafnia in soda-silica glass with ~33 mol-% of soda.[9] We generated additional models starting from NS33 glass and changing Si atoms into Hf, formally morphing silica into hafnia. This yielded a series of compositions $(HfO_2)_k(Na_2O)_{12}(SiO_2)_{24-k}$ (k=2,4,6,8,12).

We find that models with lowest energy after optimization exhibit octahedral $HfO_{6/2}{}^{2-}$ polyhedra with all six O atoms surrounding Hf bridging to the next Si. Hence, there is a strong avoidance to coordinate non-bridging O to Hf. We occasionally observe corner sharing of $HfO_{6/2}$-octahedra, but never in energetically most favorable models and, overall, in amounts less than expected in a random mixing model. This is quite different from our results on hafnia-silica glasses (without soda), where hafnia units were found to cluster in low-energy models.[36] The difference highlights the impact of soda on the structure of these mixed metal oxide silica glasses. In ternary hafnia-soda-silica glasses $HfO_{6/2}$-polyhedra form complex $Hf(OSiO_3)_6$-clusters, which are further embedded in the network either by bridging or non-bridging O at the outside of the cluster. Due to the definite coordination number and the well-defined local environment we regard Hf as network-forming element in these glasses. Non-bridging O atoms prefer bonding to Si, while Si itself is found in a variety of $Q^{n}_{m\mathrm{Hf}}$ units, with different numbers m (m = 0 to n) of Hf in second coordination. However, since the basic $HfO_{6/2}$-unit itself is charged (-2), some of the bridging O coordinating to Hf have an associated Na cation close-by. This typical environment is illustrated in Fig. 4.

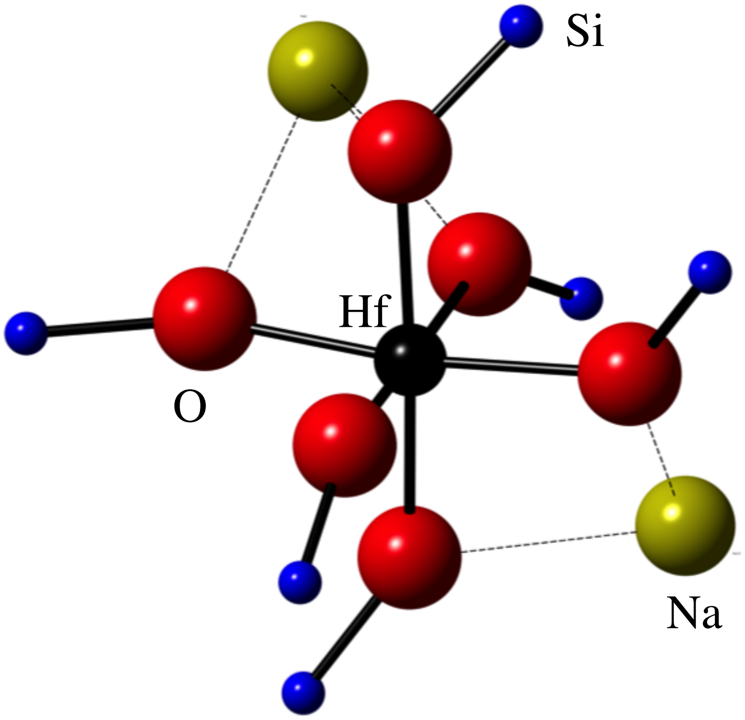

Figure 4. Characteristic chemical environment of Hf within a $[HfO_{6/2}]^{2-}\cdot 2Na^{+}$ unit in hafnia-soda-silica models.

Characterizing the ^{29}Si chemical shifts and their dependency on the local environment, we first focus on those Q^{n}-units that exhibit only Si atoms as second-nearest neighbor. With no Hf in 2nd-coordination, these units are labeled $Q^{n}_{0\mathrm{Hf}}$. The relation between ^{29}Si NMR chemical shifts and the average angle of surrounding Si-O-Si angles is shown in Fig. 5.

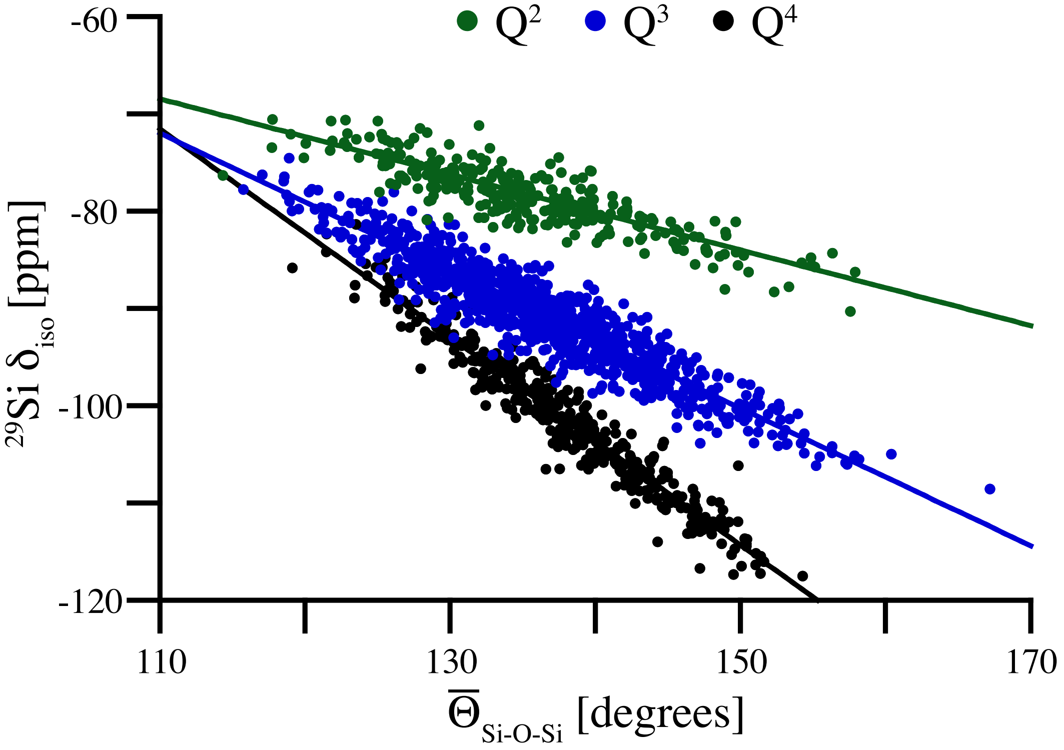

Figure 5. Relation between computed ^{29}Si NMR chemical shifts and average Si-O-Si angle on neighboring oxygens for $Q^n_{0\mathrm{Hf}}$ vertices in hafnia-soda-silica glasses.

Once again we obtain linear angular correlation functions through a least-square fit to the data:

$$\delta_{iso}^{Q^4} = (46.1 \pm 1.9) - (1.07 \pm 0.01) \cdot \bar{\Theta}_{Si-O-Si}$$
$$\delta_{iso}^{Q^3} = (5.7 \pm 1.2) - (0.71 \pm 0.01) \cdot \bar{\Theta}_{Si-O-Si}$$

$$\delta_{iso}^{Q^2} = (-25.7 \pm 1.7) - (0.39 \pm 0.01) \cdot \bar{\Theta}_{Si-O-Si} \quad (5)$$

For the range of angles that appear in our models, $115 < \Theta < 165$, the relations of Eqn (5) are consistent with those of Eqn (4), which were determined from soda-silica models free of hafnia. These results show that the chemical shift of Si within a $Si(OSiO_3)_4$-cluster, hence, Si with only Si atoms as next-nearest neighbors, is not impacted by adding hafnia to the glass. This changes, however, once Hf enters the coordination sphere of Si.

To analyze the chemical shifts of $Q^n_{m\mathrm{Hf}}$ units, in which the central Si is surrounded by *m* Hf atoms as second-nearest neighbors, we assume that Si-O-Si and Si-O-Hf angles enter independently into the linear angular correlation function. This allows us to formulate the angular correlation function as a sum of two linear terms:

$$\delta_{iso} = \frac{1}{n_{BO}}\left\{\sum_{i=1}^{n_{Si}}\left(a_{n_{BO}}^{Si} + b_{n_{BO}}^{Si}\cdot\Theta_{Si-O-Si}^{i}\right) + \sum_{j=1}^{n_{Hf}}\left(a_{n_{BO}}^{Hf} + b_{n_{BO}}^{Hf}\cdot\Theta_{Si-O-Hf}^{j}\right)\right\} \quad (6).$$

Parameters a^{Si}, b^{Si}, a^{Hf}, and b^{Hf} can be determined from the data for every Q^n–unit, and results for $Q^4_{n\mathrm{Hf}}$, $Q^3_{n\mathrm{Hf}}$, and $Q^2_{n\mathrm{Hf}}$ units are shown in Fig. 6.

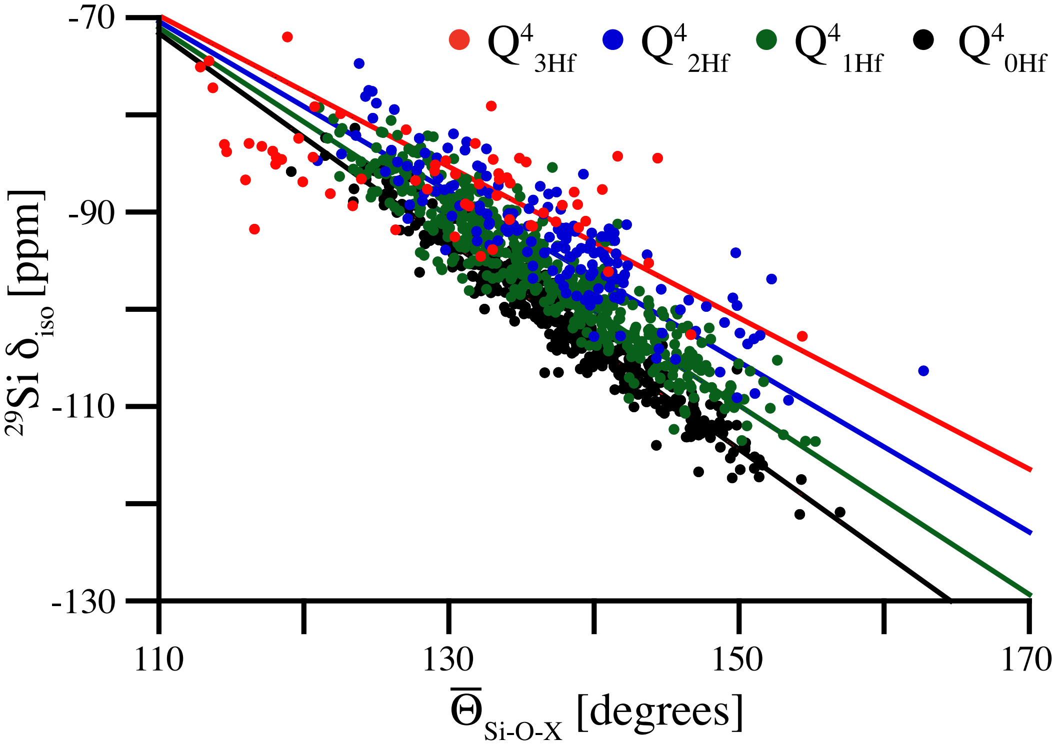

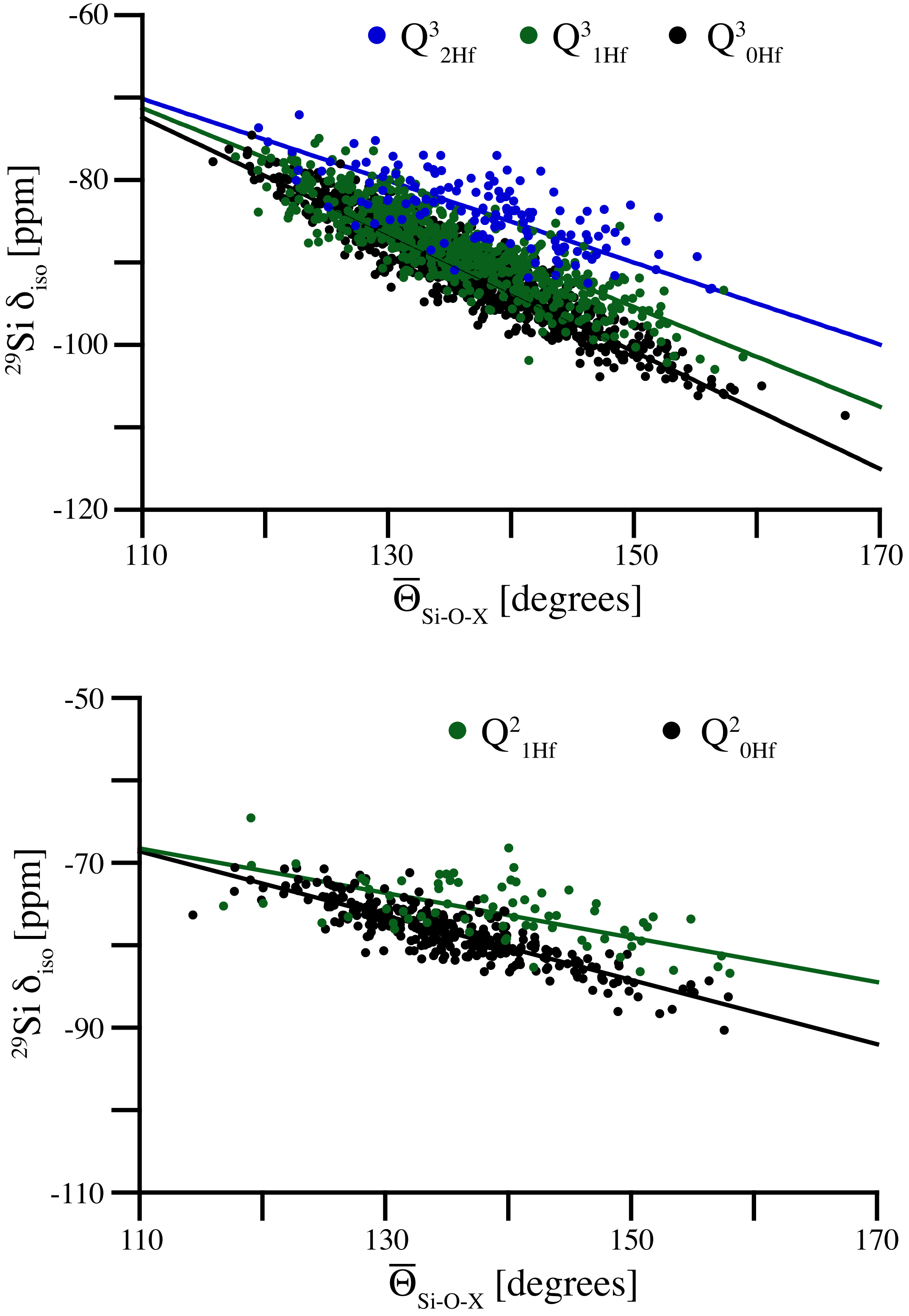

Figure 6. Relation between average Si-O-X angle (X=Si, Hf) and ^{29}Si NMR chemical shift for $Q^4_{n\mathrm{Hf}}$ (top), $Q^3_{n\mathrm{Hf}}$ (center), and $Q^2_{n\mathrm{Hf}}$ (bottom) units in hafnia-soda-silica glasses.

We obtain as before linear angular correlation functions for Si-O-Si and Si-O-Hf angles in $Q^4_{k\mathrm{Hf}}$, $Q^3_{k\mathrm{Hf}}$, and $Q^2_{k\mathrm{Hf}}$ units:

$$\delta_{iso}^{Q^4} = \frac{1}{4}\left\{\sum_{i=1}^{n_{Si}}\left[(46.1\pm1.9)-(1.07\pm0.01)\cdot\Theta_{Si-O-Si}^{i}\right]+\sum_{j=1}^{n_{Hf}}\left[(5.6\pm4.0)-(0.68\pm0.02)\cdot\Theta_{Si-O-Hf}^{j}\right]\right\}$$

$$\delta_{iso}^{Q^3} = \frac{1}{3}\left\{\sum_{i=1}^{n_{Si}}\left[(5.7\pm1.2)-(0.71\pm0.01)\cdot\Theta_{Si-O-Si}^{i}\right]+\sum_{j=1}^{n_{Hf}}\left[(-23\pm12)-(0.39\pm0.01)\cdot\Theta_{Si-O-Hf}^{j}\right]\right\}$$

$$\delta_{iso}^{Q^2} = \frac{1}{2}\left\{\sum_{i=1}^{n_{Si}}\left[(-25.7\pm1.7)-(0.39\pm0.01)\cdot\Theta_{Si-O-Si}^{i}\right]+\sum_{j=1}^{n_{Hf}}\left[(-51\pm7)-(0.15\pm0.05)\cdot\Theta_{Si-O-Hf}^{j}\right]\right\} \quad (7)$$

It turns out that the impact of Hf as second-nearest neighbor to Si is profound: comparing two Q^4-units with identical average bond angle $\bar{\Theta}$ but different numbers of Hf in second coordination, we find that each Hf changes the ^{29}Si chemical shift by 2.5 ppm ($\bar{\Theta}$ = 130°) to 5.5 ppm ($\bar{\Theta}$ =160°).

This impact of Hf on the ^{29}Si NMR is quite significant in case we use NMR data to estimate the degree of condensation of the hafnia-silica network in hafnia-soda-silica glasses or, for example, in sol-gel derived hafnia-silica products. The point is that $Q^n_{k\mathrm{Hf}}$ units may easily be misinterpreted as Q^{n-1} units with the consequence that the connectivity of the network will be severely mischaracterized. This is best illustrated for sol-gel derived glasses containing hafnia – which we will consider in the next section.

Substitution of sodium into hydrogen. Sol-gel hafnia-silica glasses.

Hafnia-silica materials find a wide range of applications in optics and dielectric materials. For example, hafnon ($HfSiO_4$) is potential high-κ dielectric material[37], and hafnia-silica thin films are used as high refractive index coatings in LIGO, the Laser Interferometric Gravitational Wave Observatory[38]. Due to the low solubility of hafnia in silica (only up to 4 mol%[39]), the sol-gel route is commonly used to obtain hafnia-silica glasses with high hafnia content. ^{29}Si NMR is then routinely used to characterize the degree of condensation (or amount of 'disruption') of the network built during the gelation process[7]. Evidently, understanding the impact of Hf on ^{29}Si NMR chemical shifts in this type of materials is critical.

Our hafnia-soda-silica glass models are simply converted into models for sol-gel derived hafnia-silica by changing sodium atoms (Na) into hydrogen (H). Since Na and H have different distances to adjacent O atoms, we optimize the H positions, while keeping cell parameters and positions of all other elements, Hf, Si, and O, fixed. This procedure facilitates to study the impact of protons (H^+), which bond covalently to a single O, in contrast to Na-cations, which are "embedded" by surrounding O. Since the remaining Si-O-Hf network remains unchanged, all geometrical parameters (distances and angles) relevant for angle correlation functions are the same as before for soda-silica models. We once again compute the NMR data and show results for Q^4 and Q^3 vertices in Fig. 7.

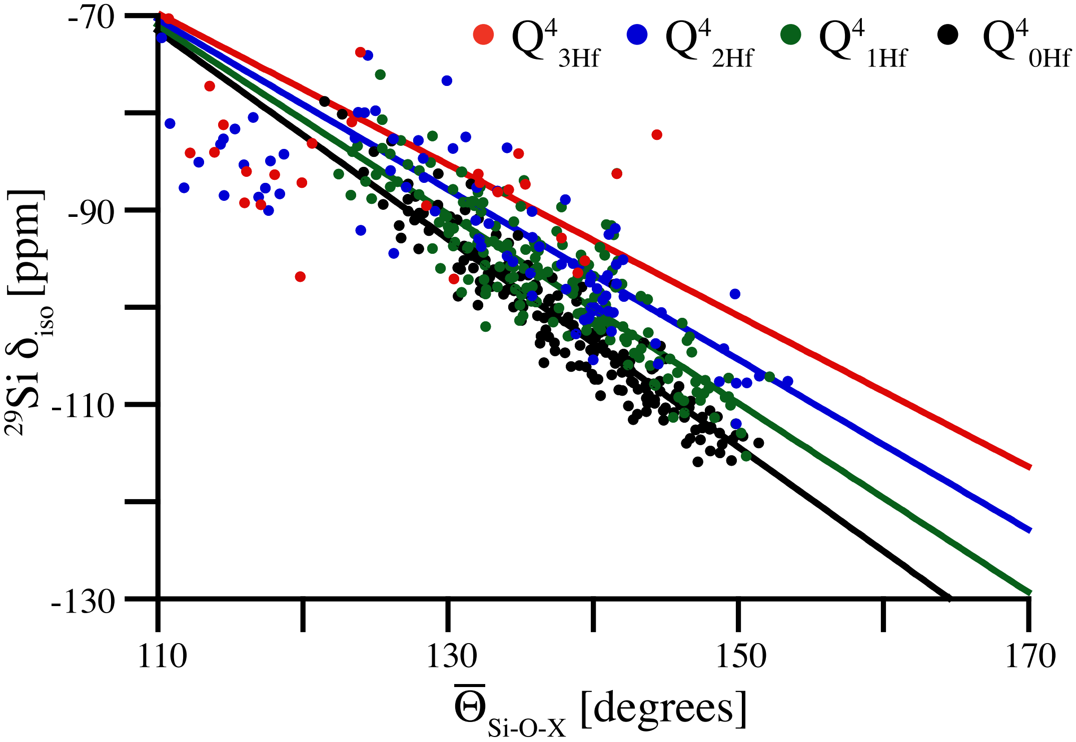

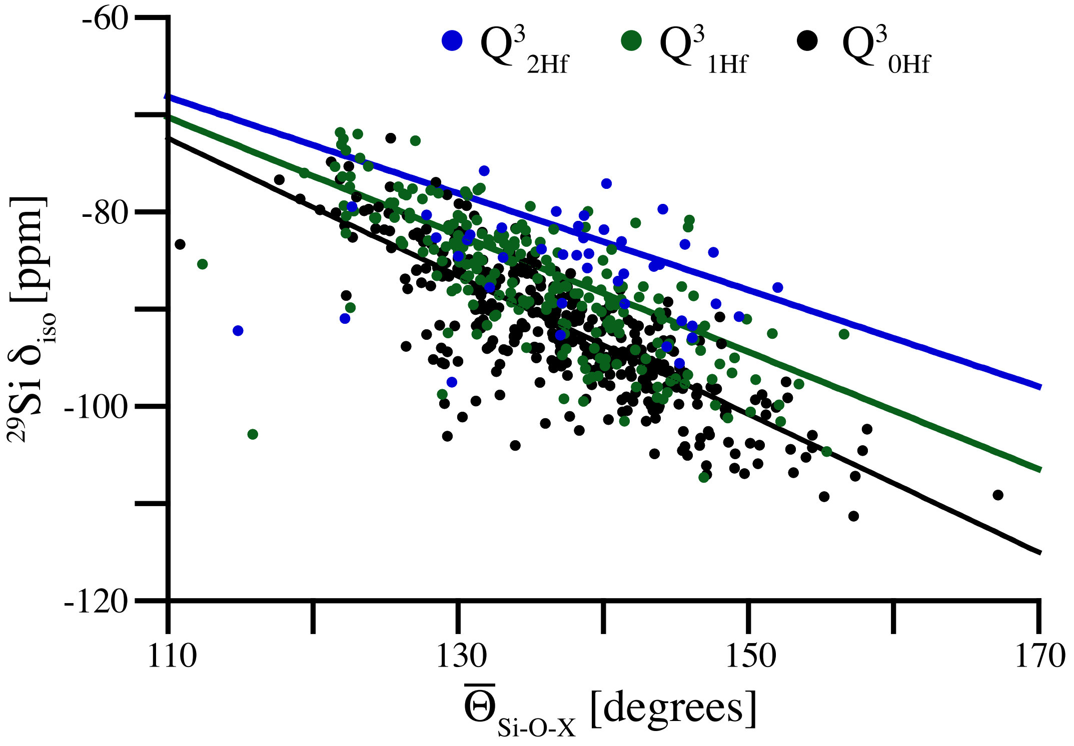

Figure 7. Relation between average Si-O-X angle and ^{29}Si NMR chemical shift for Q^4_{nHf} (left) and Q^3_{nHf} (right) vertices in hafnia-silica sol-gel glasses. Fit residuals for Q^4 units are given in supplementary information.

The data is once again used to fit a model similar to that presented in Eqn (6), but this time for HfO_2-H_2O-SiO_2 models. The resulting parameters are given in Eqn (8):

$$\delta_{iso}^{Q^4} = \frac{1}{4}\left\{\sum_{i=1}^{n_{Si}}\left[(54\pm4)-(1.12\pm0.03)\cdot\Theta^i_{Si-O-Si}\right]+\sum_{j=1}^{n_{Hf}}\left[(4.0\pm6.0)-(0.59\pm0.04)\cdot\Theta^j_{Si-O-Hf}\right]\right\}$$

$$\delta_{iso}^{Q^3} = \frac{1}{3}\left\{\sum_{i=1}^{n_{Si}}\left[(6.0\pm3.8)-(0.71\pm0.03)\cdot\Theta^i_{Si-O-Si}\right]+\sum_{j=1}^{n_{Hf}}\left[(-20\pm8)-(0.46\pm0.06)\cdot\Theta^j_{Si-O-Hf}\right]\right\} \quad (8)$$

$$\delta_{iso}^{Q^2} = \frac{1}{2}\left\{\sum_{i=1}^{n_{Si}}\left[(-25\pm16)-(0.42\pm0.12)\cdot\Theta^i_{Si-O-Si}\right]+\sum_{j=1}^{n_{Hf}}\left[(-66\pm18)-(0.08\pm0.12)\cdot\Theta^j_{Si-O-Hf}\right]\right\}$$

These parameters do not differ substantially from those for hafnia-soda-silica glasses given in Eqn (7). Consequently, the ^{29}Si chemical shift in sol-gel derived hafnia-silica glasses is profoundly impacted by the presence of Hf as second-nearest neighbor: for an average bond angle $\bar{\Theta}$ of 140° the change amount to 4 ppm for each Hf.

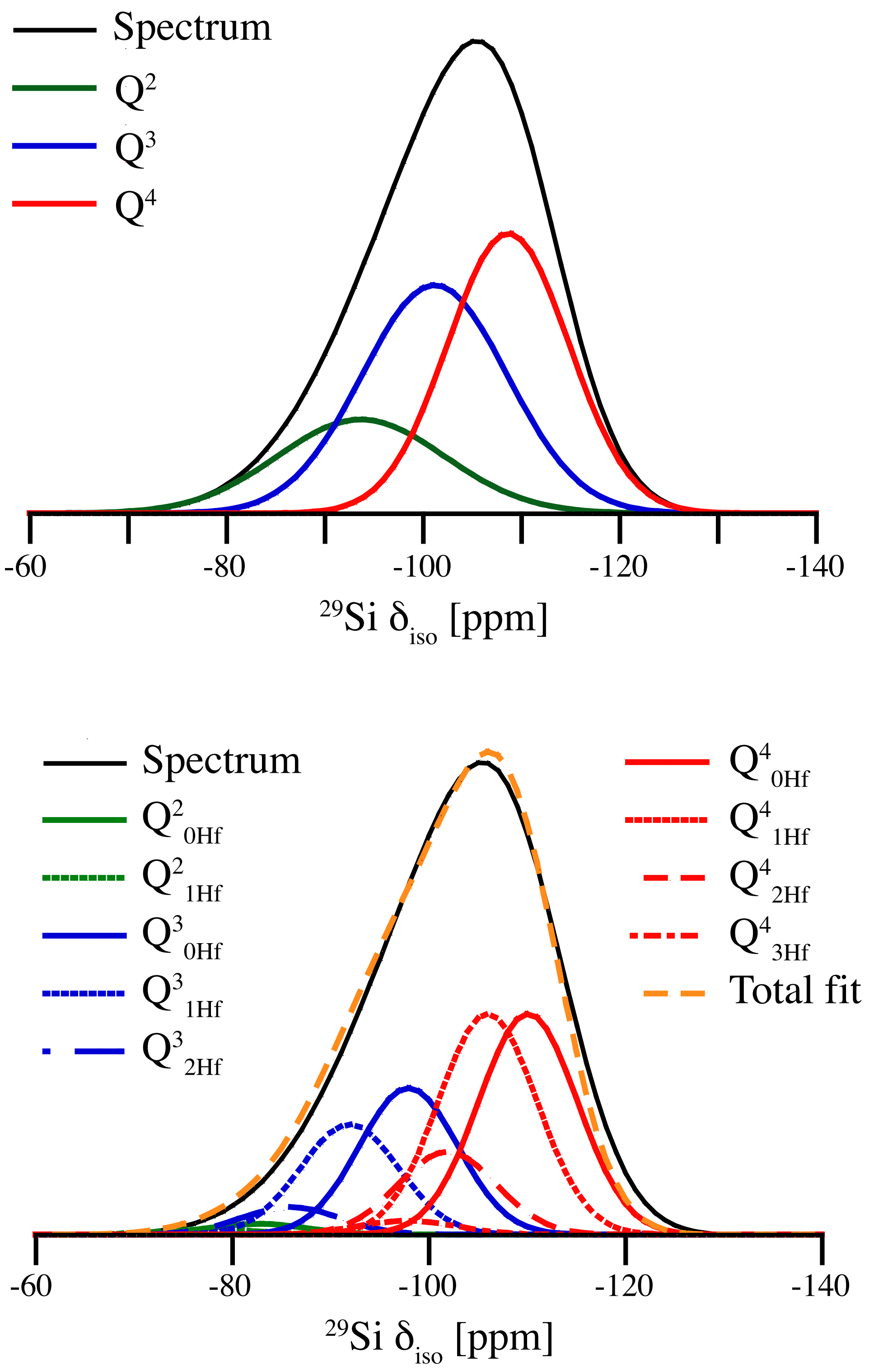

Figure 8. ^{29}Si NMR spectrum of unheated sol-gel derived $(HfO_2)_{0.1}(SiO_2)_{0.9}$ glass. Top – fitting of O'Dell et al[7], bottom – analysis presented here.

To illustrate the impact, we analyze experimental data of O'Dell et al.[7]. The authors characterize the relative proportions of Q^2, Q^3, and Q^4 units in an unheated sol-gel derived $(HfO_2)_{0.1}(SiO_2)_{0.9}$ glass by ^{29}Si NMR. The experimental spectrum is shown in Fig. 8 (top) together with their fitting, which assumes 3 Gaussian's centered at -93.7 ppm, -101.2 ppm, and -108.7 ppm for Q^2, Q^3, and Q^4 units, respectively. The relative intensities of peaks Q^2:Q^3:Q^4 are 19:40:41 and yield a fraction of NBO's of 33%.

However, we find that the peak assignment of O'Dell et al. is inconsistent with our results. A Q^4-peak located at -108.7 ppm indicates an average bond angle $\bar{\Theta}$ of 146°, a Q^3-peak located at -101.2 ppm suggests $\bar{\Theta}$ of 154°, and a Q^2-peak located at -93.7 ppm relates to $\bar{\Theta}$ of 179°. Although these predicted angles do not need to be identical (indeed, the various Q^n-species may have different involvement in rings of different size), the angles at Q^2 units would be extreme. Typical Si-O-Si angles in silica glasses are around 145°, based on neutron scattering data.[40] Besides, the peak assignment of O'Dell et al. ignores the impact of Hf as second nearest neighbor to Si.

We, therefore, contrast the evaluation of O'Dell et al.[7] by our own analysis (details provided in Supplementary Information), which is shown in Fig. 8 on the bottom. We fit the same experimental data assuming random connectivity of silica and hafnia units and applying the angular correlation functions for $Q^n_{k\mathrm{Hf}}$ units of Eqn. (8). We further assume equal average bond angles $\bar{\Theta}$ and equal width of the distribution for all Q^n-units, independent of the number of Hf coordinating the Si. We extract from the data an average Si-O-X bond angle $\bar{\Theta}$ of 146°, which is consistent with typical Si-O-Si angles in silica glasses mentioned earlier. This outcome provides strong support for the relevance of our approach. The analysis, furthermore, yields relative amounts of Q^2:Q^3:Q^4 units of 2:34:64, which is strikingly different from the numbers extracted by O'Dell et al.[7]. Notably, the amount of Q^2-units is far lower than that proposed by O'Dell et al[7]. As a consequence, we determine the fraction of NBO's to be 17%, less than a half of the value stipulated by O'Dell et al[7]. Ultimately, our analysis indicates a substantially higher degree of condensation in this material.

4. Summary and Conclusion

We studied ^{29}Si NMR chemical shifts in hafnia-soda-silica glass models using density functional theory calculations and GIPAW algorithm. Hf preferentially builds complex $[HfO_{6/2}]^{2-}\cdot 2Na^+$ units and is surrounded by bridging O only. The ^{29}Si NMR chemical shifts in Q^n-units can be described well by linear angular correlation functions, treating the contributions of each surrounding Si-O-X angle independently. Hafnium impacts δ_{iso} of ^{29}Si once it appears as second-nearest neighbor to Si: for the same bond angle at O, the coordinating Hf changes the ^{29}Si chemical shift by 2.5 to 5.5 ppm for bond angles characteristic for such glass systems, 130° to 160°. We show that results obtained for hafnia-soda-silica glasses do transfer to sol-gel derived hafnia-silica glasses. Based on our results, we provide a new approach to analyze the condensation process of sol-gel glasses by ^{29}Si NMR. Applied to a sample system, our method yields average bond angles consistent with similar silica glasses, but evinces substantially different proportions of various Q^n-units. Consequently, our study demonstrates that proper analysis of ^{29}Si NMR data in sol-gel derived metal oxide glasses benefits from computational modeling and simulation.

Acknowledgments

This work was supported by the NSF (CMMI-1634448 and DMR-1463974). Computational work was made possible through generous grants by the Texas Advance Computing Center in Austin, TACC, Texas.

References

1. Bergeron, B.; Galoisy, L.; Jollivet, P.; Angeli, F.; Charpentier, T.; Calas, G.; Gin, S., First Investigations of the Influence of IVb Elements (Ti, Zr, and Hf) on the Chemical Durability of Soda-Lime Borosilicate Glasses. *J Non-Cryst Solids* **2010**, *356*, 2315-2322.
2. Hopf, J.; Kerisit, S. N.; Angeli, F.; Charpentier, T.; Icenhower, J. P.; McGrail, B. P.; Windisch, C. F.; Burton, S. D.; Pierce, E. M., Glass-Water Interaction: Effect of High-Valence Cations on Glass Structure and Chemical Durability. *Geochim Cosmochim Ac* **2016**, *181*, 54-71.
3. R.W. Adams Jr, D. R. C., S. H. Knickerbocker, L.L. Rapp, B. Schwartz Zirconia Toughening of Glass-Ceramic Materials. US Patent 5,173,331. 1992.
4. R.W. Adams Jr, D. R. C., S. H. Knickerbocker, L.L. Rapp, B. Schwartz Zirconia Tougheniong of Glass-Ceramic Materials. US Patent 5,185,215. 1993.
5. Neumayer, D. A.; Cartier, E., Materials Characterization of ZrO_2-SiO_2 and HfO_2-SiO_2 Binary Oxides Deposited by Chemical Solution Deposition. *J Appl Phys* **2001**, *90*, 1801-1808.
6. Armelao, L.; Gross, S.; Muller, K.; Pace, G.; Tondello, E.; Tsetsgee, O.; Zattin, A., Structural Evolution Upon Thermal Heating of Nanostructured Inorganic-Organic Hybrid Materials to Binary Oxides MO_2-SiO_2 (M = Hf, Zr) as Evaluated by Solid-State NMR and FTIR Spectroscopy. *Chem Mater* **2006**, *18*, 6019-6030.
7. O'Dell, L. A.; Gunawidjaja, P. N.; Holland, M. A.; Mountjoy, G.; Pickup, D. M.; Newport, R. J.; Smith, M. E., Characterisation of Sol-Gel Prepared $(HfO_2)_{(X)}(SiO_2)_{(1-X)}$ (X=0.1, 0.2 and 0.4) by H-1, C-13, O-17 and Si-29 MAS NMR, FTIR and TGA. *Solid State Nucl Mag* **2008**, *33*, 16-24.
8. Kim, N.; Bassiri, R.; Fejer, M. M.; Stebbins, J. F., Structure of Amorphous Silica-Hafnia and Silica-Zirconia Thin-Film Materials: The Role of a Metastable Equilibrium State in Non-Glass-Forming Oxide Systems. *J Non-Cryst Solids* **2015**, *429*, 5-12.
9. Davis, L. L.; Darab, J. G.; Qian, M.; Zhao, D.; Palenik, C. S.; Li, H.; Strachan, D. M.; Li, L., Hafnium in Peralkaline and Peraluminous Boro-Aluminosilicate Glass and Glass Sub-Components: A Solubility Study. *J Non-Cryst Solids* **2003**, *328*, 102-122.
10. Charpentier, T.; Menziani, M. C.; Pedone, A., Computational Simulations of Solid State NMR Spectra: A New Era in Structure Determination of Oxide Glasses. *Rsc Adv* **2013**, *3*, 10550-10578.
11. Pickard, C. J.; Mauri, F., All-Electron Magnetic Response with Pseudopotentials: NMR Chemical Shifts. *Phys Rev B* **2001**, *63*.
12. Mauri, F.; Pasquarello, A.; Pfrommer, B. G.; Yoon, Y. G.; Louie, S. G., Si-O-Si Bond-Angle Distribution in Vitreous Silica from First-Principles Si-29 NMR Analysis. *Phys Rev B* **2000**, *62*, R4786-R4789.
13. Ferlat, G.; Charpentier, T.; Seitsonen, A. P.; Takada, A.; Lazzeri, M.; Cormier, L.; Calas, G.; Mauri, F., Boroxol Rings in Liquid and Vitreous B_2O_3 from First Principles. *Phys Rev Lett* **2008**, *101*.
14. Pedone, A.; Charpentier, T.; Malavasi, G.; Menziani, M. C., New Insights into the Atomic Structure of 45S5 Bioglass by Means of Solid-State NMR Spectroscopy and Accurate First-Principles Simulations. *Chem Mater* **2010**, *22*, 5644-5652.

15. Gambuzzi, E.; Pedone, A.; Menziani, M. C.; Angeli, F.; Florian, P.; Charpentier, T., Calcium Environment in Silicate and Aluminosilicate Glasses Probed by Ca-43 MQMAS NMR Experiments and MD-Gipaw Calculations. *Solid State Nucl Mag* **2015**, *68-69*, 31-36.
16. Hohenberg, P.; Kohn, W., Inhomogeneous Electron Gas. *Phys Rev B* **1964**, *136*, B864-+.
17. Kresse, G.; Hafner, J., Ab-Initio Molecular-Dynamics Simulation of the Liquid-Metal Amorphous-Semiconductor Transition in Germanium. *Phys Rev B* **1994**, *49*, 14251-14269.
18. Kresse, G.; Furthmuller, J., Efficient Iterative Schemes for Ab Initio Total-Energy Calculations Using a Plane-Wave Basis Set. *Phys Rev B* **1996**, *54*, 11169-11186.
19. Blochl, P. E., Projector Augmented-Wave Method. *Phys Rev B* **1994**, *50*, 17953-17979.
20. Kresse, G.; Joubert, D., From Ultrasoft Pseudopotentials to the Projector Augmented-Wave Method. *Phys Rev B* **1999**, *59*, 1758-1775.
21. Fujishita, H.; Hayashi, M.; Kanai, T.; Yamada, T.; Igawa, N.; Kihara, K., Study of Quantum Effects on Atomic Displacements in Quartz. *J Phys Chem Solids* **2010**, *71*, 1285-1289.
22. Dera, P.; Lazarz, J. D.; Prakapenka, V. B.; Barkley, M.; Downs, R. T., New Insights into the High-Pressure Polymorphism of SiO_2 Cristobalite. *Phys Chem Miner* **2011**, *38*, 517-529.
23. Hill, R. J.; Gibbs, G. V.; Craig, J. R.; Ross, F. K.; Williams, J. M., Neutron-Diffraction Study of Hemimorphite. *Z Kristallogr* **1977**, *146*, 241-259.
24. Mcdonald, W. S.; Cruickshank, D. W., A Refinement of Structure of S_3O_9. *Acta Crystallogr* **1967**, *22*, 48-+.
25. Pant, A. K.; Cruickshank, D. W., Crystal Structure of Alpha-$Na_2Si_2O_5$. *Acta Crystall B-Stru* **1968**, *B 24*, 13-+.
26. Pant, A. K., A Reconsideration of Crystal Structure of Beta-$Na_2Si_2O_5$. *Acta Crystall B-Stru* **1968**, *B 24*, 1077-&.
27. Rakic, S.; Kahlenberg, V.; Weidenthaler, C.; Zibrowius, B., Structural Characterization of High-Pressure C-Na(2)Si(2)O(5) by Single-Crystal Diffraction and (29)Si MAS NMR. *Phys Chem Miner* **2002**, *29*, 477-484.
28. Charpentier, T.; Ispas, S.; Profeta, M.; Mauri, F.; Pickard, C. J., First-Principles Calculation of O-17, Si-29, and Na-23 NMR Spectra of Sodium Silicate Crystals and Glasses. *J Phys Chem B* **2004**, *108*, 4147-4161.
29. Nimmo, J. P.; Kroll, P., First-Principles Calculations and Analysis of Si-29 Nuclear Magnetic Resonance Chemical Shifts in Silicon Oxycarbide Ceramics. *J Phys Chem C* **2014**, *118*, 29952-29961.
30. Mysen, B. O.; Frantz, J. D., Structure and Properties of Alkali Silicate Melts at Magmatic Temperatures. *Eur J Mineral* **1993**, *5*, 393-407.
31. Maekawa, H.; Maekawa, T.; Kawamura, K.; Yokokawa, T., The Structural Groups of Alkali Silicate-Glasses Determined from Si-29 Mas-Nmr. *J Non-Cryst Solids* **1991**, *127*, 53-64.

32. Ispas, S.; Charpentier, T.; Mauri, F.; Neuville, D. R., Structural Properties of Lithium and Sodium Tetrasilicate Glasses: Molecular Dynamics Simulations Versus NMR Experimental and First-Principles Data. *Solid State Sci* **2010**, *12*, 183-192.
33. Smith, J. V.; Blackwell, C. S., Nuclear Magnetic-Resonance of Silica Polymorphs. *Nature* **1983**, *303*, 223-225.
34. Oestrike, R.; Yang, W. H.; Kirkpatrick, R. J.; Hervig, R. L.; Navrotsky, A.; Montez, B., High-Resolution Na-23, Al-27, and Si-29 NMR-Spectroscopy of Framework Aluminosilicate Glasses. *Geochim Cosmochim Ac* **1987**, *51*, 2199-2209.
35. Charpentier, T.; Kroll, P.; Mauri, F., First-Principles Nuclear Magnetic Resonance Structural Analysis of Vitreous Silica. *J Phys Chem C* **2009**, *113*, 7917-7929.
36. Dasmahapatra, A.; Kroll, P., Structure and Thermochemistry of Hafnium-Silicate Glasses. *Abstr Pap Am Chem S* **2014**, *247*.
37. S. Monaghan, I. P. Single Crystal High Dielectric Constant Material and Method for Making Same. 2014.
38. Harry, G. M., Advanced Ligo: The Next Generation of Gravitational Wave Detectors. *Classical Quant Grav* **2010**, *27*.
39. T.P. Ledneva, K. A. B., Solubility of the Refractory Oxides Zirconium Dioxide and Hafnium Dioxide in Silica. *Steklo* **1973**, *2*, 84-87.
40. Grimley, D. I.; Wright, A. C.; Sinclair, R. N., Neutron-Scattering from Vitreous Silica IV. Time-of-Flight Diffraction. *J Non-Cryst Solids* **1990**, *119*, 49-64.

Summary

I explored 108-120 atom models of hafnia-soda-silica glasses with high (25 mol-% and 33 mol-%) soda content and the additions of hafnia on top of the initial composition in amounts up to 10 mol-%. My contribution here: NMR calculations, including choice of the calibration approach, data analysis, and application of the findings to the structural inversion of the experimental data.

Hf in such glasses adopts $[HfO_{6/2}]^{2-}\cdot 2Na^{+}$ environment; I find second nearest neighbor of Hf to be predominantly Si. Thermochemical data computed on the course of this investigation suggests the ΔH_{mix} values of -46±20 kJ/mol for 25 mol-% of soda and 50±10 kJ/mol for 33 mol-% of soda. Experimental value for NS25 composition is found to be -20 kJ/mol[1], which is within 2σ from our result.

It is well known that in silica and silicates ^{29}Si δ_{iso} is primarily a function of the Si-O-Si angles on its neighbor O atoms[2-5]. I find no effect of Hf presence in the glass on ^{29}Si NMR in case Hf is not a second nearest neighbor of Si: angular correlations of ^{29}Si δ_{iso} are the same as in Hf-free soda-silica glasses. In case Hf is the second nearest neighbor of Si I find the impact of Si-O-Hf angle that is different from Si-O-Si angle. This effect of Hf vs. Si in the second coordination sphere of Si constitutes, depending on the Q-unit type, 2.5 to 5.5 ppm increase of chemical shift.

I find no difference between the angular correlations in our models of hafnia-soda-silica glasses and in the models of sol-gel hafnia silica created by replacing Na into H. This allows me to apply out approach to the experimentally measures spectra of sol-gel derived hafnia-silica glasses[6]. My investigations suggest significantly different interpretation of the spectrum obtained by O'Dell[6] in terms of Q-units speciation and therefore degree of connectivity of hafnia-silica network.

References

1. Linard, Y.; Wilding, M. C.; Navrotsky, A., High Temperature Calorimetric Studies of Heat of Solution of Nio, Cuo, L,a(2)O(3), Tio2, Hfo2 in Sodium Silicate Liquids. *Geochim Cosmochim Ac* **2008**, *72*, 590-601.
2. Mauri, F.; Pasquarello, A.; Pfrommer, B. G.; Yoon, Y. G.; Louie, S. G., Si-O-Si Bond-Angle Distribution in Vitreous Silica from First-Principles Si-29 Nmr Analysis. *Phys Rev B* **2000**, *62*, R4786-R4789.
3. Charpentier, T.; Ispas, S.; Profeta, M.; Mauri, F.; Pickard, C. J., First-Principles Calculation of O-17, Si-29, and Na-23 Nmr Spectra of Sodium Silicate Crystals and Glasses. *J Phys Chem B* **2004**, *108*, 4147-4161.
4. Charpentier, T.; Kroll, P.; Mauri, F., First-Principles Nuclear Magnetic Resonance Structural Analysis of Vitreous Silica. *J Phys Chem C* **2009**, *113*, 7917-7929.
5. Ispas, S.; Charpentier, T.; Mauri, F.; Neuville, D. R., Structural Properties of Lithium and Sodium Tetrasilicate Glasses: Molecular Dynamics Simulations Versus Nmr Experimental and First-Principles Data. *Solid State Sci* **2010**, *12*, 183-192.
6. O'Dell, L. A.; Gunawidjaja, P. N.; Holland, M. A.; Mountjoy, G.; Pickup, D. M.; Newport, R. J.; Smith, M. E., Characterisation of Sol-Gel Prepared (Hfo2)(X)(Sio2)(1-X) (X=0.1, 0.2 and 0.4) by H-1, C-13, O-17 and Si-29 Mas Nmr, Ftir and Tga. *Solid State Nucl Mag* **2008**, *33*, 16-24.

CHAPTER 2: ^{29}SI NMR CHEMICAL SHIFTS IN CRYSTALLINE AND AMORPHOUS SILICON NITRIDES

Motivation and scope

Silicon nitride possesses attractive properties such as hardness[1], resistance to wear and oxidation resistance[2]. This set of properties makes it a material of choice for ball bearings, turbocharges or rocket engines. Dielectric properties and better diffusion barrier against water and sodium makes silicon nitride or Si-N-H films applicable as an insulator in microelectronics[3].

I attempt to provide more insight into silicon nitride structure via modeling and NMR calculations. First I explore Si_3N_4 crystals, both synthesized experimentally and hypothetical. I compute NMR for our library of crystalline structures, hypothetical crystalline models and distorted crystals to obtain relations between structural features, such as coordination number, bond length and pyramidalization of N.

I further compute NMR of the models of amorphous Si_3N_4, obtained via both network approach[4] and melt-quench simulations with empirical Garofalini potential[5], which was found to be the best for small model generation[6]. I test the hypotheses I came up with upon distorting crystals. Further I disprove a long list of hypotheses on the structural features that I thought might affect ^{29}Si δ_{iso}, and find the one that might be responsible for the experimentally observed asymmetry of the NMR peak[7].

I explore two other families of compounds with Si-N bonds and SiN_4 environments: silicon carbodiimide $Si(NCN)_2$ and silicon diimide $Si(NH)_2$. I study crystal structure of the former and provide support for the hypothesis that the experimentally defined one is the “averaged” one, while there is a more realistic candidate coming from computational investigations. For the latter, in amorphous silicon diimide models, generated via substitution of O into NH in silica models, I look at the effect of structure on the ^{29}Si chemical shift in this arrangement.

References

1. Zerr, A.; Kempf, M.; Schwarz, M.; Kroke, E.; Goken, M.; Riedel, R., Elastic Moduli and Hardness of Cubic Silicon Nitride. *J Am Ceram Soc* **2002**, *85*, 86-90.
2. Riley, F. L., Silicon Nitride and Related Materials. *J Am Ceram Soc* **2000**, *83*, 245-265.
3. Hector, A. L., Synthesis and Processing of Silicon Nitride and Related Materials Using Preceramic Polymer and Non-Oxide Sol-Gel Approaches. *Coordin Chem Rev* **2016**, *323*, 120-137.
4. Kroll, P., Structure and Reactivity of Amorphous Silicon Nitride Investigated with Density-Functional Methods. *J Non-Cryst Solids* **2001**, *293*, 238-243.
5. Garofalini, S. H.; Luo, W. W., Molecular Dynamics Simulations of Calcium Silicate Intergranular Films between Silicon Nitride Crystals. *J Am Ceram Soc* **2003**, *86*, 1741-1752.
6. Dasmahapatra A., K. P., Modeling Amorphous Silicon Nitride: A Comparative Study of Empirical Potentials. *Comp Mater Sci* **2018**, *148*, 165–175.
7. Carduner, K. R.; Carter, R. O.; Milberg, M. E.; Crosbie, G. M., Determination of Phase-Composition of Silicon-Nitride Powders by Si-29 Magic Angle Spinning Nuclear-Magnetic-Resonance Spectroscopy. *Anal Chem* **1987**, *59*, 2794-2797.

^{29}Si NMR chemical shifts in crystalline and amorphous silicon nitrides

Ilia Ponomarev and Peter Kroll

Department of Chemistry and Biochemistry, The University of Texas at Arlington

700 Planetarium Place, Arlington, Texas 76019, United States.

*pkroll@uta.edu

Abstract

We investigate ^{29}Si nuclear magnetic Resonance (NMR) chemical shifts δ_{iso} of silicon nitride by structural modeling and the Gauge-Included Projector Augmented Wave (GIPAW) method within Density Functional Theory (DFT) calculations. Our models comprise known and hypothetical crystalline Si_3N_4 as well as amorphous Si_3N_4 structures. We find good agreement with available experimental ^{29}Si NMR data for tetrahedral $Si^{[4]}$ and octahedral $Si^{[6]}$ in crystalline Si_3N_4, predict the chemical shift of a trigonal-bipyramidal $Si^{[5]}$ to be about -120 ppm, and quantify the impact of Si-N bond lengths on ^{29}Si δ_{iso}. We show through computations that experimental ^{29}Si NMR data indicates that silicon dicarbodiimide, $Si(NCN)_2$, exhibits bent Si-N-C units with angles of about 143° in its structure. A detailed investigation of amorphous silicon nitride shows that an observed peak asymmetry relates to the proximity of a fifth N neighbor in non-bonding distance between 2.5 and 2.8 Å to Si.

1. Introduction

Over the last decade several studies addressed NMR calculations of crystalline and amorphous silica and silicates[1-4]. Those studies show the power of state-of-the-art quantum-chemical calculations to support experimental characterization and analytics. Here we provide – for the first time – GIPAW[5] calculations for silicon nitride in crystalline and amorphous form.

We explore known and hypothetical crystalline structures of Si_3N_4 to reveal the effect of coordination number on ^{29}Si NMR and provide predictions for the chemical shift of 5-coordinated Si in nitrides, which haven't been experimentally found yet. We take a closer look on the effects of local structure on ^{29}Si δ_{iso} for $Si^{[6]}$ and $Si^{[4]}$ species. We also consider two different types of compounds comprising SiN_4 tetrahedra, but differently connected N atoms: silicon carbodiimide $Si(NCN)_2$ and silicon diimide $Si(NH)_2$.

2. Methods

We perform Density Functional Theory[6] calculations using the Vienna Ab Initio Simulation (VASP) package[7-8]. We use the Projector Augmented Wave (PAW) method[9-10] and approximate electron exchange and correlation by the Perdew-Burke-Ernzerhoff (PBE) generalized gradient approximation (GGA). For optimizations of both amorphous and crystalline models we rely on standard pseudopotentials provided with the VASP package and use an energy cutoff of 500 eV for the expansion of the wave function into the plane-wave basis set. We sample the Brillouin zone at the Γ-point only for amorphous models, while we choose appropriate k-point meshes for crystalline models. NMR calculations are carried out using the GIPAW algorithm[5] as implemented in the VASP code. For those we choose an energy cutoff of 600 eV and find ^{29}Si NMR chemical shifts converged to better than 0.2 ppm.

For calibration of chemical shifts we compute silicon nitride polymorphs as well as ternary M-Si-N structures with structural data taken from the Inorganic Crystal Structure Database[11]: α-Si_3N_4,[12] β-Si_3N_4,[13] γ-Si_3N_4,[14-15] $BaSi_6N_8$,[16] Li_2SiN_2,[17] $SrSi_6N_8$[18]. Keeping the reported experimental lattice parameters constant we first optimize atomic positions (forces lower than 5 meV/Å) and, thereafter, compute absolute ^{29}Si NMR chemical shifts. Results of NMR calculations are given in Table 1 together with experimental data. The relation between computed absolute chemical shifts and experimental isotropic chemical shifts is shown in Figure 1. A best fit is obtained by a linear gauge with the slope of unity:

$\delta_{iso} = \sigma_{iso} + 338.6$ (1).

Similar gauges have been used previously for polymorphs of SiO_2 as well as for a variety of silicates[1,4]. Using this calibration, computed chemical shifts agree with experimental data with a maximum deviation of 2 ppm.

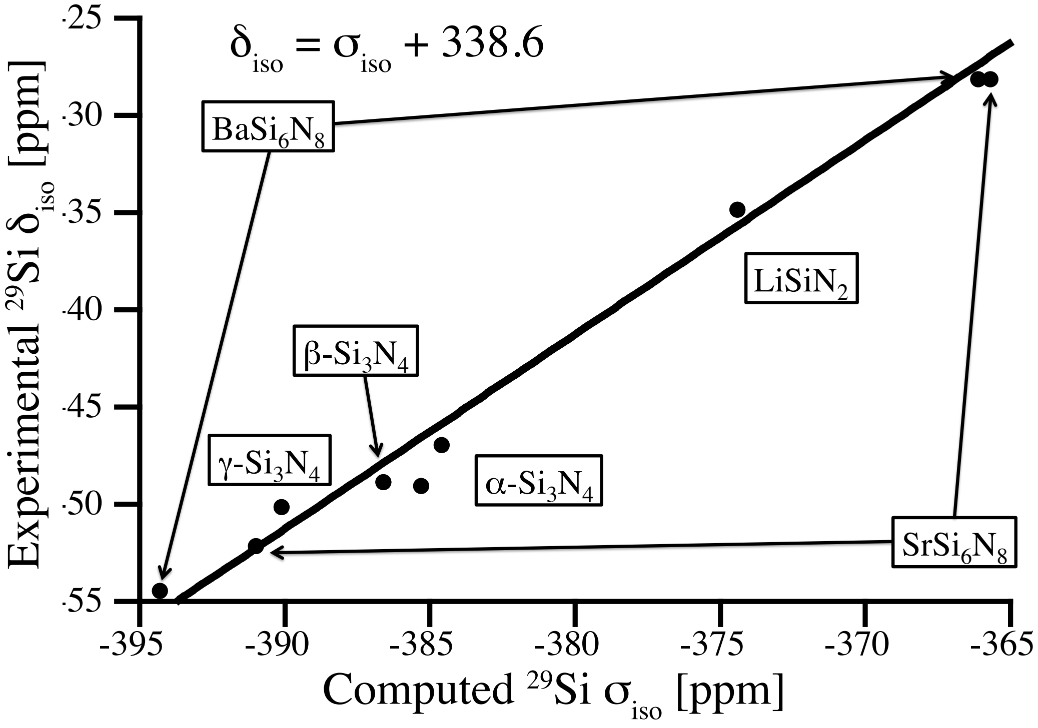

Figure 1. Relation between experimental data and computed absolute ^{29}Si NMR chemical shifts of Si sites in a variety of crystalline silicon nitrides. The calibration curve is a linear fit (unit slope) to the data.

Table 1. Experimental ^{29}Si NMR chemical shifts δ_{iso}, computed absolute shifts σ_{iso}, and predicted δ_{iso} of Si sites in a variety of crystalline silicon nitrides. The predicted value δ_{iso}^{calc} is based on a fit to the data; see Figure 1 and Eqn. 1.

Structure	Site	δ_{iso}^{exp}	σ_{iso}^{calc}	δ_{iso}^{calc}

		[ppm]	[ppm]	[ppm]
$BaSi_6N_8$[16]	1	-54.3	-394.4	-56.2
	2	-28.0	-366.2	-28.0
Li_2SiN_2[17]	1	-34.7	-374.5	-36.3
$SrSi_6N_8$[18]	1	-52.0	-391.1	-52.9
	2	-28.0	-365.8	-27.6
α-Si_3N_4[12, 19]	1	-48.9	-385.4	-47.2
	2	-46.8	-384.7	-46.5
β-Si_3N_4[13, 19]	1	-48.7	-386.7	-48.5
γ-Si_3N_4[14-15, 20]	1 ($Si^{[4]}$)	-50.0	-390.2	-52.0

The spinel-type γ-Si_3N_4 is the only silicon nitride exhibiting a 6-fold octahedrally coordinated $Si^{[6]}$ site, with a chemical shift of -225 ppm[20]. To investigate more highly coordinated Si sites (CN =5,6,7) and their ^{29}Si chemical shifts, we computed a series of hypothetical crystalline structures with composition Si_3N_4. Model structures are generated from binary A_3X_4- and ternary A_2BX_4-structure types by replacing all cations with Si and all anions with N. Crystallographic data of these structures is provided in the Supporting Information.

Amorphous silicon nitride models are generated by two different approaches. A set of network models was generated using a modified WWW algorithm[21-23] with subsequent DFT optimizations. Another set of models was produced by molecular dynamics simulations (MD) using the empirical potential of Garofalini et al.[24] integrated into the LAMMPS code[25]. In a recent study we showed that this potential produces structures with low defect concentrations and close to a DFT local minimum.[26] We followed a standard melt-quench procedure by first heating the system to 8000K and then quenching it in 280 ps ($\Delta t = 1$ fs) down to room temperature. Finally, we optimized all models within DFT as described above.

3. Results and discussion

Effects of coordination number – known and hypothetical crystalline Si_3N_4 structures

In Figure 2 we collect computed ^{29}Si NMR chemical shifts of Si sites in a variety of known and hypothetical silicon nitride, Si_3N_4, structures as a function of their nitrogen coordination number. Structural data as well as computed ^{29}Si NMR chemical shifts of each model are provided in Supporting Information (Table S1).

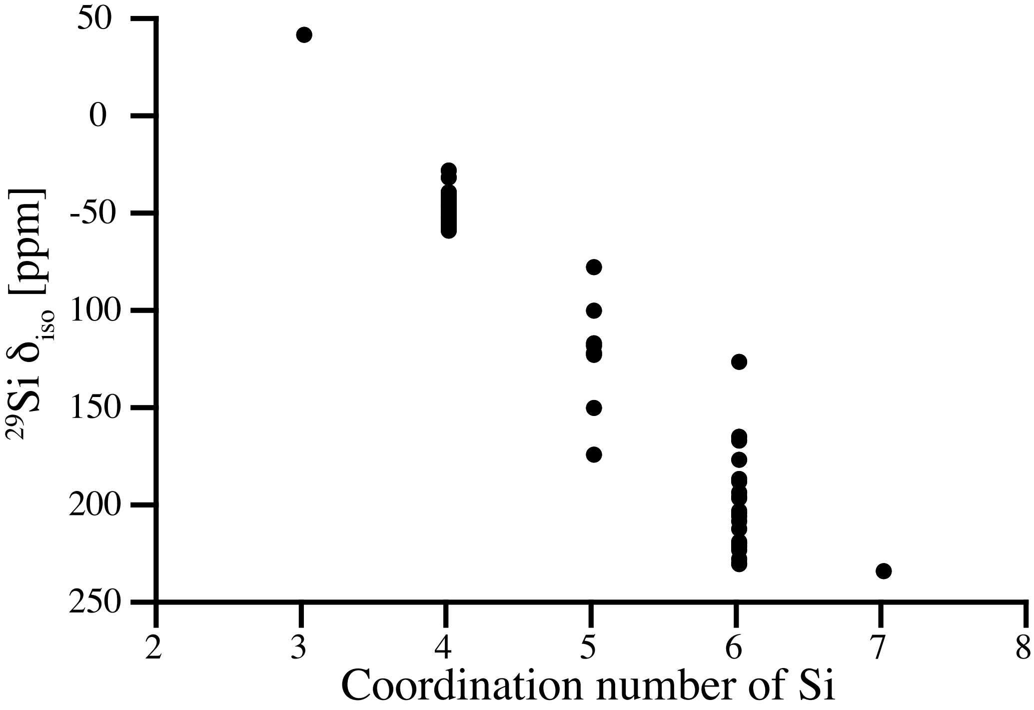

Figure 2. Relation between computed ^{29}Si δ_{iso} and coordination number of Si for hypothetical Si_3N_4 structures. To define a coordination number we use a cutoff of 2.4 Å for a Si-N bond length. In total 35 $Si^{[4]}$, 8 $Si^{[5]}$ and 24 $Si^{[6]}$ sites are collected.

In general, higher coordination number lowers the shielding of Si nucleus causing low-field shift. This is consistent with observations of chemical shifts in polymorphs of SiO_2

and silicates, where NMR chemical shifts of Si[6] have significantly more negative values (-191.1 ppm for stishovite[27], in the range from -210 to -220 ppm for silicophosphates[28]) than Si[4]. In particular, ^{29}Si NMR chemical shifts of tetrahedrally coordinated Si[4] sites fall into the range from -37 to -57 ppm. Notably examples of high-field shifts of -26.5 ppm and -30.2 ppm are two models, in which Si[4] sites are engaged into two 2-rings.

Among the five-fold coordinated Si[5]-sites, a trigonal-bipyramidal coordination (4 sites) yields δ_{iso} of -115 to -121 ppm. A square pyramidal Si[5] (two sites) is shifted to higher field, we found -76.4 ppm and -98.7 ppm, respectively. Two Si[5] sites appearing with shifts lower than -140 ppm are better described as 5+1 coordination, with a distance of only 2.5 Å to the 6th nitrogen neighbor. We discuss the impact of such "extended" bonds on ^{29}Si NMR chemical shifts more thoroughly for amorphous systems further below.

We compute the ^{29}Si NMR chemical shift of octahedrally coordinated Si[6] in spinel-type γ-Si_3N_4 to -228.4 ppm, which is consistent with the experimental value of -225 ppm[20]. Hence, our calibration is justified and applies even for significantly larger chemical shifts. The (almost perfect) octahedral coordination of Si in γ-Si_3N_4 falls onto the lowest values of chemical shifts, however. Values of δ_{iso} for other six-fold coordinated Si[6] sites fall into the range from -150 ppm to -230 ppm. We note that one "outlier" appears at -125 ppm. It displays strong differences of Si-N bond lengths to its neighbors, which is analyzed below.

We computed only one site for each three-fold (trigonal) coordinated Si[3] and seven-fold (pentagonal bipyramidal) coordinated Si[7]. They align with the overall trend: δ_{iso} of Si[3] is significantly higher than for Si[4], and δ_{iso} of Si[7] (which is better described as 5+2 coordination) is comparable to the lowest values of Si[6].

Impact of local structure – distortions of crystalline Si_3N_4 models

The key factor impacting ^{29}Si NMR chemical shifts of four-fold tetrahedrally coordinated $Si^{[4]}$ sites in silicates, where Si is coordinated by four (bridging) O atoms, is the Si-O-Si bond angle on neighboring oxygen atoms[1-4, 27, 29-31]. Hence, experimental ^{29}Si NMR data can be used for structural investigations, for instance in silicate glasses[1-3], and experimental "resolution" can be enhanced by thorough computational studies. The importance of the bond angle at O – rather than bond distances to and angles at the Si site – stems from the fact that silicates display almost perfect tetrahedral Si sites. Furthermore, the dependence of δ_{iso} on the Si-O bond distance is rather weak, as shown in Figure 5 for the structure of α–cristobalite SiO_2. Typical bond lengths between $Si^{[4]}$ and bridging O atoms in crystalline and amorphous silicates are 1.6-1.7 Å. However, the variation of δ_{iso} in this range barely exceeds 1 ppm.

In silicon nitrides Si sites are coordinated by N atoms. With N typically being three-fold coordinated by Si (for instance in α-Si_3N_4 and β-Si_3N_4), the parameter corresponding to the bond angle at O in oxide systems then is the degree of pyramidalization of N. Similar to the bond angle at O, the pyramidalization at N characterizes the localization of electrons at the anion site, which in turn impacts the shielding at the Si nucleus and, consequently, the ^{29}Si NMR chemical shifts. We express the pyramidalization of N as the ratio of height h of N above the plane formed by its three coordinating Si atoms and average Si-N bond length d (see Figure 3a). The parameter h/d, thus, is a measure of how much the N atom is out of the plane formed by its three Si neighbors.

The model structure best suited to study this potential correlation between pyramidalization and ^{29}Si NMR chemical shifts is that of (hypothetical) wII-Si_3N_4, which is the willemite-II structure[32-34]. With a single Si site and only two independent structural parameters, lattice parameter and one positional parameter of N, it allows a facile change of pyramidalization while maintaining constant Si-N bond distances. Thus, we compute the ^{29}Si NMR chemical shift for a series of different pyramidalization at N and results are shown in Figure 3. Essentially, δ_{iso} changes less than 1 ppm over a wide range until the N is so far above the plane that Si-N-Si angles are smaller than those in a regular tetrahedron (109.47°). Only for extreme distortions does a decrease of ^{29}Si δ_{iso} occur. This, however, is in this special case augmented by an increase of Si coordination from 4 to 8.

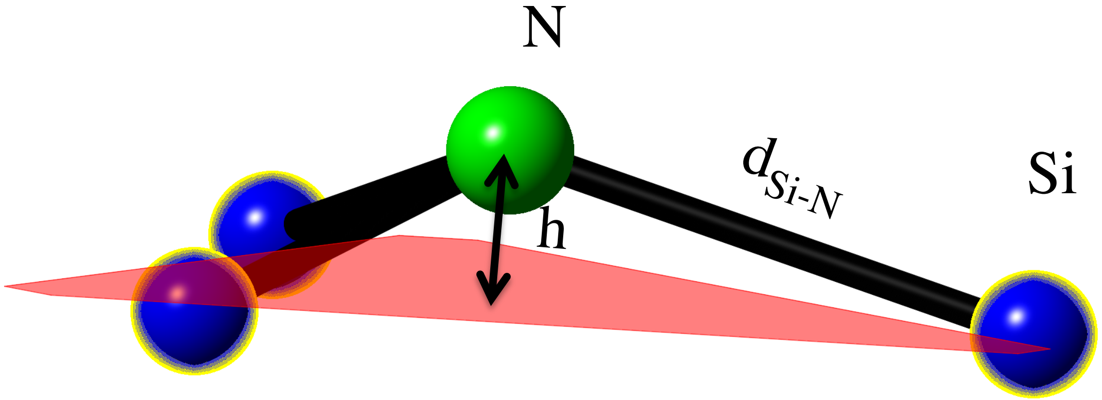

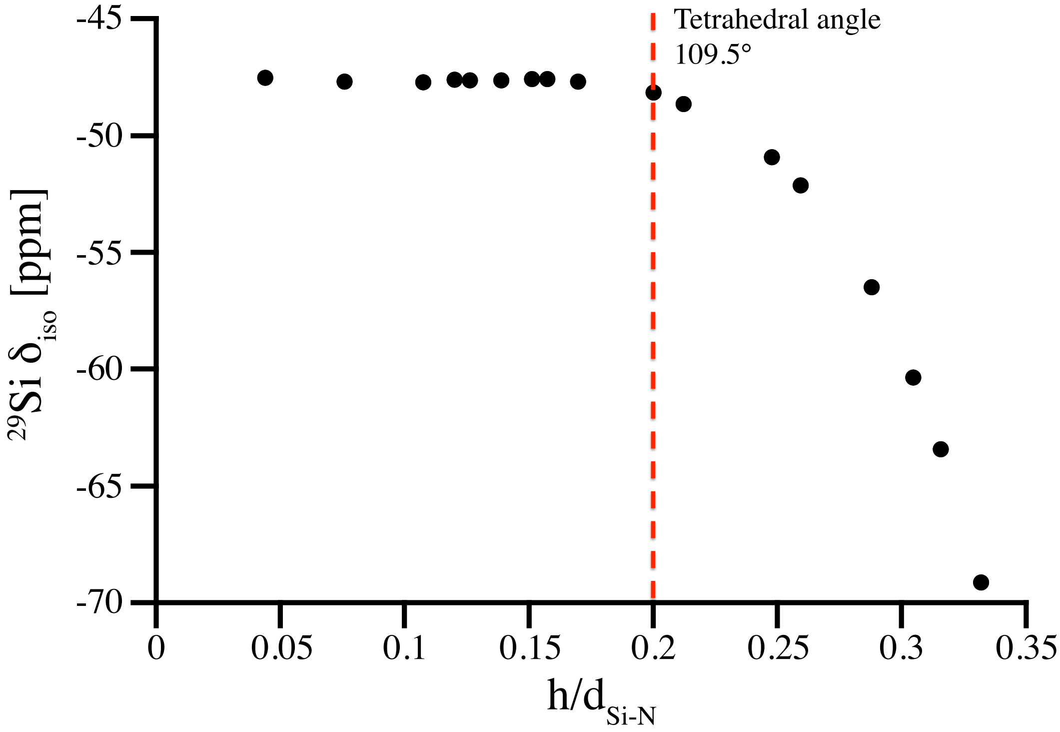

Figure 3. (top) representation of the pyramidalized N atom. (bottom) changes in ^{29}Si NMR chemical shift with increase of the degree of pyramidalization of N atom expressed as the relation of height of nitrogen over the plane of its neighboring Si atoms (h) to the Si-N bond length (d_{Si-N}). The correlation was obtained for the wII-Si_3N_4 model by changing the N position while adjusting cell parameters to maintain a Si-N bond length of 1.733 Å.

To highlight the impact of Si-N bond lengths on ^{29}Si NMR chemical shifts we scale the structure of β-Si_3N_4. The results are shown in Figure 4 and are compared with similar data obtained for α–cristobalite SiO_2. Interestingly, the bond distance dependence of δ_{iso} for tetrahedral $Si^{[4]}$ is very similar for SiO_2 and Si_3N_4. However, for the range of typical bond distances occurring in oxides and nitrides of silicon, a change in bond distance has significantly different impact on δ_{iso}. As mentioned earlier, typical $Si^{[4]}$-O bond lengths fall into a range of 1.6-1.7 Å, and small (up to 0.05 Å) bond length variations yield only small (< 1 ppm) changes of ^{29}Si NMR chemical shifts. On the other side, typical $Si^{[4]}$-N bond lengths are about 1.7-1.8 Å. In this range the slope of the curve is about significantly steeper, and a change of 1 pm (0.01 Å) in bond length yields about 1 ppm change in chemical shift.

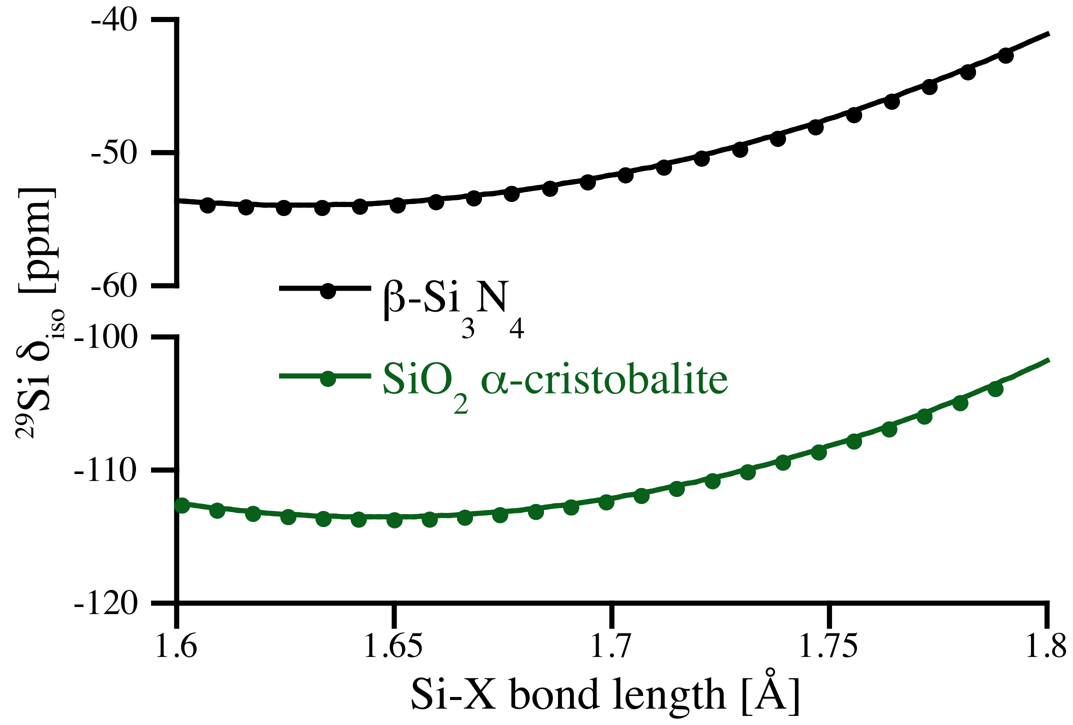

Figure 4. Correlation between average Si-O or Si-N bond lengths and ^{29}Si NMR chemical shifts. The y-axis has been adjusted to allow better comparison between the curves. The correlations are obtained by scaling of SiO_2 α-cristobalite and β-Si_3N_4 models, respectively.

The bond length dependence of ^{29}Si NMR chemical shifts appears significantly more pronounced for six-fold coordinated $Si^{[6]}$. In Figure 5 (top) we plot δ_{iso} for $Si^{[6]}$ in (hypothetical) crystalline models as a function of the average Si-N bond length around that site. The graph includes data for the octahedral $Si^{[6]}$ site in spinel-type γ-Si_3N_4 obtained by scaling the structure. Due to its location at a high symmetry position, the $Si^{[6]}$ site in spinel-type γ-Si_3N_4 exhibits six equal Si-N bonds.

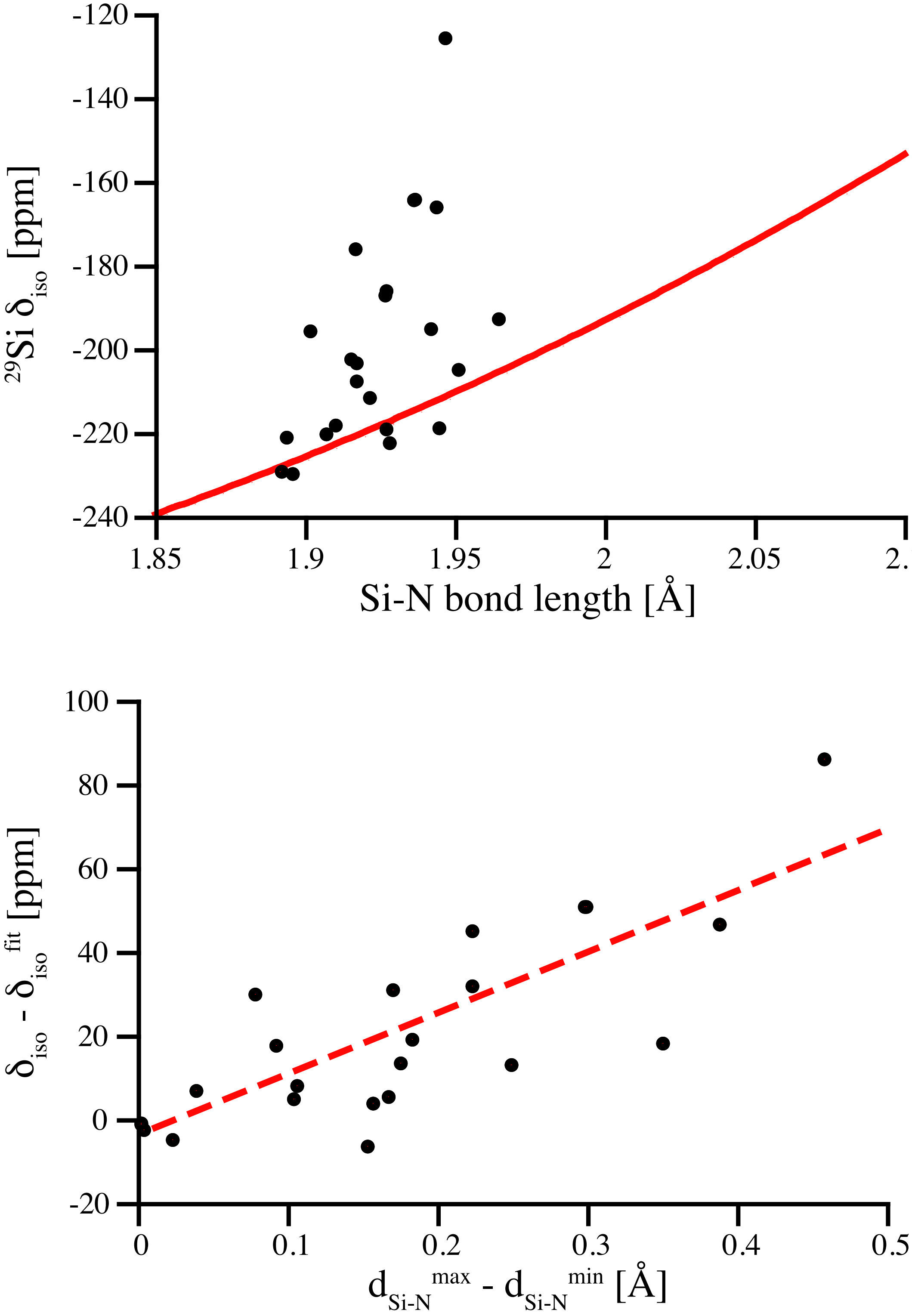

Figure 5. (top) ^{29}Si δ_{iso} of Si$^{[6]}$ sites in hypothetical crystalline Si_3N_4 plotted versus average Si-N bond length. The inserted line represents data for the Si$^{[6]}$ site in spinel-type γ-Si_3N_4,

computed after scaling the structure. (bottom) Deviation of the computed ^{29}Si NMR δ_{iso} for the distorted Si$^{[6]}$ sites plotted versus the difference between shortest and longest Si-N bond for that site. The dashed line represents a linear fit to the data.

If we regard the data for the Si$^{[6]}$ site in spinel-type γ-Si_3N_4 as a "gauge" characterizing the bond length dependency for Si$^{[6]}$ sites, we notice some significant discrepancies among the computed chemical shifts. Strong deviations from the gauge only occur towards high-field, and are related to distorted coordination environments around the Si$^{[6]}$ sites. Most important is an asymmetry among the Si-N bond lengths of that site. To illustrate this, we plot the deviation of the computed ^{29}Si NMR δ_{iso} for the distorted Si$^{[6]}$ site as a function of the difference between the shortest and the longest Si-N bond for that site (Figure 5, bottom). The data shows clearly the strong influence that an irregular environment can have on the chemical shift of Si$^{[6]}$.

Special case of the silicon dicarbodiimide – a bond angle dependence for a SiN_4-environments

Computation of ^{29}Si NMR chemical shifts and their comparison with experimental data also provide further insights into the riddle of silicon carbodiimide, $Si(NCN)_2$. The structure of $Si(NCN)_2$ is isostructural to β-cristobalite SiO_2[35], with the complex carbodiimide anion $[NCN]^{2-}$ replacing the oxide O^{2-}. With its relation to the cristobalite SiO_2-system, $Si(NCN)_2$ comprises SiN_4-tetrahedra, and since the N atoms are bonding to Si and C, there is a bond angle appearing at N. The experimental structure of $Si(NCN)_2$ (sp.gr. *Pm*-3*m*, (221)) exhibits linear Si-N-C angles with very short Si-N and N-C distances, and is considered an "average" structure only. Computational studies indicate that the lowest energy configuration of $Si(NCN)_2$ exhibits bent Si-N-C angles and relates best to the structure of α-cristobalite SiO_2.[36] However, density functional theory calculations using a variety of exchange-correlation functionals yield much larger lattice parameters than observed.[36] Only recently, negative thermal expansion (NTE) of

$Si(NCN)_2$ was proposed as the mechanism for a contraction of $Si(NCN)_2$ at higher temperatures, and a strong NTE effect was indeed measured.[37-38]

The experimental ^{29}Si NMR chemical shift determined for the $Si^{[4]}$ site in $Si(NCN)_2$ is δ_{iso} = -103 ppm.[35] Computations approach this value only within scaling studies of the proposed lowest energy model (sp.gr. *P*-4*n*2, (118)), shown in Figure 6 (top). Agreement between computed and experimental chemical shift is present, if the cell volume of the computed tetragonal model adopts a value of V = 219 $Å^3$. A cubic cell with the same volume will have a lattice parameter of a = 6.025 Å, which is only slightly smaller (by 2.5%) than the experimental cell parameter of 6.189 Å.

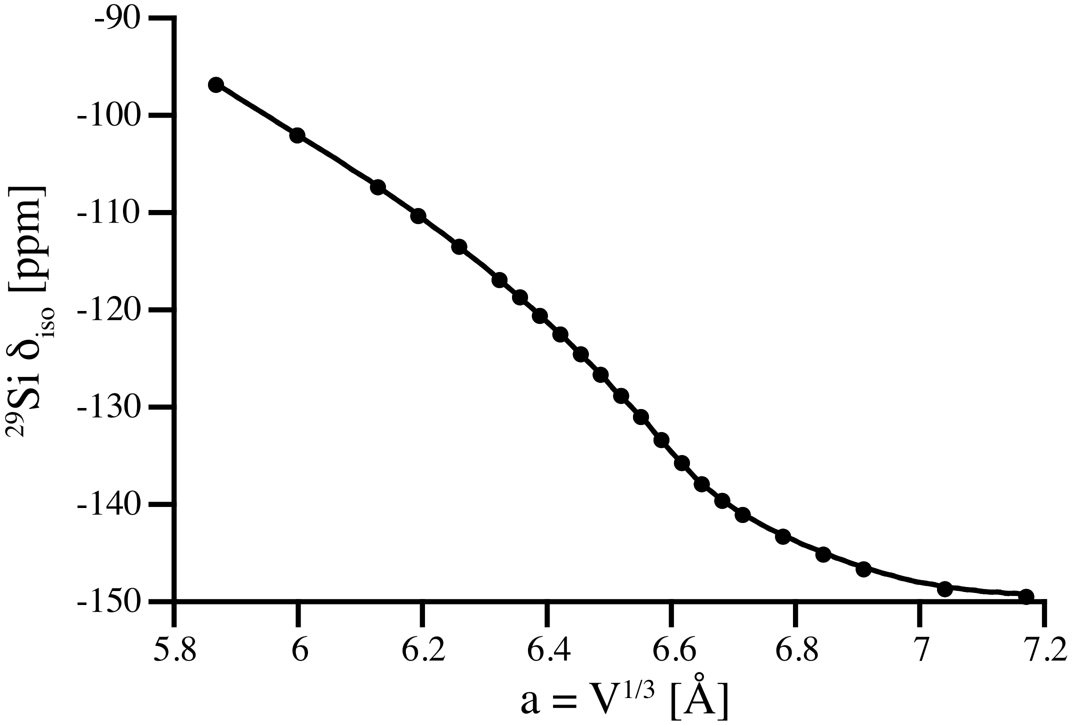

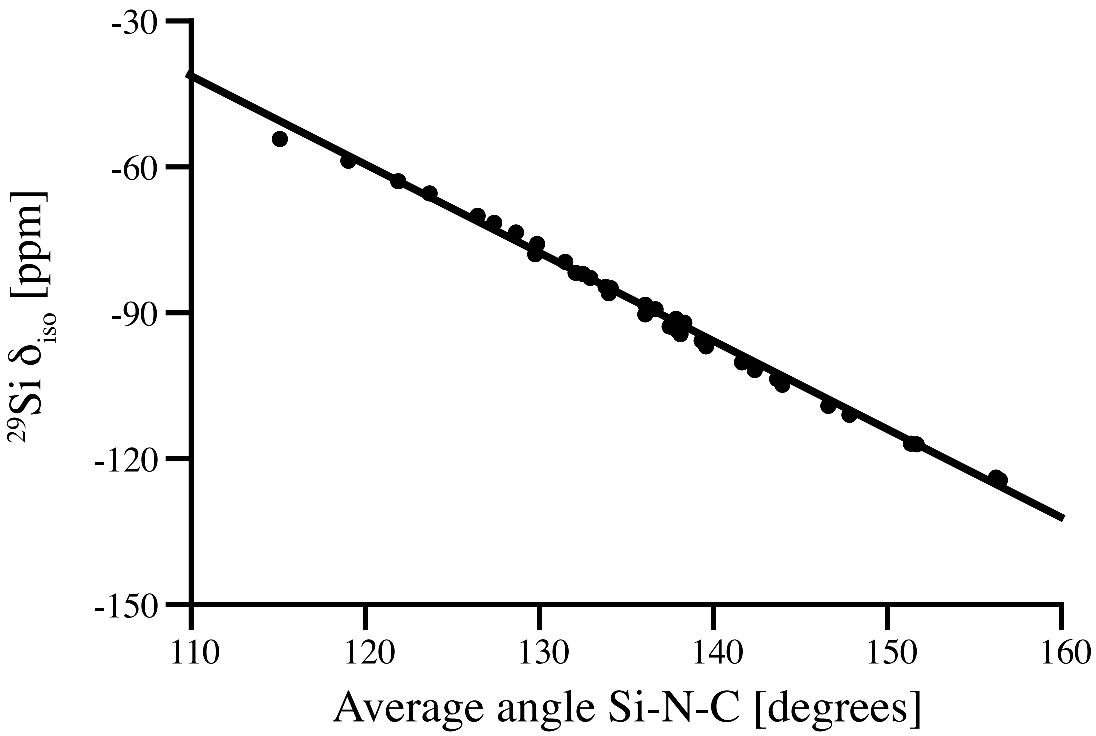

Figure 6. (top) computed ^{29}Si NMR δ_{iso} of proposed $P4n2$-Si(NCN)$_2$ obtained by contracting the volume of the structure. The chemical shift is plotted versus the corresponding "cubic" lattice parameter, a=V$^{1/3}$. (bottom) relation between computed ^{29}Si NMR δ_{iso} and average Si-N-C angle around Si site. Experimental data of δ_{iso} in Si(NCN)$_2$ is -103 ppm.[35]

Another way to support the likelihood of bent Si-N-C angles is to develop a correlation function between ^{29}Si NMR chemical shift value and Si-N-C bond angle at the N – following similar work for polymorphs of SiO$_2$ and other silicates[1,4]. Starting with a (unsymmetrical) distortion of the cubic structure of Si(NCN)$_2$, we optimize the model for a variety of volumes. As a result we obtain a set of structures with almost constant bond lengths, but quite different Si-N-C angles. We compute ^{29}Si NMR chemical shifts for both Si$^{[4]}$ sites in those structures and plot δ_{iso} as a function of the average Si-N-C angle around each site. The resulting linear correlation function is shown in Figure 6 (bottom). A chemical shift of -103 ppm as in the experiment is related to an average Si-N-C bond angle of 143° — and a linear angle can be excluded, similar to the case of β-cristobalite SiO_2.

Amorphous Si_3N_4

Over the last years, DFT calculations have become an indispensable tool enhancing the analytical strength of experimental NMR studies of glasses and amorphous materials.[2-4, 31, 39-40] Several experimental ^{29}Si NMR studies of amorphous silicon nitride, Si_3N_4, have been reported over the year.[41-43] They show a typical broad "peak" located at $\delta_{iso} \approx -46$ to -49 ppm. The width of the peak, typical is a FWHM of 20-30 ppm, depends strongly on the quality of the material and its residual hydrogen content. A characteristic feature of many spectra is an asymmetry towards low-field, as shown in Fig. 7[41].

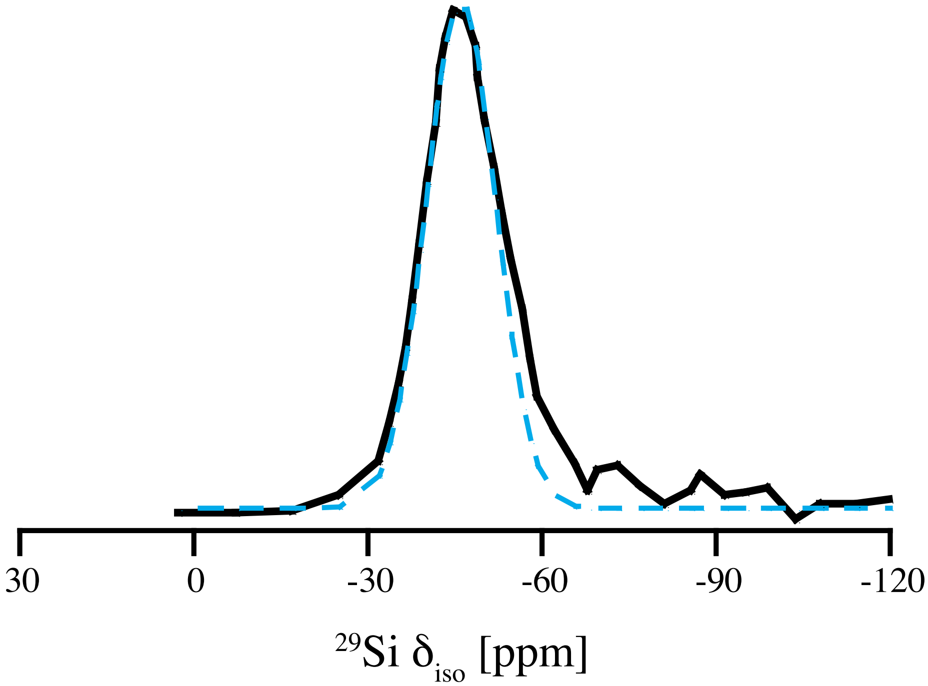

Figure 7. Reproduction of ^{29}Si NMR spectrum of amorphous Si_3N_4 according to Carduner et al. in Ref [41]. Dashed blue line represents a Gaussian centered at -46 ppm with the standard deviation of 6 ppm.

To analyze the correlations between structure and chemical shifts in amorphous Si_3N_4, we generated a variety of amorphous models comprising 112 or 224 atoms. On one side we used a network approach and on the other classical MD with an empirical potential[24]. After DFT optimization the models exhibit predominantly $Si^{[4]}$ (on average about 2% $Si^{[3]}$, 4% $Si^{[5]}$) and $N^{[3]}$ species (4% $N^{[2]}$, 6% $N^{[4]}$). About a quarter of all N atoms are involved in 2-ring structures. While we compute chemical shifts for all Si sites, we only consider $Si^{[4]}$ bonded to $N^{[3]}$ not involved in 2-rings in our further analysis. Essentially, network and classical MD models provide the same quality of NMR data.

We first study the impact of pyramidalization of N and of the Si-N bond length on ^{29}Si NMR chemical shifts, which is shown in Figure 8. For the wide range of distortions our models exhibit, we find that most of the computed δ_{iso} data fits well between -40 ppm and -60 ppm. None of the models shows extreme pyramidalization, and Si-N bond lengths fall well between 172 and 180 pm. We note, however, that the data of δ_{iso} for Si-N bond lengths does not align well with the correlation obtained by scaling β-Si_3N_4. Moreover, it shows higher scatter for longer bond lengths. Both of these issues will be addressed later. Overall, none of these plots reveals a systematic trend that may help to explain asymmetry of the experimental ^{29}Si NMR data of amorphous Si_3N_4.

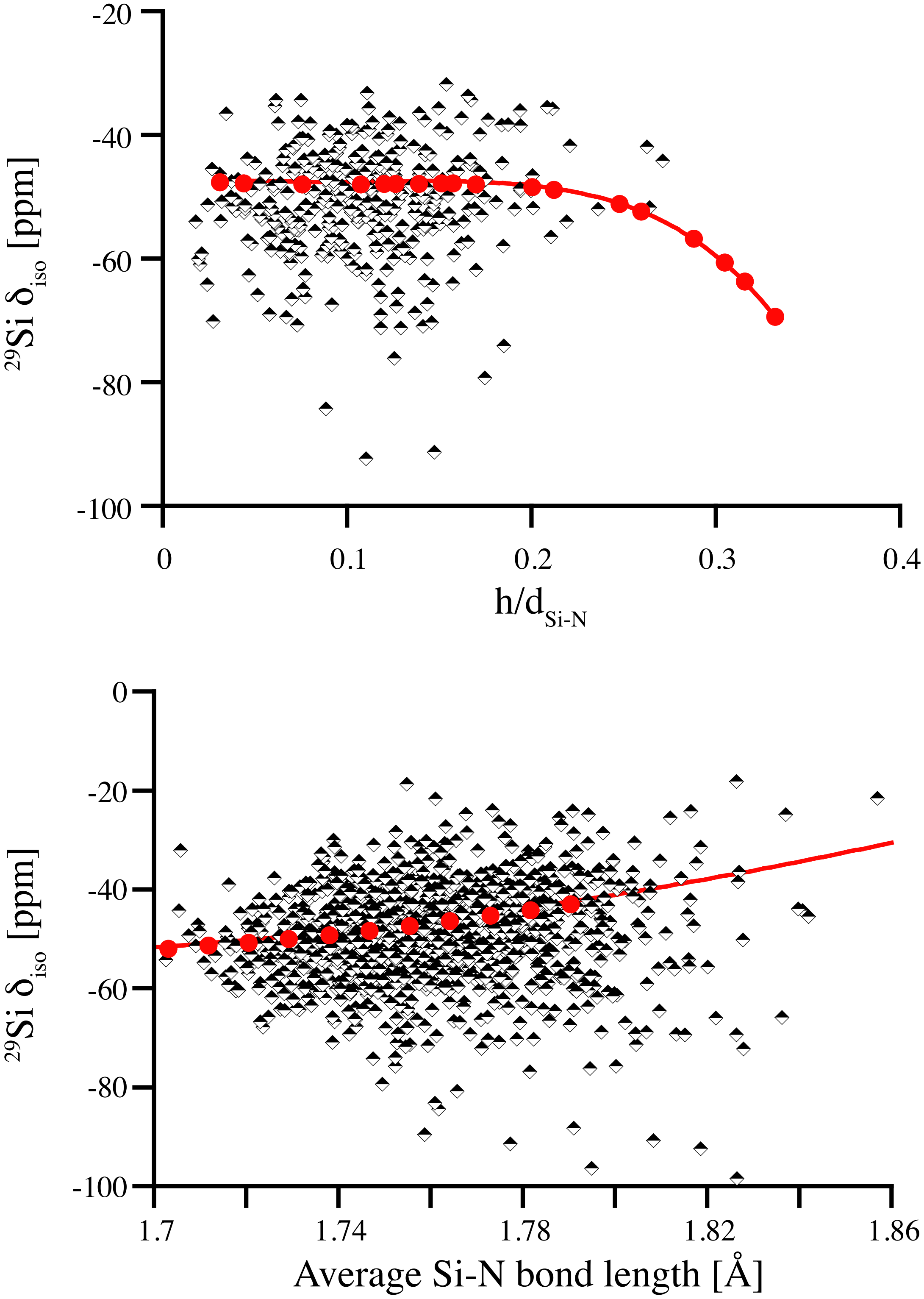

Figure 8: ^{29}Si NMR δ_{iso} in amorphous Si_3N_4, plotted versus average degree of pyramidalization of neighboring N atoms (top) and average Si-N bond length (bottom).

Red dots and lines depict the correlations obtained for distortions of crystalline models, wII-Si_3N_4 (left) and β-Si_3N_4 (right), repectively.

We the explored further correlations between ^{29}Si NMR chemical shifts and structural parameters. Among many hypotheses we studied, the proximity of the fifth closest N atom – the next-nearest beyond the four bonding N atoms – to the Si$^{[4]}$ site stood out. This correlation between ^{29}Si NMR chemical shift and distance of the fifth closest N to Si is shown in Figure 8. In contrast to crystalline models of α-Si_3N_4 and β-Si_3N_4, where the first coordination shell of Si$^{[4]}$ is well-defined and the next-nearest neighbor is another Si atom, an amorphous structure may comprise N atoms as next-nearest neighbor in proximity to Si$^{[4]}$. Interestingly, our process of distorting N positions in wII-Si_3N_4 to achieve higher pyramidalization (Figure 3, bottom) also brings additional neighbors (four at a time) into the coordination sphere of the Si site, which is why we include that data in Figure 8.

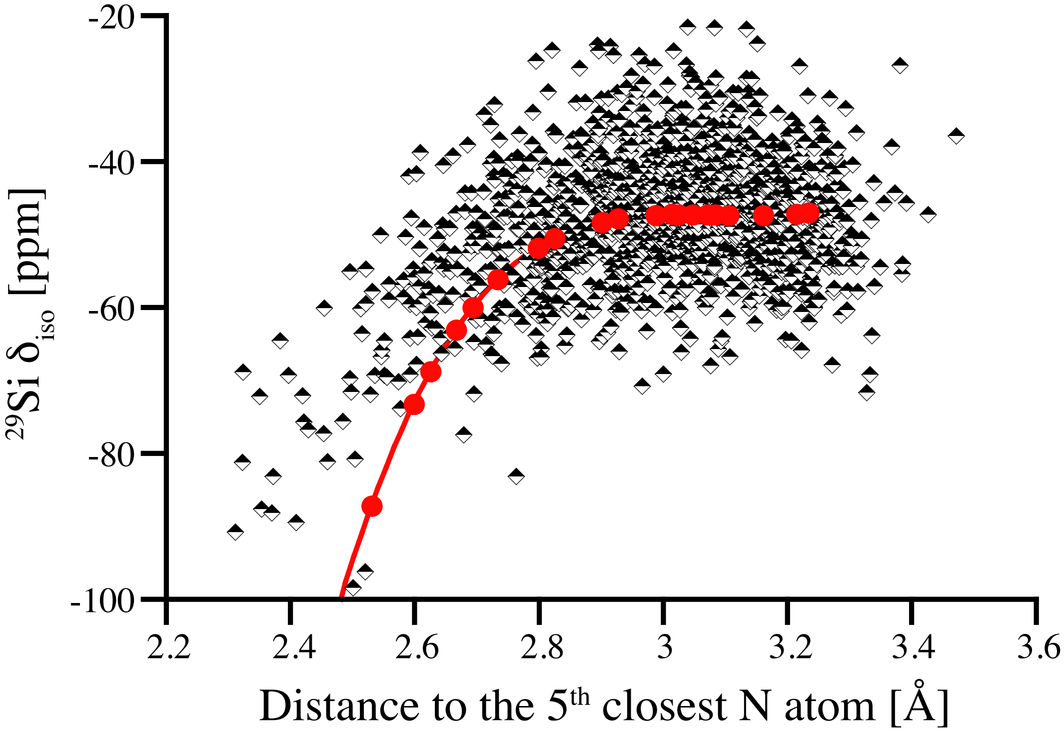

Figure 9. ^{29}Si NMR δ_{iso} plotted versus the distance to the 5th nearest N atom. Black-and-white dots represent computed results for the amorphous models. Red dots and line are results for distorted wII-Si_3N_4 models (see Figure 3).

Figure 9 shows that within a "critical" distance of 2.8 Å a fifth neighboring N atom has significant impact on the ^{29}Si NMR chemical shift. Thus, a likely explanation for the observed asymmetry of the (see Figure 7) is the proximity of a fifth N in non-bonding distance between 2.5 and 2.8 Å. Previously, Carduner et al. proposed some influence of N albeit in a much further distance of 3.8 Å. [19] We find that the intrusion of additional N atoms into the coordination sphere of Si is also the principal reason for changes in δ_{iso} when distorting wII-Si_3N_4 models earlier. The pyramidalization of N was a geometrical effect going along the much stronger impact of increasing the coordination of Si. Figure 9 indicates that the changes in ^{29}Si NMR chemical shifts upon distorting wII-Si_3N_4 are consistent with the proximity effects observed in amorphous models.

Having revealed the obvious influence of a fifth N atom in the coordination sphere of Si on its ^{29}Si chemical shift, we can identify those impacted sites and eliminate them from the correlation between ^{29}Si δ_{iso} and average Si-N bond length. Hence, we obtain a new correlation diagram shown in Figure 10. If we plot the deviation of δ_{iso} of amorphous Si_3N_4 from the correlation line β-Si_3N_4 for a given average bond length, we obtain the residual, which is given in Figure 10 on the bottom picture. This residual is centered almost at 0 and, as we confirmed, is independent from bond length. While the far majority of data falls within +/- 10 ppm of the projection obtained from scaling β-Si_3N_4, we see that a few $Si^{[4]}$ are still deviating by up to 30 ppm in chemical shift.

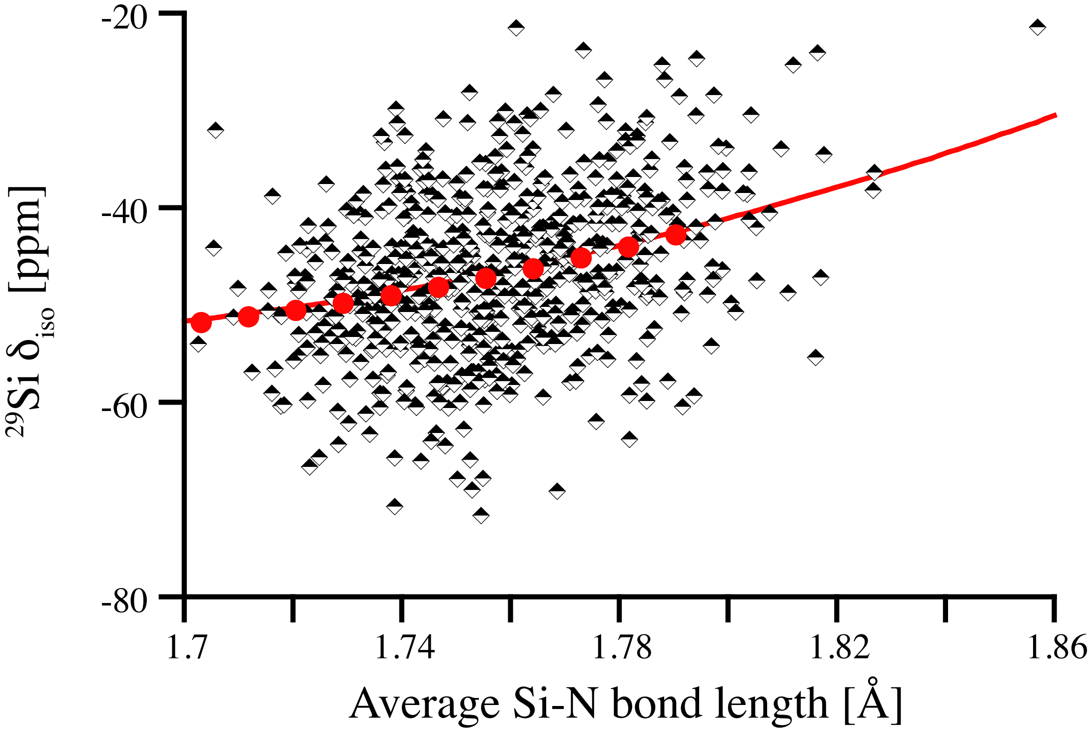

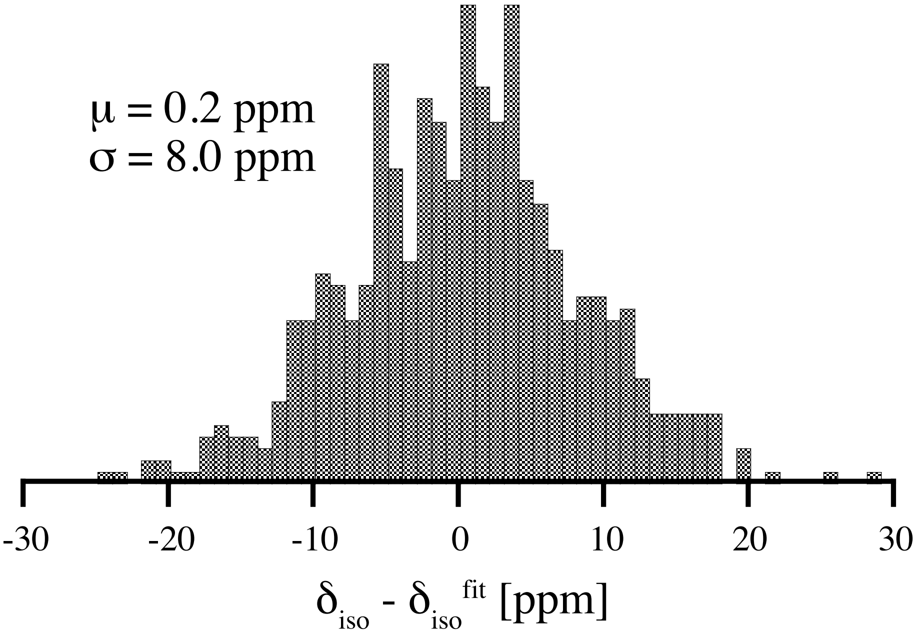

Figure 10: (left) correlation between ^{29}Si δ_{iso} and average Si-N bond length for Si[4] without a fifth N within 2.8 Å. Red dots and line depict the correlation obtained for

scaling crystalline β-Si_3N_4. (right) Histogram of deviations of data points of amorphous Si_3N_4 from correlation line β-Si_3N_4 ("Residual").

In further systematic analysis we looked for correlations between ^{29}Si δ_{iso} – or any residual – and various geometrical parameters and properties. Among these were tetrahedral angles at $Si^{[4]}$, distance to the next Si, computed charge on N, local density around $Si^{[4]}$, and involvement of $Si^{[4]}$ in small-membered rings, especially 3-membered rings. None of these tests revealed further pronounced effects on ^{29}Si NMR chemical shifts in Si_3N_4.

Overall, our results agree well with experimentally measured ^{29}Si NMR spectra of amorphous Si_3N_4 or Si_3N_4 nanopowders, which feature a broad peak centered at -46 to -49 ppm with FWHM of around 25 ppm and distorted towards lower δ_{iso} values[41-43]. We find that the asymmetry can be related to $Si^{[4]}$ sites with a fifth N atom in proximity closer than 2.8 Å. We note, however, that contamination with oxygen and the presence of oxynitride species (Si-N_3O, with ^{29}Si δ_{iso} values of -60 to -63 ppm[41]) may also held responsible for an asymmetry.

Amorphous hydrogenated silicon nitride

Amorphous silicon nitride synthesized by chemical vapor deposition (CVD) or by sol-gel methods typically contains significant amounts of hydrogen[44-46]. While hydrogen is incorporated mainly as NH_x species, it impacts the ^{29}Si NMR chemical shifts of a hydrogenated silicon nitride, SiN_x:H. To analyze the effect, we study amorphous silicon diimide, $Si(NH)_2$, as a model system.

$Si(NH)_2$ is topologically equivalent to SiO_2, which is why we can easily generate amorphous $Si(NH)_2$ models from models of amorphous silica. We start with SiO_2 models free of 3-rings,[31] replace O by N to form the Si-N-Si link, and add the H atom with a N-H distance of 1.1 Å into the Si-N-Si plane pointing outwards. We then optimize models using our standard procedure and compute NMR signals. ^{29}Si NMR chemical shifts range from -25 to -50 ppm, overlapping the range for ^{29}Si δ_{iso} that we computed for amorphous silicon nitride (-20 to -70 ppm, see above). In analogy to work on vitreous silica and amorphous silicates[1-4, 30-31], we can quickly establish a linear correlation between the ^{29}Si δ_{iso} , and the average Si-N-Si angle θ on N atoms surrounding the Si$^{[4]}$ site, see Figure 11 (top).

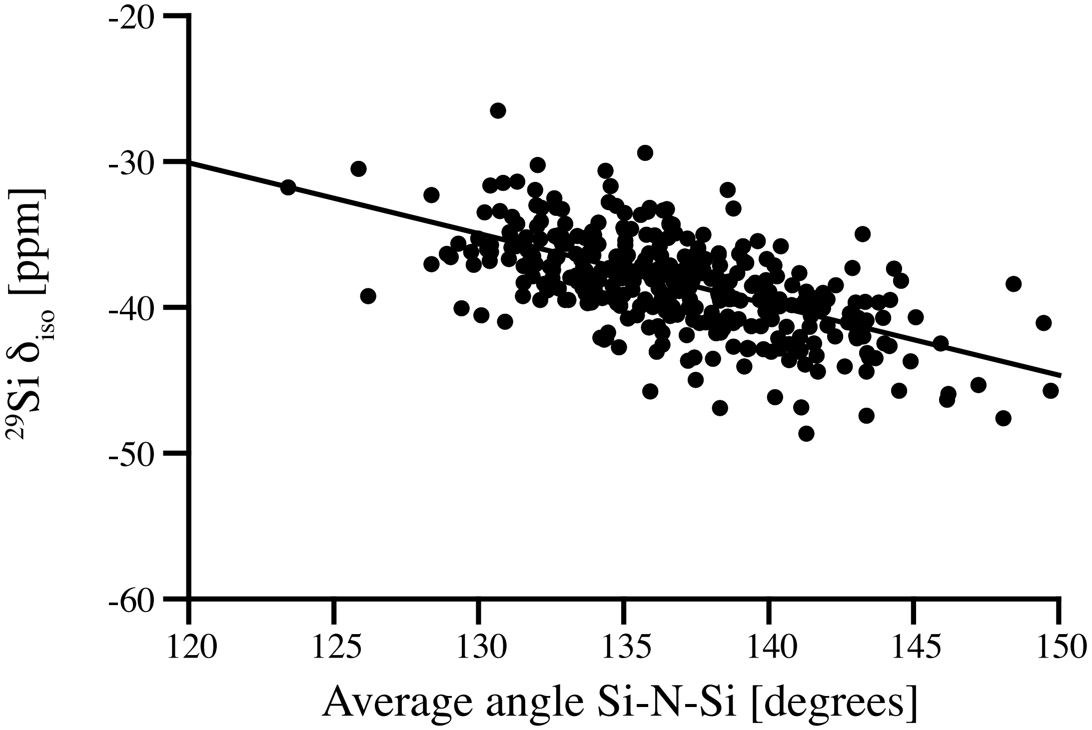

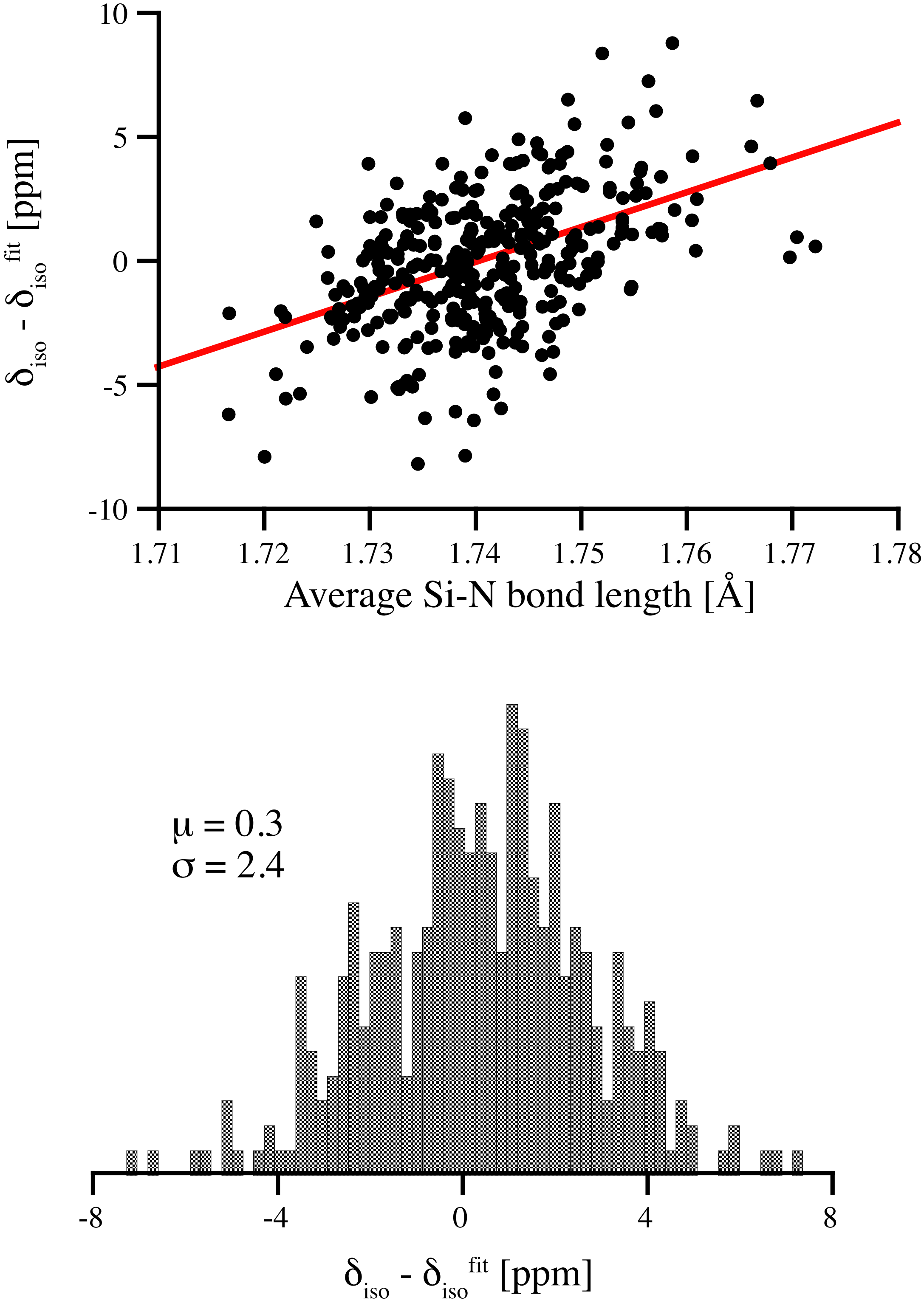

Figure 11: (top) Angular correlation between average Si-N-Si angle surrounding a Si$^{[4]}$ site in amorphous Si(NH)$_2$ and its ^{29}Si chemical shift. (center) Residual (deviations of

data points from linear fit) plotted vs. average Si-N bond legth. (bottom) Residual of the two-variable fit (bond angle and bond length; equation see text) along with the mean deviation from fit (μ) and standard deviation (σ).

For the angular correlation we find $\delta_{iso} = (28.2 - 0.486 \cdot \theta)$ ppm. Hence, the slope of the angular correlation for the nitride is just half of that for the oxide.[31] We observe a residual with a FWHM of 6.4 ppm, which is significantly higher than FWHM for SiO_2 (1.0),[31] but comparable to results obtained for soda-silica and hafnia-soda-silica glasses[4]. Further analysis shows that the residual correlates with the Si-N bond lengths at the $Si^{[4]}$ site, see Figure 11 (center). According to Figure 4, this impact of Si-N bonds lengths on δ_{iso} is expected. The effect of both bond length and bond angle is summarized in the double fit equation: $\delta_{iso} = (28.2 - 0.486 \cdot \overline{\Theta}) + (141 \cdot \overline{d}_{SiN} - 244.8)$, with the average bond angle $\overline{\Theta}$ given in degrees and the average bond length $\overline{d}_{SiN}$ given in Å. Accordingly, the resulting FWHM of the residual for the double fit is reduced to 5.7 ppm, see Figure 11 (bottom).

4. Summary and conclusion

We study the ^{29}Si NMR chemical shift δ_{iso} in crystalline and amorphous silicon nitrides using density functional theory calculations and GIPAW algorithm. The computational approach reproduces available experimental data of $Si^{[4]}$ and $Si^{[6]}$ sites in crystalline α-, β-, and γ-Si_3N_4, and predicts δ_{iso} of a trigonal-bipyramidal $Si^{[5]}$ to -120 ppm. We show the significant effect of Si-N bond lengths on ^{29}Si δ_{iso}, about 1 ppm change for 1 pm of changed bond length. For silicon dicarbodiimide, $Si(NCN)_2$, a comparison between experimental and computed chemical shifts shows that the Si-N-C angle at N is indeed bent, and not linear as the XRD patterns indicates. We propose that the peak asymmetry of $Si^{[4]}$ observed in experimental spectra of amorphous silicon nitride is related to the proximity of a fifth N neighbor in non-bonding distance between 2.5 and 2.8 Å. The chemical shift of $Si^{[4]}$ in hydrogenated silicon nitride correlates with the Si-NH-Si angle, albeit the additional dependence on Si-N bond distance increases the complexity of an analysis. Overall, we demonstrate through several examples the power of quantum-chemical calculations for improved characterization of crystalline and amorphous silicon nitride.

Acknowledgements

This work was supported by the NSF (DMR-1463974, CMMI-1634448, OISE 1743701). Computational work was made possible through generous grants by the Texas Advanced Computing Center (TACC) at The University of Texas at Austin.

References

1. Charpentier, T.; Ispas, S.; Profeta, M.; Mauri, F.; Pickard, C. J., First-principles calculation of O-17, Si-29, and Na-23 NMR spectra of sodium silicate crystals and glasses. *J Phys Chem B* **2004,** *108* (13), 4147-4161.
2. Charpentier, T.; Kroll, P.; Mauri, F., First-Principles Nuclear Magnetic Resonance Structural Analysis of Vitreous Silica. *J Phys Chem C* **2009,** *113* (18), 7917-7929.
3. Ispas, S.; Charpentier, T.; Mauri, F.; Neuville, D. R., Structural properties of lithium and sodium tetrasilicate glasses: Molecular dynamics simulations versus NMR experimental and first-principles data. *Solid State Sci* **2010,** *12* (2), 183-192.
4. Ponomarev, I.; Kroll, P., Impact of Transition Metal Cations on the Si-29 NMR Signal in Metal Oxide Glasses: A DFT Case Study of Hafnia Silica Glass. *J Phys Chem C* **2017,** *121* (43), 24152-24158.
5. Pickard, C. J.; Mauri, F., All-electron magnetic response with pseudopotentials: NMR chemical shifts. *Phys Rev B* **2001,** *63* (24).
6. Hohenberg, P.; Kohn, W., Inhomogeneous Electron Gas. *Phys Rev B* **1964,** *136* (3b), B864-+.
7. Kresse, G.; Hafner, J., Ab-Initio Molecular-Dynamics Simulation of the Liquid-Metal Amorphous-Semiconductor Transition in Germanium. *Phys Rev B* **1994,** *49* (20), 14251-14269.
8. Kresse, G.; Furthmuller, J., Efficient iterative schemes for ab initio total-energy calculations using a plane-wave basis set. *Phys Rev B* **1996,** *54* (16), 11169-11186.
9. Blochl, P. E., Projector Augmented-Wave Method. *Phys Rev B* **1994,** *50* (24), 17953-17979.
10. Kresse, G.; Joubert, D., From ultrasoft pseudopotentials to the projector augmented-wave method. *Phys Rev B* **1999,** *59* (3), 1758-1775.
11. Belsky, A.; Hellenbrandt, M.; Karen, V. L.; Luksch, P., New developments in the Inorganic Crystal Structure Database (ICSD): accessibility in support of materials

research and design. *Acta Crystallographica Section B-Structural Science* **2002,** *58*, 364-369.

12. du Boulay, D.; Ishizawa, N.; Atake, T.; Streltsov, V.; Furuya, K.; Munakata, F., Synchrotron X-ray and ab initio studies Of beta-Si3N4. *Acta Crystallogr B* **2004,** *60*, 388-405.

13. Toraya, H., Crystal structure refinement of alpha-Si3N4 using synchrotron radiation powder diffraction data: unbiased refinement strategy. *J Appl Crystallogr* **2000,** *33*, 95-102.

14. Zerr, A.; Miehe, G.; Serghiou, G.; Schwarz, M.; Kroke, E.; Riedel, R.; Fuess, H.; Kroll, P.; Boehler, R., Synthesis of cubic silicon nitride. *Nature* **1999,** *400* (6742), 340-342.

15. Schwarz, M.; Miehe, G.; Zerr, A.; Kroke, E.; Poe, B. T.; Fuess, H.; Riedel, R., Spinel-Si3N4: Multi-anvil press synthesis and structural refinement. *Adv Mater* **2000,** *12* (12), 883-887.

16. Stadler, F.; Schnick, W., The reduced nitridosilicate BaSi6N8. *Z Anorg Allg Chem* **2007,** *633* (4), 589-592.

17. Pagano, S.; Zeuner, M.; Hug, S.; Schnick, W., Single-Crystal Structure Determination and Solid-State NMR Investigations of Lithium Nitridosilicate Li2SiN2 Synthesized by a Precursor Approach Employing Amorphous "Si(CN2)(2)". *Eur J Inorg Chem* **2009,** (12), 1579-1584.

18. Stadler, F.; Oeckler, O.; Senker, J.; Hoppe, H. A.; Kroll, P.; Schnick, W., SrSi6N8 - A reduced nitridosilicate with a Si-Si bond. *Angew Chem Int Edit* **2005,** *44* (4), 567-570.

19. Carduner, K. R.; Blackwell, C. S.; Hammond, W. B.; Reidinger, F.; Hatfield, G. R., Si-29 Nmr Characterization of Alpha-Silicon and Beta-Silicon Nitride. *J Am Chem Soc* **1990,** *112* (12), 4676-4679.

20. Sekine, T.; Tansho, M.; Kanzaki, M., Si-29 magic-angle-spinning nuclear-magnetic-resonance study of spinel-type Si3N4. *Appl Phys Lett* **2001,** *78* (20), 3050-3051.

21. Kroll, P., Modelling polymer-derived ceramics. *J Eur Ceram Soc* **2005,** *25* (2-3), 163-174.

22. Kroll, P., Structure and reactivity of amorphous silicon nitride investigated with density-functional methods. *J Non-Cryst Solids* **2001,** *293*, 238-243.

23. Kroll, P., A DFT study of amorphous silicon oxynitride. *J Non-Cryst Solids* **2005,** *351* (12-13), 1127-1132.

24. Garofalini, S. H.; Luo, W. W., Molecular dynamics simulations of calcium silicate intergranular films between silicon nitride crystals. *J Am Ceram Soc* **2003,** *86* (10), 1741-1752.

25. Plimpton, S., Fast Parallel Algorithms for Short-Range Molecular-Dynamics. *J Comput Phys* **1995,** *117* (1), 1-19.

26. Dasmahapatra A., K. P., Modeling amorphous silicon nitride: A comparative study of empirical potentials. *Computational Materials Science* **2018,** *148*, 165–175.

27. Smith, J. V.; Blackwell, C. S., Nuclear Magnetic-Resonance of Silica Polymorphs. *Nature* **1983,** *303* (5914), 223-225.

28. Bonhomme, C.; Gervais, C.; Coelho, C.; Pourpoint, F.; Azais, T.; Bonhomme-Coury, L.; Babonneau, F.; Jacob, G.; Ferrari, M.; Canet, D.; Yates, J. R.; Pickard, C. J.;

Joyce, S. A.; Mauri, F.; Massiot, D., New perspectives in the PAW/GIPAW approach: J(P-O-Si) coupling constants, antisymmetric parts of shift tensors and NQR predictions. *Magn Reson Chem* **2010,** *48*, S86-S102.

29. Oestrike, R.; Yang, W. H.; Kirkpatrick, R. J.; Hervig, R. L.; Navrotsky, A.; Montez, B., High-Resolution Na-23, Al-27, and Si-29 Nmr-Spectroscopy of Framework Aluminosilicate Glasses. *Geochim Cosmochim Ac* **1987,** *51* (8), 2199-2209.

30. Mauri, F.; Pasquarello, A.; Pfrommer, B. G.; Yoon, Y. G.; Louie, S. G., Si-O-Si bond-angle distribution in vitreous silica from first-principles Si-29 NMR analysis. *Phys Rev B* **2000,** *62* (8), R4786-R4789.

31. Nimmo, J. P.; Kroll, P., First-Principles Calculations and Analysis of Si-29 Nuclear Magnetic Resonance Chemical Shifts in Silicon Oxycarbide Ceramics. *J Phys Chem C* **2014,** *118* (51), 29952-29961.

32. Marumo, F.; Syono, Y., Crystal Structure of Zn2sio4-Ii, a High-Pressure Phase of Willemite. *Acta Crystall B-Stru* **1971,** *B 27* (Oct15), 1868-&.

33. Kroll, P., Pathways to metastable nitride structures. *J Solid State Chem* **2003,** *176* (2), 530-537.

34. Teter, D. M.; Hemley, R. J., Low-compressibility carbon nitrides. *Science* **1996,** *271* (5245), 53-55.

35. Riedel, R.; Greiner, A.; Miehe, G.; Dressier, W.; Fuess, H.; Bill, J.; Aldinger, F., The first crystalline solids in the ternary Si-C-N system. *Angew Chem Int Edit* **1997,** *36* (6), 603-606.

36. Kroll, P.; Riedel, R.; Hoffmann, R., Silylated carbodiimides in molecular and extended structures. *Phys Rev B* **1999,** *60* (5), 3126-3139.

37. Kroll, P.; Andrade, M.; Yan, X. H.; Ionescu, E.; Miehe, G.; Riedel, R., Isotropic Negative Thermal Expansion in beta-Si(NCN)(2) and Its Origin. *J Phys Chem C* **2012,** *116* (1), 526-531.

38. Riedel, R.; Horvath-Bordon, E.; Kroll, P.; Miehe, G.; Dzivenko, D.; Kleebe, H. J.; van Aken, P. A.; Lauterbach, S., Novel binary and ternary phases in the Si-C-N system. *J Ceram Soc Jpn* **2008,** *116* (1354), 674-680.

39. Ferlat, G.; Charpentier, T.; Seitsonen, A. P.; Takada, A.; Lazzeri, M.; Cormier, L.; Calas, G.; Mauri, F., Boroxol rings in liquid and vitreous B2O3 from first principles. *Phys Rev Lett* **2008,** *101* (6).

40. Pedone, A.; Charpentier, T.; Malavasi, G.; Menziani, M. C., New Insights into the Atomic Structure of 45S5 Bioglass by Means of Solid-State NMR Spectroscopy and Accurate First-Principles Simulations. *Chem Mater* **2010,** *22* (19), 5644-5652.

41. Carduner, K. R.; Carter, R. O.; Milberg, M. E.; Crosbie, G. M., Determination of Phase-Composition of Silicon-Nitride Powders by Si-29 Magic Angle Spinning Nuclear-Magnetic-Resonance Spectroscopy. *Anal Chem* **1987,** *59* (23), 2794-2797.

42. Sun, X.; Liu, H. T.; Cheng, H. F., Oxidation behavior of silicon nitride fibers obtained from polycarbosilane fibers via electron beam irradiation curing. *Rsc Adv* **2017,** *7* (75), 47833-47839.

43. Yue, Y.; Li, D. H.; Ye, C. H., Characterization of laser synthesized silicon nitride powders with nanoscale by solid-state NMR. *J Mater Sci Lett* **1996,** *15* (12), 1079-1080.

44. Sardar, K.; Bounds, R.; Carravetta, M.; Cutts, G.; Hargreaves, J. S. J.; Hector, A. L.; Hriljac, J. A.; Levason, W.; Wilson, F., Sol-gel preparation of low oxygen content, high surface area silicon nitride and imidonitride materials. *Dalton T* **2016,** *45* (13), 5765-5774.
45. Yamamoto, Y.; Yokota, H.; Kojima, N.; Hayashi, S.; Kobayashi, T.; Sekine, T.; Sugahara, Y., Effects of structural differences in starting materials on the formation behavior of cubic silicon nitride by shock compression. *J Ceram Soc Jpn* **2013,** *121* (1416), 741-744.
46. Hector, A. L., Synthesis and processing of silicon nitride and related materials using preceramic polymer and non-oxide sol-gel approaches. *Coordin Chem Rev* **2016,** *323*, 120-137.

Summary

I explored structure vs. NMR relations in a variety of crystalline and amorphous silicon nitrides. My contribution here was generating amorphous Si_3N_4 models via melt-quench, NMR calculations and data processing.

My main conclusions are:

- NMR chemical shift of 5-coordinated Si in crystalline or amorphous nitrides will be ~ -115 ppm
- ^{29}Si δ_{iso} of 4-coordinated Si in nitrides, unlike oxides, is dependent on Si-N bond length; the effect of bond length is even more pronounced for 6-coordinated Si
- Pyramidalization of N isn't a factor in silicon nitrides, unlike angle on O in oxides[1]
- ^{29}Si NMR chemical shift depends on the distance to 5th nearest N neighbor, if this distance is shorter that 2.8-2.9 Å; this effect is a possible reason of the experimentally observed peak asymmetry of ^{29}Si NMR spectra in amorphous silicon nitrides[2].
- In compounds with SiN_4 environment where N atom is 2-connected (or can be considered 2-connected) the angle on N becomes the factor affecting ^{29}Si NMR.
- The P-4n2 (118) structural model of $Si(NCN)_2$[3] with the unit cell volume of 219 Å^3 and Si-N-C angle of 143° aligns with both experimental NMR and X-Ray observations.

Future research can be dedicated to the exploration of other factors that might affect ^{29}Si NMR in amorphous Si_3N_4. I've found the effects of the average bond length and the distance to the nearest 5th N if it's close enough. Those two factors leave a symmetrical and centered on 0 but wide ($\sigma = 8$ ppm) residual behind; it might be caused by some other factor yet to be revealed. I tested a large number of other potential structural causes of changes in NMR. The first idea was about pyramidalization of N as an analogue of angle on O in oxides. This hypothesis got disproved quite quickly. I further tested a set of other potential causes (charges on atoms, chemical shift of nitrogen, tetrahedral angles on Si, involvement in 6-membered rings) with zero result, but there can still be something left behind.

References

1. Mauri, F.; Pasquarello, A.; Pfrommer, B. G.; Yoon, Y. G.; Louie, S. G., Si-O-Si Bond-Angle Distribution in Vitreous Silica from First-Principles Si-29 Nmr Analysis. *Phys Rev B* **2000**, *62*, R4786-R4789.
2. Carduner, K. R.; Carter, R. O.; Milberg, M. E.; Crosbie, G. M., Determination of Phase-Composition of Silicon-Nitride Powders by Si-29 Magic Angle Spinning Nuclear-Magnetic-Resonance Spectroscopy. *Anal Chem* **1987**, *59*, 2794-2797.
3. Kroll, P.; Riedel, R.; Hoffmann, R., Silylated Carbodiimides in Molecular and Extended Structures. *Phys Rev B* **1999**, *60*, 3126-3139.

CHAPTER 3: STRUCTURAL INSIGHT INTO LAYERED HYDROGEN SILICOPHOSPHATES CONTAINING [SiO_6] OCTAHEDRA PREPARED BY DIFFERENT REACTION ROUTES

Motivation and scope

SiO_2-P_2O_5 glasses find applications as biocompatible materials[1] or rare-earth ion hosts[2]. Another feature causing theoretical interest to this family of glasses is the presence of 6-coordinated Si[3], which is common at high pressure[4], but doesn't normally happen at normal pressure, besides some specific cases like sulfates[5].

Within this work silicophosphates were experimentally synthesized via different approaches: sol-gel from alkoxysilanes and pyrophosphoric acid or dissolution of silicon nanoparticles in phosphoric acid. The NMR signals of the products were similar, besides by-products; however, XRD didn't provide a conclusive spectrum that could be refined to figure out the crystalline structure of the product.

From the computational side I tested a list of potential candidates among Si/P/O/H compounds to figure out the structure that would agree with the experimental observations. I further explored potential modifications of the structure that could explain other features of the experimentally measured NMR spectra.

References

1. Krishnan, V.; Lakshmi, T., Bioglass: A Novel Biocompatible Innovation. *J Adv Pharm Technol Res* **2013**, *4*, 78-83.
2. Izumitani T., M. M., Hata C. Silicophosphate Laser Glass. 1989.
3. Dupree, R.; Holland, D.; Mortuza, M. G.; Collins, J. A.; Lockyer, M. W. G., An Mas Nmr-Study of Network - Cation Coordination in Phosphosilicate Glasses. *J Non-Cryst Solids* **1988**, *106*, 403-407.
4. Sinclair, W.; Ringwood, A. E., Single-Crystal Analysis of Structure of Stishovite. *Nature* **1978**, *272*, 714-715.

5. Logemann, C.; Kluner, T.; Wickleder, M. S., The [Si(S2o7)(3)](2-) Anion: A First Example of Octahedral Silicon Coordination by Three Chelating Inorganic Ligands. *Chem-Eur J* **2011**, *17*, 758-760.

Structural Insight into Layered Silicon Hydrogen Phosphates Containing $[SiO_6]$ Octahedra Prepared by Different Reaction Routes

Janine Kowalke[1], Christine Arnold[2], Ilia Ponomarev[3], Christian Jäger[4], Peter Kroll[3], Erica Brendler[2] and Edwin Kroke*[1]

[1] Technische Universität Bergakademie Freiberg, Department of Chemistry and Physics,
Institute of Inorganic Chemistry
Leipziger Straße 29, 09599 Freiberg, Germany
[2] Technische Universität Bergakademie Freiberg, Department of Chemistry and Physics,
Institute of Analytical Chemistry
Leipziger Straße 29, 09599 Freiberg, Germany
[3]The University of Texas at Arlington, Department of Chemistry and Biochemistry
700 Planetarium Place, Arlington, Texas 76019, United States.
[4]BAM Federal Institutre of Materials Research and Testing, Division I.3
Richard Willstaetter Strasse 11, 12489 Berlin, Germany
*kroke@tu-freiberg.de

Abstract

The layered silicophosphate $Si(HPO_4)_2$ was prepared via a novel synthesis approach using silicon nanopowder and orthophosphoric acid at 150 °C providing a polycrystalline product. Silicophosphate compounds with six-fold coordinated silicon atoms exhibiting the same short-range order obtained from pyrophosphoric acid $H_4P_2O_7$ and tetraalkoxysilanes via a sol-gel route. The solid products were analyzed with XRD, elemental analysis (ICP-AES) and detailed NMR studies, including ^{1}H, ^{13}C, ^{29}Si and ^{31}P MAS-, ^{31}P-^{29}Si-REDOR, HETCOR and CP-RFDR experiments. DFT optimizations support the structure of $Si(HPO_4)_2$ consisting of layers of $[SiO_6]$ octahedra linked by

$PO_3(OH)$ tetrahedra. The OH-groups point to the neighboring layers and may be substituted by ethoxy or other groups

Introduction

Silicophosphates, i.e. in narrower sense compounds in the element system Si/P/O/(H), show in contrast to naturally occurring silicates and related silicon-oxygen compounds an unusual structural characteristics, namely six-fold coordination of the silicon atoms with oxygen atoms.[1] Typically, this phenomenon is only known from several high pressure silicates, e.g. stishovite.[2] Not only in phosphorus containing glasses[3–5] but also in a number of crystalline silicophosphates, e.g. SiP_2O_7,[6–8] $Si_5P_6O_{25}$[9] and $Si(HPO_4)_2{\cdot}xH_2O$ (x=0,1),[10,11] the silicon is present in $[SiO_6]$ units at normal pressure. The role of phosphorus for building up $[SiO_6]$ octahedra in silicophosphates has been discussed in several theoretical investigations.[12,13] Furthermore, the optical[14] and material properties[15] of silicophosphates, which are partly different from silicate materials due to the phosphorus content, are of basic interest relating to applications in laser technique,[16,17] implants research[18] or catalysis.[19,20] For the synthesis of such silicophosphate compounds transport reactions[9] or high temperatures[6,21] are useful. Alternatively, the sol-gel technique is used.[22,23] The formation of $[SiO_6]$ moieties is controlled by parameters such as temperature, precursor concentration and pH value. In the case of these sol-gel reactions, water or ethanol are used as solvents. Another possible reaction pathway is the non-hydrolytic sol-gel route. Silicophosphates with $[SiO_6]$ units were synthesized via ester elimination from silicon acetate, $Si(OAc)_4$ and tris(trimethylsilyl)phosphate, $OP(OSiMe_3)_3$ in different organic solvents.[24–26] In contrast to hydrolytic sol-gel and non-hydrolytic sol-gel reactions we used in this and in preceding works[27–29] a "water free" sol-gel-route. That means no water or alcohols were used as solvents, but the starting materials could include hydroxy groups. This "water free" synthesis is performed normally with crystalline phosphoric acid and tetraalkoxysilanes in diethyl ether. It leads to amorphous silicophosphate compounds containing $[SiO_6]$ octahedra and $[SiO_4]$ tetrahedra.[28] By varying the alkoxy residue of the silane or by replacing the phosphoric acid by pyrophosphoric acid the resulting products are amorphous as well. According to their ^{31}P and ^{29}Si NMR chemical shift data they have in common that a compound consisting of hydrogen phosphate and six-fold coordinated silicon is formed. The same chemical shifts and therefore structural elements are observed after the synthesis of silicophosphates from SiO_2 and concentrated phosphoric acid. Based on reported NMR data[19] and X-ray powder diffraction[10,11] a structural conformity to $Si(HPO_4)_2$ is noticed.

Although this silicophosphate $Si(HPO_4)_2$ has already been investigated in the past,[10,11,30–32] to the best of our knowledge its structure has not been reported in detail so far in literature and is still under discussion. Therefore, we developed a DFT optimized structure model, which was the basis to determine corresponding NMR chemical shift data.

In addition, we present here two new synthetic routes for silicophosphates, which are completely different from each other (Scheme 1), but nevertheless resulting silicophosphate compounds with $[SiO_6]$ octahedra exhibiting the same short-range order. One approach is based on the mentioned "water free" sol-gel route using pyrophosphoric acid $H_4P_2O_7$ and tetraalkoxysilanes $Si(OR)_4$, while the other route is based on reactions of silicon with ortho-phosphoric acid H_3PO_4 at 150 °C.

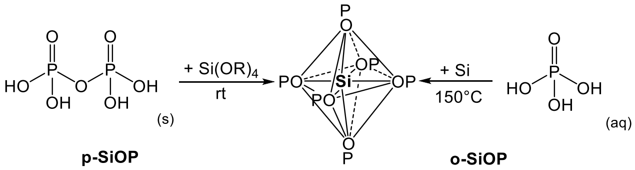

Scheme 1. Two different reaction pathways to obtain layered hydrogen silicophosphates with [SiO6] octahedra (R = Et, iPr).

The products were analysed by ^{1}H, ^{13}C, ^{29}Si and ^{31}P MAS NMR spectroscopy. For further information about the steric arrangement ^{31}P-^{29}Si REDOR (Rotational Echo Double Resonance), HETCOR (Heteronuclear Correlation) and CP-RFDR (Radio Frequency-Driven Recoupling) NMR experiments were performed as well.

Results and discussion

Different reaction routes for layered hydrogen silicophosphates

Synthesis of Si(HPO$_4$)$_2$ with silicon nanopowder

For structural investigations on $Si(HPO_4)_2$ a phase pure sample is recommendable. Literature syntheses of hydrogen silicophosphates frequently start from SiO_2 and accordingly silica gels and concentrated orthophosphoric acid.[6,7,31] If NMR spectroscopy was used for characterization, a ^{29}Si CP/MAS NMR spectrum was recorded, pretending pure $Si(HPO_4)_2$.[31] The ^{29}Si MAS NMR spectrum of such a silicophosphate product, o-SiOP2, is given in Figure 1.

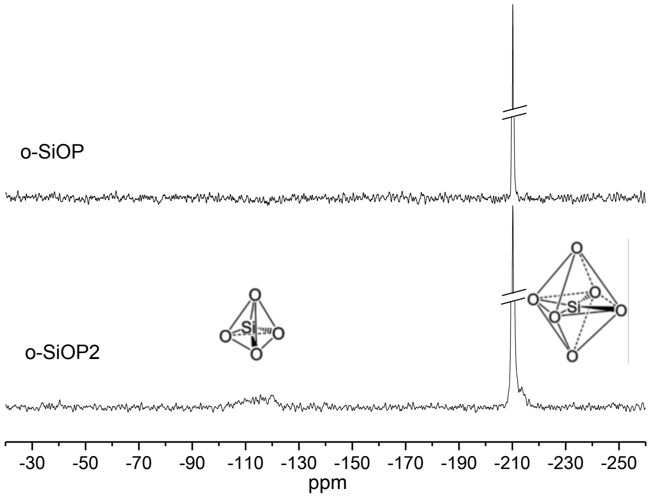

Figure 1. ^{29}Si MAS NMR spectra of o-SiOP obtained from silicon and 85 % H_3PO_4 and o-SiOP2 obtained from silica and concentrated H_3PO_4.

Besides the intensive signal of $Si(HPO_4)_2$ at about -210 ppm[31] broad signals between -110 ppm and -120 ppm are observed. These correspond to $[SiO_4]$ environments of not or partially reacted SiO_2 (10.4 Mol%).[33] In addition to the target product small amounts of $Si_5P_6O_{25}$ (-119 ppm, -213 ppm, -217 ppm; 7.9 Mol%) are formed in this synthesis.[9,19] From our point of view, the formation of $Si_5P_6O_{25}$ is promoted due to the given tetrahedral structure of the used silica in the synthesis of o-SiOP2. Note that these side products and unreacted SiO_2 can be observed for a wide range of applied reaction temperatures and SiO_2: H_3PO_4 molar ratios. They are hardly detectable in CP/MAS spectra because due to the lack of hydrogen in their structure no polarization is transferred into these regions. In order to avoid these side products, we exchanged silica for silicon nanopowder.

$Si + 2\ H_3PO_4 \rightarrow Si(HPO_4)_2 + 2\ H_2$ (1)

The ^{29}Si MAS NMR spectrum of the obtained product o-SiOP is also shown in Figure 1. In contrast to the silicophosphate o-SiOP2 there is only one intensive signal at -210 ppm, which, as already shown, corresponds to $Si(HPO_4)_2$.[31] This is confirmed by the X-ray powder diffraction pattern of o-SiOP, which is given in Figure 2.

The main reflexes correspond to the data of $Si(HPO_4)_2$ published by Lelong in 1964.[10] Furthermore, no reflexes of remaining silicon can be observed. Hence, the XRD results are in line with the ^{29}Si MAS NMR spectrum of o-SiOP.

In contrast to products obtained from silica, no other silicon structures, neither SiO_4 moieties nor remaining silicon, can be observed within the experimental error (≤1%). Therefore, silicon as starting material yields to a purer synthesis product.

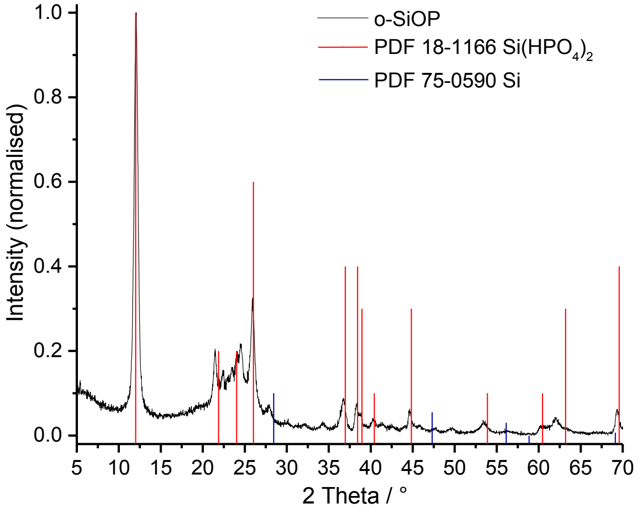

Figure 2. X-ray powder diffraction pattern of o-SiOP compared to reported data of $Si(HPO_4)_2$ and silicon.

Silicophosphates prepared by the "water free" sol-gel route

For the synthesis of hydrogen containing silicophosphates we used the "water free" sol-gel route according to literature.[28,29] Therefore, tetraalkoxysilanes were added to a stirred solution of pyrophosphoric acid in THF (Scheme 2).

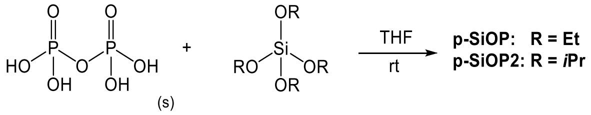

Scheme 2. Synthesis of hydrogen containing silicophosphates from solid pyrophosphoric acid and tetraalkoxysilanes (R = Et, iPr,…).

As the reaction proceeds, a precipitate is formed. The ^{29}Si CP/MAS NMR spectra of the obtained product p-SiOP and additional of o-SiOP are given in Figure 3. For this group of compounds CP and single pulse experiments exhibit the same signals, thus the CP MAS spectrum is shown here due to better intensity. For p-SiOP the ^{29}Si CP/MAS NMR spectrum shows two broad signals in the range of -97 ppm to -120 ppm. The peaks at about -97 ppm and -107 ppm represent Q units of self-condensation products from

TEOS[34,35] or Q groups with neighboring phosphorus.[33,36] The shoulder at around -115 ppm can be attributed to Q^4 units ($(Si(OSi)_{4-x}(OP)_x$ with x = 1, 2, 3) with Si-O-P bonds.[36] For p-SiOP the signal stretches to a chemical shift around -120 ppm, which is assigned to disilicates surrounded by PO_4 moieties as known from $Si_5P_6O_{25}$.[9] Additionally, a narrow signal at -210 ppm represents $[SiO_6]$ units in silicophosphates.[29,35,37] Its chemical shift is in line with reported data for $[SiO_6]$ units in $Si(HPO_4)_2$[31] and corresponds also to o-SiOP, which was prepared by a completely different synthetic route. In the case of o-SiOP no Q-units are observable in the ^{29}Si CP/MAS NMR spectrum.

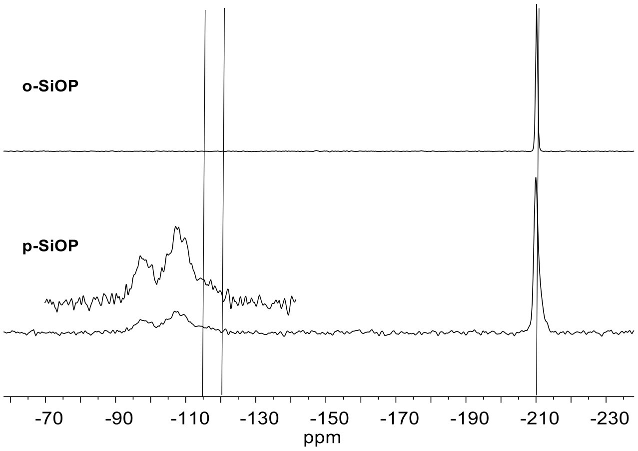

Figure 3. ^{29}Si CP/MAS NMR spectra of p-SiOP and o-SiOP. Dashed lines represent -115 ppm, -120 ppm and -210 ppm.

The 31P MAS NMR spectra of p-SiOP and o-SiOP are presented in Figure 4. The 31P MAS NMR spectrum of o-SiOP is dominated by the signal at -30 ppm. According to XRD, o-SiOP has the composition $Si(HPO_4)_2$ without water molecules in the structure. But nevertheless, the ^{31}P chemical shift of the HPO_4 groups is analogue to published data of $Si(HPO_4)_2{\cdot}H_2O$.[19] Additionally, a signal around 0 ppm represents remaining ortho-phosphoric acid. Signals for other phosphorus environments are insignificantly small. For p-SiOP the intensive peak at -30 ppm again corresponds to the reported ^{31}P NMR chemical shift for the $[PO_4]$ tetrahedra in $Si(HPO_4)_2{\cdot}H_2O$.[19] Additional signals at about 0 ppm, -10 ppm, -20 ppm and -40 ppm are detected. The chemical shifts of these signals are similar to published NMR data for Q^0 to Q^4 groups in silicophosphates.[19,36–38]

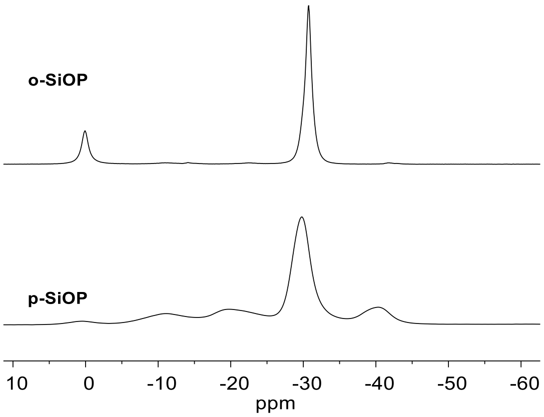

Figure 4. ^{31}P MAS NMR spectra of o- and p-SiOP.

Although pyrophosphoric acid was used as starting material, the solid material contains HPO_4-groups and no diphosphate units are detected. To investigate this fact, we used ^{31}P NMR spectroscopy to monitor the reaction progress.

Reaction monitoring

Here, the reaction of $H_4P_2O_7$ with tetra(isopropoxy)silane (TiPOS) was performed, because the solid material precipitates only after a few hours. In the case of TEOS a precipitation was observed after 20 minutes. Figure 5 (a) shows the ^{31}P NMR spectra of the reaction.

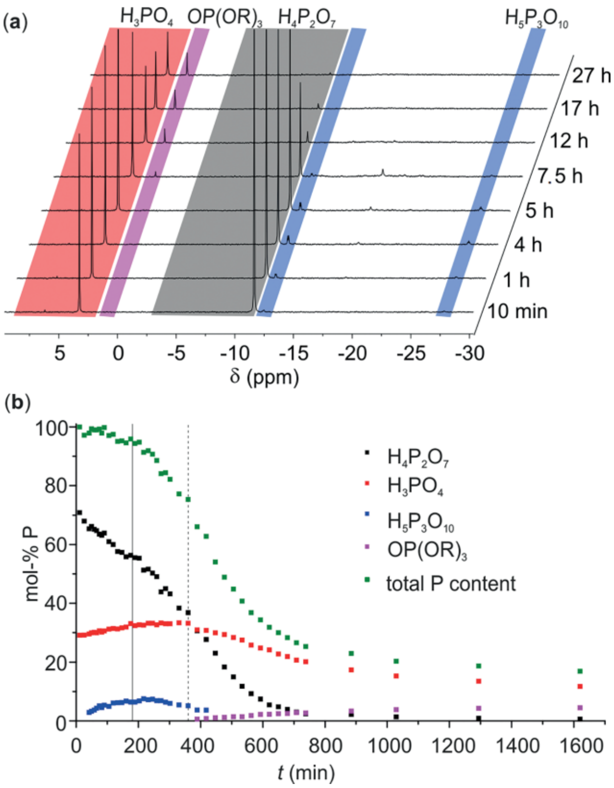

Figure 5. (a) Selected stacked ^{31}P NMR spectra of the reaction between $H_4P_2O_7$ and TiPOS in THF. (b) Change of mol-% P for the different substances with time; ortho-phosphoric acid, phosphate esters, pyrophosphoric acid and triphosphoric acid represent signals at δ ~ 3.2, 0.9, -11.6 and -12.5 ppm (d, 2J(31P,31P) = 13.3 Hz), -27.9 ppm (t, 2J(31P,31P) = 13.3 Hz); black line represents ~3 hours, dashed line represents 6 hours.

First of all, we used pyrophosphoric acid in technical grade. Thus, in addition to $H_4P_2O_7$ (-11.8 ppm) we observed ortho-phosphoric acid (3.0 ppm) and also a small amount of triphosphoric acid (-12.5 ppm and -27.9 ppm) in the ^{31}P NMR spectrum of the starting material.

The change of the integral for the different ^{31}P signals was used to monitor the reaction progress over time. When TiPOS was added to a solution of pyrophosphoric acid (1:1 molar ratio) in THF, decomposition of the P-O-P linkage occurred and ortho-phosphoric acid and triphosphoric acid were formed in the first hours of the reaction.

$2\ H_4P_2O7 \rightarrow H_3PO_4 + H_5P_3O_{10}$ (2)

The esterification of the phosphoric acid occurs in the reaction mixture as well and can be observed after approximately 6 hours. Isopropanol and Q1 units ((OH/OR)2OP(OSi), -18.5 ppm)[36] are generated in the condensation reaction of phosphoric acid and TiPOS.

"H_3PO_4 + Si(OiPr)$_4$ $\rightarrow$ (OH)$_2$OP(OSi(OiPr)$_3$) + i-PrOH" (3)

"H_3PO_4 + n i-PrOH $\rightarrow$ OP(OH)$_{3-x}$(OiPr)$_x$ + n H_2O" (4)

During the first hours of the reaction, the total P content decelerates slowly (Figure 5(b)). The building of condensed phosphates started and the formation of a white solid was observed after about 3 hours. This is indicated by the rapid decrease of the total P content. A comparable reaction procedure can be expected for the synthesis of p-SiOP, because the obtained ^{31}P CP/MAS NMR spectra of the solid materials show similar environments for phosphorus.

Due to the analogy of the ^{29}Si CP/MAS NMR spectra of p-SiOP and o-SiOP the same short-range order is expected for both, although no reflexes for p-SiOP were observed in X-ray powder diffraction pattern (Figure S3, supporting information).

DFT calculations. Structural model for Si(HPO$_4$)$_2$

To find a suitable candidate structure for the observed NMR data we first investigated the only known crystalline Si/P/O/H structure – SiPO$_4$OH[39]. Thereafter, we explored zirconium phosphate structures τ-Zr(HPO$_4$)$_2$[40] and α-Zr(HPO$_4$)$_2$·H$_2$O[41], replacing Zr by Si to obtain silicophosphates. For the latter one we also built the anhydrous form. We optimized all structures and computed the NMR parameters. Results are collected in Table 1. Si(HPO$_4$)$_2$·H$_2$O and Si(HPO$_4$)$_2$, both derived from an isotypic Zr compound, indeed provide the best correspondence between computed and observed NMR parameters.

Table 1. Computed ^{31}P and ^{29}Si chemical shifts for hydrogen-containing silicophosphate structures

Model	^{31}P δ_{iso} [ppm]		^{29}Si δ_{iso} [ppm]
	P1	P2	
$Si(HPO_4)_2 \cdot H_2O$	-27.9	-28.1	-211.2
$Si(HPO_4)_2$	-31.5		-211.9
$SiPO_4OH$	-43.7		-208.2
τ-$Si(HPO_4)_2$	-49.0		-223.9

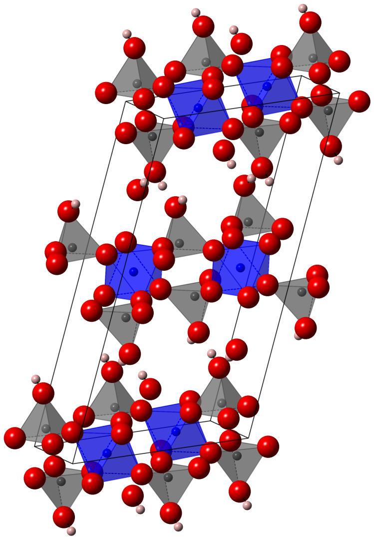

Figure 6. Structure of $Si(HPO_4)_2$. Si is at center of blue octahedra, and P in the center of grey tetrahedra. Large red and small pink spheres correspond to O and H atoms, respectively.

The structure of $Si(HPO_4)_2$ is shown in Figure 6. It exhibits layers built of $[SiO_{6/2}]$ octahedra (Figure 6, blue) sharing corners with $[PO_{3/2}OH]$ tetrahedra (Figure 6, gray). OH groups point towards the interlayer space, and all other oxygen atoms bridge between Si^{VI} and P^{IV}. Layers of the anhydrous form are interconnected via hydrogen bonds between OH groups of adjacent layers. The water-containing structure includes two H_2O molecules in the interlayer space inserted between and then connecting OH groups of adjacent layers via hydrogen bonds.

The XRD pattern calculated from the DFT optimized structural model conforms qualitatively to the experimental data, which were in agreement with results published for $Si(HPO_4)_2$.[11] Therefore, we can propose a structural model for $Si(HPO_4)_2$ without a single crystal analysis, which was confirmed by XRD and the comparison of experimental and computed NMR chemical shifts.

The optimized structural model of $Si(HPO_4)_2$ raises the expectation of a specific thermal decomposition behavior. Therefore, a thermogravimetric analysis (TG/DTA) of o-SiOP was performed. The resulting steps of the TG-curve are comparable to previous investigations.[36] The first mass loss (3.5 wt.-%) can be explained by the evaporation of acetone from washing step (b.p. 56 °C). The other steps are in agreement with the literature and reflect the loosing of adsorbed and chemically bound water.[36]

Correlations between DFT optimized model and synthesized hydrogen silicophosphates

^{31}P-^{29}Si-REDOR measurements at o-SiOP

As already mentioned, the shown DFT optimized structural model contains only six-fold coordinated silicon atoms. These $[SiO_6]$ octahedra are surrounded by six $[PO_4]$ tetrahedra, which are connected at the corners to three $[SiO_6]$ octahedra and one OH group. NMR spectroscopy was used to verify this model for $Si(HPO_4)_2$.

The ^{1}H-^{31}P HETCOR NMR spectrum of o-SiOP proofs that the hydroxy groups are linked to the phosphorus atoms in the structure (Figure S5, supporting information). As already shown in the ^{31}P MAS NMR spectrum (Figure 4), o-SiOP has the dominating signal at -30 ppm and therefore, it corresponds to the HPO4 groups.

Additional to traditional scattering techniques rotational echo double resonance spectroscopy (REDOR) can be used to evaluate distances between spin pairs.[42] Spin echo spectra with and without re-introduction of the heteronuclear dipolar coupling between ^{31}P and ^{29}Si are recorded for an increasing recoupling time (rotor periods). The difference between the full and the thus reduced spin echo represents the ^{31}P- ^{29}Si REDOR dephasing. The experimental values obtained for the signal at -30 ppm are presented in Figure 7 (black circles).

On the basis of the evolution of the ^{31}P-^{29}Si REDOR dephasing, it is possible to derive structural information about o-SiOP. The experimental data show a first inflexion point at 16 % dephasing. Due to the natural abundance of ^{29}Si (4,7 %), we can deduce that one phosphorus atom is linked to three silicon atoms.[43] Therefore, the short-range order of phosphorus and silicon in the DFT optimized structure is confirmed. Due to the ^{29}Si NMR MAS spectrum of o-SiOP (Figure 1), every connected silicon atom is six-fold coordinated.

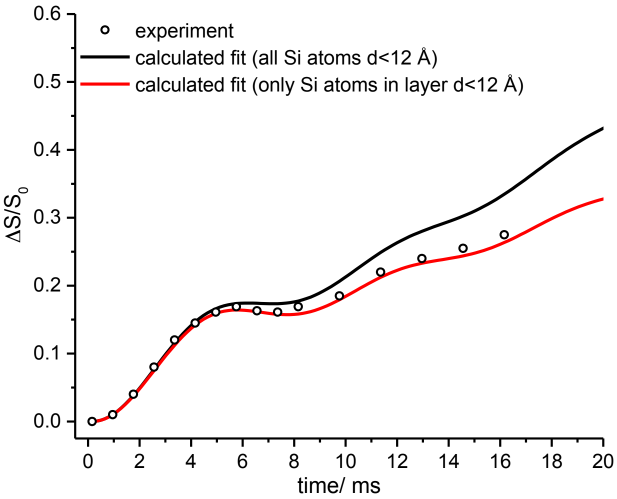

Figure 7. Experimental (circles) and calculated (lines) 31P-29Si REDOR dephasing of o-SiOP, assuming P atoms interact only with Si atoms in layer (red line) or with all Si atoms in the surroundings (black line). The distances for SIMPSON simulations are taken from the DFT calculated model of Si(HPO4)2.

For further structural examination REDOR dephasing curves were calculated with SIMPSON,[44] taking the P-Si-distances from the DFT optimized structural model of Si(HPO$_4$)$_2$. Two distance depending REDOR dephasing curves were determined: (i) assuming the P atoms to interact only with Si atoms within the layer up to a distance of 12 Å (Figure 7, red line) and (ii) including also the interaction to Si atoms of the neighboring layers within a distance of 12 Å (Figure 7, black line). The calculated curve for P-Si interactions within the layer is in better agreement with the experimental ^{31}P-^{29}Si REDOR dephasing data. Therefore, the P-Si dipolar couplings from layer to layer seem to be smaller than expected from the model. This can be explained by the X-ray powder diffraction pattern (Figure 2). Due to the broad reflex at $2\Theta = 12.1°$ we suppose that the layered arrangement of o-SiOP is not accurate well ordered as in the DFT optimized model. Thus, the dipolar couplings from P and Si atoms, localised in different layers, are defective. As already shown, the silicophosphate layers are made of [SiO_6] octahedra and [PO_4] tetrahedra. According to the small signals in the ^{29}Si (-210.2 ppm, FWHM: 49.5 Hz) and ^{31}P (-30.7 ppm, FWHM: 168.6 Hz) NMR spectra (Figure 1 and 4) of o-SiOP, the connection of these polyhedra yield to well-ordered layers. Therefore, the experimental REDOR dephasing data points are localised between both calculated dephasing curves and confirm more to the red one.

Due to the agreement of the calculated and the experimental ^{31}P-^{29}Si REDOR dephasing behaviour, the layered DFT optimized structural model for $Si(HPO_4)_2$ can be confirmed with REDOR measurements, too.

Structural correlation with p-SiOP

Because the synthesis was executed with $Si(OEt)_4$, the existence of ethoxy units can be expected in the structure. This was confirmed by ^{1}H and ^{13}C CP/MAS NMR spectroscopy . To obtain information about the incorporation of the ethoxy groups ^{1}H-^{29}Si and ^{1}H-^{31}P HETCOR spectra were recorded, the latter is shown in Figure 8.

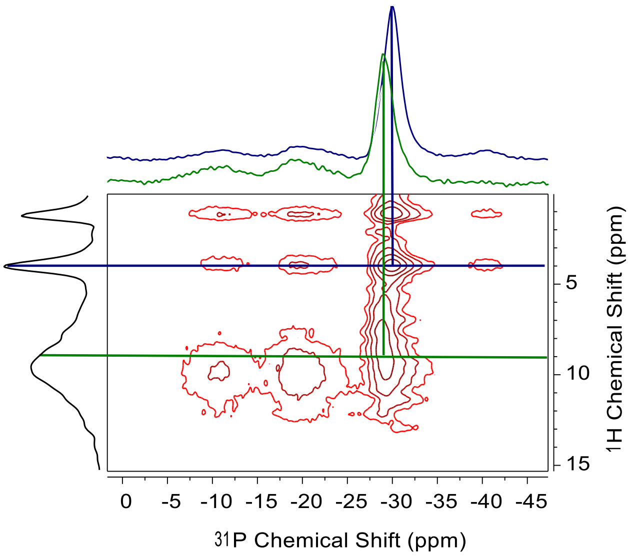

Figure 8. ^{1}H-^{31}P HETCOR NMR spectrum of **p-SiOP**, contact time 200 ms, dashed blue trace at d(1H) of OCH2; dashed green at d(1H) of OH.

Distinct analysis of the peak at -30 ppm reveals two components; one of them indicates correlations of ^{31}P structural units with OH groups and the other with methyl and methylene groups, which represent the ethoxy moieties. The corresponding traces are shown at the top of the 2D spectrum (Figure 8). The green horizontal trace goes through the OH correlation peak and the blue one through the CH_2 correlation peak. Beside this ^{31}P species with chemical shifts of about -40 ppm exhibit only correlations with alkyl groups. The signals at about -10 ppm and -20 ppm show correlations with both alkyl and OH groups.

Therefore, the DFT calculated structural model for $Si(HPO_4)_2$ was modified and the calculated NMR chemical shifts were compared to experimental data. As already shown, $Si(HPO_4)_2$ has a layered structure and there are P-OH units, which extend into the space between the layers. They are connected via hydrogen bonds. In the DFT calculated structural model of $Si(HPO_4)_2$ one half of the P-OH groups was substituted by P-OEt (Figure 9). The calculated chemical shifts for ^{31}P and ^{29}Si, before and after this substitution, are shown in Table 2. On average the P-OEt substituted ^{31}P signals are slightly shifted to the high field (cf. Table 2). ^{31}P NMR of non-substituted sites, where the P-OH unit remains, shifts in the opposite direction (downfield) by up to +3 ppm. This as well aligns nicely with observed ^{31}P NMR data when comparing peak positions for p-SiOP versus o-SiOP (Figure 4) and comparing the results of the ^{1}H-^{31}P HETCOR NMR spectrum of p-SiOP (Figure 8).

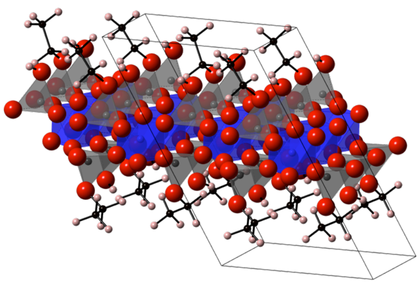

Figure 9. The model of a single layer Si(HPO4)(EtPO4).

Table 2. Calculated NMR chemical shift data of P and Si sites based on the structural model of Si(HPO4)2 before and after substituting half of the P-OH by P-OEt (cf. site labels Figure 5). Bold indicates the P-OEt groups.

Site	$Si(HPO_4)_{2-x}(EtPO_4)_x$		Site	$Si(HPO_4)_{2-x}(EtPO_4)_x$	
	x = 0 δ [ppm]	x = 1 δ [ppm]		x = 0 δ [ppm]	x = 1 δ [ppm]
P1	-31.5	**-30.8**	Si1	-211.9	-212.3
P2	-31.5	-28.7	Si2	-211.9	-212.3
P3	-31.5	**-32.0**	Si3	-211.9	-212.2
P4	-31.5	-28.7	Si4	-211.9	-212.0
P5	-31.5	**-31.2**			
P6	-31.5	-28.3			
P7	-31.5	-28.1			

P8	-31.5	**-31.9**			

Due to the structural change at phosphorous the ^{29}Si chemical shifts in the $[SiO_6]$ octahedra are affected too. The calculation indicates a small high field shift, which is very nicely reflected by the tailing of the p-SiOP signal at -210 ppm in Figure 3. In addition for long contact times (5 ms) the 2D ^{1}H-^{29}Si HETCOR NMR spectrum shows a correlation of the ^{1}H of ethyl groups with the six-fold coordinated ^{29}Si atoms (Figure S8, supporting information), which gives a further confirmation for the calculations. Thus, the tailing of the SiO_6-peak is caused by the PO-bound ethyl groups in the layered silicophosphate structure.

With reference to the NMR data calculations and to the ^{1}H-^{31}P HETCOR NMR spectrum (Figure 8), we conclude that the main structure in p-SiOP is a layered structure with its composition $Si(HPO_4)_{2-x}(EtPO4)_x$ (x = 1.5 ± 0.1) derived from the structural model developed for $Si(HPO_4)_2$. The ratio between P-OH and P-OEt groups was determined by deconvolution of the ^{31}P MAS NMR spectrum of p-SiOP (Figure 4).

Due to the reaction procedure several other structural motives were detected in the material, indicated by the additional signals in the ^{31}P MAS NMR spectrum (Figure 4). The heterogeneity of the material cannot be completely avoided using the sol-gel synthesis. The peak at -40 ppm indicates the existence of $[PO_4]$ tetrahedra linked to four silicon atoms. As can be seen in Figure 3, the material contains remaining $[SiO_4]$-units, thus the formation of P-O-Si^{IV} linkages can occur. Therefore, a structural element consisting of phosphorus linked via oxygen to three six-fold coordinated silicon atoms and to one four-fold coordinated is possible. Such a unit is known in the crystal structure of the silicon orthophosphate Si5P6O25.[9] In the 2D 31P-31P CP-RFDR NMR spectrum a correlation between signals at -30 ppm and

-40 ppm could be observed (Figure 10). Therefore, we suggest that there are [SiO4] tetrahedra (with ethyl groups), which are connected to phosphorus atoms integrated in the layered structure Si(HPO4)2-x(EtPO4)x (x = 1.5 ± 0.1).

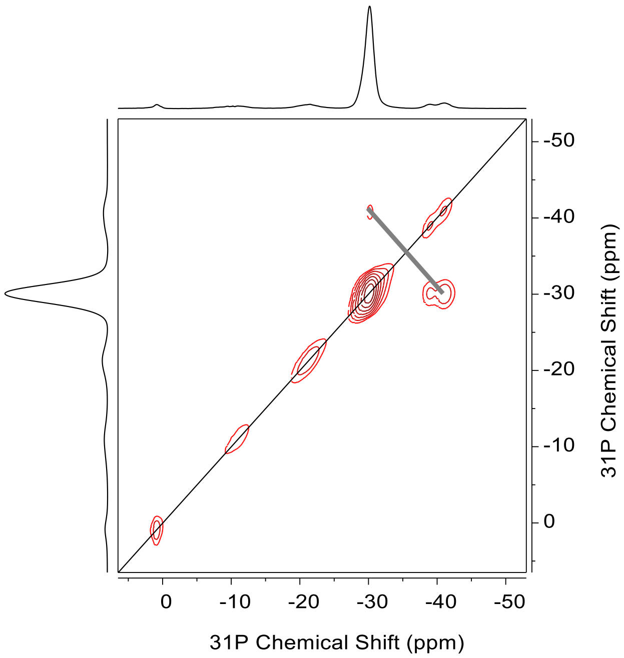

Figure 10. 31P/ 31P CP-RFDR NMR spectrum of p-SiOP, mixing time 32 ms.

To find also a computational explanation, we modeled a silicophosphate layer like in $Si(HPO_4)_2$ (Figure 7), but with H atoms substituted into triethoxysilyl groups. After optimization we computed again NMR data for this structure. Results are given in Table 3.

The triethoxysilyl group as substituent causes similar changes as alkyl substitutions. The ^{31}P signal at the P-OR site shifts upfield even stronger to -44.1 ppm. For the ^{29}Si NMR of the P-O-Si(OEt)$_3$ site we compute a chemical shift of -92.8 ppm, which falls into the broad peak related to Si^{IV} in p-SiOP (Figure 3). The substitution as well affects the chemical shifts of the six-fold coordinated silicon atoms next to the P-OR site in the same way like the ethyl groups. This aligns nicely with the observed tailing of the [SiO$_6$]-peak in Figure 3.

In summary, the occurrence of a substitution of H atoms by Si(OEt)$_3$ can be computational shown and is in agreement with the results given by HETCOR and CP-RFDR NMR experiments.

Table 3. NMR chemical shifts, ^{31}P or ^{29}Si for respective site, computed substituted silicophosphate layer structures. Bold data in a row indicates that substitution occurred at the site of that row.

Site	$Si(HPO_4)_2$	+ $Si(OEt)_3$	Site	$Si(HPO_4)_2$	+ $Si(OEt)_3$
P1	-31.5	-28.6	Si1	-211.9	-213.0
P2	-31.5	**-44.1**	Si2	-211.9	-212.6
P3	-31.5	-28.3	Si3	-211.9	-212.8
P4	-31.5	-28.5	Si4	-211.9	-212.3
P5	-31.5	-31.3			
P6	-31.5	-29.5			
P7	-31.5	-28.7			
P8	-31.5	-29.0			

According to the correlations in the ^{1}H-^{31}P HETCOR NMR spectrum (Figure 8) and the ^{31}P-^{31}P RFDR NMR spectrum (Figure 10), the other signals in 31P NMR spectrum of p-SiOP (Figure 4) are generated by phosphorus atoms, which are less crosslinked to other P-or Si- groups and in correlation to ethyl groups. We suggest that these structural patterns only occur on the surface of the layered material or in regions connected to the side products formed by self-condensation of TEOS.

Conclusions

Hydrogen containing silicophosphates $Si(HPO_4)_2$ – comprising layers consisting of [SiO_6] octahedra which are interconnected via corner-sharing [$O_3P(OH)$] tetrahedra – may be prepared by different routes. The synthesis using silica and H_3PO_4, which has been reported in literature before, generally yields impure specimens. An improved method to obtain phase pure polycrystalline $Si(HPO_4)_2$ starts from silicon nanopowder and H_3PO_4.

Its structure is similar to layered $Zr(HPO_4)_2 \cdot H_2O$ and a structural model was generated using DFT optimizations. A "water-free" sol-gel route using pyrophosphoric acid $H_4P_2O_7$ and tetraalkoxysilanes $Si(OR)_4$ provides amorphous products, which contain OR-groups mainly replacing the OH-groups, but are primarily composed of layered $Si(HPO_4)_2$ too. This structure was investigated in detail using DFT modeling and NMR measurements, which nicely support the developed structural model. Due to the relatively weak interactions between the layers, slight amounts of water, H_3PO_4, ethanol, and solvents may be intercalated into $Si(HPO_4)_2$, leading to varying interlayer distances.

Experimental Section

Preparation

Tetraethoxysilane (TEOS) was purchased from Sigma Aldrich and solid pyrophosphoric acid (technical grade) from Fluka. Tetra-i-propoxysilane (TiPOS) was prepared by the alcoholysis of silicon tetrachloride (Acros Organics) with extra dry i-propanol (Acros Organics). Silicon nanopowder (particle size < 100 nm) was purchased from ChemPUR and silica gel (high-purity grade, particle size: 40-63 μm) from Fluka Analytical Sigma-Aldrich. 85 % H_3PO_4 (analytical grade) was acquired from Carl Roth and acetone (analytical grade) from Sigma Aldrich, which was used as washing solvent.

p-SiOP: All reactions and manipulations were performed under inert conditions (argon) using standard Schlenk techniques, a glove box (N_2, $O_2 < 0.5$ ppm, $H_2O < 0.5$ ppm) and anhydrous solvents. The tetraethoxysilane (0.85 g, 4.1 mmol) was added in a 1:1 molar ratio to a stirred solution of pyrophosphoric acid (0.73 g, 4.1 mmol) in tetrahydrofuran (60 mL). After 20 minutes a white precipitation was observed at the glass wall.

^1H MAS NMR (400.30 MHz): $\delta = 1.35$ (CH_3), 3.96 (CH_2), 10.48 (P-OH) ppm. ^{13}C CP/MAS NMR (100.67 MHz): $\delta = 16.2$ (CH_3), 25.8 (CH_2 - THF), 59.3 (-CH_2-O-Si), 62.6 (-CH_2-O-P) 69.2 (O-CH_2 - THF) ppm. ^{31}P MAS NMR (162.04 MHz): $\delta = 0.44$ ($OP(OH)_{3-}$

$_x$(OEt)$_x$), -11.09 (OP(OSi/OP)(OH/OEt)$_2$), -19.75 (OP(OSi/OP)$_2$(OH/OEt)), -29.79 ((HO)P(OSi)$_3$), -40.33 (P(OSi^{IV})(OSi^{VI})$_3$) ppm. ^{29}Si MAS NMR (79.52 MHz): δ = -97.1, -106.8, -114.6 (SiO$_4$), -209.9 (SiO$_6$) ppm.

o-SiOP: Silicon nanopowder (0.2 g, 7.12 mmol) was weighed in a closed platinum crucible. Concentrated o-phosphoric acid (6.57 g, 56.96 mmol) was added by carefully stirring in a 1:8 molar ratio. The brownish slurry was heated at 150 °C for 7 days. Afterwards, the grey substance (1.5 g) was suspended in acetone (4 mL) and centrifuged at 5000 rpm for 5 min. This step was repeated twice to remove the excess of H_3PO_4. Afterwards, the product was dried at 80 °C.

ICP-OES: Si:P = 1:2.05

^{1}H MAS NMR (400.30 MHz): δ = 2.15 (CH$_3$ - acetone), 9.21 (P-OH) ppm. ^{31}P MAS NMR (162.04 MHz): δ = 0.08 (H_3PO_4), -10.55, -14.12 (OP(OSi/OP)(OH)$_2$), -22.51 (OP(OSi/OP)$_2$(OH)), -30.73 ((HO)P(OSi)$_3$), -41.83 (P(OSi^{IV})(OSi^{VI})$_3$) ppm. ^{29}Si MAS NMR (79.52 MHz): δ = -210.2 (SiO$_6$) ppm.

o-SiOP2: Additionally, this synthetic instruction was used in the same way to prepare silicophosphate made of SiO_2 and concentrated o-phosphoric acid in a 1:2 molar ratio. Silica gel (1.5 g, 0.025 mol) and H_3PO_4 (5.76 g, 0.05 mol) were mixed and treated as described above.

^{1}H MAS NMR (400.30 MHz): δ = 9.45 (P-OH) ppm.^{31}P MAS NMR (162.04 MHz): δ = 0.04 (H_3PO_4), -12.41, -14.74 (OP(OSi/OP)(OH)$_2$), -22.89 (OP(OSi/OP)$_2$(OH)), -30.73 ((HO)P(OSi)$_3$), -42.85 (P(OSi^{IV})(OSi^{VI})$_3$) ppm. ^{29}Si MAS NMR (79.52 MHz): δ = -103.3, -110.8, -115.4, -119.4 (SiO$_4$), -210.2, -213.5, -216.2 (SiO6) ppm.

Reaction monitoring: To monitor the reaction progress TiPOS instead of TEOS was used. Therefore, $H_4P_2O_7$ (0.14 g, 0.79 mmol) was dissolved in THF (10 mL) and TiPOS (0.20 g, 0.75 mmol) was added. In the case of TiPOS a precipitate (p-SiOP2) formed after a few hours. Reaction mixture: ^{31}P-NMR (161.97 MHz, external standard Ph$_4$PCl in D$_2$O): δ = ~ 3.2 (H_3PO_4), 0.9 (OP(OH)$_{3-x}$(OiPr)$_x$, -11.6 ($H_4P_2O_7$) -12.5 (d, 2J(^{31}P,^{31}P) = 13.3 Hz,

$H_5P_3O_{10}$), -18.5 (OP(OSi/OP)(OH/OR)$_2$), -27.9 (t, 2J(^{31}P,^{31}P) = 13.3 Hz. $H_5P_3O_{10}$) ppm. p-SiOP2: 31P MAS NMR (162.04 MHz): δ = 0.79,. -0.98 (OP(OH)$_{3-x}$(OiPr)$_x$, -11.19 (OP(OSi/OP)(OH/OiPr)$_2$), -20.28 (OP(OSi/OP)$_2$(OH/OiPr)), -29.31, -31.34 ((H/iPrO)P(OSi)$_3$), -40.10 (P(OSi^{IV})(OSi^{VI})$_3$) ppm.

NMR spectroscopy

Solid state NMR: The experiments were performed on a Bruker Avance 400 MHz WB spectrometer using a 4 mm triple resonance CP/MAS probe with ^{1}H (400.30 MHz), ^{13}C (100.67 MHz), ^{29}Si (79.52 MHz), ^{31}P (162.04 MHz). Zirconia rotors were used, the spinning rate was depended on the nucleus and the experiment; usually 5 kHz for ^{13}C and ^{29}Si, 10 kHz for ^{31}P and 14 kHz for ^{1}H and 12.5 or 14 kHz for two dimensional experiments. ^{31}P NMR chemical shift was referenced to 85 % H_3PO_4 and to TMS for ^{1}H, ^{13}C and ^{29}Si. Usually, single pulse experiments were performed with 30° pulses and 300 s recycle delay for ^{29}Si and 75 s for ^{31}P. For quantifying dmFit is used

Cross polarisation (CP) NMR experiments were carried out with 5 ms contact time for ^{29}Si, 1 ms for ^{31}P and 2 ms for ^{13}C. An 80 % ramp was used for ^{29}Si and ^{31}P and a 70% ramp for ^{13}C. Normally, the recycle delay of all CP experiments was 5 s, if it is not otherwise mentioned.

2D HETCOR NMR spectra for ^{1}H-^{29}Si and ^{1}H-^{31}P were recorded with contact times given in the Figure captions. For 2D ^{31}P CP-RDFR NMR experiments with Lee-Goldberg decoupling 1 ms contact time was used. The mixing time was varied between 8 to 32 ms. ^{31}P-^{29}Si REDOR experiments were performed on a Bruker 400 MHz DMX spectrometer with a wide bore magnet using a 4 mm triple resonance CP/MAS probe. The spinning speed was 12.5 kHz. To avoid drifting effects the spectra with dephasing pulse on and off were recorded in succession. For simulating the experimental REDOR dephasing curve SIMPSON was used.

Solution NMR: The spectra were recorded on a Bruker Nanobay 400 MHz spectrometer (^{31}P, 161.97 MHz; ^{1}H, 400.13 MHz)) using a 5 mm BBO probe to monitor the reaction of $H_4P_2O_7$ and TiPOS. The sample was measured in a NMR tube with coaxial insert containing the external standard tetraphenylphosphonium chloride (^{31}P $\delta = 22.47$ ppm) in D_2O.

Computational methods

We perform Density Functional Theory[45] calculations using the Vienna Ab Initio Simulation (VASP) package[46,47]. We use the Projector Augmented Wave (PAW) method[48,49] and approximate electron exchange and correlation by the Perdew-Burke-Ernzerhoff (PBE) generalized gradient approximation (GGA). We rely on standard pseudopotentials provided with the VASP package and use an energy cutoff of 500 eV for the expansion of the wave function into the plane-wave basis set. We choose appropriate k-point meshes for crystalline models and optimize forces to lower than to 5 meV/Å. NMR calculations are carried out using the GIPAW algorithm[50] as implemented in the VASP code. For those we choose an energy cutoff of 600 eV and find the ^{29}Si NMR chemical shifts converged to better than 0.2 ppm.

We calibrate ^{29}Si and ^{31}P chemical shifts basing on the experimentally measured chemical shifts[51] for AIV-SiP_2O_7[52], HexI-SiP_2O_7[53] and $Si_5O(PO_4)_6$[54] structures. We optimize the structures under constant cell parameters and further compute NMR chemical shifts of the optimized models. We relate the computed chemical shifts and experimental relative chemical shifts: $\delta_{iso} = \sigma_{iso} - \delta^0$. Offsets δ^0 for the chemical shifts of Si^{VI} and P^{IV} sites are -324.7 ppm and -302.6 ppm respectively.

Other analytical techniques

XRD measurements were recorded on a powder diffractometer D8 Discover from Bruker using Cu-Kα radiation ($\lambda = 1.5418$ nm). Samples were protected with foil, because of the possible instability when exposed to air.

The Si:P ratio was determined via ICP-AES analyses. Samples were dissolved in a 1 % NAOH-solution and analysed on an iCAP 6500 with ETV-4000c.

In order to analyze the chemical composition of p-SiOP and to study the morphology, a scanning electron microscope Tescan Vega equipped with a Si/Li EDX detector from Oxford Industries was used. SEM image was obtained at an acceleration voltage of 20 kV.

The thermogravimetric analysis (TG/DTA) was performed on a Seiko SSC 5200 TG/DTA 22 instrument from Seiko Instruments in a platinum crucible over the temperature range of 25 °C to 800 °C (heating rate: 5 K/min) in a flowing atmosphere of argon (300 mL/min).

Acknowledgments

The financial support from the German Research Foundation (DFG; KR 1739-32-1) is gratefully acknowledged. Peter Kroll and Ilia Ponomarev acknowledge the support by the NSF (DMR-1463974, CMMI-1634448). Our sincere thanks also go to Regina Moßig for performing XRD and TG/DTA, Melanie Pannach for SEM-EDX, and Katharina Strecker for the ICP-AES analyses.

References

1. J. A. Duffy, D. E. Macphee, *J. Phys. Chem. B* **2007**, *111*, 8740–8745.
2. L. W. Finger, R. M. Hazen, *Acta Cryst.* **1991**, *B47*, 561–580.
3. R. Dupree, D. Holland, M. G. Mortuza, J. A. Collins, M. W. G. Lockyer, *J. Non-Cryst. Solids* **1988**, *106*, 403–407.

4. N. J. Clayden, S. Esposito, P. Pernice, A. Aronne, *J. Mater. Chem.* **2001**, *11*, 936–943.
5. D. Li, M. E. Fleet, G. M. Bancroft, M. Kasrai, Y. Pan, *J. Non-Cryst. Solids* **1995**, *188*, 181–189.
6. F. Liebau, G. Bissert, N. Köppen, *Z. Anorg. Allg. Chem.* **1968**, *359*, 113–134.
7. H. Makart, Helv. *Chim. Acta* **1967**, *50*, 399–405.
8. E. Tillmanns, W. Gebert, W. H. Baur, *J. Solid State Chem.* **1973**, *7*, 69–84.
9. H. Mayer, *Monatshefte für Chemie* **1974**, *105*, 46–54.
10. B. Lelong, *Ann. Chim.* **1964**, *9*, 229–260.
11. A. Winkler, E. Thilo, *Z. Anorg. Allg. Chem.* **1966**, *346*, 92–112.
12. H. Rabaâ, F. Bkiri, *Can. J. Chem.* **2006**, *84*, 1024–1030.
13. I. P. Beletskii, A. G. Grebenyuk, V. E. Klimenko, *Russ. J. Coord. Chem.* **1996**, *22*, 163–165.
14. W. A. Gambling, D. N. Payne, C. R. Hammond, S. R. Norman, *Proc. Inst. Electr. Eng. UK* **1976**, *123*, 570–576.
15. H. Zeng, Q. Jiang, X. Li, F. Ye, T. Tian, H. Zhang, G. *Chen, Appl. Phys. Lett.* **2015**, *106*, 021903-1-021903-4.
16. T. Izumitani, M. Matsukawa, C. Hata, Silikophosphatlaserglas **1986**, DE 3609247 A1 19860925.
17. T. Izumitani, H. Toratani, Silicophosphate laser glass **1985**, DE 3435133 A1 19850411.
18. A. Ignatius, K. Unterricker, K. Wenger, M. Richter, L. Claes, P. Lohse, H. Hirst, *J. Mater. Sci.: Mater. Med.* **1997**, *8*, 753–756.
19. T. R. Krawietz, P. Lin, K. E. Lotterhos, P. D. Torres, D. H. Braich, A. Clearfield, J. F. Haw, J. *Am. Ceram. Soc.* **1998**, 8502–8511.
20. Y. Maki, K. Sato, A. Isobe, N. Iwasa, S. Fujita, M. Shimokawabe, N. Takezawa, *Appl. Catal., A* **1998**, *170*, 269–275.
21. K. Leinenweber, L. A. Stearns, J. M. Nite, P. Németh, T. L. Groy, *J. Solid State Chem.* **2012**, 221–225.
22. M. D. Apuzzo, A. Aronne, S. Esposito, P. Pernice, *J. Sol-Gel Sci. Technol.* **2000**, *17*, 247–254.
23. A. Aronne, M. Turco, G. Bagnasco, P. Pernice, M. Di Serio, N. J. Clayden, E. Marenna, E. Fanelli, *Chem. Mater.* **2005**, *17*, 2081–2090.
24. A. Styskalik, D. Skoda, Z. Moravec, C. E. Barnes, J. Pinkas, *New J. Chem.* **2016**, *40*, 3705–3715.
25. A. Styskalik, D. Skoda, Z. Moravec, M. Babiak, C. E. Barnes, J. Pinkas, *J. Mater. Chem. A* **2015**, *3*, 7477–7487.
26. A. Styskalik, D. Skoda, Z. Moravec, J. G. Abbott, C. E. Barnes, J. Pinkas, *Microporous Mesoporous Mater.* **2014**, *197*, 204–212.
27. S. Jähnigen, U. Böhme, E. Kroke, E. Brendler, G. Heide, Silikat-Phosphat-Materialien (SiPOs) - Verfahren zu deren Herstellung und Anwendungen **2013**, DE102012011034 A1.
28. S. Jähnigen, E. Brendler, U. Böhme, G. Heide, E. Kroke, *New J. Chem.* **2014**, *38*, 744–751.
29. S. Jähnigen, E. Brendler, U. Böhme, E. Kroke, *Chem. Commun.* **2012**, *48*, 7675–7677.

30. J. Goubeau, K. O. Christe, W. Teske, W. Wilborn, Z. *Anorg. Allg. Chem.* **1963**, *325*, 26-42.
31. S. Kitaoka, K. Kuroda, C. Kato, Rikogaku Kenkyusho Hokoku, *Waseda Daigaku*, **1988**, *120*, 89–93.
32. A. Boullé, R. Jary, C. R. hebd. *Séances Acad. Sci.* **1953**, *161*, 328.
33. E. Lippmaa, M. Maegi, A. Samoson, G. Engelhardt, A. R. Grimmer, *J. Am. Ceram. Soc.* **1980**, *102*, 4889–4893.
34. H. C. Marsmann, E. Meyer, M. Vongehr, E. F. Weber, *Makromol. Chem.* **1983**, *184*, 1817–1822.
35. C. Lejeune, C. Coelho, L. Bonhomme-Coury, T. Azaïs, J. Maquet, C. Bonhomme, *Solid State Nucl. Magn. Reson.* **2005**, *27*, 242–246.
36. C. Coelho, T. Azais, C. Bonhomme, L. Bonhomme-Coury, C. Boissière, G. Laurent, D. Massiot, *C. R. Chim.* **2008**, *11*, 387–397.
37. C. Coelho, T. Azaïs, L. Bonhomme-Coury, G. Laurent, C. Bonhomme, *Inorg. Chem.* **2007**, *46*, 1379–1387.
38. S.-P. Szu, L. C. Klein, M. Greenblatt, *J. Non-Cryst. Solids* **1992**, 21–30.
39. L. A. Stearns, T. L. Groy, K. Leinenweber, *J. Solid State Chem.* **2005**, *178*, 2594–2601.
40. A. M. K. Andersen, P. Norby, J. C. Hanson, T. Vogt, *Inorg. Chem.* **1998**, *37*, 876–881.
41. J. M. Troup, A. Clearfield, *Inorg. Chem.* **1977**, *16*, 3311–3314.
42. T. Gullion, *Concepts Magn. Reson.* **1998**, *10*, 277–289.
43. C. Jäger, to be published, in preparation.
44. M. Bak, J. T. Rasmussen, N. C. Nielsen, *J. Magn. Reson.* **2000**, *147*, 296–330.
45. P. Hohenberg and W. Kohn, *Phys. Rev.* **1964,** *136*, B864-B871.
46. G. Kresse, J. Hafner, *Phys. Rev. B* **1994**, *49*, 14251–14269.
47. G. Kresse, J. Furthmüller, *Phys. Rev. B* **1996**, *54*, 11169–11186.
48. P. E. Blöchl, *Phys. Rev. B* **1994**, *50*, 17953–17979.
49. G. Kresse, D. Joubert, *Phys. Rev. B* **1999**, *59*, 1758–1775.
50. C. J. Pickard, F. Mauri, *Phys. Rev. B* **2001**, *63*, 245101-1 - 245101-13.
51. C. Bonhomme, C. Gervais, C. Coelho, F. Pourpoint, T. Azais, L. Bonhomme-Coury, F. Babonneau, G. Jacob, M. Ferrari, D. Canet et al., *Magn. Reson. Chem.* **2010**, *48*, 86–102.
52. K. F. Hesse, *Acta Crystallogr., Sect. B* **1979**, *B35*, 724–725.
53. D. M. Poojary, R. B. Borade, A. Clearfield, *Inorg. Chim. Acta* **1993**, *208*, 23–29.
54. D. M. Poojary, R. B. Borade, Campbell, F. L., Iii, A. Clearfield, *J. Solid State Chem.* **1994**, *112*, 106–112.

Summary

I found the $Si(HPO_4)_2$ layered structure derived from α-$Zr(HPO_4)_2 \cdot H_2O$[1] to agree with the experimental observations. The structure comprises layers of silicophosphate constructed of $[SiO_{6/2}]$ octahedra and $[PO_{3/2}]OH$ tetrahedra. OH-groups directed into interlayer space provide connectivity between the layers via hydrogen bonding.

Computed ^{29}Si and ^{31}P δ_{iso} matched with the experimental values. Peak positions of X-Ray pattern calculated from the computationally derived structure match the experimental ones as well. The structural model explains well why the NMR spectrum is quite well defined, while obtaining a good XRD pattern is a challenge: the model is comprised of layers with very regular local structure (that creates NMR pattern), while the order of layer arrangement can not be as neat.

I also tested substitution of H atoms of OH-groups into alkyl groups or O-$Si(OEt)_3$; the changes in ^{31}P and ^{29}Si NMR signals that happen upon substitution aligned well with the additional NMR experiments on sol-gel synthesized product.

My contribution here is the very idea to try to find the model of Si/P/O/H compound that would match the observations from the computational side. I was happy to quite easily run into a good hypothesis that explains the whole bulk of the observations: well-defined NMR signals along with the inability to produce a good XRD spectrum, easy transition into SiP_2O_7[2] at higher temperatures or longer times of the synthesis (through condensation of OH-groups), easy substitutions of H into alkyl, alkoxysilyl or phosphate groups that would explain ^{31}P δ_{iso} signals at ~ -40 ppm. Without computations experimental side would have spent a very long time attempting to obtain a good powder or single-crystal XRD from the product any of the paths, which is quite hard due to the nature of the crystal and purity issues.

References

1. Troup, J. M.; Clearfield, A., Mechanism of Ion-Exchange in Zirconium-Phosphates .20. Refinement of Crystal-Structure of Alpha-Zirconium Phosphate. *Inorg Chem* **1977**, *16*, 3311-3314.
2. Poojary, D. M.; Borade, R. B.; Campbell, F. L.; Clearfield, A., Crystal-Structure of Silicon Pyrophosphate (Form-I) from Powder Diffraction Data. *J Solid State Chem* **1994**, *112*, 106-112.

PART II: REACTIVE FORCE FIELD FOR SILICON OXYCARBIDE CERAMICS

CHAPTER 1: A REACTIVE FORCE FIELD FOR SIMULATIONS OF THE PYROLYSIS OF POLYSILOXANES INTO SILICON OXYCARBIDE CERAMICS

Motivation and scope

Amorphous silicon oxycarbide is family of materials with a wide range of attractive properties, such as chemical durability[1], creep resistance[2], mechanical properties[3], and electrical conductivity[4] (or, on the contrast, good dielectric properties[5]). The applications of silicon oxycarbide include gas separation membranes[6], thermal barrier coatings[7], anodes for Li-ion batteries[8] or advanced drug delivery systems[9].

Synthesis of silicon oxycarbide utilizes molecular approach, such as sol-gel[4], polymer-to-ceramic[10] or vapor deposition methods[11]. Choice of the precursors and processing techniques is extremely essential for the final outcome, which is why better understanding of the material formation is highly desirable for more predictable outcome.

Quantum chemistry methods (such as DFT) are a valuable approach to get structural insights. DFT calculations combined with network modeling or crystal structure prediction algorithm provided important information on the structure of "SiCO glass" and its tendencies of carbon segregation[12-14]. However, DFT calculations are computationally expensive: simulation comprising 192 atoms within nanoseconds can take months; scaling of the simulation wall-clock time with the number of atoms is $\sim N^3$, which makes thousands of atoms for nanoseconds a limit for reasonably long simulations. At the same time, realistic size and length scales will be at least several nanometers and several thousand atoms for nanoseconds; this won't become viable for DFT within next years.

Reactive Force Field (ReaxFF)[15] is an attempt to bridge the gap between accurate first principle methods and simple empirical potentials. It is a very complicated force field that takes into account numerous interactions and achieves success for the molecular reactions. However, the parameterizations that existed so far[16-18] did not provide a description of a-SiCO that would satisfy our needs in modeling. This is why I started developing a new parameter set.

References

1. Soraru, G. D.; Modena, S.; Guadagnino, E.; Colombo, P.; Egan, J.; Pantano, C., Chemical Durability of Silicon Oxycarbide Glasses. *J Am Ceram Soc* **2002**, *85*, 1529-1536.
2. Rouxel, T.; Soraru, G. D.; Vicens, J., Creep Viscosity and Stress Relaxation of Gel-Derived Silicon Oxycarbide Glasses. *J Am Ceram Soc* **2001**, *84*, 1052-1058.
3. Soraru, G. D., Kundanati, L., Santhosh, B., Pugno, N., Influence of Free Carbon on the Young's Modulus and Hardness of Polymer ‐ Derived Silicon Oxycarbide Glasses. *Journal of American Ceramic Society* **2019**, *102*, 907-913.
4. Pantano, C. G.; Singh, A. K.; Zhang, H. X., Silicon Oxycarbide Glasses. *J Sol-Gel Sci Techn* **1999**, *14*, 7-25.
5. Chen, J. W.; Calvin, J.; Asplund, M.; King, S. W.; Woodfield, B. F.; Navrotsky, A., Heat Capacities, Entropies, and Gibbs Free Energies of Formation of Low-K Amorphous Si(O)Ch Dielectric Films and Implications for Stability During Processing. *J Chem Thermodyn* **2019**, *128*, 320-335.
6. Juttke, Y.; Richter, H.; Voigt, I.; Prasad, R. M.; Bazarjani, M. S.; Gurlo, A.; Riedel, R., Polymer Derived Ceramic Membranes for Gas Separation. *Chem Engineer Trans* **2013**, *32*, 1891-1896.
7. Chiang, C. C.; Ko, I. H.; Chen, M. C.; Wu, Z. C.; Lu, Y. C.; Jang, S. M.; Liang, M. S., Physical and Barrier Properties of Pecvd Amorphous Silicon-Oxycarbide from Trimethylsilane and Co2. *J Electrochem Soc* **2004**, *151*, G704-G708.
8. David, L.; Bhandavat, R.; Barrera, U.; Singh, G., Silicon Oxycarbide Glass-Graphene Composite Paper Electrode for Long-Cycle Lithium-Ion Batteries. *Nat Commun* **2016**, *7*.
9. Tamayo, A.; Ruiz-Caro, R.; Mazo, A.; Veiga-Ochoa, M. D.; Rubio, J., Chemical Oxidation of Silicon Oxycarbide Ceramics for Advanced Drug Delivery Systems. *J Mater Sci* **2016**, *51*, 1382-1391.
10. Colombo, P.; Mera, G.; Riedel, R.; Soraru, G. D., Polymer-Derived Ceramics: 40 Years of Research and Innovation in Advanced Ceramics. *J Am Ceram Soc* **2010**, *93*, 1805-1837.
11. Ryan, J. V.; Pantano, C. G., Synthesis and Characterization of Inorganic Silicon Oxycarbide Glass Thin Films by Reactive Rf-Magnetron Sputtering. *J Vac Sci Technol A* **2007**, *25*, 153-159.
12. Kroll, P., Modelling and Simulation of Amorphous Silicon Oxycarbide. *J Mater Chem* **2003**, *13*, 1657-1668.
13. Kroll, P., Searching Insight into the Atomistic Structure of Sico Ceramics. *J Mater Chem* **2010**, *20*, 10528-10534.

14. Nimmo, J. P.; Kroll, P., First-Principles Calculations and Analysis of Si-29 Nuclear Magnetic Resonance Chemical Shifts in Silicon Oxycarbide Ceramics. *J Phys Chem C* **2014**, *118*, 29952-29961.

15. van Duin, A. C. T.; Dasgupta, S.; Lorant, F.; Goddard, W. A., Reaxff: A Reactive Force Field for Hydrocarbons. *J Phys Chem A* **2001**, *105*, 9396-9409.

16. Newsome, D. A.; Sengupta, D.; Foroutan, H.; Russo, M. F.; van Duin, A. C. T., Oxidation of Silicon Carbide by O-2 and H2o: A Reaxff Reactive Molecular Dynamics Study, Part I. *J Phys Chem C* **2012**, *116*, 16111-16121.

17. Soria, F. A.; Zhang, W. W.; van Duin, A. C. T.; Patrito, E. M., Thermal Stability of Organic Monolayers Grafted to Si(111): Insights from Reaxff Reactive Molecular Dynamics Simulations. *Acs Appl Mater Inter* **2017**, *9*, 30969-30981.

18. Soria, F. A.; Zhang, W. W.; Paredes-Olivera, P. A.; van Duin, A. C. T.; Patrito, E. M., Si/C/H Reaxff Reactive Potential for Silicon Surfaces Grafted with Organic Molecules. *J Phys Chem C* **2018**, *122*, 23515-23527.

A Reactive Force Field for Simulations of the Pyrolysis of Polysiloxanes into Silicon Oxycarbide Ceramics

Ilia Ponomarev[1], Adri C. T. van Duin[2], and Peter Kroll[1,*]

[1]Department of Chemistry and Biochemistry, The University of Texas at Arlington

[2]Department of Mechanical and Nuclear Engineering, Pennsylvania State University

700 Planetarium Place, Arlington, Texas 76019, United States.

*pkroll@uta.edu

Abstract

We provide a new Reactive Force Field (ReaxFF) for simulations of silicon oxycarbide (SiCO) ceramics and of their syntheses from inorganic polymer precursors. The validity of the force field is tested extensively against experimental and computational thermochemical data. Its performance in simulation at elevated temperature is gauged by results of extensive ab-initio molecular dynamic simulations. We apply the force field to the formation of amorphous SiCO in a simulated polymer pyrolysis. Modeling results are in good agreement with experimental observations and allow new insight into the formation of graphene segregations embedded in an amorphous oxycarbide matrix. The new reactive force field for Si-C-O-H compounds enables large-scale and long-time atomistic simulations with unprecedented fidelity.

1. Introduction

Silicon oxycarbide (SiCO) materials possess a wide range of attractive properties such as chemical durability[1], high-temperature stability[2], high creep-resistance and other specific mechanical properties[3-4]. SiCO materials are used or proposed to be used in applications for gas separation[5-6], thermal protection [7], radiation protection[8-9], advanced drug delivery[10], low-κ dielectric electronics[11], and energy storage[12]. Synthesis of SiCO proceeds via "bottom-up" processes: sol-gel syntheses[13], polymer-to-ceramic routes[14], and different flavors of vapor deposition methods.[15-17]

Composition and structure of SiCO materials depend on the involved chemistry, details of the processing and, not at least, on the thermal history of the material. Synthesized at temperatures below 1200°C the material remains amorphous, and crystallization occurs only at significantly higher temperatures[18]. Even in the amorphous state significant differences exists. For instance, low-κ SiCO thin films for electronic application contain significant amounts of hydrogen and methyl groups[19]. Here we focus on carbon-rich SiCO ceramic materials produced by the polymer-to-ceramic route. These ceramics exhibit a "SiCO glass" phase with so-called "free" carbon embedded in the matrix[14]:

$$SiC_{x+y}O_{2(1-x)} = \{x \cdot SiC + (1-x)SiO_2\} + y \cdot C_{free}$$

The SiCO glass, a stoichiometric mixture of SiO_2 and SiC, comprises a random network of Si-O and Si-C bonds forming mixed SiC_nO_{4-n}-tetrahedra. [18, 20-21] Carbon within the glass appears ("carbidic") in CSi_4 tetrahedra like in SiC, while O atoms bridge between Si atoms as in silica glass. The "free" carbon phase expresses similar to graphite or graphene[22]. Stoichiometric SiCO glass without "free" carbon can be synthesized[3]. The morphology of the "free" carbon, its interface to the glass matrix as well as the amount of hydrogen remaining in the material are hotly debated issues in concurrent research[23-24].

Atomistic modeling and accurate Density Functional Theory (DFT) calculations have contributed to better understanding local structures in SiCO materials. The SiCO glass has been characterized early on[25] and various interfaces between SiCO and “free” carbon have been studied.[26] Combining computational and experimental ^{29}Si NMR illuminated bonding at interfaces in amorphous SiCO.[21] Unfortunately, DFT calculations are computationally very expensive, which limits model sizes to a few hundred atoms and simulation times to below one nanosecond. Through empirical potential simulations, on the other side, it is feasible to explore mechanical properties of SiCO in models with millions of atoms extending several nm[27]. However, these models lack accuracy of chemical bonding, proper atomic environments, and acceptable thermochemistry.

The reactive force field (ReaxFF)[28] bridges the gap between accurate DFT simulations and empirical potential simulations. It achieves a level of accuracy comparable to DFT simulations for a wide set of molecular reactions in gas phase[28] and on surfaces[29-30]. At the same time ReaxFF is significantly less computationally expensive, which allows modeling chemical processes in larger systems for longer simulation times as compared to DFT simulations. A few studies of modeling reactive processes in SiCO using ReaxFF have been published recently[31-33]. As we will show further below, the particular parameterization of ReaxFF used in these studies fails to model many distinct features of SiCO and resulting structures are inadequate. Thus, to achieve the desired level of fidelity for a wide range of local atomic configurations it requires careful development of the numerous parameters describing interaction.

Here we represent new ReaxFF parameters describing interactions among Si, C, O, and H atoms in SiCOH materials. Starting with an existing ReaxFF parameterization[31], we take advantage of data of several thousands of DFT-computed models of SiCO and involve a self-learning process to eliminate pitfalls and traps. The new reactive force field is then applied to simulate the polymer-to-ceramic conversion of a cross-linked polysiloxane precursor.

2. Computational methods

The reactive force field (ReaxFF) has been designed to model chemical reaction through molecular dynamics simulations[28]. Guided by quantum chemical calculation, the energy of a system is partitioned into a variety of terms, including two-center covalent bond energy, ionic and dipole interactions, van der Waals interactions, a description for under- and over-coordination of atoms, angular and torsional terms, additional bond conjugation and penalties. A detailed description is given in the Reference [[28]]. A typical parameter set comprises 39 general parameters, another 32 parameters per atom and 16 parameters per bond, plus 7 additional off-diagonal bond parameters for heteroatomic bonds, 7 angular parameters, 5 torsion parameters and 4 parameters to describe hydrogen bonding. With more than 100 parameters to describe a system such as polysiloxane and SiCO ceramics, the chance of over-parameterization is immanent. Therefore, deriving a high-fidelity parameter set requires careful optimization against quality data, either experimental or computed via quantum mechanics (QM) methods.

We started with an existing parameters set for SiCO developed by Newsome et al.[31] This force field was developed with the purpose to model oxidation of silicon carbide. It incorporates essential thermochemistry of the Si-C-O system, including enthalpies of formation of SiC and SiO_2, reaction enthalpies of carbothermal reduction of SiO_2, and enthalpies of formation for a variety of small molecules. We then added recent force field parameters by Srinivasan[34] for the description of carbon-carbon interactions. Thereafter, we provided structure and energy data from our library of DFT-optimized SiCO models. The library comprises over 10000 hypothetical crystalline SiCO structures[35] and more than 1000 models of amorphous SiCO generated via a network algorithm or through melt-quench ab initio molecular dynamics simulations.[21, 25-26, 36-37] Using the accumulated data we optimized force field parameters for SiCOH within the ReaxFF software[28]. At this stage we achieved mapping of DFT energy differences to ReaxFF energy differences.

However, the reverse mapping lacked strong correlation. Consequently, we augmented the training set with $SiC_xO_yH_z$ models created by ReaxFF itself via melt-quench simulations and subsequently optimized in DFT. This recursive learning strategy expanded the range of configurations explored and enabled the development of robust force field parameters.

The Density Functional Theory[38] calculations in this work are carried out with the Vienna Ab Initio Simulation (VASP) package[39-40]. We use the Projector Augmented Wave (PAW)[41-42] method and approximate electron exchange and correlation by the Perdew-Burke-Ernzerhoff (PBE) generalized gradient approximation (GGA)[43-44]. The DFT-D2 method of Grimme[45] is applied to account for van der Waals interactions. The energy cutoff for the expansion of the wave function into the plane-wave basis is 500 eV. Ab-initio molecular dynamic simulations are performed at reduced energy cutoff under constant volume with a time step of 1 fs.

Molecular dynamics (MD) simulations with ReaxFF are performed with the Large-scale Atomic/Molecular Massively Parallel Simulator (LAMMPS) software[46] distributed by Sandia National Laboratories and its reax/c user's package[47]. We apply the Bussi-Donadio-Parrinello thermostat (temp/csvr command)[48] for temperature control. Depending on the hydrogen content of the model we use a time step of 0.1 fs to 1.0 fs for the integration of the equations of motion.

3. Force Field development

Challenges calling/identifying the need for a new Force Field

A proper Si-C-O-H force field must provide accurate description of the stoichiometric silicon oxycarbide glass phase that develops during synthesis of SiCO ceramics[3, 13-14, 18], but also occurs at reaction fronts during oxidation of SiC[49-50]. A fundamental characteristic of the SiCO glass are SiC_nO_{4-n} tetrahedra[18, 20]. These so-called mixed tetrahedra emerge in the glass phase of sol-gel processed or polymer-derived SiCO ceramics[51], but also develop upon oxidation of SiC (starting with only SiC_4-tetrahadra). Unfortunately, the parameter set developed by Newsome et al. cannot properly describe mixed SiC_nO_{4-n} tetrahedra, as we show in Figure 1. A perfect network of SiCO glass previously optimized using DFT is severely distorted in a MD simulation at 300K using Newsome et al. parameters. The force filed ruptures several Si-C bonds in mixed SiC_nO_{4-n} tetrahedral units, creating defects such as under- and over-coordinated sites.

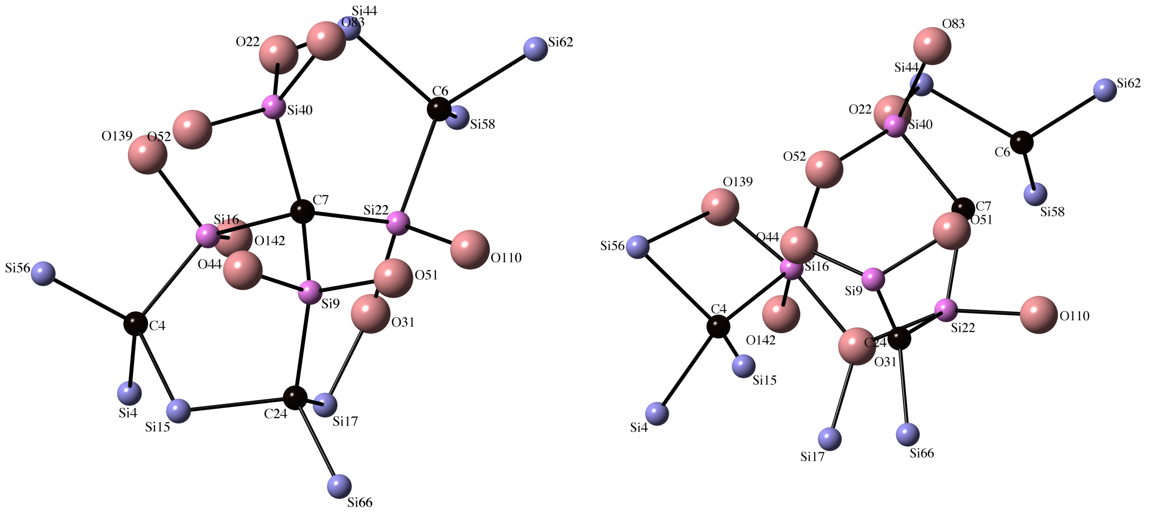

Figure 1. A fragment of the model of stoichiometric SiCO glass (composition $Si_{104}C_{24}O_{160}$) before (left) and after (right) 100 ps long MD simulation at 300K using Newsome ReaxFF parameters. We emphasize four mixed SiC_nO_{4-n} tetrahedral (Si in magenta) bonding to C (label C7). Sphere represent atoms: C (black), Si (blue and magenta), O (red).

We find another deficiency of the existing parameters by comparing ReaxFF energies with those calculated by DFT for stoichiometric SiCO glass models. This is shown in detail further below, when we highlight the performance of the new set of parameters we developed. Finally, the parameter set of Newsome et al. does not catch properly the remarkable kinetic stability of stoichiometric SiCO glass. Network models of glass SiCO are kinetically stable in ab-initio molecular dynamic simulations (aiMD) at elevated temperatures, for example at 2600K for 20 ps and longer[25]. The aiMD simulations show "melting" (i.e. breaking of bonds) only at higher temperatures. In sharp contrast, a ReaxFF MD simulation using the parameter set of Newsome et al. significantly deteriorates the model already at 1200K, a temperature at which a-SiCO remains stable in the experiment. Simulation at 2000K ruptures the model completely and leaves none of the existing carbidic carbon units, CSi_4-tetrahedra, intact, see Figure 2. The formation of C-C and C-O bonds in the simulation goes along with under-coordination of Si and formation of Si-Si bonds in the final model.

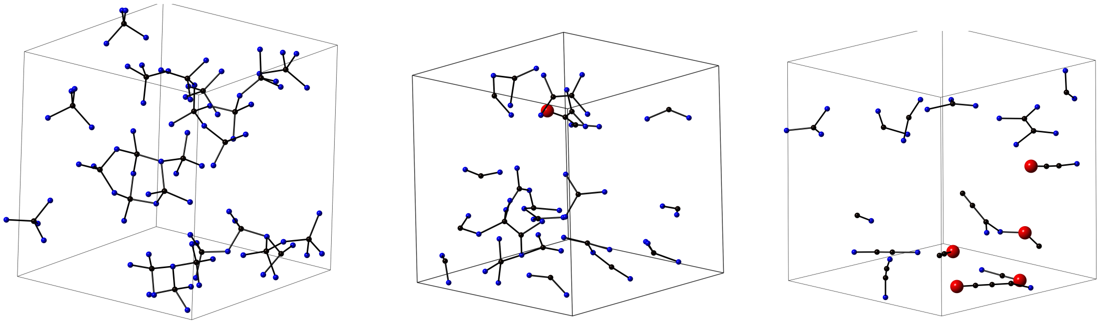

Figure 2. A model of stoichiometric SiCO glass (composition $Si_{104}C_{24}O_{160}$) before (left) and after 100 ps long MD simulation at 1200K (center) and 2000K (right) using Newsome ReaxFF parameters. Only C atoms and their nearest neighbors are displayed.

Deficiencies of the Newsome parameters have recently been identified by Takamoto et al. as well[52]. Their study underlines the call for developing a new set of parameters for ReaxFF, which can properly handle the variety of Si-C-O interactions occurring in polysiloxanes and silicon oxycarbide ceramics.

Performance of the newly developed force field

Part 1a: stoichiometric SiCO models: energy

The significant improvement of correspondence between DFT-computed energies and ReaxFF energies using the new parameter set is shown in Figure 4. We compare DFT computed energies for a standard set[25] of network models with composition $Si_{48}C_{16}O_{64}$

with energies computed by ReaxFF. In comparison with the previous force field, the new developed force field parameters UTA1 yield almost a unit slope, indicating that energy differences in DFT agree with those in ReaxFF. While the graph displays the relation for models with composition $Si_{48}C_{16}O_{64}$ only, we obtain equivalent agreement for all other stoichiometric compositions as well.

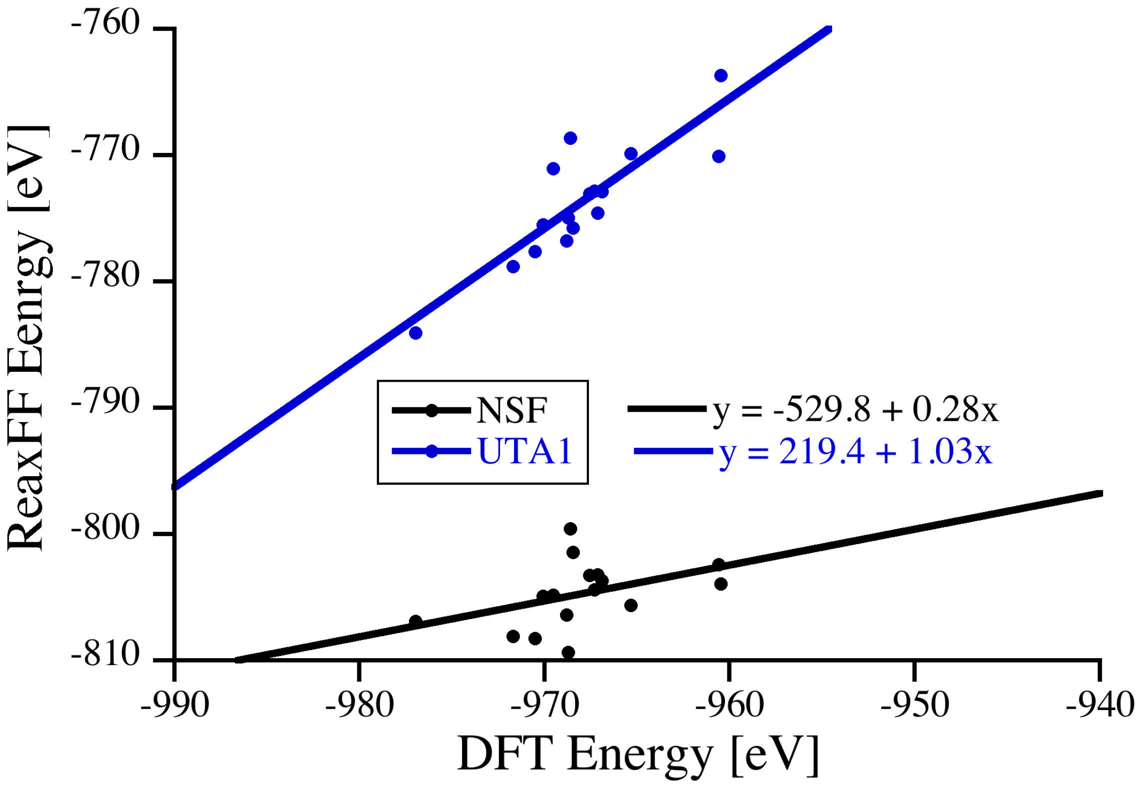

Figure 3. Comparison of DFT-energies of stoichiometric SiCO glass models with composition $Si_{48}C_{16}O_{64}$ with ReaxFF energies using parameters of Newsome et al.[31] and UTA1 ReaxFF parameters.

Part 1b: dynamic evolution of stoichiometric SiCO models

Besides achieving correspondence of energy differences, we also improve dynamic stability of SiCO glass structures. We performed MD simulations of stoichiometric SiCO with composition $Si_{104}C_{24}O_{160}$ (24·SiC+80·SiO_2, 24 mol-% SiC) using two different sets of models, each comprising three independent structures. One cohort exhibits a random distribution of mixed SiC_nO_{4-n}–tetrahedral. This is typical for SiCO glass synthesized at about 1000 °C[2, 18, 53]. Models in the second set are “segregated”, with preference of SiC_4- and SiO_4-tetrahedra on the cost of mixed units. One structure even exhibits a large SiC-nucleus embedded by SiO_2. Such configurations are typical for the partitioned yet still disordered state of SiCO materials annealed to higher temperatures (1200°C)[18]. They also occur at the interface between silicon carbide and its natural oxide, silica. After heating to 2000K and annealing at this temperature for 100 ps, we analyzed all structures. We focus on persistence and stability of (carbidic) C atoms within CSi_4-tetrahedra and of mixed SiC_nO_{4-n}–tetrahedra. Figure 4 displays one of the “random” a-SiCO models before and after completed simulation. Structural information on the models is summarized in Tables 1 and 2.

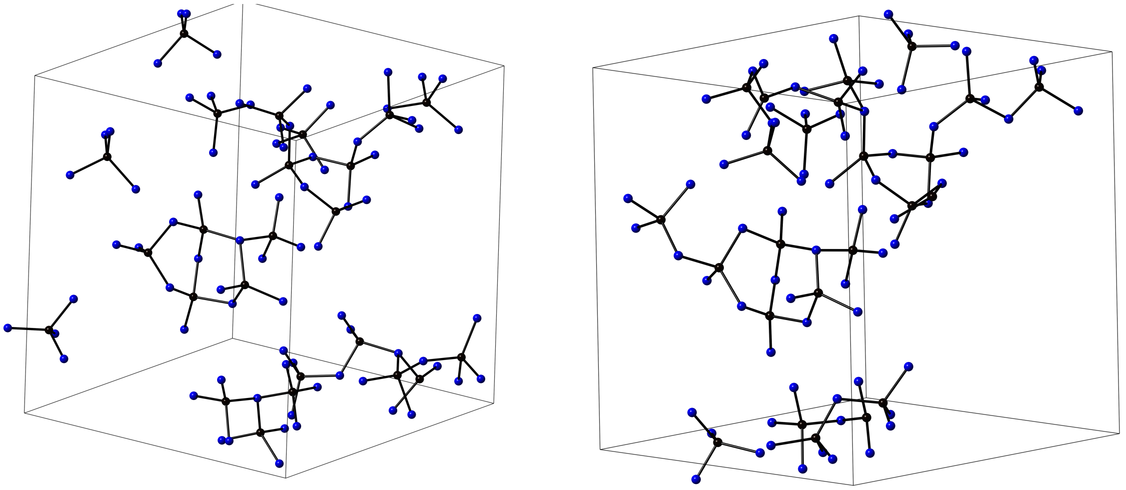

Figure 4. A model of stoichiometric SiCO glass (composition $Si_{104}C_{24}O_{160}$) before (left) and after (right) 100 ps long MD simulation at 2000K using the UTA1 ReaxFF parameters set. Only C atoms and their nearest neighbors are displayed.

Table 1. Amount (in %) of carbidic C atoms in $Si_{104}C_{24}O_{160}$ retaining tetrahedral coordination (CSi_4) after 100 ps simulation at 2000K.

Models	NSF	UTA1
Random	3	83
Segregated	4	96

All models	3	90

Table 2. Amount (in %) of unchanged SiC_nO_{4-n}–tetrahedral in $Si_{104}C_{24}O_{160}$ after 100 ps simulation at 2000K.

Si unit	NSF		UTA1	
	Random	Segregated	Random	Segregated
SiO_4	0	1	76	70
SiO_3C	0	0	76	67
SiO_2C_2	0	0	62	82
$SiOC_3$	0	0	82	86
SiC_4		0		95
All units	0		74	

Overall, the new force field provides stability of carbidic carbon at elevated temperatures and retains most of the mixed SiC_nO_{4-n}–tetrahedral environments. This will be important for modeling phase separation in SiCO, which involves formation of SiC nuclei. Moreover, it is essential for the simulation of pyrolysis of polymer precursors, for example of poly-methyl-siloxanes. Those encounter a Kumada-like rearrangement[54] as their most critical step[14]. Thermal activation leads to the cleavage of Si–O bonds and insertion of carbon forming Si–C bonds in the polymer backbone. This process yields the random distribution of mixed SiC_nO_{4-n}-tetrahedra, even if the molecular or polymeric precursors have a singular distinct environment only[18, 55].

Part 1c: modeling SiO_2 glass

Besides providing description of SiCO glass, our ReaxFF parameterization is also suitable to model pure SiO_2 glass. We performed melt-quench simulations to generate amorphous SiO_2 models. Starting with a 1032 atom model at 4000K, we quenched the system with a rate of 5 K/ps. Throughout the simulation we maintained a NPT ensemble, allowing the density of a-SiO_2 to adjust. A brief analysis of structural parameters of a-SiO_2 model is given in Table 3, and compared with data from models generated similarly using the parameters of Newsome et al.[31] We also include results obtained using yet another set of ReaxFF parameters especially designed for modeling a-SiO_2[56-57]. Our new

ReaxFF parameters yield less than 5% of defects such as under- or over-coordinated Si and O atoms. Density, average Si-O bond length and average Si-O-Si bond angle are close to the experimental values. Overall, our model compares well to structures obtained using a parameterization of ReaxFF developed especially for silicates[56-57].

Table 3. Structural parameters of SiO_2 models (1032 atoms) generated via melt-quench using ReaxFF with original Newsome parameters[31] (NSF), Pitman parameters[56-57] and the parameters presented in this work (IP).

Force field	ρ [g/cm^3]	Number of atoms per model adopting coordination				Number of bonds per model		Average	
		Si[3]	Si[5]	O[1]	O[3]	Si-Si	O-O	d_{Si-O} [Å]	<Si-O-Si> [°]
NSF	2.52	1	22	15	37	0	4	1.60	148
UTA1	2.17	13	9	13	9	1	2	1.62	146
Pitman	2.10	9	10	6	7	0	2	1.64	138

Part 1d: inclusion of "free" C into SiCO

The "free" carbon phase is characteristic of most silicon oxycarbide ceramics. Its genesis during synthesis and processing is the focus of many investigations, and tailoring its emergence through the molecular of polymer structure is a key issue for synthesis. Indeed, the development of the interface between glass matrix and "free" carbon is still an unresolved topic. A library of SiCO models comprising "free" carbon has been part of the parameter development[21, 26]. Here we show the performance of the new ReaxFF parameter set for the generation of SiCO structures via melt-quench MD simulations. 20 models of composition Si_5CO_8+$10C_{free}$, each comprising 120 atoms and a density of 2.2 g/cm^3, were generated via melt-quench simulations using a cooling rate of 20 K/ps. The models were finally optimized within ReaxFF. Subsequently, we switched to DFT calculations for direct comparison between ReaxFF energies and DFT energies. We computed the energy of each model at the beginning and the end of its DFT optimization. The difference between the two energies is a measure of "proximity" of potential energy surfaces of ReaxFF and DFT. Figure 5 provides a comparison for different compositions, with and without free carbon, generated within ReaxFF and further optimized in DFT.

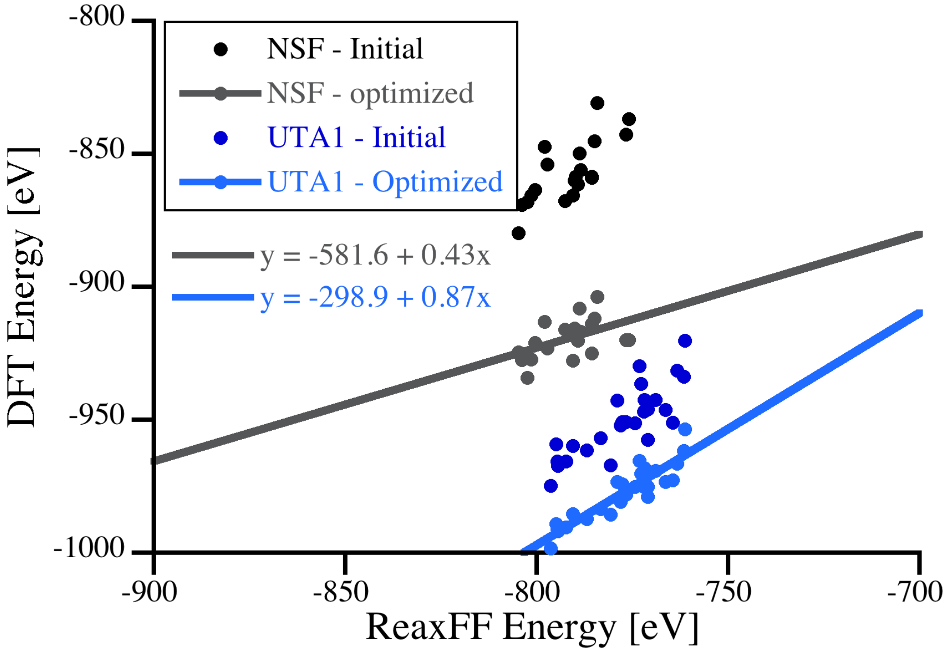

Figure 5. Energies of the models Si_5CO_8+$10C_{free}$ (ρ = 2.2 g/cm^3) generated via ReaxFF melt-quench simulation and optimized in DFT. "Initial" – first energy computed via DFT. "Optimized" – final DFT energy. NSF – original Newsome force field[31], UTA1 – force field parameters developed in this work.

Structures generated with the new parameter set come out much closer to the DFT optimized state than models generated with parameters of Newsome et al.. The average energy gained during DFT optimization (0.22 eV/atom compared to 0.69) is much lower for the new than for the previous parameter set. Although we do not obtain perfect agreement, the new ReaxFF parameters set generates models very similar to those we obtain via DFT melt-quench simulations. Figure 6 shows a comparison between models generates via ab-initio and ReaxFF melt-quench MD simulations for the composition Si_5CO_8+$10C_{free}$ with the initial density of 2.2 g/cm^3. Both models comprise a layer of "SiCO glass" sandwiched between a buckled graphene layers of "free carbon" phase.

Note that size, periodic boundary conditions and composition have a major impact on the final structure. Nevertheless, the resemblance of both models is striking.

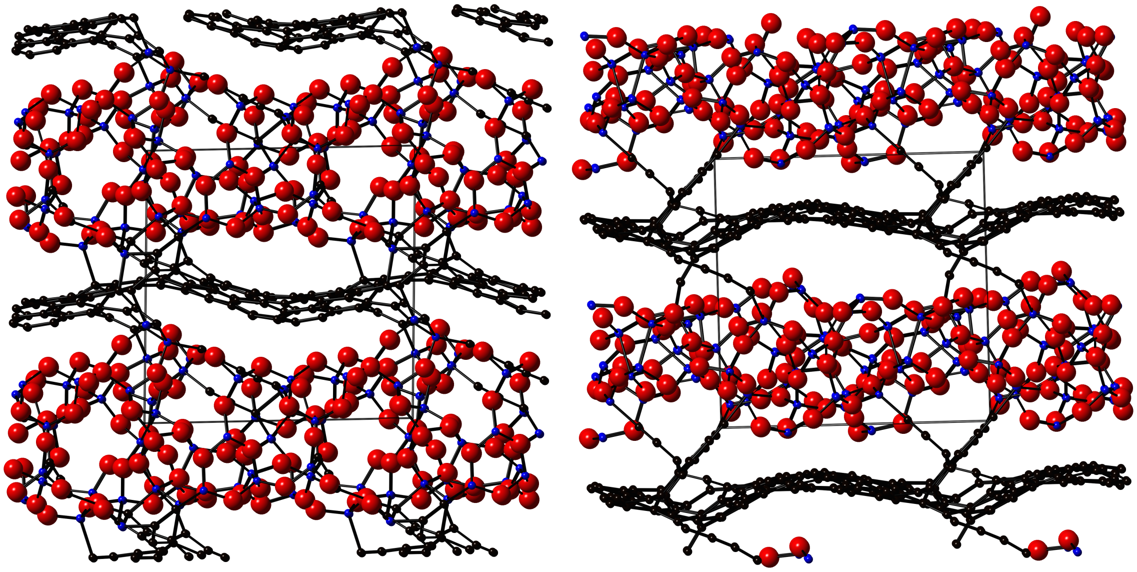

Figure 6. Amorphous models [left: DFT; right: ReaxFF using UTA1 parameters] of $Si_5CO_8+10C_{free}$ (192 atoms) generated via melt-quench MD simulation with a cooling rate of 12.5 K/ps starting from 5000K.

Part 1e: hydrogen as well

Silicon oxycarbide ceramics are produced by pyrolysis of molecular or polymeric precursors that contain substantial amounts of hydrogen.[13-14] Presence and content of hydrogen plays significant part in carbon segregation[32], electric properties of the final material[15], or withstanding radiation damage by a-SiCO(H)[8]. We included parameters for the interaction between H and the other elements, C, O, and Si from Newsome et al[31]. Some modifications were necessary to avoid unphysical bonding situations, and once again we located optimum parameter through repeating learning cycles of model generation and DFT optimization. Results for SiCOH models are quite similar to what has been shown before (e.g. Figure 5). Here we support "robustness" and "proximity" of ReaxFF and DFT energy minima in yet another way. We first generated a model of composition $Si_{25}C_{55}O_{40}H_{12}$ via melt-quench MD simulation (cooling rate 25 K/ps) in ReaxFF. Thereafter we started a cycle of optimizations first using ReaxFF then using DFT. After the first DFT optimization we keep the volume of the model constant. The cycle was the repeated several times. If potential energy surfaces of ReaxFF and DFT would not correspond well to each other, this cycling would produce more and more different structures. This happens, indeed, if "cycling" is done using a Tersoff-potential with parameters taken from Ref[58-61] and DFT. Using ReaxFF parameters of Newsome et al. and performing "cycling" creates many diverging structures as well. With the new parameter set, on the other side, models converge back to almost identical positions in every cycle. The sequence of energies of optimized structures is shown in Figure 7. We followed the same process also with a second model generated first using ab-initio melt quench simulations in DFT, and performed repeatedly optimizations in DFT followed by optimizations using ReaxFF. Here too, models converge back to almost the initial positions after every cycle.

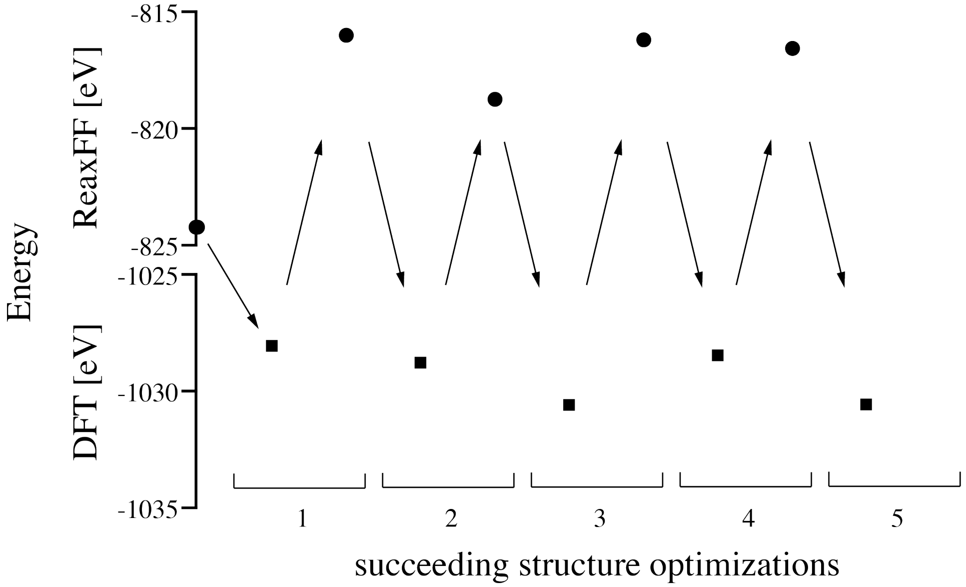

Figure 7. Final energies in repeated optimizations of SiCOH model (composition $Si_{25}C_{55}O_{40}H_{12}$) within DFT and ReaxFF.

Part 1f: summary of accomplishments

Before we go on and apply the new force field to model chemical processes, we can summarize the accomplishments of the parameter development. The new force field has been adjusted to provide a mapping of DFT energy differences to ReaxFF energy differences. For a variety of SiCO models, including those with "free" carbon, we show that energy differences agree on average. Moreover, modeling structures within ReaxFF and subsequently optimizing them in DFT shows that the reverse mapping holds as well. Thus, ReaxFF simulations of SiCO do not provide artificial structures that are local minima only with respect to the reactive force field. Those situations have been eliminated by the extensive learning strategy, repeatedly using results of ReaxFF simulations as test models for the development process.

Despite the obvious progress, our current set of ReaxFF parameters for SiCO is not perfect. For instance, we notice higher tolerance of ReaxFF for three-coordinated Si[3] and O[3] species. Those rarely appear in DFT-generated models of SiCO, and reactivity of Si[3] is well-known in experiments[62]. We also notice that modeling SiCO by ReaxFF yields a discernible preference for density of SiCO depending on composition. Simulations at constant volume show clear dependence of energy on density. On the other side, this dependency is much weaker when using network modeling or ab-initio MD simulations at constant volume to model SiCO[25]. Such remaining imperfections will be addressed in future work. With the new ReaxFF parameters at hand we can advance to the simulations of SiCO formation via thermal treatment of polymer precursors.

Part 2. Modeling the polymer-to-ceramic conversion: pyrolysis and annealing of PHMS-DVB

Providing deeper insight into processing of polymers into ceramics is essential for tailoring materials properties and for developing optimized chemical precursors. Quantum-chemical calculations provide accurate simulations, but unfortunately hit barriers associated with size and time. Simple (semi-) empirical potentials (e.g. Tersoff[63]) on the other side lack accuracy (and ability) in the description of chemical reactions and processes. This is where the reactive force field finds its application: tuned to accurate quantum-chemical calculations with the benefits of scalability of empirical simulations. As an example of a polymer-to-ceramic conversion, we model the pyrolysis of polymethylhydridosiloxane (PMHS) cross-linked with divinylbenzene (DVB).[64] This polymeric precursor has been used for synthesis of bulk and porous SiCO ceramics.[65-66] Ceramics obtained after pyrolysis are well characterized and comprise an amorphous SiCO phase with high "free" carbon content.[66] Materials synthesized from PMHS and DVB have been investigated as Li-anode material[67-68], for environmental remediation[24], sensors[69], gas separation[6], and as molecular sieves[24].

We start our simulation with modeling a cross-linked PMHS/DVB polymer, connecting different strands of PMHS with DVB. Figure 8 (left) shows a fragment of the structure. Note that the ratio of polymer units [-Si(H,Me)-O-] to double bonds [-H_2C=CH-] of DVB vinyl group is 2:1. This corresponds to a mass ratio of 4:1 between PMHS polymer units and molecular DVB. Essentially, it leaves every other Si-H bond available for further reactions. The fragment shown in Figure 8 is then interpenetrated by a second similar cross-linked polymer, yielding an entangled three-dimensional polysiloxane, as shown in Figure 8 (right). The model is replicated in all three directions and placed into a rectangular box with dimensions of approximately 4.0 x4.5x4.0 nm^3 under periodic boundaries. The composition is $Si_{512}C_{1792}O_{512}H_{3328}$ (6144 atoms) with a density of 1.08 g/cm^3. This polymer model serves as starting configuration for further simulations.

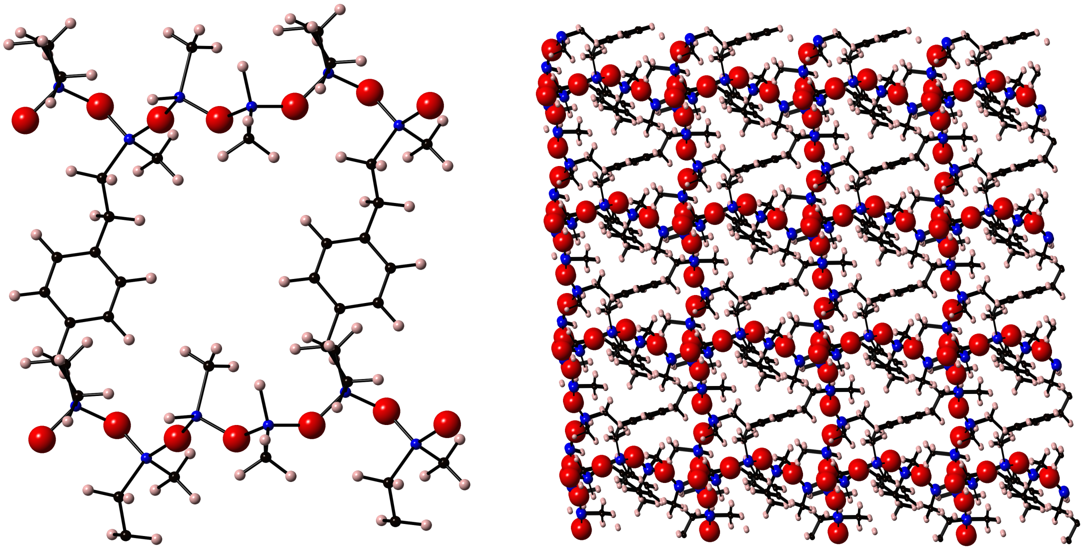

Figure 8. Left - fragment of the PHMS-DVB polymer structure. Right – entangled 3D polymer structure. Spheres are Si (blue), C (black), O (red), H (pink).

After an initial equilibration at room temperature, we heat the model to 2500K at constant volume with the rate of 25 K/ps. This process is required to observe reactions within feasible simulation times[70]. Experimental processing conducts the pyrolysis with heating rates of 5 K/min to temperatures between 900 ºC and 1200 ºC[14, 67] Once the maximum temperature is reached, we anneal the system for 1 ns ($5{\cdot}10^6$ time steps using Δt=0.2 fs). Throughout the annealing we maintain a constant pressure of 2000 bar to prevent "foaming" of the model. We also monitor the formation of gaseous reaction products, H_2, CO, CO_2, H_2O, O_2, CH_2O, C_2H_2, C_2H_4. Every 5 ps we remove persistent gas molecules. This process effectively simulates the evolution of gaseous species as monitored by mass-spectrometry[71]. Finally, we cool the system down to 0K while continuing removal of gaseous species as they appear. In Figure 9 we display the temperature profile for the simulation together with the evolution of composition of the system.

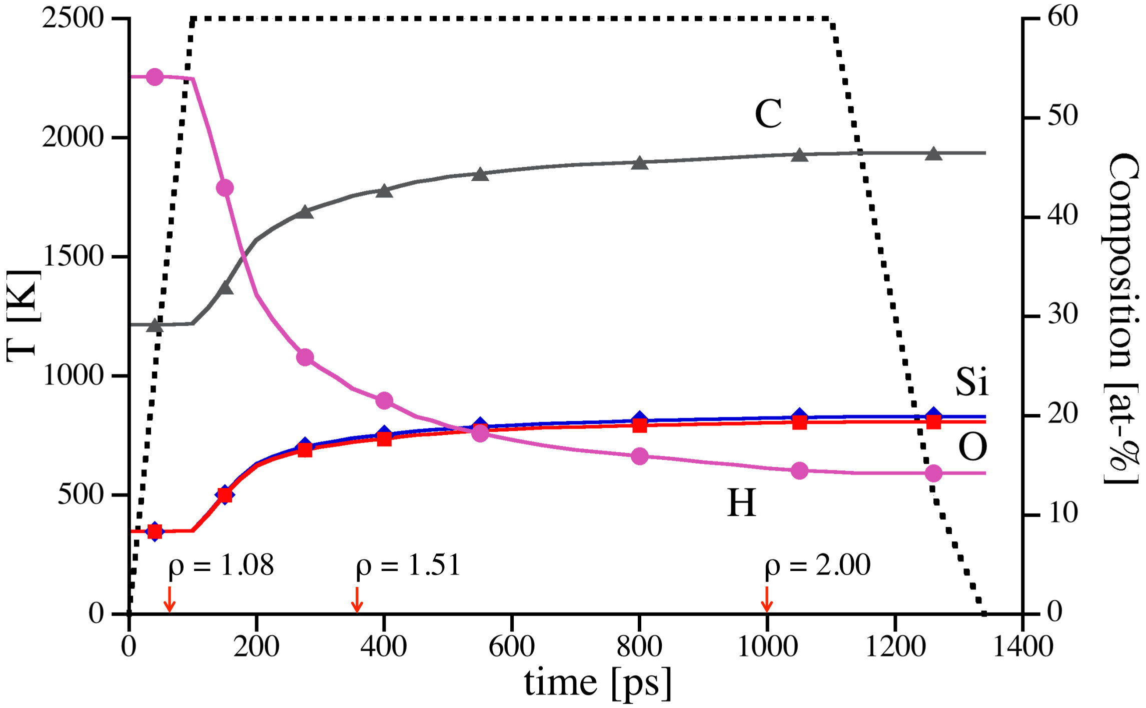

Figure 9. Time-temperature scheme (black dotted line) of simulated annealing of PMHS-DVB polymer. The second y-axis refers to the composition of the model (in atom-%) as a function of annealing time. Density (in g/cm^3) milestones are marked with arrows on x-axis.

Details of the chemical process will be given elsewhere. In brief, first processes we observe are H and CH_3-groups forming gaseous CH_4, leaving behind under-coordinated Si. These quickly react in various ways, creating Si-Si bonds, forming three-coordinated O, or terminating by H. With increasing temperature, the polymer -Si-O- backbone becomes flexible enough to allow insertion of methyl groups into the polymer chain (Kumada-like rearrangement). Only very few CO molecules develop, and the Si:O ratio is almost maintained throughout the simulation. At the same time, DVB units dissociate leaving behind vinyl-fragments and phenyl-rings. The latter then start to form larger agglomerates like poly-aromatic carbon. The latter process is facilitated by the openness of the polymer backbone, which allows large windows to appear in the structure suitable for the migration of larger carbon units. Ultimately, we observe segregation of tubular carbon and SiCO glass (Figure 10). At this stage of the simulation, mass loss happens through removal of H_2 only.

Table 4. Annealing of PMHS-DVB polymer precursor with PMHS:DVB mass ratio of 2:1 – computations vs. experiment. “C_{free}” represents mass-% of continuous C structure, not attached to Si.

Property	ρ [g/cm^3]	Mass loss [%]	Composition [mass-%]				
			Si	C	O	H	C_{free}
Simulation	2.02	22.6	39.2	38.1	21.8	0.9	32.8
Experiment[4, 51, 72]	1.95	23	38.1	40.3	21.3	0.3	32

Composition and density of models obtained, averaged over 2 simulations, are summarized in Table 4 and compared with experimental results[4, 51, 72]. Mass loss and final density matches experimental data auspiciously. In the course of the simulations the linear dimensions of the model shrink by 25%. The final structure of a-SiCO ceramic produced by simulated pyrolysis of a PMHS/DVB polymer is shown in Figure 10.

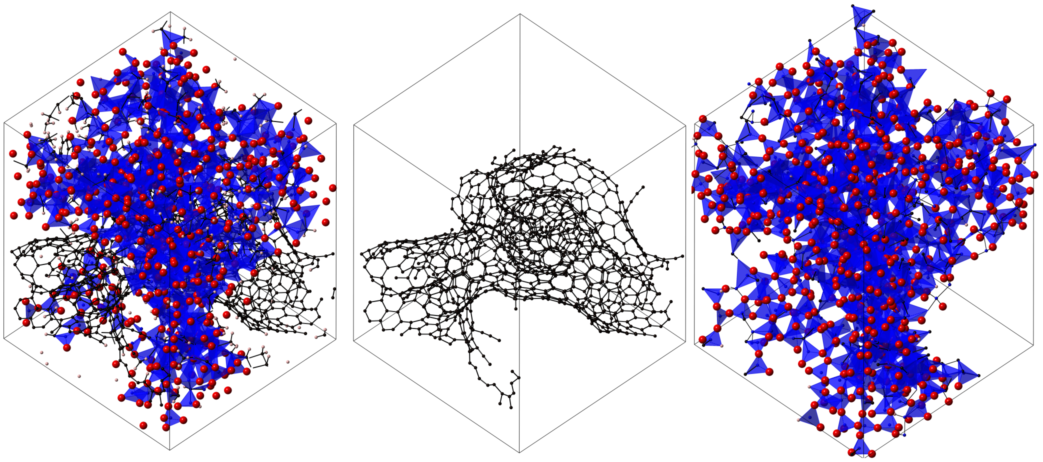

Figure 10. The structure of a-SiCO obtained by simulated annealing of PMHS-DVB polymer precursor: the whole structure (left), free carbon phase (center), and a-SiCO phase (right).

4. Conclusion

We developed new ReaxFF potential parameters for interactions among elements Si, C, O, and H through optimization and learning algorithms. The force field shows excellent agreement with Density Functional Theory calculations for energy differences for a vast variety of compositions and configurations. Moreover, local minima on the potential energy surfaces of both methods agree with each other. The force field demonstrates its predictive capability in simulations of thermal treatment of polysiloxanes. Modeling the polymer-to-ceramic conversion[14] of a cross-linked PHMS/DVB[64] polymer we find remarkable agreement of composition, mass loss, and density of ceramic between experimental data[4, 51, 72-73] and simulation.

The force field enables simulations of fundamental chemical reactions in synthesis and processing of new materials. This encompasses new SiCO ceramic materials, either synthesized by a polymer-to-ceramic route or via the sol-gel process. Preliminary results show successful simulations of condensation reactions for trimethylethoxysilane into a gel-type system. Further applications are reactions occurring during deposition of during low-k dielectric SiCO:H materials, as well as thermal treatment of these materials (post or concurrent synthesis) in reactive atmospheres such as H_2O, CO_2, or H_2. Future direction involve thermodynamic and kinetic stability of dielectric films[74], thermal conductivity[75], and the effects of radiation damage[8, 76] or ion implantation[74]. Obviously, force field development is an ongoing process with room for improvement and progress. Adding additional elements, especially N and B, will broaden the scope of applications. With concurrent computer facilities, it becomes possible to perform simulations of several nanoseconds on the length scale of several nanometers with fidelity comparable to quantum-chemical calculations.

References

1. Soraru, G. D.; Modena, S.; Guadagnino, E.; Colombo, P.; Egan, J.; Pantano, C., Chemical Durability of Silicon Oxycarbide Glasses. *J Am Ceram Soc* **2002**, *85*, 1529-1536.
2. Rouxel, T.; Massouras, G.; Soraru, G. D., High Temperature Behavior of a Gel-Derived Sioc Glass: Elasticity and Viscosity. *J Sol-Gel Sci Techn* **1999**, *14*, 87-94.
3. Walter, S.; Soraru, G. D.; Brequel, H.; Enzo, S., Microstructural and Mechanical Characterization of Sol Gel-Derived Si-O-C Glasses. *J Eur Ceram Soc* **2002**, *22*, 2389-2400.
4. Soraru, G. D., Kundanati, L., Santhosh, B., Pugno, N., Influence of Free Carbon on the Young's Modulus and Hardness of Polymer ‐ Derived Silicon Oxycarbide Glasses. *Journal of American Ceramic Society* **2019**, *102*, 907-913.
5. Lee, L. L.; Tsai, D. S., A Hydrogen-Permselective Silicon Oxycarbide Membrane Derived from Polydimethylsilane. *J Am Ceram Soc* **1999**, *82*, 2796-2800.
6. Juttke, Y.; Richter, H.; Voigt, I.; Prasad, R. M.; Bazarjani, M. S.; Gurlo, A.; Riedel, R., Polymer Derived Ceramic Membranes for Gas Separation. *Chem Engineer Trans* **2013**, *32*, 1891-1896.
7. Chiang, C. C.; Ko, I. H.; Chen, M. C.; Wu, Z. C.; Lu, Y. C.; Jang, S. M.; Liang, M. S., Physical and Barrier Properties of Pecvd Amorphous Silicon-Oxycarbide from Trimethylsilane and Co2. *J Electrochem Soc* **2004**, *151*, G704-G708.
8. Ding, H. P.; Demkowicz, M. J., Hydrogen Enhances the Radiation Resistance of Amorphous Silicon Oxycarbides. *Acta Mater* **2017**, *136*, 415-424.
9. Nastasi, M.; Su, Q.; Price, L.; Santana, J. A. C.; Chen, T. Y.; Balerio, R.; Shao, L., Superior Radiation Tolerant Materials: Amorphous Silicon Oxycarbide. *J Nucl Mater* **2015**, *461*, 200-205.
10. Tamayo, A.; Ruiz-Caro, R.; Mazo, A.; Veiga-Ochoa, M. D.; Rubio, J., Chemical Oxidation of Silicon Oxycarbide Ceramics for Advanced Drug Delivery Systems. *J Mater Sci* **2016**, *51*, 1382-1391.
11. Suyal, N.; Krajewski, T.; Mennig, M., Microstructural and Dielectric Characterization of Sol-Gel Derived Silicon Oxycarbide Glass Sheets. *J Sol-Gel Sci Techn* **1999**, *14*, 113-123.
12. David, L.; Bhandavat, R.; Barrera, U.; Singh, G., Silicon Oxycarbide Glass-Graphene Composite Paper Electrode for Long-Cycle Lithium-Ion Batteries. *Nat Commun* **2016**, *7*.
13. Pantano, C. G.; Singh, A. K.; Zhang, H. X., Silicon Oxycarbide Glasses. *J Sol-Gel Sci Techn* **1999**, *14*, 7-25.
14. Colombo, P.; Mera, G.; Riedel, R.; Soraru, G. D., Polymer-Derived Ceramics: 40 Years of Research and Innovation in Advanced Ceramics. *J Am Ceram Soc* **2010**, *93*, 1805-1837.
15. Gallis, S.; Nikas, V.; Huang, M.; Eisenbraun, E.; Kaloyeros, A. E., Comparative Study of the Effects of Thermal Treatment on the Optical Properties of Hydrogenated Amorphous Silicon-Oxycarbide. *J Appl Phys* **2007**, *102*.
16. Rouessac, V.; Favennec, L.; Remiat, B.; Jousseaume, V.; Passernard, G.; Durand, J., Precursor Chemistry for Ulk Cvd. *Microelectron Eng* **2005**, *82*, 333-340.

17. Ryan, J. V.; Pantano, C. G., Synthesis and Characterization of Inorganic Silicon Oxycarbide Glass Thin Films by Reactive Rf-Magnetron Sputtering. *J Vac Sci Technol A* **2007**, *25*, 153-159.
18. Brequel, H., et al., Systematic Structural Characterization of the High-Temperature Behavior of Nearly Stoichiometric Silicon Oxycarbide Glasses. *Chem Mater* **2004**, *16*, 2585-2598.
19. Das, G.; Mariotto, G.; Quaranta, A., Microstructural Evolution of Thermally Treated Low-Dielectric Constant Sioc : H Films Prepared by Pecvd. *J Electrochem Soc* **2006**, *153*, F46-F51.
20. Bois, L.; Maquet, J.; Babonneau, F.; Mutin, H.; Bahloul, D., Structural Characterization of Sol-Gel Derived Oxycarbide Glasses .1. Study of the Pyrolysis Process. *Chem Mater* **1994**, *6*, 796-802.
21. Nimmo, J. P.; Kroll, P., First-Principles Calculations and Analysis of Si-29 Nuclear Magnetic Resonance Chemical Shifts in Silicon Oxycarbide Ceramics. *J Phys Chem C* **2014**, *118*, 29952-29961.
22. Mera, G.; Navrotsky, A.; Sen, S.; Kleebe, H. J.; Riedel, R., Polymer-Derived Sicn and Sioc Ceramics - Structure and Energetics at the Nanoscale. *J Mater Chem A* **2013**, *1*, 3826-3836.
23. Mera, G.; Gallei, M.; Bernard, S.; Ionescu, E., Ceramic Nanocomposites from Tailor-Made Preceramic Polymers. *Nanomaterials-Basel* **2015**, *5*, 468-540.
24. Stabler, C.; Ionescu, E.; Graczyk-Zajac, M.; Gonzalo-Juan, I.; Riedel, R., Silicon Oxycarbide Glasses and Glass-Ceramics: "All-Rounder" Materials for Advanced Structural and Functional Applications. *J Am Ceram Soc* **2018**, *101*, 4817-4856.
25. Kroll, P., Modelling and Simulation of Amorphous Silicon Oxycarbide. *J Mater Chem* **2003**, *13*, 1657-1668.
26. Kroll, P., Searching Insight into the Atomistic Structure of Sico Ceramics. *J Mater Chem* **2010**, *20*, 10528-10534.
27. David Marshall, B. C., Peter Kroll, Greg Hilmas, William Fahrenholtz, Rishi Raj, Robert Ritchie, Qingda Yang, Frank Zok *National Hypersonic Science Center for Materials and Structures*; 2014; p 61.
28. van Duin, A. C. T.; Dasgupta, S.; Lorant, F.; Goddard, W. A., Reaxff: A Reactive Force Field for Hydrocarbons. *J Phys Chem A* **2001**, *105*, 9396-9409.
29. Soria, F. A.; Zhang, W. W.; van Duin, A. C. T.; Patrito, E. M., Thermal Stability of Organic Monolayers Grafted to Si(111): Insights from Reaxff Reactive Molecular Dynamics Simulations. *Acs Appl Mater Inter* **2017**, *9*, 30969-30981.
30. Soria, F. A.; Zhang, W. W.; Paredes-Olivera, P. A.; van Duin, A. C. T.; Patrito, E. M., Si/C/H Reaxff Reactive Potential for Silicon Surfaces Grafted with Organic Molecules. *J Phys Chem C* **2018**, *122*, 23515-23527.
31. Newsome, D. A.; Sengupta, D.; Foroutan, H.; Russo, M. F.; van Duin, A. C. T., Oxidation of Silicon Carbide by O-2 and H2o: A Reaxff Reactive Molecular Dynamics Study, Part I. *J Phys Chem C* **2012**, *116*, 16111-16121.
32. Ding, H. P.; Demkowicz, M. J., Hydrogen Reverses the Clustering Tendency of Carbon in Amorphous Silicon Oxycarbide. *Sci Rep-Uk* **2015**, *5*.
33. Gao, H. F.; Wang, H. J.; Zhao, Z. H.; Niu, M.; Su, L.; Wei, Y., Reactive Dynamics Simulation Study on the Pyrolysis of Polymer Precursors to Generate Amorphous Silicon Oxycarbide Structures. *J Phys Chem C* **2018**, *122*, 5767-5773.

34. Srinivasan, S. G.; van Duin, A. C. T.; Ganesh, P., Development of a Reaxff Potential for Carbon Condensed Phases and Its Application to the Thermal Fragmentation of a Large Fullerene. *J Phys Chem A* **2015**, *119*, 571-580.

35. Bodifort, N. Crystalline Sico: Implication on Structure and Thermochemistry of Ternary Silicon Oxycarbide Ceramics. The University of Texas at Arlington, 2013.

36. Wooten, F.; Winer, K.; Weaire, D., Computer-Generation of Structural Models of Amorphous Si and Ge. *Phys Rev Lett* **1985**, *54*, 1392-1395.

37. Kroll, P., Structure and Reactivity of Amorphous Silicon Nitride Investigated with Density-Functional Methods. *J Non-Cryst Solids* **2001**, *293*, 238-243.

38. Hohenberg, P.; Kohn, W., Inhomogeneous Electron Gas. *Phys Rev B* **1964**, *136*, B864-+.

39. Kresse, G.; Hafner, J., Ab-Initio Molecular-Dynamics Simulation of the Liquid-Metal Amorphous-Semiconductor Transition in Germanium. *Phys Rev B* **1994**, *49*, 14251-14269.

40. Kresse, G.; Furthmuller, J., Efficiency of Ab-Initio Total Energy Calculations for Metals and Semiconductors Using a Plane-Wave Basis Set. *Comp Mater Sci* **1996**, *6*, 15-50.

41. Blochl, P. E., Projector Augmented-Wave Method. *Phys Rev B* **1994**, *50*, 17953-17979.

42. Kresse, G.; Joubert, D., From Ultrasoft Pseudopotentials to the Projector Augmented-Wave Method. *Phys Rev B* **1999**, *59*, 1758-1775.

43. Perdew, J. P.; Burke, K.; Ernzerhof, M., Generalized Gradient Approximation Made Simple. *Phys Rev Lett* **1996**, *77*, 3865-3868.

44. Perdew, J. P.; Burke, K.; Ernzerhof, M., Generalized Gradient Approximation Made Simple (Vol 77, Pg 3865, 1996). *Phys Rev Lett* **1997**, *78*, 1396-1396.

45. Grimme, S., Semiempirical Gga-Type Density Functional Constructed with a Long-Range Dispersion Correction. *J Comput Chem* **2006**, *27*, 1787-1799.

46. Plimpton, S., Fast Parallel Algorithms for Short-Range Molecular-Dynamics. *J Comput Phys* **1995**, *117*, 1-19.

47. Aktulga, H. M.; Fogarty, J. C.; Pandit, S. A.; Grama, A. Y., Parallel Reactive Molecular Dynamics: Numerical Methods and Algorithmic Techniques. *Parallel Comput* **2012**, *38*, 245-259.

48. Bussi, G.; Donadio, D.; Parrinello, M., Canonical Sampling through Velocity Rescaling. *J Chem Phys* **2007**, *126*.

49. Hornetz, B.; Michel, H. J.; Halbritter, J., Arxps Studies of Sio2-Sic Interfaces and Oxidation of 6h Sic Single-Crystal Si-(001) and C-(001)over-Bar Surfaces. *J Mater Res* **1994**, *9*, 3088-3094.

50. Onneby, C.; Pantano, C. G., Silicon Oxycarbide Formation on Sic Surfaces and at the Sic/Sio2 Interface. *J Vac Sci Technol A* **1997**, *15*, 1597-1602.

51. Dibandjo, P.; Dire, S.; Babonneau, F.; Soraru, G. D., Influence of the Polymer Architecture on the High Temperature Behavior of Sico Glasses: A Comparison between Linear- and Cyclic-Derived Precursors. *J Non-Cryst Solids* **2010**, *356*, 132-140.

52. Takamoto, S.; Yamasaki, T.; Ohno, T.; Kaneta, C.; Hatano, A.; Izumi, S., Elucidation of the Atomic-Scale Mechanism of the Anisotropic Oxidation Rate of 4h-

Sic between the (0001) Si-Face and (000(1)over-Bar) C-Face by Using a New Si-O-C Interatomic Potential. *J Appl Phys* **2018**, *123*.
53. Rouxel, T.; Soraru, G. D.; Vicens, J., Creep Viscosity and Stress Relaxation of Gel-Derived Silicon Oxycarbide Glasses. *J Am Ceram Soc* **2001**, *84*, 1052-1058.
54. Shiina, K.; Kumada, M., Thermal Rearrangement of Hexamethyldisilane to Trimethyl(Dimethylsilylmethyl)-Silane. *J Org Chem* **1958**, *23*, 139-139.
55. Radovanovic, E.; Gozzi, M. F.; Goncalves, M. C.; Yoshida, I. V. P., Silicon Oxycarbide Glasses from Silicone Networks. *J Non-Cryst Solids* **1999**, *248*, 37-48.
56. Yu, Y. T.; Wang, B.; Wang, M. Y.; Sant, G.; Bauchy, M., Revisiting Silica with Reaxff: Towards Improved Predictions of Glass Structure and Properties Via Reactive Molecular Dynamics. *J Non-Cryst Solids* **2016**, *443*, 148-154.
57. Pitman, M. C.; van Duin, A. C. T., Dynamics of Confined Reactive Water in Smectite Clay-Zeolite Composites. *J Am Chem Soc* **2012**, *134*, 3042-3053.
58. Tersoff, J., Empirical Interatomic Potential for Silicon with Improved Elastic Properties. *Phys Rev B* **1988**, *38*, 9902-9905.
59. Tersoff, J., Empirical Interatomic Potential for Carbon, with Applications to Amorphous-Carbon. *Phys Rev Lett* **1988**, *61*, 2879-2882.
60. Kroll, P. Computersimulationen Und Röntgennahkantenabsorptionsspektroskopie Von Siliciumnitrid Und Siliciumcarbidnitrid Keramiken. TU Darmstadt, 1996.
61. Munetoh, S.; Motooka, T.; Moriguchi, K.; Shintani, A., Interatomic Potential for Si-O Systems Using Tersoff Parameterization. *Comp Mater Sci* **2007**, *39*, 334-339.
62. Chatgilialoglu, C., Structural and Chemical-Properties of Silyl Radicals. *Chem Rev* **1995**, *95*, 1229-1251.
63. Liao, N. B.; Xue, W.; Zhou, H. M.; Zhang, M., Molecular Dynamics Investigation of Structure and High-Temperature Mechanical Properties of Sibco Ceramics. *J Alloy Compd* **2014**, *610*, 45-49.
64. Blum, Y. D.; MacQueen, D. B.; Kleebe, H. J., Synthesis and Characterization of Carbon-Enriched Silicon Oxycarbides. *J Eur Ceram Soc* **2005**, *25*, 143-149.
65. Lu, K., Porous and High Surface Area Silicon Oxycarbide-Based Materials-a Review. *Mat Sci Eng R* **2015**, *97*, 23-49.
66. Kleebe, H. J.; Blum, Y. D., Sioc Ceramic with High Excess Free Carbon. *J Eur Ceram Soc* **2008**, *28*, 1037-1042.
67. Sasikumar, P. V. W.; Zera, E.; Graczyk-Zajac, M.; Riedel, R.; Soraru, G. D., Structural Design of Polymer-Derived Sioc Ceramic Aerogels for High-Rate Li Ion Storage Applications. *J Am Ceram Soc* **2016**, *99*, 2977-2983.
68. Graczyk-Zajac, M.; Vrankovic, D.; Waleska, P.; Hess, C.; Sasikumar, P. V.; Lauterbach, S.; Kleebe, H. J.; Soraru, G. D., The Li-Storage Capacity of Sioc Glasses with and without Mixed Silicon Oxycarbide Bonds. *J Mater Chem A* **2018**, *6*, 93-103.
69. Liao, N. B.; Zhou, H. M.; Zheng, B. R.; Xue, W., Silicon Oxycarbide-Derived Carbon as Potentia No2 Gas Sensor: A First Principles' Study. *Ieee Electr Device L* **2018**, *39*, 1760-1763.
70. Du, T.; Li, H.; Sant, G.; Bauchy, M., New Insights into the Sol-Gel Condensation of Silica by Reactive Molecular Dynamics Simulations. *J Chem Phys* **2018**, *148*.

71. Soraru, G. D.; Pederiva, L.; Latournerie, M.; Raj, R., Pyrolysis Kinetics for the Conversion of a Polymer into an Amorphous Silicon Oxycarbide Ceramic. *J Am Ceram Soc* **2002**, *85*, 2181-2187.
72. Prandeep, V. S. Study of Silicon Oxycarbide (Sioc) as Anode Materials for Li-Ion Batteries. University of Trento, 2013.
73. Hourlier, D.; Venkatachalam, S.; Ammar, M. R.; Blum, Y., Pyrolytic Conversion of Organopolysiloxanes. *J Anal Appl Pyrol* **2017**, *123*, 296-306.
74. Chen, J. W.; Calvin, J.; Asplund, M.; King, S. W.; Woodfield, B. F.; Navrotsky, A., Heat Capacities, Entropies, and Gibbs Free Energies of Formation of Low-K Amorphous Si(O)Ch Dielectric Films and Implications for Stability During Processing. *J Chem Thermodyn* **2019**, *128*, 320-335.
75. Harikrishna, H.; Lanford, W. A.; King, S. W.; Huxtable, S. T., Thermal Conductivity of Plasma Deposited Amorphous Hydrogenated Boron and Carbon Rich Thin Films. *J Nucl Mater* **2019**, *514*, 154-160.
76. Su, Q.; Wang, T. Y.; Gigax, J.; Shao, L.; Lanford, W. A.; Nastasi, M.; Li, L. Y.; Bhattarai, G.; Paquette, M. M.; King, S. W., Influence of Topological Constraints on Ion Damage Resistance of Amorphous Hydrogenated Silicon Carbide. *Acta Mater* **2019**, *165*, 587-602.

Summary

I successfully developed a ReaxFF parameter set to describe Si-C-O-H interactions through optimization and learning algorithm. The force field was extensively tested in a variety of simulations:

- Structural optimizations of network-generated and DFT-optimized models
- High temperature MD simulations of network-generated and DFT-optimized models
- Melt-quench generation of silica
- Melt-quench generation of silicon oxycarbide

In all tests the force field performed well: 1 “ReaxFF eV” ≈ 1 “DFT eV” for a vast variety of systems; high temperature stability within ReaxFF is at acceptable level; ReaxFF generates good models via melt-quench approach.

I further apply our ReaxFF parameterization to the simulation of the polymer-to-ceramic process, and perform simulated annealing of PHMS-DVB[1] copolymer with removing of gaseous products in the course of simulation. The outcome of the simulation exhibits outstanding agreement with the experimentally available data[2-4] in terms of density, composition and mass change upon the process. The final structure agrees well with the proposed structural models of silicon oxycarbide[5-7].

Further outlook will include:

- Exploring annealing of the different polymers; exploring annealing in the reactive atmospheres
- Future development of the ReaxFF parameterization: making the existing set for Si-C-O-H more realistic, including parameters for the new elements, primarily N and B that find broad application in the field of polymer-derived ceramics.[8-9]

Some of the results are represented in the chapters below

References

1. Blum, Y. D.; MacQueen, D. B.; Kleebe, H. J., Synthesis and Characterization of Carbon-Enriched Silicon Oxycarbides. *J Eur Ceram Soc* **2005**, *25*, 143-149.
2. Dibandjo, P.; Dire, S.; Babonneau, F.; Soraru, G. D., Influence of the Polymer Architecture on the High Temperature Behavior of Sico Glasses: A Comparison between Linear- and Cyclic-Derived Precursors. *J Non-Cryst Solids* **2010**, *356*, 132-140.
3. Sasikumar, P. V. W.; Zera, E.; Graczyk-Zajac, M.; Riedel, R.; Soraru, G. D., Structural Design of Polymer-Derived Sioc Ceramic Aerogels for High-Rate Li Ion Storage Applications. *J Am Ceram Soc* **2016**, *99*, 2977-2983.
4. Soraru, G. D., Kundanati, L., Santhosh, B., Pugno, N., Influence of Free Carbon on the Young's Modulus and Hardness of Polymer‐Derived Silicon Oxycarbide Glasses. *Journal of American Ceramic Society* **2019**, *102*, 907-913.
5. Kroll, P., Searching Insight into the Atomistic Structure of Sico Ceramics. *J Mater Chem* **2010**, *20*, 10528-10534.
6. Kroll, P., Modelling and Simulation of Amorphous Silicon Oxycarbide. *J Mater Chem* **2003**, *13*, 1657-1668.
7. Nimmo, J. P.; Kroll, P., First-Principles Calculations and Analysis of Si-29 Nuclear Magnetic Resonance Chemical Shifts in Silicon Oxycarbide Ceramics. *J Phys Chem C* **2014**, *118*, 29952-29961.
8. Liao, N. B.; Xue, W.; Zhou, H. M.; Zhang, M., Molecular Dynamics Investigation of Structure and High-Temperature Mechanical Properties of Sibco Ceramics. *J Alloy Compd* **2014**, *610*, 45-49.
9. Harikrishna, H.; Lanford, W. A.; King, S. W.; Huxtable, S. T., Thermal Conductivity of Plasma Deposited Amorphous Hydrogenated Boron and Carbon Rich Thin Films. *J Nucl Mater* **2019**, *514*, 154-160.

Technical details of the parameter development

For the force field parameter development I used ReaxFF software package by Adri van Duin[1]. Reference DFT calculations were preformed within VASP software (PAW, PBE, Grimme-D2 correction or ULG correction)[2-8]. Molecular dynamics simulations were preformed within LAMMPS[9] software using reax/c[10] user package.

Implementation of ReaxFF parameters is different in LAMMPS and the software by Adri van Duin. Difference is minor: LAMMPS doesn't use overcoordination parameter (2 * 13 parameter), utilizing a combination of undercoordination (2 * 12 parameter) and ov/un (2 * 25 parameter).

ReaxFF MD simulations within LAMMPS sometimes encounter "flying ice cube" problem. To avoid this I used Bussi-Donadio-Parrinello[11] thermostat. Another problems that can happen with ReaxFF in LAMMPS: lost atoms or too quick changes of hydrogen bond list that cause memory allocation issues ("*hbondchk failed*"). For the former – reduction of the time step is the solution. For the latter – reduction of time step would prevent significant changes; higher "*safezone*" and "*mincap*" keyword values increase the memory allocation for the bond lists, which would solve problem with increasing this list.

My parameter development was performed in a "step-by-step" approach. At every step I applied some not directly connected testing procedure: energy correspondence of network SiCO models not included in the fitting, high temperature stability of network SiCO models, generation of 1032-atom SiO_2 model within ReaxFF, energy correspondence of ReaxFF-generated models.

First I fitted mixed angle parameters (C-O-Si, C-Si-O, O-C-Si angles) vs. Newsome training set and a set of data computed for small crystalline SiCO models. Next step – I manually increased force constant for the C-Si-O angle ("5 70 2" parameter in terms of ReaxFF software) so that its value is aligned with the other force constants for angles on

Si. This step solved the problem of energy mismatch for network-generated SiCO(H) models.

Then I explored a variety of ReaxFF melt-quench models (SiO_2, SiC, SiCO of various compositions, SiO, SiO_3) and the relations between ReaxFF and DFT energies. I've found fitting vs. ReaxFF MQ-generated SiC to be the most beneficial in terms of increase of SiCO model high temperature stability. Exploring Si-O system finally led to reasonable density and amounts of defects for ReaxFF-generated a-SiO_2.

Further I incorporated of Srinivasan[12] force field parameters (general + C atom + C-C bond + C-C-C angle + C-C-C-C torsion) into Newsome set, adjusted H electronegativity parameter so that the simulation wouldn't crash and incorporated mixed angle parameters that I obtained in the beginning. Then I used the experience I obtained during "exploration" to fit, one by one, Si-C parameters vs. crystalline and amorphous SiC (until acceptable high temperature stability is reached), Si-O parameters vs. crystalline SiO_2 polymorphs and amorphous SiO_2 (until reasonable SiO_2 is generated within ReaxFF in melt-quench simulations), and then the whole set of Si-C-O parameters vs. SiC, SiO_2 and SiCO models. (until MQ-generated SiCO is well-described).

For H-parameters fitting I used initial Newsome training set along with ReaxFF melt-quench generated models. I also did some initial manual adjustments of H-Si/C/O/H bond energies by comparing the outcomes ab initio melt-quench simulations and ReaxFF melt-quench simulations. The necessity of this step came from significant changes in electronegativity parameters of the atoms due to Srinivasan set incorporation.

For the polymer annealing simulation I wrote c code and a script to work along with it to remove gases 5 times during heating and cooling, and every 5 ps of annealing.

References

1. van Duin, A. C. T.; Dasgupta, S.; Lorant, F.; Goddard, W. A., Reaxff: A Reactive Force Field for Hydrocarbons. *J Phys Chem A* **2001**, *105*, 9396-9409.

2. Hohenberg, P.; Kohn, W., Inhomogeneous Electron Gas. *Phys Rev B* **1964**, *136*, B864-+.

3. Kresse, G.; Hafner, J., Ab-Initio Molecular-Dynamics Simulation of the Liquid-Metal Amorphous-Semiconductor Transition in Germanium. *Phys Rev B* **1994**, *49*, 14251-14269.

4. Kresse, G.; Furthmuller, J., Efficiency of Ab-Initio Total Energy Calculations for Metals and Semiconductors Using a Plane-Wave Basis Set. *Comp Mater Sci* **1996**, *6*, 15-50.

5. Kresse, G.; Joubert, D., From Ultrasoft Pseudopotentials to the Projector Augmented-Wave Method. *Phys Rev B* **1999**, *59*, 1758-1775.

6. Blochl, P. E., Projector Augmented-Wave Method. *Phys Rev B* **1994**, *50*, 17953-17979.

7. Grimme, S., Semiempirical Gga-Type Density Functional Constructed with a Long-Range Dispersion Correction. *J Comput Chem* **2006**, *27*, 1787-1799.

8. Kim, H.; Choi, J. M.; Goddard, W. A., Universal Correction of Density Functional Theory to Include London Dispersion (up to Lr, Element 103). *J Phys Chem Lett* **2012**, *3*, 360-363.

9. Plimpton, S., Fast Parallel Algorithms for Short-Range Molecular-Dynamics. *J Comput Phys* **1995**, *117*, 1-19.

10. Aktulga, H. M.; Fogarty, J. C.; Pandit, S. A.; Grama, A. Y., Parallel Reactive Molecular Dynamics: Numerical Methods and Algorithmic Techniques. *Parallel Comput* **2012**, *38*, 245-259.

11. Bussi, G.; Donadio, D.; Parrinello, M., Canonical Sampling through Velocity Rescaling. *J Chem Phys* **2007**, *126*.

12. Srinivasan, S. G.; van Duin, A. C. T.; Ganesh, P., Development of a Reaxff Potential for Carbon Condensed Phases and Its Application to the Thermal Fragmentation of a Large Fullerene. *J Phys Chem A* **2015**, *119*, 571-580.

CHAPTER 2: METAL-CATALYST-FREE ACCESS TO MULTIWALL CARBON NANOTUBES/SILICA NANOCOMPOSITES (MWCNT/SIO$_2$) FROM A SINGLE-SOURCE PRECURSOR

Motivation and scope

Multiwall Carbon Nanotubes (MWCNT)[1] is a desirable target of synthesis, especially the nanotubes with exotic morphologies[2]. Synthesis of those often utilizes 3d metals like Fe or Co[3].

This research suggests a different approach to the MWCNT synthesis that is free from heavy metals and utilizes a single molecular precursor: a product of sol-gel condensation of tetrametoxysilane (TMOS) with the 4,4'-Dyihydroxybiphenyl. The resulting amorphous silicon oxycarbide ceramic was subjected to the thorough investigations.

From the computational side we attempted to look at the a-SiCO structure formation at three different size scales and three different approaches:

- 100-atom models with nanometer dimensions via DFT[4]
- Up to million atom models with tens of nanometers sizes via Tersoff[5] empirical potential
- Tens of thousands of atoms and several nanometer scale, "realistic" annealing simulations with ReaxFF[6]

We show that carbon segregates in graphite sheets in small SiCO ab initio melt-quench generated models and as a result of simulated annealing and repeat it within ReaxFF. We show tubular structures formation at larger scale with both Tersoff potential and ReaxFF. We perform "realistic" annealing simulations of idealized polymer precursor model and see the experimentally observed segregation of silica and the beginning of formation of tubular carbon structures.

References

1. Iijima, S., Helical Microtubules of Graphitic Carbon. *Nature* **1991**, *354*, 56-58.
2. Nath, M.; Satishkumar, B. C.; Govindaraj, A.; Vinod, C. P.; Rao, C. N. R., Production of Bundles of Aligned Carbon and Carbon-Nitrogen Nanotubes by the Pyrolysis of Precursors on Silica-Supported Iron and Cobalt Catalysts. *Chem Phys Lett* **2000**, *322*, 333-340.
3. Rummeli, M. H., et al., Investigating the Outskirts of Fe and Co Catalyst Particles in Alumina-Supported Catalytic Cvd Carbon Nanotube Growth. *Acs Nano* **2010**, *4*, 1146-1152.
4. Hohenberg, P.; Kohn, W., Inhomogeneous Electron Gas. *Phys Rev B* **1964**, *136*, B864-+.
5. Tersoff, J., Empirical Interatomic Potential for Silicon with Improved Elastic Properties. *Phys Rev B* **1988**, *38*, 9902-9905.
6. van Duin, A. C. T.; Dasgupta, S.; Lorant, F.; Goddard, W. A., Reaxff: A Reactive Force Field for Hydrocarbons. *J Phys Chem A* **2001**, *105*, 9396-9409.

Metal-Catalyst-Free Access to Multiwall Carbon Nanotubes/Silica Nanocomposites ($MWCNT/SiO_2$) from a Single-Source Precursor

Gabriela Mera,[§]* Peter Kroll,[#]* Ilia Ponomarev,[#] Jiewei Chen,[$] Koji Morita,[&] Moritz Liesegang,[§] Emanuel Ionescu,[§] Alexandra Navrotsky[$]

[§] Technische Universität Darmstadt, Institut für Materialwissenschaft, Otto-Berndt-Str. 3, D-64287 Darmstadt, Germany

[#] The University of Texas at Arlington, Department of Chemistry and Biochemistry, 700 Planetarium Place, Arlington, TX 76019, USA

[&] National Institute for Materials Science, Materials Engineering Laboratory, Tsukuba, Ibaraki, Japan

[$] University of California at Davis, Peter A. Rock Thermochemistry Laboratory and NEAT ORU, Davis, CA 95616, USA

Abstract

The present study introduces a facile single-source precursor preparative access to bamboo-like multiwalled carbon nanotubes (MWCNTs) highly dispersed within a mesoporous silica matrix. The metal-free single-source precursor was synthesized via a one-pot sol-gel process using tetramethyl orthosilicate (TMOS) and 4,4′-dihydroxybiphenyl (DHBP) and converted subsequently via pyrolysis in argon atmosphere into MWCNT/silica nanocomposites. The in-situ segregation of the highly defective bamboo-like MWCNTs was carefully investigated and has been shown to occur within the mesopores of the silica matrix at relatively low temperatures and without the use of a metal catalyst. The experimental results have been supported by extensive computational simulations, which correlate the molecular architecture of the single-source precursor with the structural features of the carbon phase segregating from the silica matrix. Furthermore, the role of hydrogen on the stability of the prepared nanocomposites as well as on the high-temperature evolution and morphology of the segregated MWCNTs has been discussed based on vibrational spectroscopy, calorimetric studies and empirical potential calculations. The results attained within the present study

may allow for designing highly-defined CNT-containing nanocomposites with tailored structural features and property profiles.

1. Introduction

Carbon nanotubes (CNTs) as important one-dimensional nanomaterials with outstanding electrical, thermal and mechanical properties, have a great potential for various applications in electronics, energy, composites, drug delivery, nanoimaging etc. Since the Iijima's report in 1991 on the synthesis of multiwall carbon nanotubes (MWCNTs) [1], various methods have been explored in order to access this type of 1D nanocarbon. Significant scientific interest was focused especially on CNTs exhibiting exotic structures such as bamboo and fish-bone morphologies [2-4]. Bamboo-like MWCNTs, firstly reported by Saito and Yoshika Yoshikawa,[5] consist of graphene shells with a "stacked cone" morphology and consequently possess significantly higher concentrations of structural defects as compared to hollow MWCNTs. These defects are formed due to the incorporation of heteroatoms in the graphene shells. Since the mechanical and electronic properties of CNTs strongly depend on their chirality, diameter, defect structure, etc., such nanotubes have entered the spotlight of nano-science [6]. Having a structure composed of separated hollow compartments and bamboo knots, bamboo-like nanotubes found applications in several fields, such as sensors, adsorbents, catalysts, hydrogen-storage, lithium-ion battery electrodes materials and silicon-based technology [7].

Typically, CNTs are produced *via* vapor-liquid-solid (VLS) processes catalyzed by 3d valence transition metals (Fe, Co and Ni), noble metals such as Au, Ag and Cu, as well as main group metals such as Pb and In [8-16]. Unfortunately, the catalysts remain in the CNTs as undesired impurities after synthesis. The catalyst poisoning, as reported in several publications [17, 18], constitutes the major drawback of this route due to the ability of the metals to decompose hydrocarbons and to induce the post-rearrangements of the

CNTs. The catalysts can be removed post-synthesis through aggressive chemical treatments, however the purification usually does not fully eliminate metal particles and introduces defects into the carbon nanotubes.

Recently, non-metallic catalysts for the synthesis of nanotubes such as SiC [19], Ge [20], MgO [21], Al_2O_3 [22], ZrO_2 [23], magnesium borates [24, 25] as well as SiO_2 [26-29] were reported. Templated CNT can be grown in porous alumina without catalyst particles, as published by Schneider et al. [30]. Especially oxides were demonstrated to be capable of graphitizing carbon [31].

Metal-free carbon nanotubes are desirable materials for wide potential applications [32]. The use of SiO_2 as a catalytically active species is particularly attractive for integration into Si based technology and its use as a carbon nanotube catalyst has been reported by various groups.[26-28, 33] A key question regarding the use of SiO_2 as a graphitization catalyst relates to the possible transient generation of SiC forms during the process [29, 34].

Herein we are reporting for the first time on the catalyst-free *in situ* generation of MWCNTs within a silica-rich matrix during the thermal decomposition of a carbon-rich polysiloxane. Typically, preceramic polysiloxanes and polysilsesquioxanes may be used as suitable precursors for silicon oxycarbides.[35-39] Depending on their substitution pattern, the preceramic polymers may deliver so-called carbon-rich polymer-derived silicon oxycarbides (i.e., ceramics containing more than 20 wt % excess carbon, also denoted as *free carbon*),[40] which represent a special class of unique materials with the free carbon phase conferring a multitude of interesting functional properties like electro-optical, magnetic, sensorics, Li-ion permeability and storage as well as high adsorption/desorption for several gases. [35-39] The *free carbon* in silicon oxycarbides not only makes these materials “smart” but also strongly influences their thermal stability against crystallization and decomposition, their ceramic yield as well as the sizes of composing nanodomains. Thus, they possess a much higher stability against crystallization than their low-carbon containing analogues.

Amorphous silicon oxycarbide polymer-derived ceramics (PDCs), synthesized from polysiloxanes, contain carbon and silica -rich nanodomains, the latter with extensive substitution of carbon for oxygen, linking Si-centered SiO_xC_{4-x} tetrahedra.[36, 38] Calorimetric studies demonstrated these PDCs to be thermodynamically more stable than a mixture of SiO_2, C, and SiC.[37] Nevertheless, the thermodynamic stability of these materials depends on a high extent on the microstructural features of *free* carbon phase, as well as on the presence and concentration of hydrogen in their composition.[37]

Many characterization methods have several restrictions with respect to the investigation of amorphous ceramic systems. The rearrangement reactions of carbon phase as function of temperature, is a very complex process. Therefore, a significant emphasis was placed on computational methods to elucidate the structure of as well to understand the organization of *free* carbon during thermal decomposition process. Modeling and simulations of amorphous materials thus can greatly enhance the experimental resolution and provide new insights into the structure of disordered materials.

2. Experimental Section

2.1 Synthetic Procedure.

All chemicals were obtained from Sigma Aldrich and used as-received. 4,4′-Dihydroxybiphenyl (DHBP) 97 %, tetramethyl orthosilicate (TMOS), methanol and ethanol were provided from Sigma-Aldrich and used as received. The biphenyl-containing single-source precursor was prepared using 0.1 wt % of DHBP with respect to TMOS. The sol was prepared upon adding ethanol and TMOS to a dispersion of DHBP in water. The gelation process was performed at 60 °C and the as obtained wet gel was placed into a drying cabinet at 60 °C and allowed to age for 5 days. The resulting xerogel

(DHBP0.1_SG) was first dried under vacuum, at room temperature. Same procedure was used in order to prepare a standard silica sample, using TMOS, water and ethanol. Subsequent pyrolysis process was conducted at 900 °C under argon atmosphere (100°C/h heating rate, 2 h dwelling time) (Samples name: DHBP0.1_P, Silica). The pyrolyzed powder was hot-pressed in graphite dies into a monolith (labeled DHBP0.1_HP) (KCE hot press HP W 150/200, argon atmosphere, 30 MPa, T = 1600 °C). In order to avoid carbon diffusion into the sample from the graphite dies, its walls were covered with boron nitride.

2.2 Characterization

FTIR spectroscopy was performed on a Bruker Vertex 70/70v spectrometer.

Micro-Raman spectra were recorded using a Horiba HR800 micro-Raman spectrometer (Horiba Jobin Yvon, Bensheim, Germany) equipped with an Ar+(514.5 nm) laser. The excitation line has its own interference filter (to filter out the plasma emission) and a Raman notch filter (for laser light rejection). The measurements were performed with a grating of 600 g mm^{-1} and a confocal microscope (magnification 100x, NA 0.5) with a 100 μm aperture. The laser power (ca. 20 mW) on the sample was attenuated in the range of 2 mW–20 μW using neutral density (ND) filters. The minimum achievable laser spot diameter is approx. 0.69 µm. The laser spot size is primarily defined by the laser wavelength and microscope objective being used. The minimum achievable spot size is diffraction limited, according to the laws of physics and optics: *laser spot diameter* = 1.22 λ / NA, where λ is the wavelength of the laser, and NA is the numerical aperture of the microscope objective being used (in this case 0.90/100x). Thus, the theoretical diffraction limited spatial resolution which is achievable using an optical microscope is defined as *spatial resolution* = 0.61 λ / NA, being in this case 0.348 µm. Nevertheless, this value is strongly influenced by the scattering of the laser/ Raman photons and interaction with interfaces in the sample, issue which can reduce this resolution. Two different holographic notch filters were used for the pyrolyzed samples, compared to the hot-pressed ceramic. The pyrolyzed ceramics were re-measured with a novel 514.5 nm laser which takes advantages of the Ultra-Low Frequency (ULF) module, giving access to ultralow frequency down to 5 cm^{-1} on the LabRAM HR spectrometer. The hot-pressed sample was characterized with the old-setup having an edge of notch filter at about 170 cm^{-1}.

X-Ray Diffraction measurements were performed on a Bruker D8 Advance Diffractometer (Bruker, USA) and on a Seifert PTS 3003 diffractometer for powders and monoliths, respectively.

The electrical properties of the samples were assessed using four-point resistance measurements (Keithley 2400 devices).

The silicon, carbon, oxygen and hydrogen contents were determined at Mikroanalytisches Labor Pascher (Remagen, Bendorf-Germany).

N_2 adsorption was performed at −196 °C using an Autosorb-3B (Quantachrome Instruments, USA). The samples were preheated at 150 °C for 24 h under vacuum before the measurements.

Transmission electron microscopy (TEM) of the powder ceramics was performed using an JEOL-2010F instrument (JEOL Ltd., Tokyo, Japan) operating at an acceleration voltage of 200 kV (wavelength λ=2.51 pm). For the TEM sample preparation, the ceramic powders were dispersed in an ultrasonic bath (high purity methanol 99.5 %, Wako Chem. Ltd. Japan) and a small droplet of the suspension was placed on holey carbon (Cu) grit. The chemical analysis was performed using scanning transmission electron microscopy (STEM) and a nano-probe X-ray energy dispersive spectrometer (EDS) with a probe size of 1.5 nm.

2.3 Calorimetry

The enthalpy of formation of DHBP0.1_P was measured using high temperature oxidative molten salt solution calorimetry. A sample (~ 1 – 2 mg) was pressed into a pellet and dropped into molten sodium molybdate ($3Na_2O$•$4MoO_3$) solvent at 800 °C in an AlexSYS Setaram microcalorimeter. Oxygen gas ~ 5 mL/min was constantly bubbled through the solvent in order to warrant full oxidation and also to stir the melt. The gaseous byproducts were flushed out of the system with an oxygen flow of ~ 40 mL/min. Statistically reliable data (within two standard error) were obtained by dropping at least eight pellets. The calorimeter was calibrated against the heat content of platinum. This methodology has been used in our previous reports on similar materials[41] and is well established[42-44].

2.4 Modeling

For modeling of polymer-derived silicon oxide ceramics we apply three different methods of atomistic simulations, each acting on its own length scale. The smallest length scale is addressed by Density Functional Theory (DFT) calculations, including ab initio Molecular Dynamic (aiMD) simulations. Using aiMD simulations we generate and investigate SiOC models on a length scale between 1 and 2 nm, comprising 100-400 atoms. We also optimize larger models (up to 3 nm lengths scale; ~3000 atoms) generated by other methods (see below) to compute their energy and structural characteristics.

Models at length scales above 6 nm and up to 20 nm are created via Monte-Carlo (MC) and Molecular Dynamic (MD) simulations using an empirical potential (Tersoff). While the empirical potential lacks the accuracy of DFT calculations and may not describe all configurations with equal fidelity, it allows to model significantly larger systems and to gain valuable insight.

To bridge the gap between accurate DFT calculations and empirical potential simulations we have recently developed a new reactive force-field (ReaxFF).[45]

Parameters for the reactive force-field have been carefully fitted to thermodynamic data including a library of DFT data of amorphous SiOC(:H) structures and properties. The new ReaxFF parameter set yields correspondence between ReaxFF and DFT simulations at small length scales. With its significantly lower computational demand in comparison to the electronic structure method, however, ReaxFF simulations can extend to larger length scales ultimately meeting the empirical potential simulations. The three atomistic simulation techniques together provide a multi-scale approach that corroborates the experimental data.

DFT Calculations

The simulations within Density Functional Theory[46] use the Vienna Ab Initio Simulation (VASP) package[47, 48]. We use the Projector Augmented Wave (PAW) method[49, 50] and approximate electron exchange and correlation by the Perdew-Burke-Ernzerhoff (PBE) generalized gradient approximation (GGA). All simulations include a van-der-Waals correction.[51] We sample the Brillouin zone at the Γ-point.

We generate amorphous models of SiOC via ab initio molecular dynamics (aiMD) simulations with a "melt-quench" approach (aiMD-mq). Efficient model generation uses a "softer" version of carbon and oxygen pseudopotential, a time-step $\Delta t=1.0$ fs, and a cutoff of 283 eV at this stage. The temperature of the system is adjusted by velocity scaling, and the volume is kept constant. We start the aiMD-mq simulation at 5000 K and use cooling rates of 12.5 to 100 K/ps until we reach T=1500K. Below 1500 K we use a cooling rate of 100 K/ps throughout. The last configuration of the trajectory (at 0 K) is optimized using "standard" pseudopotentials and a cutoff of 500 eV for the expansion of the wave function into the plane-wave basis set. Atomic positions and cell parameters relax to adjust to a local energy minimum state. Forces are converged to $5\cdot10^{-2}$ eV/Å and stresses to lower than 2 kbar.

Annealing of DHBP0.1_SG started with a model shown in Figure 10b. We then heated the system in steps of 400 K to 3000 K, holding the system for 10 ps at every step. At 3000K we let the system evolve for another 100 ps.

Empirical Calculations

For empirical potential simulations of SiCO we use the Tersoff potential. [52-54] The hetero-atomic interaction parameters χ_{ij} and ω_{ij} are used to modify attractive interactions C–Si and C–O. Since neither DFT nor ReaxFF simulations yield meaningful fractions of C-O bonds, we use only repulsive interactions between C and O ($\omega_{C\text{-}O} = 0$). General features of models – appearance of layered graphene and tubular, clustered carbon structures – are independent on whether attractive Si–C interactions are included not. Setting $\omega_{C\text{-}Si} = 0$ only enhances clarity and is used for simulations shown in Figures 11 and 12. All structure simulations are performed using a Monte-Carlo method, introducing a random-walk between configurations. A new configuration is generated by displacing an atom (chosen at random) and its energy is computed. To decide whether a new configuration is accepted or not the energy difference ΔE between old and new configuration enters the Boltzmann factor $\exp(\Delta E/k_B \cdot T_{MC})$, ($k_B$ is the Boltzmann constant, T_{MC} the Monte-Carlo temperature) which is then compared to random number. In a model comprising N atoms, N such successful configuration changes equal one (1) Monte-Carlo sweep (MCS). The distance for displacing atoms is adjusted at intervals to have a "success rate" of 10-20% for individual moves, but is limited between 0.1 and 50 pm. Starting with $T_{MC} = 0$, we increase T_{MC} to a maximum value within $5 \cdot 10^4$ MCS. We remain at the maximum T_{MC} for $1 \cdot 10^5$ MCS, and gradually decrease T_{MC} thereafter until it reaches zero. Choosing maximum values of T_{MC} of 0.3, 0.4, 0.5, and 0.6 the typical total length of a simulation is about $1.6 \cdot 10^6$ MCS. Structures depend somewhat on the length of annealing, but differences in final structures don't appear significant. Hence, the key parameter for developing a structure is the maximum value of T_{MC}.

ReaxFF modeling

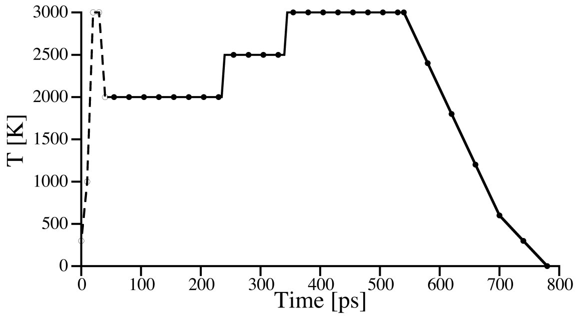

Figure 1. Time vs. temperature scheme of annealing the polymer (Fig.2) model of composition $SiC_{12}O_3H_8$ model comprising 12288 atoms. Dashed line – NVT ensemble, time step 0.1 fs; solid line – NPT ensemble, time step 0.2 fs. At the moments of time marked with points we removed gaseous molecules H_2, CO, CO_2, H_2O, O_2, CH_2O, C_2H_2, C_2H_4.

For molecular dynamics (MD) simulations within ReaxFF we use LAMMPS software[55] and reax/c user's package[56]. We used Bussi-Donadio-Parrinello thermostat[57] for temperature control. Time steps in our simulations vary from 0.1 fs to 1.0 fs depending on the hydrogen content of the simulated system. Parameters for the ReaxFF simulations have recently been published. [45] Melt-quench simulations of structures follow a standard approach, similar to the aiMD-MQ modeling described above. With ReaxFF we use cooling rates between 1 K/ps and 100 K/ps. Annealing a polymer follows a different approach. The time-temperature profile for polymer-to-ceramic simulations is displayed in Figure 1. We first heat models of composition $SiC_{12}O_3H_8$ comprising 12288 atoms to 3000K to initiate reactions. Subsequently we anneal systems at 2000K for 200ps, followed by heating at 2500 and 300K for 100 and 200 ps, respectively, before cooling it to 0K. Every 25 ps in course of simulations, we remove persistent gas molecules (H_2, CO, CO_2, H_2O, O_2, CH_2O, C_2H_2, C_2H_4) from the system.

3. Results and discussion

Polymer-derived silicon oxycarbide (SiOC) ceramics are materials which can be obtained by the thermal treatment of polysiloxanes in inert atmosphere [38]. Even if SiOC PDCs are X-ray amorphous materials, they are exhibiting unique structural features such as reduced mass fractal dimension and nano-heterogeneity (mass fractal dimension of 2.4-2.5 and nanodomains of 1-3 nm in size), which significantly affect and/or dictate their properties and behavior. The short-range structure of the silicon oxycarbide glass is composed of a network of corner-shared silicon-centered tetrahedra incorporating both Si–C and Si–O but no C–O bonds (SiO_xC_{4-x} tetrahedra). The network is distinct from a mixture of separate, intergrown silicon carbide and silicon oxide nanophases and exhibits the full range of *mixed bonded* SiO_xC_{4-x}tetrahedra (i.e., SiO_4, SiO_3C, SiO_2C_2, $SiOC_3$, and SiC_4). A different microstructural organization was reported for the silicon oxycarbide ceramics synthesized under CO_2 flow (Figure 2a) [58-60]. In this case, no mixed SiO_xC_{4-x} units were found, their structure being composed exclusively of SiO_2 and free C nanodomains.

The aim of the present study was to produce novel amorphous silicon oxycarbide ceramics with non-mixed bonds by simple thermal decomposition of polysiloxanes in inert atmosphere. In order to achieve that, the molecular structure of the precursor was designed in such a way in order to comprise exclusively Si-O bondings. The carbon-containing groups should be bonded to silicon through C-O-Si bridges (i.e., no Si-C direct bondings) (Figure 2). This approach can assess the design of microstructures with controlled carbon phases in a porous silica matrix.

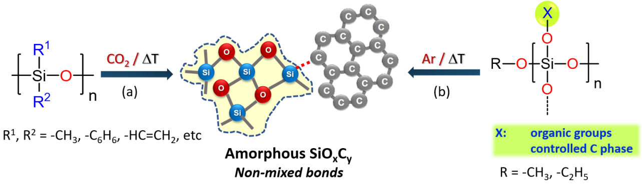

Figure 2. Synthesis approach toward non-mixed bonded SiO_xC_y ceramics (i.e., C/SiO_2 nanocomposites) via pyrolysis of polysiloxanes in CO_2 atmosphere [59] (a) or via thermal decomposition of orthosilicate-based sol-gel systems containing large, aromatic organic

substituents (b). The difference of the novel approach (b) consists in using precursors containing no Si-C bonding in the structure, silicon being bonded only to oxygen.

The synthesis of the single-source precursors was accomplished via a one-pot sol-gel process using tetramethyl orthosilicate (TMOS), 4,4′-dihydroxybiphenyl (DHBP) and ethanol as co-solvent (Figure 3). The white xerogel obtained after hydrolysis and condensation of the mixture in the presence of water was pyrolyzed at 900 °C in argon atmosphere to deliver amorphous Si-O-C powders which were subsequently hot pressed at 1600 °C and 30 MPa in Argon to produce dense monolithic specimens.

Figure 3. Sol-gel synthesis of orthosilicate-based single-source precursors containing large, aromatic substituents (a); their ceramization at 900°C and hot pressing at 1600°C in Ar atmosphere to produce monolithic ceramic samples (b).

X-Ray Diffraction.

The ceramic samples obtained via pyrolysis at 900 °C are X-ray amorphous (Figure 4). The amorphous halo at 2-theta values of ~22-25° corresponds to an overlapping of amorphous silica and carbon. Surprisingly, even after the hot-pressing step at 1600 °C, the ceramic nanocomposite presents only amorphous halos in XRD, corresponding to nanosilica and nanocarbon. Rather unusual for SiOC PDCs, no carbothermal reaction ($SiO_2 + C \rightarrow ß\text{-}SiC + 2\ CO$) was registered.

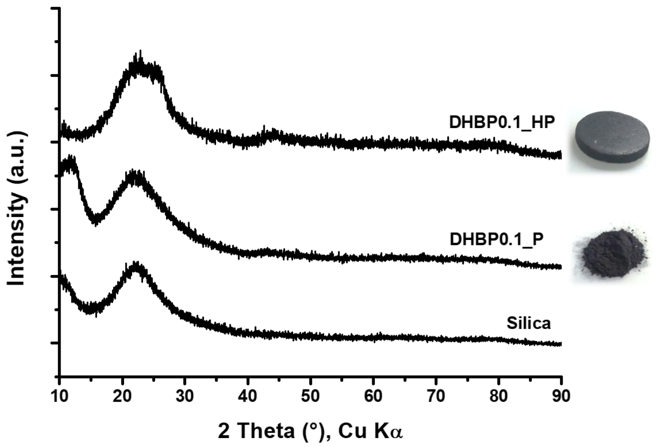

Figure 4. X-ray diffraction of the powder sample synthesized at 900 °C (DHBP0.1_P), of the ceramic pellet produced at 1600 °C (DHBP0.1_HP) as compared to silica obtained at 900 °C.

High-resolution TEM microscopy (HRTEM) is a powerful method in order to locally investigate the nanostructure of polymer-derived ceramics, especially with respect to the nature and organization of nanocarbon phase. Even if the PDCs are X-ray amorphous at low temperatures (T< 1400 °C), they are typically heterogeneous at the nanoscale, by various TEM studies[37, 61, 62].

No major contrast variation was observed for the sample annealed at 900 °C, indicating its amorphous nature. This information is underlined also by the SAED inset in figure 5a showing a diffuse elastically scattered ring pattern, typical for amorphous samples. High resolution TEM micrograph (Figure 5b) reveals the mesoporous nature of the sample with pores of ~6-10 nm in size. The mesopores are embedded in an amorphous matrix consisting of round silica nanoparticles of 5-7 nm in size. Surprisingly, as shown in figure 5c, the free carbon phase is represented by long and short multiwall carbon nanotubes (MWCNTs) (length > 300 nm) as well as a minor phase of bean-like graphene nanocages (100 nm long and ~30 nm broad).

The presence of short defective bamboo-like MWCNTs (~6 walls) is observed in Figure 5d. The external wall of the tube seems to contain several point-like defects and/or functional groups on the surface. The inner chambers of the bamboo-like tube are separated by two graphene walls. The curvature of the compartment layers is directed to the tip.

The measured length of CNTs is in between 80 nm to 300 nm or more. Representative micrographs of long MWCNTs are displayed in figure 5e and f. The defective structure of MWCNTs can be clearly identified by the difference in the inner and outer diameter along the tube, and coexistence of scrolls within the tubes. The external defective wall of the tubes and the scroll structure underline the presence of functional groups at its surface and on edges of scroll.[63, 64] The slip plane defects are also visible. At higher magnification (FFT image - inset figure 5f), there is an indication of crystalline graphitic phase due to the stacking of the walls. The electronic properties of CNTs can be affected by the variation of interwall spacing. In this study, an interlayer/intershell distance of 0.31 to 0.325 nm was observed. The interwall spacing strongly depends on the inner diameter of the tubes. The inner diameter of CNTs from 2.5 to maximum 8.7nm was detected. The outer diameter CNTs was in the range of 9.5 to 16.8 nm. The irregular layer spacing as consequence of the presence of scrolls within a single MWCNT, provides an information about the formation mechanism of the tubes from graphene layers to scrolls and then to nanotubes through progression of defects.[64] MWCNTs have closed and empty tips. Thus, a base growth mechanism of bamboo-like MWCNTs within the pores of the matrix is proposed.

The minor phase consisting of graphene nanocages is explained by the bending of graphene sheets as effort to eliminate the highly energetic dangling bonds present at the edges of this structure.[65]

Bright field STEM (BF-STEM, Figure 6a) was used to assess the distribution of the elements. The composition of the sample, as measured by EDX under bright field STEM, is displayed as inset in figure 6a. As shown in figure 6b-d, the composing elements O, C and Si are homogeneous distributed in the ceramic sample. Based on this measurement, we can assume that 1D nanocarbon is embedded in the silica rich matrix and, as demonstrated for most of the PDCs sample, carbon should be located in the pores of the matrix material. Looking to the outer diameter of the MWCNTs measured at the edges of the samples (d~9.5-16.8 nm), it is reasonable to assume that the average pore size of this material should be in the same range size as the diameter of MWCNTs. No other elements were identified in this material, especially the presence of any metal which can catalyze the formation of CNTs can be ruled out. Moreover, no SiC phase was found. It seems that silica phase plays the role of "catalyst" for the formation of tubes and cages and its porous nature is crucial as template for the elongation of the tubes in the matrix.

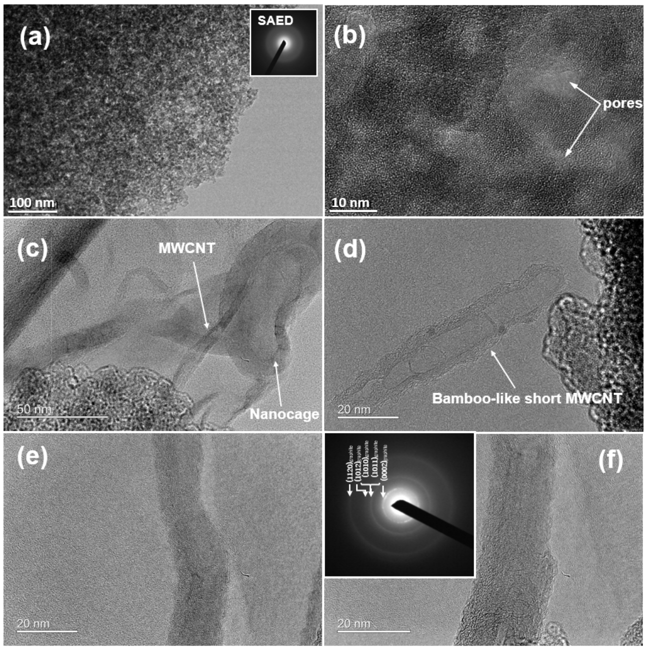

Figure 5. Transmission electron microscopy of DHBP0.1_P revealing a) and b) the microporous structure, c) the presence of long defective MWCNTs as well as bean-like carbon nanocages; d) short bamboo-like carbon nanotubes; e) and f) defective long bamboo-like MWCNTs where scrolls coexist within a tube.

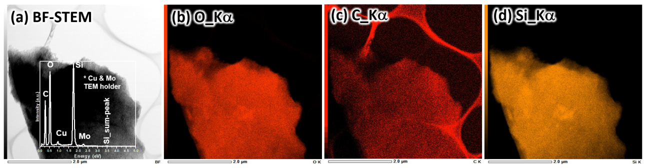

Figure 6. a) Bright field scanning electron microscopy (BF-STEM) of DHBP0.1_P. Inset of EDX measured under BF-STEM. Element mapping of O_Kα (b), C_Kα (c) and Si_Kα (d) under STEM.

Remarkably, the sample DHBP0.1_P represents the first polymer-derived ceramic with a free-carbon phase consisting on bamboo-like multiwall carbon nanotubes, as well as few exotic bean-like graphene nanocages. For this sample, elemental analysis was performed (Table 1). The ceramic contains a relatively low content of carbon and it is rich in silicon and oxygen, in a 1:2 ratio. As shown by the phase composition, the sample can be described as a SiO_2/C nanocomposite.

Table 1. Elemental analysis, empirical formula as well as phase composition of the ceramics sample DH

Sample name	C [wt%]	Si [wt%]	O [wt%]	H [wt%]	Empirical Formula
DHBP0.1_P	11.43	41.12	46.75	0.70	$Si_1C_{0.65}O_{1.99}H_{0.48}$

Fourier-Transform Infrared Spectroscopy (FTIR) is an important integral method for the characterization of the bonding situation and respectively, the microstructure of the polymers and ceramics. Figure 7a presents the FTIR analysis of the single source precursor as well as the ceramic powder synthesized at 900 °C.

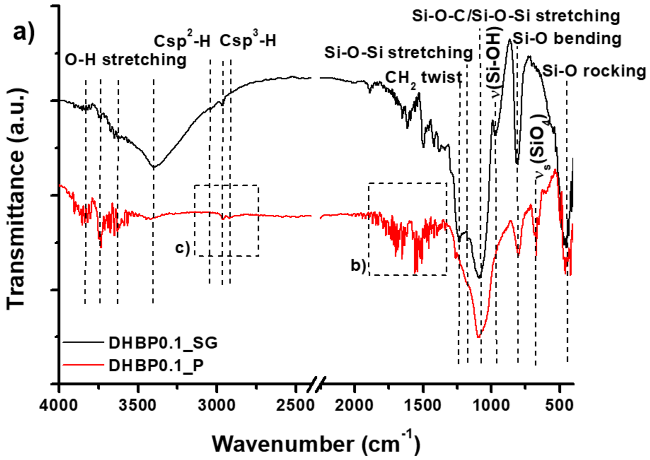

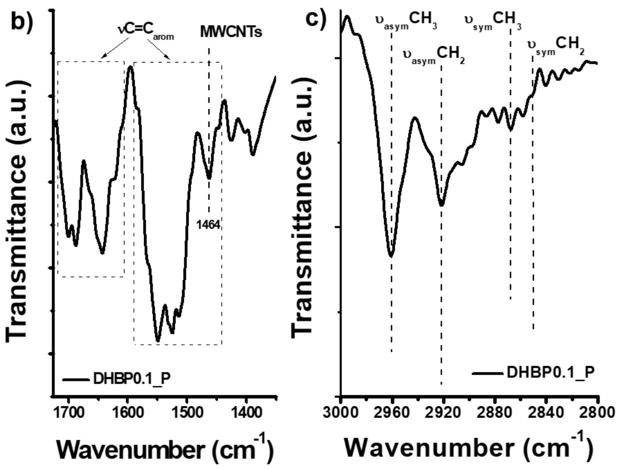

Figure 7. a) FTIR spectrum of single source precursor DHBP0.1_SG as compared to DHBP0.1_P prepared via pyrolysis at 900 °C. b) The region corresponding to conjugated C=C vibration bands of free carbon phase in DHBP0.1_P; c) The presence of -CH_2- and -CH_3 vibration modes in DHBP0.1_P. Please note the absence of any Csp^2-H bonds in ceramic.

FTIR spectroscopy is usually used to probe the atomic-scale structure of silica species in glasses as well as of silicon oxycarbide ceramics, giving a direct hint to the state of the silica framework and possible bonding with *free* carbon phase. Absorption bands in the range of wave numbers of 467 to 486 cm^{-1}, 800 to 812 cm^{-1}, and 1095 to 1175 cm^{-1} were assigned to tetrahedral SiO_4 units, symmetrical Si-O-Si, and asymmetrical Si-O-Si vibration, respectively. Particularly, the asymmetrical Si-O-Si valence vibration shifts significantly to lower values with a raising number of the framework defects. The most intensive absorption band at 1095 cm^{-1} is also related to Si-O-C stretching vibration and indicates the covalent bonding between silica phase and free carbon phase at the interface between nanodomains. Si-O-Si valence vibration depends also on the different bond length and angle in $Si(OSi)_4$, $Si(OSi)_3(OH)$ or $Si-(OSi)_2(OH)_2$ tetrahedra.

The ceramic sample prepared via pyrolysis at 900 °C contains Si-OH groups and also seems to adsorb a significant amount of water on its surface, as indicated by the presence of absorption bands at 3365-3850, 970 and 467 cm^{-1}, corresponding to ν(OH/H_2O) and γ(OH) respectively. This behavior can indicate a high surface area as well as high porosity for this ceramic material. The shoulder at ~970 cm^{-1} corresponds to the stretching vibration of Si-OH bonds. There are also three other important contribution of Si-OH groups in the IR spectrum of the pyrolyzed sample, namely at 3400 cm^{-1} (symmetric feature), 3650 cm^{-1} (asymmetric feature) as well as at 3850 cm^{-1} (symmetric feature). Depending on the local environment of Si-OH groups in silica, these bands can be assigned to near-neighbor Si-OH groups with strong H-bonding interactions, to Si-OH groups that are only partially shielded from other similar neighboring groups and with very weak interaction between the H atom of Si-OH and O atoms of Si-O-Si network and to Si-OH groups isolated from other, e.g. OH on the surface of the material, respectively.

The presence of sp^{3}C -H corresponding bands and the absence of sp^{2}C-H vibration modes is rather unusual for a ceramic synthesized at 900 °C. Normally, hydrogen is bonded to sp^{2}C and it was found up to very high temperatures (T~1600 °C) in polymer-derived ceramics. In our case, exclusively sp^{3}C is bounded to hydrogen and it should compose the external highly defective wall of CNTs as well as the edges of graphene scrolls observed in HRTEM (Figure 5e and f). As shown in Figure 7c, the symmetric and asymmetric stretching vibrations of -CH$_2$- and -CH$_3$ bands can be found in the wavenumber range 2840-2960 cm^{-1}. The presence of (sp^3) CH$_2$ twisting mode is also observed at 1260 cm^{-1}. As reported few years ago,[66] the folding of multilayer graphene to form graphene nanocages is also related to its hydrogenation of round corners. The sp^3 hybridization of carbon bonds and the resultant geometry as well as the van der Waals forces between graphene layer and sp^{3}C-H bonds act together as driving force to tackle the energy barrier of folding process.[66]

While Raman spectroscopy is the established method for the identification of free carbon in ceramics, few FTIR studies were reported due to the poor infrared transmittance of graphene-like carbons. The reported IR-active modes of graphite are at 868 (out-of-plane vibration mode) and 1590 cm^{-1} (in-plane vibration mode). Phonons modes at 850 (radial mode) and 1590 cm^{-1} (tangential mode), independently on symmetries or diameter of carbon nanotubes, were reported previously for SWCNTs [67, 68]. The radial mode vanishes in the infrared spectra of DWCNTs. As reported in the literature [69], the number of IR active modes is independent of nanotube diameter. However, the location of the peaks is a sensitive function of the diameter that becomes less marked for tubes with a diameter larger than 1.57 nm. Nevertheless, ab initio calculations predict an upshift of the frequency of this mode with the diameter of the carbon nanotubes.[70]

In the present study, the free carbon phase was formed by the thermal decomposition/rearrangement of biphenyl groups; its presence is proved by several aromatic C-C stretching vibrations (see Figure 7b) between 1400 and 1700 cm^{-1}. A complex distribution of bands was only reported for MWCNTs and cannot be found in SWCNTs- or graphite-containing materials [71]. The presence of the vibration band at approximatively 1464 cm^{-1} was reported by Misra et al., as being unique for MWCNTs [72].

Micro-Raman Spectroscopy

Micro-Raman spectroscopy is a powerful tool in order to identify sp^2 hybridized carbon species. The representative features of sp^2 carbon in the Raman spectra are the so-called disorder-induced D-band at approx. 1350 cm^{-1} and the G band at approx. 1582 cm^{-1} due to in-plane bond stretching of sp^2 carbon, as well as the 2D-band (the overtone of the G-band which is always observed in defect-free samples at ~2700 cm^{-1}). Other overtones and combination bands, namely (D" + D, D + G, 2D') (Figure 8) can be identified in the Raman spectra of nanocarbons. Moreover, the D and G bands can vary in intensity, position and width, depending on the structural organization of the sample under investigation.

Two representative spectra were registered for the sample DHBP0.1_P, synthesized at 900°C (Figure 8 a and their deconvolution of the frequency range 850-1800 cm^{-1} in Figure 8b and c).

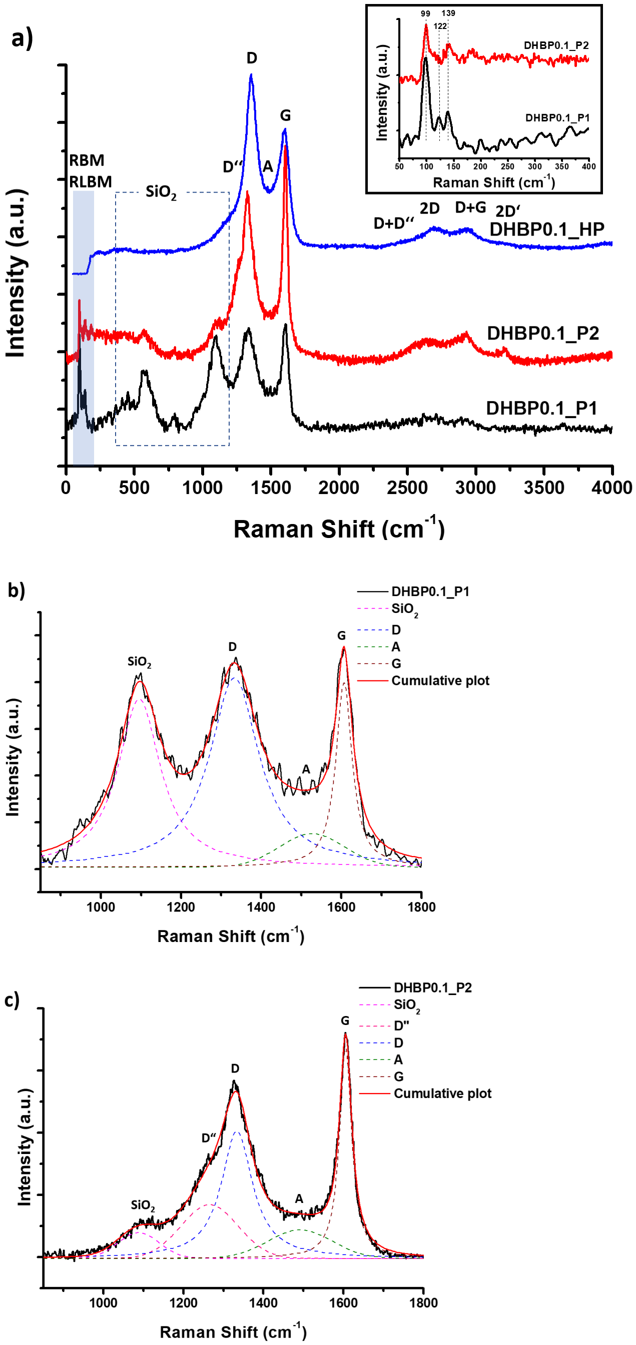

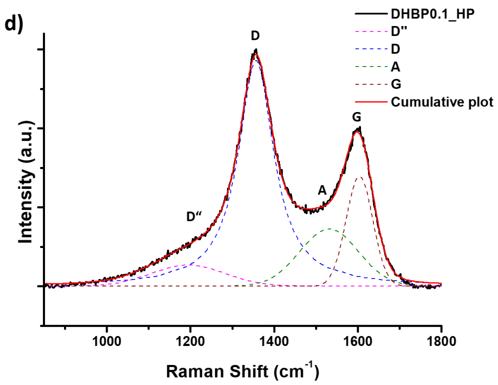

Figure 8. Micro-Raman analysis of the ceramic sample as prepared at 900 (2 distinctive profiles, DHBP0.1_P1 and DHBP0.1_P2) and 1600°C (DHBP0.1_HP). Fitting of the region 850-1800 cm^{-1} for b) DHBP0.1_P1, c) DHBP0.1_P2 and d) DHBP0.1_HP.

In the low-energy range, several bands resulting from radial-like breathing modes (RLBM) of the resonantly excited graphene scrolls reported by HRTEM analysis in Figure 5e and f, were observed. For a single wall carbon nanotube, only a single radial-breathing mode peak should be observed. The RBM frequency depends on diameter of the tubes and is typically located between 100 cm^{-1} to 400 cm^{-1} and is often considered in the literature as their fingerprint. Nevertheless, the curvature in the graphene scrolls transforms this translation into a phonon mode similar to the radial breathing mode in SWNTs. As shown in the inset of figure 8a, RLBM bands were found at 99, 122 and 139 cm^{-1} (in DHBP0.1_P) As reported in literature, the edges of graphene scrolls are playing an important role on the activation of RLBM bands.[73]

The multiwall carbon nanotubes (MWCNTs) are composed of multiple concentric graphite cylinders. Their Raman spectra depend on their crystalline arrangement given by the A_D/A_G ratio, which is commonly taken as a measure of the graphitization index and reflects the concentration of structural defects and the A_{2D}/A_D ratio which is sensitive to the overall crystalline quality of the graphitic network and increases with long-range ordering.[74]

The Raman spectrum of MWCNTs show a high A_D/A_G ratio and low A_{2D}/A_D ratio. The position of the G band in MWCNTs is somehow higher (~1605 cm^{-1}) than that of other carbonaceous materials, and this was associated to a large compressive stress affecting the C=C bonds in highly defective tube walls. Nevertheless, this apparent blue shift of the broadened G band may be explained as well by an overlap with the unresolved D' band at 1610 cm^{-1}, which is also a disorder-induced double resonance process and is often found in nano-crystalline graphite. Its overtone band, 2D', can be identified in the frequency range of 3200-3246 cm^{-1} for all samples.

The slightly disordered state indicated by the existence of both bands D'' (shoulder at ~1200 cm^{-1} attributed to the presence of sp^2–sp^3 C–C and C=C bonds) and A band (at ~1500 cm^{-1}, corresponding to the fraction of amorphous carbon contained in the samples) correlates to the presence of edges in the graphene scrolled layers, by the deviation from planarity of graphene layers, by the existence of pores, and by the presence of carbon atoms with sp^3 hybridization, as shown previously in the FTIR and HRTEM discussion.

The intensity ratio of the D and G modes, A_D/A_G, enables the evaluation of the carbon-cluster size by using the formula reported by Cançado [75] (Eq. 1)

$$L_a\ (nm) = \frac{560}{E_l^4}\left[\frac{A_D}{A_G}\right]^{-1} \qquad (1)$$

with L_a being the size of the carbon domains along the six-fold ring plane (lateral size between *line defects*) and E_L the energy of laser used in the study (2.41 eV corresponding to 514.5 nm laser wavelength). Lorentzian and gaussian curve fitting of the Raman bands was performed in order to extract the A_D/A_G intensity ratios and to determine the size of the free carbon cluster formed in the ceramics. The peak fitting was done including the minor bands D'' and A bands.

The dependence of A_D/A_G ratio on the degree of disorder in graphene-like materials was also reported [76]. The disorder was quantified as depending on *point-like defects*, precisely on the inter-defect distance, L_D, which can be calculated with the Eq. (2). Pristine graphene has $L_D \rightarrow \infty$, and fully disordered graphene has $L_D \rightarrow 0$.

$$L_D\,(nm) = \sqrt{\frac{4300}{E_L^4(eV^4)}\left[\frac{A_D}{A_G}\right]^{-1}} \qquad (2)$$

Average distance between point defects, the defect density ($\sigma = 1/L_D^2$) can be calculated. In this study, the defect density of the ceramic at 900°C, $\sigma_{900°C} = 0.02$ is compared to 1600°C where a value of $\sigma_{1600°C} = 0.03$ was calculated. A slightly higher value of defect density can be registered for the sample hot-pressed at 1600°C indicating that the applied temperature and pressure influenced the carbon structure, creating more defect states at higher temperature.

The average continuous carbon precipitate size, including tortuosity can be determined by the equation (3) as described by Larouche et al. [77]:

$$L_{eq}(nm) = 8.8\cdot\left(\frac{A_{2D}}{A_D}\right)$$

The inter-defect distances L_D, lateral cluster size L_a, the tortuosity parameter L_{eq} together with the ratio of D and G, 2D and G and are summarized in Table 2.

Table 2. Raman graphitization parameters for the samples prepared at 900 (DHBP0.1_P1 and DHNP0.1_P2) and hot-pressed at 1600°C(DHBP0.1_HP).

Sample	ω_D [cm^{-1}]	ω_G [cm^{-1}]	ω_{2D} [cm^{-1}]	A_D/A_G	A_{2D}/A_G	L_a nm	L_D nm	L_{eq} nm
DHBP0.1_P1	1335.7	1606.5	2660.8	2.95	0.64	5.63	6.57	1.90
DHBP0.1_P2	1334.0	1605.4	2646.5	1.92	0.66	8.63	8.14	3.04
DHBP0.1_HP	1356.6	1603.6	2797.2	3.99	0.63	4.16	5.65	1.38

*Where ω represents the wavenumber position of the respective Raman bands.

Complementary to FTIR, Raman spectroscopy can be used for the identification of molecular structure of silica phase in this study. As seen in figure 8a, different Raman bands corresponding to SiO_2-phase are present in DHBP0.1_P ceramic. They can be found at 1095, 795, 568 and 452 cm^{-1}. The bands at 452 and 568 cm^{-1} are attributed to the rocking and respectively bending vibration (ν_b) of Si-O-Si linkages. The band at 795 cm^{-1} have been related to the symmetric stretching vibration (ν_s) of Si-O-Si. The band with maxima at 1095 cm^{-1} is assigned to the transverse optical asymmetric stretching vibration (ν_{as}) of Si-O-Si linkage or/and Si-OC units. The broad and intensive Raman band at 1095 cm^{-1} in DHBP0.1_P1 can be attributed also to the stretching vibration of Si-O bond of SiO_4 tetrahedral units with one NBO (OH), i.e. Q^3 $SiO_3(OH)$ structural units.

To conclude, the vibrational spectroscopy studies underline the presence of defective (bamboo-like) MWCNTs observed by HRTEM. The observation of low-frequency radial breathing-like modes by Raman spectroscopy confirms that the curvature in the scroll activates new modes that are absent in folded or flat graphene. The graphene scrolls have a large concentration of saturated $-CH_3$ and $-CH_2-$ containing edges, as revealed by FTIR analysis as well as Raman spectroscopy.

Brunauer-Emmet-Teller (BET) Analysis.

The porosity and specific surface area of pyrolyzed ceramic at 900 °C as compared to silica were evaluated via nitrogen adsorption studies (Figure 9, Table 3). It has been observed that the specific surface area decreases with the incorporation of the carbon phase in DHBP0.1_P, indicating that the carbon phase is located in the pores of the matrix. This observation was previously done in several polymer-derived ceramics[37].

DHBP0.1_P is a mesoporous ceramic nanocomposite (isotherm IVa) with relatively large specific surface area, therefore suitable for a whole range of applications such as gas adsorption, gas separation and catalyst support. It can be observed that already a very low concentration of biphenyl induces a decrease in the specific surface area of the ceramic and in the average pore size. Due to it relatively high specific surface area, the ceramic can adsorb a large concentration of water in its pores, as observed by FTIR analysis for the formation of silanol units.

Table 3. Nitrogen adsorption data for DHBP0.1_P as compared with silica produced via pyrolysis at 900°C.

Sample name	Specific Surface Area [m^2/g]	Average Pore Size [nm]	Pore Volume [cm^3/g]
Silica	637	7.4	1.53
DHBP0.1_P	371	6.2	0.51

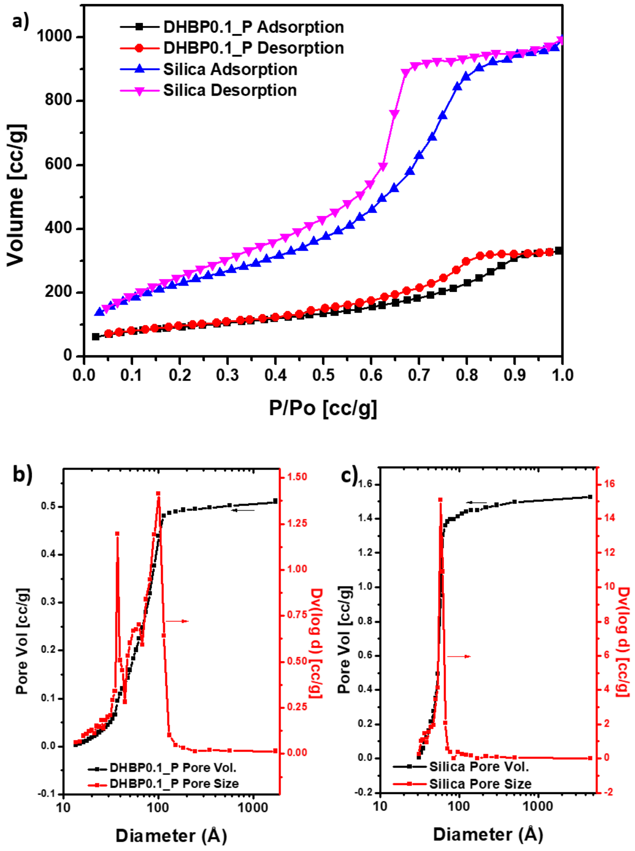

Figure 9. a) BET isotherm analysis of DHBP0.1_P as compared with silica. Pores size distribution and pore volume for b) DHBP0.1_P and b) Silica. Please note that both samples were produced by pyrolysis at 900 °C in Argon atmosphere.

The hysteresis loop scanning gives information on interconnectivity of the pores as well as on the geometry/shapes of pores. In the case of DHBP0.1_P, the curvature upon decompression is less steep than for silica sample. This hysteresis appearing in the multilayer range of physisorption isotherms is usually associated with capillary condensation in mesopore structures. N_2 isotherms of type IVa accompanied by a type H2 hysteresis loop, according to IUPAC classification, are indicating a more random distribution of pores and an interconnected pore system. Thus, a different behavior of the adsorption and desorption branch of the isotherm, in particular around p=p0 /p0=0.45 (for N2 at 77 K), leading to a forced closure of the hysteresis loop is registered. The tensile strength effect of $(p/p0)_{TSE}$ of 0.46182 was calculated for DHBP0.1_P. As shown in figure 8 b and c, the pore sizes of DHBP0.1_P are in the same range as the external diameter of DWCNTs observed by micro-Raman spectroscopy as well as MWCNTs identified by HRTEM analysis.

Electrical conductivity.

The existence of a continuous network of carbon nanotubes was proved by four-probe measurement at room temperature. Astonishing, the monolithic hot-pressed DHBP0.1_HP sample, containing only 11.43 wt % free carbon, showed a specific resistance of $4.588 \cdot 10^{-4}$ Ωm, corresponding to an electrical conductivity value of $2.179 \cdot 10^{3}$ S/m. This surprisingly high value for the electrical conductivity can be explained only by the nature of nanocarbon phase in the structure. As comparison, another amorphous SiOC ceramic with similar content of carbon but of different type of free carbon phase, namely multilayer-graphene like phase, and hot-pressed in the same way at 1600°C, displays an electrical conductivity of approximatively 10^{-2} S/m (for 13.95 wt % C)[78].

As previously indicated in this paper, the nanocarbon phase is made of multiwall carbon nanotubes and carbon nanocages. The nanotubes are growing through the pores (voids) of silica matrix, as underlined by the BET analysis as well, and form an interconnected network. As compared with reference [78], the presence of interconnected 1D nanocarbon phase can explain the great electrical conductivity of this material.

Energetics.

The pyrolyzed ceramic at 900°C was analyzed by means of high temperature oxide melt calorimetry. Through calculation by using proper thermocycles, the standard oxidation enthalpies at room temperature and standard formation enthalpies at room temperature are obtained, listed in Table 4.

Table 4. Energetics of DHBP0.1_P as compared to other SiOC ceramics reported in the literature

	Atomic Percentage (%)				$\Delta\mathbf{H}_{ds}$	$\Delta\mathbf{H}_{ox,\,25℃}$	$\Delta\mathbf{H}_{f,\,ele}$	$\Delta\mathbf{H}_{f,\,com}$
	Si	O	C	H	kJ/g-at.	kJ/g-at.	kJ/g-at.	kJ/g-at.
DHBP0.1_P	24.27	48.44	15.78	11.51	-40.58 ± 0.44	-58.13 ± 0.44	-232.65 ± 0.99	-12.60 ± 1.51
SiOC1[79]	36.4	51.3	12.3	-	-101.2 ± 7.1	-118.3 ± 7.1	-260.5 ± 7.1	-19.8 ± 7.1
	29.5	44.0	26.5	-	-143.4 ± 7.0	-159.6 ± 7.0	-212.5 ± 7.0	-7.3 ± 7.0
	27.1	37.4	35.5	-	-159.7 ± 7.2	-175.6 ± 7.2	-210.1 ± 7.2	-34.2 ± 7.2
	27.8	27.8	44.4	-	-257.0 ± 7.0	-273.0 ± 7.0	-154.1 ± 7.0	-17.8 ± 7.0
	25.9	23.8	50.3	-	-170.9 ± 7.1	-186.6 ± 7.1	-246.4 ± 7.1	-128.2 ± 7.1
SiOCH2[80]	22	32	20	26	-110.1 ± 3.10	-129.90 ± 3.10	-185.80 ± 3.60	-36.06 ± 4.31
SiOCH3[58]	34.5	52.3	8.8	4.4	-80.1 ± 3.20	-97.68 ± 3.20	-256.64 ± 3.96	-12.98 ± 5.03
	31.8	48.5	19.2	0.5	-116.5 ± 2.20	-133.02 ± 2.20	-232.12 ± 2.91	-6.31 ± 3.90
SiOCH4[41]	37.1	0.3	36.3	26.3	-458.32 ± 5.80	-479.94 ± 5.80	-37.50 ± 6.62	-9.57 ± 8.91
	25.4	19.6	22.6	32.5	-211.04 ± 2.79	-232.40 ± 2.79	-133.71 ± 3.36	-33.27 ± 4.54
	18.5	25.6	17.7	38.3	-149.95 ± 1.21	-171.52 ± 1.21	-120.92 ± 1.63	-0.47 ± 2.26
	16.4	26.1	15	42.5	-101.71 ± 1.45	-123.75 ± 1.45	-144.98 ± 1.82	-23.98 ± 2.31
	36.1	45.2	10	8.6	-94.61 ± 0.65	-113.10 ± 0.65	-266.47 ± 1.44	-53.85 ± 2.23

For comparison, the energetics of compounds with similar elemental compositions but different structures are tabulated as well. According to structural analysis discussed previously, it was found that carbon nanotubes are formed in the voids of the silica matrix, so it is reasonable to compare the energetics of this CNT-Silica composite with a mixture of amorphous silica and carbon nanotube/nanocages with similar structure (diameters, number of layers and other structural features). Table 5 presents the energetics of several carbon allotropes as well as various silica forms for reference. Considering the following reaction, the standard enthalpy of this reaction depends on the choice of silica and carbon forms.

$$0.2427\, SiO_2 + 0.1578\, C + \ 0.0576\, H_2(g) \rightarrow \ D0.1P$$

In this context, it is important to note that thermodynamic functions strongly depend on the number of carbon layers, defectiveness and presence of heteroatoms.[81] The enthalpy of formation of multi-walled CNTs strongly depends on their structure. The enthalpy of formation of multi-walled CNTs with cylindrical and conical structures is 8.60 ± 0.52 and 21.70 ± 1.32 kJ mol^{-1}, respectively[82]. There is no data available for the minor carbon nanocages phase in this ceramic, thus, the discussion will focus on CNTs. As for silica, the energetics are strongly dependent on the crystallinity and surface area. We can choose two end situations to discuss, the most and the least thermodynamic stable combination of the reactants. For the thermodynamic most stable case, that is SiO_2 as cristobalite and C as most stable CNTs, the standard enthalpy at room temperature of the reaction above is approximately -12.9 kJ/mol, which means that DHBP0.1_P is actually energetically more stable than the most stable mixture. As for the least thermodynamic stable case, the standard enthalpy at room temperature becomes even more negative, indicating that the formation of DHBP0.1_P is energetically favorable. Moreover, even we use graphite as the reactants, the standard enthalpy of the reaction above is -12.6 kJ/mol, meaning that it is still energetically favorable to form DHBP0.1_P. This tells us that there are other sources of energetic benefit from the formation of DHBP0.1_P. Looking back to the structural analysis, the strong covalent bonds at the interface between free carbon phase and amorphous silica phase can account for this energetics benefits, which is similar to the mixed bonds found in PDCs. Another possible source is the existence of sp^3 C-H bonds which is unusual after pyrolysis under 900 ºC, as well as the existence of Si-OH bonds in the structure. The sp^3C-H bonds presented at the highly defected walls of MWCNTs inside the pores of silica matrix, can saturate surface bonding and eliminate defects, such as dangling bonds. Similar to SiOCH presented in Table 4 for comparison[41], these sp^3C-H bonds can convey the system with more thermodynamic stability. However, unlike other PDC or low-k SiOCH listed in Table 4, there is a substantial amount of Si-OH bonds found in the structure of this DHBP0.1_P sample. This can be attributed to the fact that the silica matrix of this DHBP0.1_P sample contains Si-OH network units and has also a very high surface area and is likely to adsorb water into the structure. The chemisorbed water forms Si-OH bonds with the amorphous silica matrix, and this fact confers the system extra energetics benefits.

Table 5. Room temperature oxidation enthalpies and standard enthalpies of formation at room temperature of various carbon nanotubes and various silica forms

Sample	**$\Delta H_{ox,25°C}$ (kJ/mol)**	**$\Delta H_{f,25°C}$ (kJ/mol)**	**Remarks**
Graphite		0	
SWCNTs[83]	-393.52±0.05	7	
Cylindrical MWCNTs[82]	-395.42±0.50	8.6	
Herringbone MWCNTs[82]	-432.76±0.19	21.70	
SiO_2 (cristobalite)[84]		-908.4±2.1	
SiO_2 (amorphous)[85]		-895.52	Surface area: 198.08 m^2/g
SiO_2 (amorphous)[85]		-910.86	Surface area: 25.11 m^2/g

In our study, the formation of defect-rich bamboo-like MWCNTs is explained by the presence of porous silica matrix. As shown in 2009, a major breakthrough in the carbon nanotubes science was made by few reports on CH_4- or ethanol-CVD (900°C for 10 min) which have shown that silica can act as catalytically active nucleation point for SWCNTs formation [26, 27, 34]. Silica is neither able to dissolve carbon nor does catalyze the decomposition of hydrocarbons. The surprising catalytical activity of silica was explained by the mobility of Si and O atoms in the molten SiO_2 which can cause the intermediate formation of holes or defects, strongly enhancing the catalytic capacity to decompose hydrocarbons. Moreover, the curved surface of silica nanoparticles can act as template for the formation of graphitic hemispherical nanotube end cap. Therefore, the catalytic function of silica is size dependent, only small nanoparticles (diameter < 2 nm) are active as nucleation sites.

Furthermore, the high concentration of hydrogen induces the highly defective structure of the nanotubes. Same issue was observed in the case of CVD processes. In the case of CVD processes, the presence of hydrogen normally accelerates the CNTs growth and favorably produced the bamboo-like microstructures [86]. Moreover, the formation of bamboo-like microstructures was related to a fast CNT growth. The formation of well graphitized crystallized CNTs usually needs long(er) time.

The diameter of the tubes seems to depend on the pore sizes of silica matrix. As reported in 2008, CNTs can be formed also in a porous alumina matrix (40 nm pore size) by using CVD method [30]. The homogeneous distribution of elements in the matrix, as showed by EDX element mapping under STEM, indicates that the nanotubes are forming an interconnected network in the pores of entire matrix, information underlined also by the extremely high value for the electrical conductivity.

The formation of the nanotubes from a carbon-rich polysiloxane is attributed to an early phase separation of carbon-phase from the silica phase, formation of nanorings [87] followed by physical vapor elongation and self-assembly in the mesoporous silica matrix.

Our experimental studies were paralleled by computational efforts providing detailed atomistic simulations of the formation mechanism.

Density Functional Theory calculations

Models of SiO_2 and stoichiometric SiOC glass (Si_5CO_8) containing additional "free" carbon have been generated with *ab initio* molecular dynamic simulations through a variety of procedures. We either cooled or heated random arrangements of Si, C, and O to observe structure formation. Consistently we find that "free" carbon segregates into planar sheets extending throughout the unit cell. This essentially creates slab models with a carbon layer separated from a glass layer. The genesis of planar carbon structures, the quality of the glass structure, and the enthalpy of formation of the complete models generally depend on cooling or heating rates. As a caveat, we note that models with 112-152 atoms extend only 1.2 to 1.5 nm, and that periodic boundary conditions may impact structure formation. Nevertheless, the findings motivated a series of further investigations, in particular the force-field simulations described further below. In models of SiO_2 with "free" carbon we observe almost exclusively Si-O and C-C bonds only. This implies that SiO_2 and C (almost) separate. Interestingly, most models are void of C-O bonds unless an excess of O atoms is present. Eventually this yields C-O bonds at the edges of carbon segregations. Few Si-C bonds appear at the edges of carbon segregations. By inserting additional CO_2 and continuing simulations at elevated temperatures, however, the number of Si-C bonds can be depleted. Models with an excess of O, e.g. SiO_3C_2, develop CO and CO_2 until the composition SiO_2:C is reached, with only small deviations from an "ideal" SiO_2. Summarizing, the key observation from structure simulations via DFT is the development of carbon segregations ("*graphene layers*") without covalent bonds perpendicular to their surface normal.

We encounter the development of carbon segregations when annealing a model of DHBP0.1_SG (DHBP0.1_DG) as well. We built a periodic model of the polymer, see

Figure 10, and annealed this in constant pressure *ab initio* molecular dynamic simulations. No particles were removed during the simulation, so the optimized models contain some H_2, CO, but also larger hydrocarbons (C_4H_8). Prevalent, however, is the extended carbon segregation that formed by fusing bis-phenol rings together. It combines almost all carbon atoms of the model into one joint fragment.

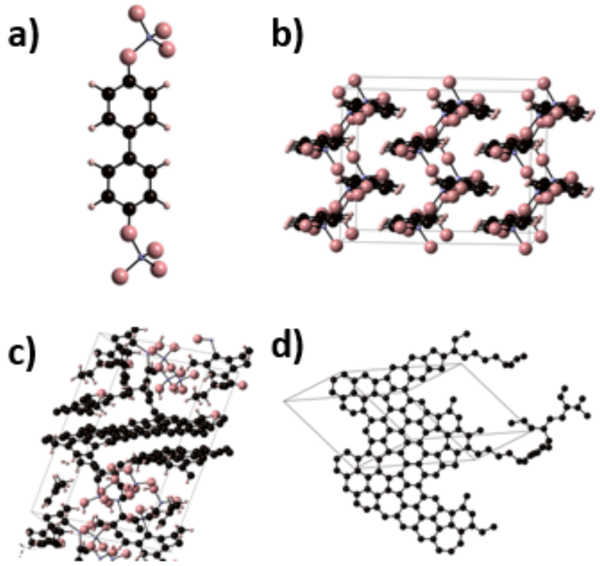

Figure 10. Polymer fragment (a) used to build periodic models. Optimized structures obtained from ab-initio molecular dynamic simulations of heating a model of the DA-polymer at 1200 K (b) and 3000 K (c). The extended carbon arrangement found in the 3000 K model (d). The simulation was performed for about 150 ps under constant pressure allowing the cell to change its shape, though the density remained almost constant (r=1.6 g/cm^3) throughout the simulation. The composition is $Si_8O_{24}C_{96}H_{64}$, no gaseous species were removed during the simulation.

Empirical potential simulations

Throughout our empirical potential simulations of SiOC we observe a characteristic development of structures upon annealing. In Figure 11 we show this for models with composition SiO_2:$C_{0.5}$, which mimics the experimental data reported in Table 1. Figure 11 only shows the carbon atoms of the SiOC structure, with Si and O atoms omitted for clarity. At low temperatures, we observe small carbon fragments dispersed in the model. Typical is the appearance of C_6-rings which have joined to small aromatic units. Increasing the temperature fuses many such small fragments *via edges* to form pieces of graphene sheets. At this stage, some sheets show already curvature. Further increase of temperature produces balls and tubular structures. The amount of “free” carbon impacts the spatial extend of the carbon fragments, see Figure 12. In models with low carbon content, graphene sheets appear isolated and do not form a continuous network. Hence, they are embedded in continuous glass phase. For structures with higher C-content the graphene sheets form extended networks that resemble funnel-webs of certain spiders (e.g. agelenidae). The principle characteristic is again the formation of sheet-like structures separated by and embedded in a glass phase. At higher temperature, these sheets coil up to form balls or tubular structures. Depending on the amount of “free” carbon, the carbon tubes may form a continuous network. These are still embedded in a continuous glass phase. Hence, carbon segregation and glass phase form a bi-continuous system. Our simulations described here yield characteristic diameters of tubular carbon segregations of 1-2 nm. Interestingly, these diameters as well as the typical distance between sheet-like graphene, hence the thicknesses of the glass between carbon segregations, relate to typical scattering lengths observed in SANS and SAXS experiments.[88]

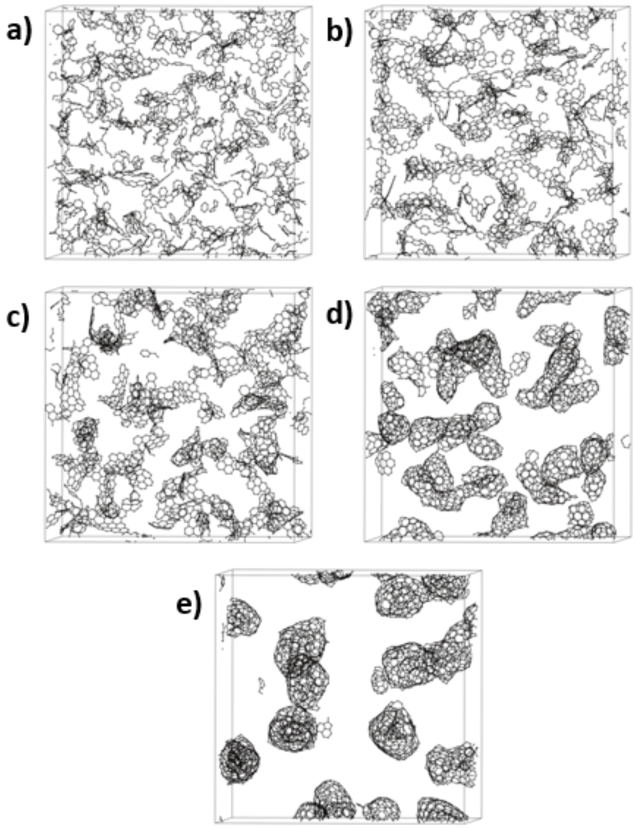

Figure 11. Carbon structures in SiOC for the composition SiO_2:$C_{0.5}$, C:Si = 1:2 obtained in empirical potential simulations. Only C atoms are shown, Si and O have been omitted. The sequence of pictures corresponds to annealing at increasingly higher temperature (parameter T_{MC} in MC-simulations). The size of the (periodic) simulation box is 7.4 nm, the density of all SiOC models is 2.2 g/cm^3.

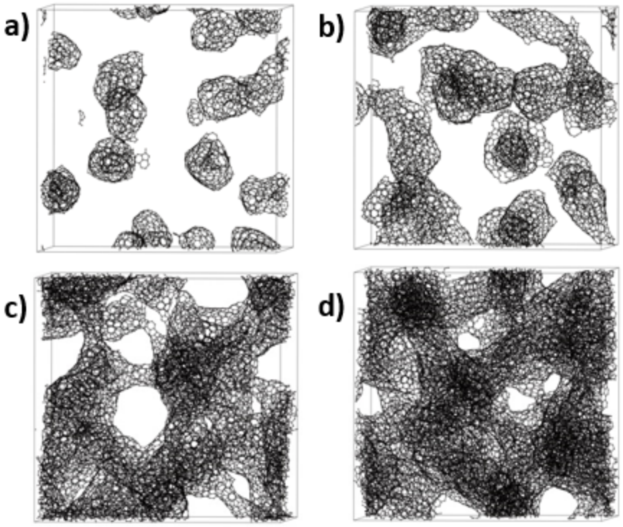

Figure 12. Carbon structures in SiOC obtained at high annealing temperature in empirical potential simulations. The amount of “free” carbon increases in the sequence, C:Si = 0.5, 1, 2, 3. Only C atoms are shown, while Si and O have been omitted. All models exhibit a density of 2.2 g/cm^3, the size of the (periodic) simulation box increases from 7.4 to 8.4 nm with increasing carbon content.

Reactive-Force-Field simulations

To bridge the gap between accurate density functional theory calculations with ab initio simulations and empirical potential molecular dynamics simulations, we recently developed a new reactive force field (ReaxFF[89]) capable to describe properly energy and structure of amorphous silicon oxycarbide.[45] Fitted extensively to quantum-chemical calculations, the reactive force field achieves an accuracy comparable to DFT calculations at significantly lower computational cost. This allows simulations of large system for long times with high fidelity, and is particularly well suited to investigate the polymer-to-ceramic processes.[45]

We investigated the formation of amorphous silicon oxycarbide using ReaxFF using a variety of approaches, including melt-quench simulations and heating polymer structures. Figure 13 shows outcomes, which on one side match ab-initio MD simulations and on the other side connect up to empirical potential simulations.

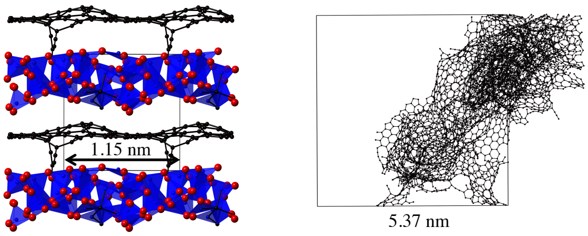

Figure 13. Amorphous silicon oxycarbide models (composition Si_5CO_8+10C; density 2.2 g/m^3) generated via melt-quench simulations using the reactive force field. On the left a

small 120-atom model showing graphene sheet segregated between "glassy" SiOC. Box sizes of this model are ~1.2 nm. On the right the "free" carbon structure in a 12288-atom model (box sizes ~5.4 nm). Si and O are not shown in this model for clarity.

Phase development in small models (100-200 atoms) follows similar patterns in reactive force field simulations as in ab initio molecular dynamic simulations: "Free" carbon segregates into a sheet-like structures. Depending on composition, a small fragment is embedded in silica or an extended sheet separates thin glass layers, see Figure 13. Larger models exhibit carbon sheets with high curvature. Depending on composition, the sp^2-carbon structures resemble fragments of multi-wall tubular carbon structures (Figure 13, right).

Mimicking the processing of DHBP0.1_SG we performed the described simulation several times. Although outcomes vary slightly, final structures show the same features as shown in Figure 14. We observe bean-like segregations of silica (in the moel shown in Figure 14 approximately 6 nm long and 2 nm wide). Carbon atoms "surround" the silica segregations forming various curved carbon fragments. As visible in Figure 14, hydrogen terminates the carbon segregations at various places and may impact further condensation of graphene.

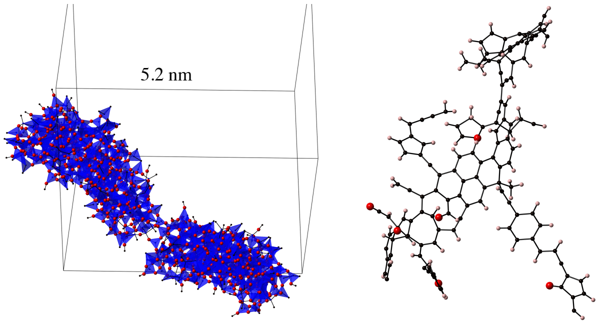

Figure 14. SiOC structure obtained through reactive force field simulations after annealing DHBP0.1_SG. (left) two segregated silica beans; (right) a typical fragment of carbon with curvature.

Unfortunately, mass loss and removal of similar proportions of the initial polymer like in the experiment (Table 1 indicates that 95% of all carbon is lost) appears unfeasible at the time-scales available (~ 1ns) to the simulation: we only removed about 30% of H atoms and ~25% of C atoms as gas molecules. Careful analysis of trajectories yields that during initial heating DHBP0.1_SG tends to dissociate into siloxane and DHBP. Experimentally, DHBP is volatile at 900ºC. Thus, DHBP and its fragments are most likely species lost during annealing, and, consequently, the major source of mass loss. In simulations, however, we don't remove such big fragments, and these become part of the continuous carbon phase, eventually. This difference between experiment and simulation does not impact the general trends.

Conclusions

In summary, we propose a simple and effective method for the formation of metal-catalyst-free bamboo-like MWCNTs in a mesoporous silica matrix using the polymer-derived ceramic process. The influence of initial structure of the precursor, the low temperature of the phase separation as well as the role of the of silica particle sizes and the pore sizes on the formation and microstructural particulars of bamboo-like MWCNTs were discussed. The influence of hydrogen on the bamboo defective structure was highlighted as well. The MWCNTs are formed through a base growth mode within the silica mesoporous structure. The pores are interconnected; therefore, the hot-pressed sample shows a very high electrical conductivity of $2.179 \cdot 10^3$ S/m for only 11.43 wt% carbon in its composition. To our knowledge, this is the highest value reported so far in the literature for SiOC ceramics as well as for MWCNTs/SiO_2 composites.

As shown by high-temperature oxide melt calorimetry, the formation of MWCNTs in a silica matrix is energetically favorable. The thermodynamic stability of the composite is explained by the interface bonding between silica phase and carbon, by the presence of saturated C-H bonds (on the surface of nanotubes, at edges of graphene scrolls and on the corners of nanocages) as well as of silanols units in silica pores.

These new findings further confirm that polymer-derived ceramics route can be used as efficient tool in order to create well-defined carbon-containing nanocomposites just by simple tailoring of the chemical structure of the precursors.

Computational simulations corroborate the formation of tubular carbon apart from silica. Atomistic simulations on three different lengths scales show a consistent picture of carbon segregating from the amorphous glass matrix. The partitioning into two distinct phases is enhanced by the structure of the polymer, which provides ample of intrinsic oxygen for reactions during the polymer-to-ceramic conversion.

To conclude, due to their exceptional properties, such as high electric conductivity, porous structure, high specific surface area, etc., these materials can find applications in several fields such as vehicle/aircraft technology, health & safety, energy storage and conversion, air/water pollution control, airspace applications, etc.

While this study remains the first related to the catalyst-free generation of carbon nanotubes in PDCs, systematic studies are needed to understand the synthesis-structure-property relationship of these ceramics, particularly variation in parameters such as polymeric precursor, chemical composition of ceramic, thermolysis temperature, and free carbon content.

Acknowledgements

GM acknowledges the financial support from DFG (Eigene Stelle grant IO 83/2-1) PK acknowledges support by the National Science Foundation (NSF) through award CMMI-1634448. The computational work was made possible through generous grants by the Texas Advance Computing Center (TACC) in Austin, TACC, Texas, and by the High-Performance Computing facilities at UTA. The calorimetric measurements were performed at the University of California Davis supported by the A.P. Sloan

Foundation's Deep Carbon Observatory. EI acknowledges financial support from DFG (project "Micro-patterned polymer-derived ceramic catalysts and sensors" and the grant IO 64/14-1 within the Heisenberg program,)

References

1. S. Iijima, Nature, 1991. **354**: 56.
2. X. Wang, W. Hu, Y. Liu, C. Long, Y. Xu, S. Zhou, D. Zhu, L. Dai, Carbon, 2001. **39**(10): 1533.
3. M. Nath, B.C. Satishkumar, A. Govindaraj, C.P. Vinod, C.N.R. Rao, Chemical Physics Letters, 2000. **322**(5): 333.
4. M. Terrones, H. Terrones, N. Grobert, W.K. Hsu, Y.Q. Zhu, J.P. Hare, H.W. Kroto, D.R.M. Walton, P. Kohler-Redlich, M. Rühle, J.P. Zhang, A.K. Cheetham, Applied Physics Letters, 1999. **75**(25): 3932.
5. Y. Saito, T. Yoshikawa, Journal of Crystal Growth, 1993. **134**(1): 154.
6. M. Terrones, A. Jorio, M. Endo, A.M. Rao, Y.A. Kim, T. Hayashi, H. Terrones, J.C. Charlier, G. Dresselhaus, M.S. Dresselhaus, Materials Today, 2004. **7**(10): 30.
7. Z.R. Jia, K.C. Kou, M. Qin, H.J. Wu, F. Puleo, L.F. Liotta, Catalysts, 2017. **7**(9).
8. M. Lin, J.P.Y. Tan, C. Boothroyd, K.P. Loh, E.S. Tok, Y.L. Foo, Nano Lett, 2007. **7**(8): 2234.
9. R.T.K. Baker, B Am Phys Soc, 1981. **26**(3): 200.
10. T. Baker, Chem Ind-London, 1982(18): 698.
11. H. Yoshida, S. Takeda, T. Uchiyama, H. Kohno, Y. Homma, Nano Lett, 2008. **8**(7): 2082.
12. S. Costa, E. Borowiak-Palen, A. Bachmatiuk, M.H. Rummeli, T. Gemming, R.J. Kalenezuk, Phys Status Solidi B, 2007. **244**(11): 4315.
13. A. Bachmatiuk, E. Borowiak-Palen, M.H. Rummeli, T. Gemming, R.J. Kallenczuk, Phys Status Solidi B, 2007. **244**(11): 3925.
14. M. Audier, A. Oberlin, M. Oberlin, M. Coulon, L. Bonnetain, Carbon, 1981. **19**(3): 217.
15. O.C. Carneiro, M.S. Kim, J.B. Yim, N.M. Rodriguez, R.T.K. Baker, J Phys Chem B, 2003. **107**(18): 4237.
16. M.H. Rummeli, F. Schaffel, A. Bachmatiuk, D. Adebimpe, G. Trotter, F. Borrnert, A. Scott, E. Coric, M. Sparing, B. Rellinghaus, P.G. McCormick, G. Cuniberti, M. Knupfer, L. Schultz, B. Buchner, Acs Nano, 2010. **4**(2): 1146.
17. P.T.A. Reilly, W.B. Whitten, Carbon, 2006. **44**(9): 1653.
18. M.H. Rummeli, A. Bachmatiuk, F. Borrnert, F. Schaffel, I. Ibrahim, K. Cendrowski, G. Simha-Martynkova, D. Placha, E. Borowiak-Palen, G. Cuniberti, B. Buchner, Nanoscale Res Lett, 2011. **6**.
19. M. Kusunoki, M. Rokkaku, T. Suzuki, Applied Physics Letters, 1997. **71**(18): 2620.
20. D. Takagi, H. Hibino, S. Suzuki, Y. Kobayashi, Y. Homma, Nano Lett, 2007. **7**(8): 2272.

21. M.H. Rummeli, E. Borowiak-Palen, T. Gemming, T. Pichler, M. Knupfer, M. Kalbac, L. Dunsch, O. Jost, S.R.P. Silva, W. Pompe, B. Buchner, Nano Lett, 2005. **5**(7): 1209.
22. H. Liu, D. Takagi, H. Ohno, S. Chiashi, T. Chokan, Y. Homma, Appl Phys Express, 2008. **1**(1).
23. S.A. Steiner, T.F. Baumann, B.C. Bayer, R. Blume, M.A. Worsley, W.J. MoberlyChan, E.L. Shaw, R. Schlogl, A.J. Hart, S. Hofmann, B.L. Wardle, J Am Chem Soc, 2009. **131**(34): 12144.
24. M. Bystrzejewski, A. Bachmatiuk, J. Thomas, P. Ayala, J. Serwatowski, H.W. Hubers, T. Gemming, E. Borowiak-Palen, T. Pichler, R.J. Kalenczuk, B. Buchner, M.H. Rummeli, Phys Status Solidi-R, 2009. **3**(6): 193.
25. A. Bachmatiuk, M. Bystrzejewski, F. Schaffel, P. Ayala, U. Wolff, C. Mickel, T. Gemming, T. Pichler, E. Borowiak-Palen, R. Klingeler, H.W. Hubers, M. Ulbrich, M. Knupfer, D. Haberer, B. Buchner, M.H. Rummeli, Phys Status Solidi B, 2009. **246**(11-12): 2486.
26. B.L. Liu, W.C. Ren, L.B. Gao, S.S. Li, S.F. Pei, C. Liu, C.B. Jiang, H.M. Cheng, J Am Chem Soc, 2009. **131**(6): 2082.
27. S.M. Huang, Q.R. Cai, J.Y. Chen, Y. Qian, L.J. Zhang, J Am Chem Soc, 2009. **131**(6): 2094.
28. A. Bachmatiuk, F. Borrnert, M. Grobosch, F. Schaffel, U. Wolff, A. Scott, M. Zaka, J.H. Warner, R. Klingeler, M. Knupfer, B. Buchner, M.H. Rummeli, Acs Nano, 2009. **3**(12): 4098.
29. A. Bachmatiuk, F. Borrnert, F. Schaffel, M. Zaka, G.S. Martynkowa, D. Placha, R. Schonfelder, P.M.F.J. Costa, N. Ioannides, J.H. Warner, R. Klingeler, B. Buchner, M.H. Rummeli, Carbon, 2010. **48**(11): 3175.
30. J.J. Schneider, N.I. Maksimova, J. Engstler, R. Joshi, R. Schierholz, R. Feile, Inorg Chim Acta, 2008. **361**(6): 1770.
31. M.H. Rummeli, C. Kramberger, A. Gruneis, P. Ayala, T. Gemming, B. Buchner, T. Pichler, Chem Mater, 2007. **19**(17): 4105.
32. L.-L. Tan, W.-J. Ong, S.-P. Chai, A.R. Mohamed, Catalysis Today, 2013. **217**: 1.
33. H.P. Liu, D. Takagi, S. Chiashi, Y. Homma, Carbon, 2010. **48**(1): 114.
34. A. Hirsch, Angew Chem Int Edit, 2009. **48**(30): 5403.
35. R. Riedel, G. Mera, R. Hauser, A. Klonczynski, J Ceram Soc Jpn, 2006. **114**(1330): 425.
36. P. Colombo, G. Mera, R. Riedel, G.D. Soraru, J Am Ceram Soc, 2010. **93**(7): 1805.
37. G. Mera, A. Navrotsky, S. Sen, H.-J. Kleebe, R. Riedel, J Mater Chem A, 2013.
38. C. Stabler, E. Ionescu, M. Graczyk-Zajac, I. Gonzalo-Juan, R. Riedel, J Am Ceram Soc, 2018. **101**(11): 4817.
39. G. Mera, M. Gallei, S. Bernard, E. Ionescu, Nanomaterials-Basel, 2015. **5**(2): 468.
40. S. Widgeon, G. Mera, Y. Gao, E. Stoyanov, S. Sen, A. Navrotsky, R. Riedel, Chem Mater, 2012. **24**(6): 1181.
41. J. Chen, S.W. King, E. Muthuswamy, A. Koryttseva, D. Wu, A. Navrotsky, J Am Ceram Soc, 2016. **99**(8): 2752.
42. A. Navrotsky, J Am Ceram Soc, 2014. **97**(11): 3349.

43. A. Navrotsky, Physics and Chemistry of Minerals, 1977. **2**(1): 89.
44. A. Navrotsky, Physics and Chemistry of Minerals, 1997. **24**(3): 222.
45. I. Ponomarev, A.C.T. van Duin, P. Kroll, J Phys Chem C, 2019.
46. P. Hohenberg, W. Kohn, Phys Rev B, 1964. **136**(3b): B864.
47. G. Kresse, J. Hafner, Phys Rev B, 1994. **49**(20): 14251.
48. G. Kresse, J. Furthmuller, Phys Rev B, 1996. **54**(16): 11169.
49. P.E. Blochl, Phys Rev B, 1994. **50**(24): 17953.
50. G. Kresse, D. Joubert, Phys Rev B, 1999. **59**(3): 1758.
51. S. Grimme, Journal of Computational Chemistry, 2006. **27**(15): 1787.
52. J. Tersoff, Physical Review B, 1988. **38**(14): 9902.
53. J. Tersoff, Physical Review Letters, 1988. **61**(25): 2879.
54. Y. Umeno, T. Kitamura, K. Date, M. Hayashi, T. Iwasaki, Comput. Mater. Sci., 2002. **25**(3): 447.
55. S. Plimpton, J Comput Phys, 1995. **117**(1): 1.
56. H.M. Aktulga, J.C. Fogarty, S.A. Pandit, A.Y. Grama, Parallel Comput, 2012. **38**(4-5): 245.
57. G. Bussi, D. Donadio, M. Parrinello, J Chem Phys, 2007. **126**(1).
58. A.H. Tavakoli, M.M. Armentrout, M. Narisawa, S. Sen, A. Navrotsky, J Am Ceram Soc, 2015. **98**(1): 242.
59. M. Narisawa, F. Funabiki, A. Iwase, F. Wakai, H. Hosono, J Am Ceram Soc, 2015. **98**(10): 3373.
60. M. Graczyk-Zajac, D. Vrankovic, P. Waleska, C. Hess, P.V. Sasikumar, S. Lauterbach, H.J. Kleebe, G.D. Soraru, J Mater Chem A, 2018. **6**(1): 93.
61. H.J. Kleebe, C. Turquat, G.D. Soraru, J Am Ceram Soc, 2001. **84**(5): 1073.
62. C. Turquat, H.-J. Kleebe, G. Gregori, S. Walter, G.D. Sorarù, J Am Ceram Soc, 2001. **84**(10): 2189.
63. D. Tománek, *Guide Through the Nanocarbon Jungle*, in *Buckyballs, nanotubes, graphene and beyond*. 2014, Morgan & Claypool Publishers.
64. J. Gerard Lavin, S. Subramoney, R.S. Ruoff, S. Berber, D. Tománek, Carbon, 2002. **40**(7): 1123.
65. J. Liu, L. Xu, W. Zhang, W.J. Lin, X. Chen, Z. Wang, Y. Qian, The Journal of Physical Chemistry B, 2004. **108**(52): 20090.
66. L. Zhang, X. Zeng, X. Wang, Scientific Reports, 2013. **3**: 3162.
67. P.C. Eklund, J.M. Holden, R.A. Jishi, Carbon, 1995. **33**(7): 959.
68. D.E.H. Jones, Nature, 1996. **381**(6581): 384.
69. C. Branca, F. Frusteri, V. Magazu, A. Mangione, J Phys Chem B, 2004. **108**(11): 3469.
70. C. Branca, F. Frusteri, V. Magazù, A. Mangione, The Journal of Physical Chemistry B, 2004. **108**(11): 3469.
71. J.L. Bantignies, J.L. Sauvajol, A. Rahmani, E. Flahaut, Phys Rev B, 2006. **74**(19).
72. A. Misra, P.K. Tyagi, P. Rai, D.S. Misra, J Nanosci Nanotechno, 2007. **7**(6): 1820.
73. R. Podila, R. Rao, R. Tsuchikawa, M. Ishigami, A.M. Rao, ACS Nano, 2012. **6**(7): 5784.
74. S. Santangelo, G. Messina, G. Faggio, M. Lanza, C. Milone, Journal of Raman Spectroscopy, 2011. **42**(4): 593.

75. L.G. Cançado, K. Takai, T. Enoki, M. Endo, Y.A. Kim, H. Mizusaki, A. Jorio, L.N. Coelho, R. Magalhães-Paniago, M.A. Pimenta, Applied Physics Letters, 2006. **88**(16): 163106.
76. L.G. Cançado, A. Jorio, E.H.M. Ferreira, F. Stavale, C.A. Achete, R.B. Capaz, M.V.O. Moutinho, A. Lombardo, T.S. Kulmala, A.C. Ferrari, Nano Lett, 2011. **11**(8): 3190.
77. N. Larouche, B.L. Stansfield, Carbon, 2010. **48**(3): 620.
78. F. Rosenburg, *The state of carbon and the piezoresistive effect in silicon oxycarbide ceramics*. 2018, Technische Universität Darmstadt: Darmstadt.
79. T. Varga, A. Navrotsky, J.L. Moats, R.M. Morcos, F. Poli, K. Müller, A. Saha, R. Raj, J Am Ceram Soc, 2007. **90**(10): 3213.
80. A.H. Tavakoli, M.M. Armentrout, S. Sen, A. Navrotsky, J Mater Res, 2015. **30**(2): 295.
81. E.V. Suslova, S.V. Savilov, J. Ni, V.V. Lunin, S.M. Aldoshin, Physical Chemistry Chemical Physics, 2017. **19**(3): 2269.
82. N.B. Cherkasov, S.V. Savilov, A.S. Ivanov, V.V. Lunin, Carbon, 2013. **63**: 324.
83. A.A. Levchenko, A.I. Kolesnikov, O. Trofymluk, A. Navrotsky, Carbon, 2011. **49**(3): 949.
84. B.S. Hemingway, J.L. Haas Jr, G.R. Robinson Jr, *Thermodynamic properties of selected minerals in the system Al2O3-CaO-SiO2-H2O at 298.15 K and 1 bar (105 Pascals) pressure and at higher temperatures*, in *Bulletin*. 1982.
85. L. Peng, W. Qisui, L. Xi, Z. Chaocan, Journal of Thermal Analysis and Calorimetry, 2009. **95**(2): 667.
86. D.H. Kuo, M.Y. Su, Surf Coat Tech, 2007. **201**(22-23): 9172.
87. H. Omachi, T. Nakayama, E. Takahashi, Y. Segawa, K. Itami, Nat Chem, 2013. **5**(7): 572.
88. A. Saha, R. Raj, D.L. Williamson, J Am Ceram Soc, 2006. **89**(7): 2188.
89. A.C.T. van Duin, S. Dasgupta, F. Lorant, W.A. Goddard, J Phys Chem A, 2001. **105**(41): 9396.

Summary

The outcome of sol-gel process was synthesized and characterized. The results showed the porous conductive composite material comprising segregated silica phase "wrapped" into multi-wall tubular carbon structures and abundance of MWCNTs in the material.

Our computational findings provided the support to the observations: on different levels we show that carbon indeed exhibits tendency to segregate from silica matrix and, if size and periodic boundary conditions wouldn't be an issue, forms curved tube-like structures.

Melt-quench simulations for the composition Si_5CO_8+10C_{free} yield a layer of silica, strongly resembling silica bilayer[1], "sandwiched" between graphite layers; bonds between silica and "free" carbon mostly connect C atoms that are not incorporated into graphite layer. The same king of structure was obtained with ReaxFF parameterization, descending from Srinivasan[2] and Newsome[3] sets.

Simulations on the bigger scale: tens of thousands to millions of atoms – within Tersoff potential revealed formation of the other type of carbon morphology – curved sheets, multi-walled "beans" and "tubes", that might form continuous carbon structures. I found similar outcome in the ReaxFF melt-quench simulations that comprised 10000 to 50000 atoms.

We annealed the "idealized" model of the polymer precursor in both DFT (192 atoms) and ReaxFF (initially 12288 atoms) of the composition $SiC_{12}O_3H_{10}$. Again, as for SiCO models, DFT simulation yielded the formation of stacked graphite layers, while ReaxFF final outcome exhibits bean-like silica segregations and the beginning of the formation of the curved carbon fragments like those "wrapping" and interconnecting silica domains in the experimentally obtained pictures (Fig.6).

My contribution here, besides developing the ReaxFF parameterization, is setting up and performing ReaxFF simulations that bridged the gap between DFT (small models, carbon as sheets) and Tersoff simulations (huge models, carbon as curved sheets, tubes and “beans”. I showed that ReaxFF simulations yield the outcome similar to DFT (for small models) or Tersoff (for larger ones). “Realistic” annealing simulations also yielded the development of the system into the right direction.

References

1. Huang, P. Y., et al., Direct Imaging of a Two-Dimensional Silica Glass on Graphene. *Nano Lett* **2012**, *12*, 1081-1086.
2. Srinivasan, S. G.; van Duin, A. C. T.; Ganesh, P., Development of a Reaxff Potential for Carbon Condensed Phases and Its Application to the Thermal Fragmentation of a Large Fullerene. *J Phys Chem A* **2015**, *119*, 571-580.
3. Newsome, D. A.; Sengupta, D.; Foroutan, H.; Russo, M. F.; van Duin, A. C. T., Oxidation of Silicon Carbide by O-2 and H2o: A Reaxff Reactive Molecular Dynamics Study, Part I. *J Phys Chem C* **2012**, *116*, 16111-16121.

CONCLUSION

My computational materials research is divided into 2 separate areas. Part I, mostly done within Density Functional Theory approach, is dedicated to enhancing the capabilities of NMR spectroscopy to reveal structure of the amorphous materials by providing computational insights into the structure vs. NMR signal relations. The second part is focused on the development of the empirical Reactive Force Field parameterization suitable to describe silicon oxycarbide ceramics.

Chapter 1 of my computational NMR research concentrates on hafnia-soda-silica and "sol-gel" hafnia-silica models. I've found the correlations between ^{29}Si NMR δ_{iso} and the Si-O-Si or Si-O-Hf angles of the O atoms surrounding this Si site. These findings allow suggesting another approach to the interpretation of the experimental NMR spectra of this amorphous system.

Studies of the NMR vs. structure relations in silicon nitrides constitute my Chapter 2. I explore a wide variety of structures with Si-N bonds, not only limited by Si_3N_4 composition. I reveal the effects of coordination number and Si-N bond length on the chemical shift in silicon nitrides; I suggest the possible reason of NMR peak asymmetry that had been experimentally observed. Compounds with "2-connected" N, however, show the angle vs. NMR relation, familiar from the previous studies of oxides.

In Chapter 3 I contribute to solving the crystal structure of the silicophosphate that was synthesized via sol-gel condensation of tetraalkoxysilanes with pyrophosphoric acid and dissolution of Si in the phosphoric acid. My computationally derived structure aligns well with the experimental observations regarding NMR signals, XRD peak positions and future evolution of the system.

Reactive Force Field development and applications are the content of Part II of my dissertation. It took a while to learn the ways of parameter development and come up with a usable parameterization that approaches DFT level of accuracy for a wide variety of geometries involving Si-C-O-H atoms.

My current ReaxFF parameterization is capable of generating reasonable structures in melt-quench and polymer annealing simulations. Chapter 1 is mostly dedicated to the development strategy and listing its successes. The newly developed UTA1 parameterization is now capable to provide accurate energies of the models and generate reasonable structures in melt-quench and annealing simulations.

Chapter 2 is an experimental research augmented with a multi-scale modeling and computations. In this case ReaxFF is indeed bridging the gap between DFT calculations at small scale and simpler empirical potentials at bigger scale: the outcomes of the simulations for ~100 atoms in ~1 nm cell exhibit similar carbon structure as DFT, while at ~10000 atoms it looks more like the structure generated with Tersoff potential.

ReaxFF simulations of sol-gel condensation with my UTA1 parameterization show promising results; the preliminary outcomes of annealing simulations with reactive atmospheres also reproduce experimental findings. This might be one of the directions to go having it in hands.

Another direction of future investigations – improvement of the parameter set. Nobody's perfect, and my parameters aren't the exception. Improvement, besides fixing problems, might also mean including the description of other elements in order to not be limited by only Si/C/O/H system, but to also be able to describe, for example, Si_3N_4 formation upon annealing of a-SiCO in nitrogen atmosphere.